Research Thesis: Declaration of Authorship

Print name: JOSE MIGUEL GARRO FERNANDEZ

Title of thesis: TRANSITIONAL FLOW MODELLING FOR FLOW PAST A CIRCULAR CYLINDER

I declare that this thesis and the work presented in it is my own and has been generated by me as the result of my own original research.

I confirm that:

1. This work was done wholly or mainly while in candidature for a research degree at this University;
2. Where any part of this thesis has previously been submitted for a degree or any other qualification at this University or any other institution, this has been clearly stated;
3. Where I have consulted the published work of others, this is always clearly attributed;
4. Where I have quoted from the work of others, the source is always given. With the exception of such quotations, this thesis is entirely my own work;
5. I have acknowledged all main sources of help;
6. Where the thesis is based on work done by myself jointly with others, I have made clear exactly what was done by others and what I have contributed myself;

Signature: Date:

UNIVERSITY OF SOUTHAMPTON

Transitional Flow Modelling for Flow Past a Circular Cylinder

by

Jose M. Garro Fernandez

Thesis submitted for PhD

in the
Faculty of Engineering and Physical Sciences
School of Engineering

September 2023

UNIVERSITY OF SOUTHAMPTON

ABSTRACT

FACULTY OF ENGINEERING AND PHYSICAL SCIENCES
SCHOOL OF ENGINEERING

Doctor of Philosophy

by Jose M. Garro Fernandez

This thesis focuses on implementing and analyzing the original transitional Amplification Factor Transport (AFT) model, its extended version with Reynolds Stress Model (RSM) closure using Unsteady Reynolds Averaged Navier Stokes (URANS), and Delayed Detached-Eddy Simulation (DDES) approaches in OpenFOAMv1912. The aim is to enable transition prediction for correlation with wind tunnel tests at scaled-model Reynolds numbers. Verification confirms the required conditions for transition prediction, while validation demonstrates agreement between the implemented and original models. Predictions for transitional flow over a backward-facing step are first investigated. Results highlight the sensitivity in the laminar and transitional regions. AFT and AFT-RSM models demonstrate varying recirculation lengths, whereas Spalart-Allmaras (S-A) and $k-\epsilon$ models show constant recirculation lengths in both regimes. Additionally, AFT and AFT-RSM successfully predict the presence of a tertiary bubble, which is not captured by turbulence models. The performance of AFT-based models for flow past a circular cylinder is then explored. The findings reveal improved predictions compared to fully turbulent approaches across the upper-subcritical, critical, and supercritical regimes. In the upper subcritical regime, the AFT model enhances predictions of pressure, skin friction coefficient, and recirculation length. In the critical regime, although the models struggle with separation-transition interaction, they successfully capture the stretched wake and resulting drag reduction. AFT models demonstrate constant values of C_D and St in the supercritical regime, distinguishing them from $\gamma - Re_\theta$ and γ models. Additionally, the AFT-DDES model exhibits similar performance to AFT and AFT-RSM, while providing an improved description of wake behavior. The correlation study reveals differences between original AFT boundary layer properties and LES simulations for circular cylinder flow. The growth of H_{12} vs H_L in the original model is steeper than LES results, while k_v vs H_{12} shows faster growth in LES due to smaller momentum thicknesses. A single correlation is achieved by averaging both behaviours using two Reynolds numbers. Implemented in OpenFOAM, the new correlations delay transition by approximately two degrees compared to the modified original AFT model.

Contents

Nomenclature **xvii**

1 Introduction **1**
1.1 General Background 1
1.2 Aims and Objectives 5
1.3 Layout of the Thesis 6

2 Literature Review **9**
2.1 Transition Mechanisms 9
2.1.1 Natural Transition 9
2.1.2 Bypass Transition 10
2.1.3 Separation-Induced Transition 11
2.1.4 Reverse Transition 12
2.2 Flow Parameters Influencing Transition 13
2.2.1 Freestream Turbulence 13
2.2.2 Pressure Gradient 13
2.2.3 Other types of Disturbances 13
2.3 The intermittency γ concept 14
2.3.1 Origin and Development of Intermittency 14
2.4 Intermittency Integration 18
2.4.1 Conditionally Averaged Flow Equations 18
2.4.2 Algebraic Correlations 19
2.4.3 Intermittency Transport Equations 21
2.5 Transitional Flow Modelling 23
2.5.1 Local-Correlation-Based $\gamma - Re_\theta$ Model 23
2.5.2 Local-Correlation-Based γ Model 24
2.5.3 Laminar Fluctuation Energy Method 27
2.5.4 LES and DNS for Transition 28
2.5.5 Summary of Transitional Modelling Methods 29
2.6 Backward Facing Step 30
2.6.1 Review of experimental studies 31
2.6.2 Review of numerical studies 33
2.6.3 Summary 34
2.7 Flow past a circular cylinder 35
2.7.1 Review of experimental studies 35
2.7.2 Review of numerical studies 37
2.7.3 Summary 38

3 Amplification Factor Transport Model 41
3.1 Amplification Factor Transport Model . . . 41
3.2 Transitional Amplification Factor Transport with Reynolds Stress Model . 47
3.2.1 Reynolds Stress Model . . . 47
3.2.2 Transitional AFT with Reynolds Stress model . . . 50
3.3 Transitional Delayed Detached Eddy Simulation Amplification Factor Transport Model . . . 52
3.4 Summary . . . 55

4 Zero Pressure Gradient Flat Plate 57
4.1 Details of numerical simulation . . . 58
4.1.1 Simulation domain and boundary conditions . . . 58
4.1.2 Design of the grids . . . 58
4.1.3 Numerical schemes . . . 59
4.2 Zero Pressure Gradient Flat Plate Verification and Validation . . . 59
4.2.1 Sensitivity to wall-normal grid distribution . . . 59
4.2.2 N_{crit} effect . . . 62
4.2.3 Verification of the AFT and AFT-RSM models . . . 62
4.2.4 Validation for AFT and AFT-RSM . . . 66
4.3 Summary . . . 68

5 Backward Facing Step 71
5.1 Details of numerical simulation . . . 71
5.1.1 Simulation domain and boundary conditions . . . 71
5.1.2 Numerical properties . . . 73
5.1.3 Design of the grids . . . 73
5.2 Results and Discussion . . . 75
5.2.1 Laminar Region - $Re < 1200$ . . . 75
5.2.2 Transitional Region - $1200 < Re < 6600$ . . . 78
5.2.3 Turbulent Region - $Re > 6600$ . . . 81
5.3 Summary . . . 83

6 Validation at $Re_D = 3900$ for a circular cylinder flow 85
6.1 Details of numerical simulations . . . 86
6.1.1 Simulation domain and boundary conditions . . . 86
6.1.2 Numerical properties . . . 87
6.2 Validation - $Re_D = 3900$ . . . 88
6.2.1 Transitional URANS . . . 88
6.2.2 Transitional DDES . . . 97
6.2.3 Summary . . . 102

7 Performance of AFT models at different Reynolds number regimes 107
7.1 Sub-critical - $Re_D = 1.5 \times 10^5$ . . . 108
7.1.1 Mesh and computational setup . . . 108
7.1.2 Prediction of the flow-field . . . 108
7.1.3 Summary . . . 116
7.2 Critical - $Re_D = 3.5 \times 10^5$ . . . 118
7.2.1 Mesh and computation setup . . . 118

7.2.2 Predictions of the flow-field . . . 119
7.2.3 Summary . . . 127
7.3 Super-critical - $Re_D = 6.5 - 8.5 \times 10^5$ . . . 130
7.3.1 Mesh and computation setup . . . 130
7.3.2 Predictions of the flow-field . . . 130
7.3.3 Summary . . . 141
7.4 Mean Flow quantities at different Reynolds numbers . . . 144
7.4.1 Drag coefficient C_D . . . 144
7.4.2 Strouhal number St . . . 145
7.4.3 Minimum pressure ($-C_{p,min}$) and separation point $\phi_{i,sep}$ . . . 148
7.4.4 Base pressure $-C_{p,b}$ and recirculating length L_r/D . . . 149
7.5 Summary . . . 152

8 Analysis of the Amplification Factor Transport Correlations 155
8.1 Initial correlations . . . 156
8.2 Circular cylinder vs Falkner-Skan profiles . . . 158
8.2.1 Relation between the integral shape factor (H_{12}) and local shape factor (H_L) . . . 158
8.2.2 Relation between Re_θ and Re_V via proportionality function k_v . . . 160
8.2.3 Function for the critical Reynolds number Re_{cr} . . . 161
8.2.4 Function for the growth of amplification factor dn/dRe_θ . . . 162
8.3 Analysis of Correlations Impact . . . 163
8.3.1 Sub-critical regime, $Re_D = 1 \times 10^5$ . . . 163
8.3.2 Critical regime, $Re_D = 3.5 \times 10^5$ . . . 166
8.3.3 Super-critical regime, $Re_D = 8.5 \times 10^5$ . . . 166
8.3.4 Summary . . . 167
8.4 Conclusions . . . 168

9 Conclusion and Future work 171
9.1 Contribution of the AFT . . . 171
9.2 Analysis of AFT performance . . . 172
9.3 Future Work Suggestions . . . 174

Bibliography 177

List of Figures

1.1 (a) Discrepancies in pressure distribution for a section of an airfoil profile and (b) boundary layer shock-induced separation discrepancies presented by Blackwell (2013) for low and high Reynolds numbers. 2
1.2 Drag coefficient distribution in terms of Reynolds number for flow past a circular cylinder and its regimes based on Schewe (1983) and Zdravkovich (1997) discussions. 3
1.3 Pressure distribution on a single cylinder with transition trip by Jenkins et al. (2006) 4

2.1 Transition process starting from T-S waves and finishing in fully-turbulent flow illustrated by White (2006) 10
2.2 Long and short bubble effects on freestream velocity and wake Malkiel and Mayle (1996). 12
2.3 Illustration of the observations made by Emmons (1951) 14
2.4 Digitalized Orr-Sommerfeld spatial amplification curves for different frequencies (dashed line) along the envelope of the growth-rate $\tilde{n}$ (solid line) versus the momentum thickness Reynolds number (Re_θ) from Gleyzes et al. (1985). Both terms are presented for three shape factors as denoted in the top side. 26
2.5 Schematic domain for backward-facing step and recirculating regions. . . . 31
2.6 Dimensionless recirculation regions (x/S) in terms of Reynolds number based on the hydraulic diameter of the channel (Re_{D_h}) reported in experiments by Armaly et al. (1983). 31

3.1 Variation of the k_v, dn/dRe_θ and $Re_{\theta,cr}$ factors in terms of the H_{12}. . . . 44
3.2 Definition of f_{t2} method in OpenFOAM C++ code. 45
3.3 Definition of γ variable in OpenFOAM C++ code. 46
3.4 Definition of γ transport equation in OpenFOAM C++ code. 46
3.5 Definition of $\tilde{d_m}$ in OpenFOAM C++ code. 54

4.1 Domain and Boundary conditions for the zero-pressure-gradient flat plate case. (Figure not to scale) 58
4.2 Residuals behaviour of AFT for SIMPLEC method using finest grid from AIAA family grid. 60
4.3 The y^+ distribution for a zero-pressure-gradient flat plate cases given in Table 4.2. 60
4.4 The y^+ impact on C_f for the transitional AFT and AFT-RSM models. . . 61
4.5 Maximum value of $\tilde{n}$ varying N_{crit} at 5 and 9 for AFT transition model using TMW 137×97 Grid. 62

4.6 Maximum value of $\tilde{n}$ varying N_{crit} at 5 and 9 for AFT-RSM transition model using TMW 137×97 Grid. 63
4.7 Validation of transition prediction using AFT for TMW and AIAA Grid families with $N_{crit} = 10.3$. 63
4.8 Validation of transition prediction using AFT-RSM for TMW and AIAA Grid families with $N_{crit} = 10.3$. 64
4.9 Distribution of $\tilde{n}$ and H_{12} for AFT transition model using TMW 545×385 Grid. 65
4.10 Distribution of $\tilde{n}$ and H_{12} for AFT-RSM transition model using TMW 545×385 Grid. 65
4.11 Velocity profiles at laminar and turbulent regions of the flow with AFT and AFT-RSM transition models using TMW 545×385 Grid. 66
4.12 C_f distribution for AFT and AFT-RSM transition model using TMW 545×385 Grid with experimental data and γ, $\gamma - Re_\theta$ models, theoretical C_f and experimental data by Schubauer and Skramstad (1947). 67
4.13 Dimensionless velocity profiles for AFT and AFT-RSM transition model using TMW 545×385 Grid compared to Blasius and Law of the wall theoretical predictions. 68

5.1 Schematic domain for backward-facing step and recirculating regions. (Figure not to scale) 72
5.2 Predictions of x_1/S throughout the laminar region using AFT, AFT-RSM and S-A, including experimental data by Armaly et al. (1983), laminar DNS simulations by Erturk (2008) and $k - \epsilon$ simulations by Ratha and Sarkar (2015). 75
5.3 Normalized velocity profile predictions at $Re = 100$ for AFT, AFT-RSM and S-A, including experimental data by Armaly et al. (1983) at positions $x/S = 0,\ 2.55,\ 3.06,\ 3.57,\ 4.18,\ 6.12,\ 12.04$. 76
5.4 Normalized velocity profile predictions at $Re = 300$ for AFT, AFT-RSM and S-A, including experimental data by Armaly et al. (1983) at positions $x/S = 0,\ 2.55,\ 3.06,\ 3.57,\ 4.18,\ 6.12,\ 8.52,\ 11.84,\ 13.57$. 77
5.5 Predictions of x_2/S and x_3/S throughout the laminar region using AFT, AFT-RSM and S-A, including experimental data by Armaly et al. (1983), laminar DNS simulations by Erturk (2008) and $k - \epsilon$ by Ratha and Sarkar (2015). 78
5.6 Predictions of x_i/S where $i = [1, 5]$ throughout laminar, transitional and turbulent regime for AFT, including experimental data by Armaly et al. (1983). 79
5.7 Predictions of x_i/S where $i = [1, 5]$ throughout laminar, transitional and turbulent regime for AFT-RSM, including experimental data by Armaly et al. (1983). 81
5.8 Predictions of x_i/S where $i = [1, 5]$ throughout laminar, transitional and turbulent regime for S-A, including experimental data by Armaly et al. (1983) and $k - \epsilon$ by Ratha and Sarkar (2015). 81
5.9 Velocity profile predictions at $Re = 1295$ for AFT, AFT-RSM and S-A, including experimental data by Armaly et al. (1983) at positions $x/S = 0,\ 3.06,\ 6.12,\ 10.2,\ 12.24,\ 15.32,\ 18.37,\ 22.45,\ 24.49,\ 26.53$. 82
5.10 Distribution of γ at $Re = 7000$ using transitional AFT model. 82

6.1 Schematic domain for circular cylinder simulation case including the inner cylinder for the wake refinement of $5D$. (Figure not to scale) 86
6.2 Example of instantaneous velocity magnitude contour plot for circular cylinder flow at $Re = 1.5\times10^5$ to show that any spurious data is generated with the joint forward facing and backward facing boundaries of the domain. 87
6.3 (a) C_p and (b) C_f distribution for AFT-G1, AFT-G2, AFT-RSM-G1 and AFT-RSM-G2 transition models for validation case at $Re_D = 3900$. 90
6.4 Mean normalized streamwise velocity $\overline{U}/U_\infty$ at centerline downstream the cylinder surface. 92
6.5 Normalized (a) $\overline{U}/U_\infty$ distribution and (b) $\overline{V}/U_\infty$ distribution for AFT-G1, AFT-G2, AFT-RSM-G1 and AFT-RSM-G2 transition models (see Figure 6.4 for legend) and experimental data by (∘) Parnaudeau et al. (2008), (□) Lourenco and Shih (1993) and (△) Ong and Wallace (1996) . 93
6.6 Mean variance of normalized streamwise velocity fluctuations $\overline{u'u'}/U_\infty^2$ at centerline downstream of the cylinder surface. 95
6.7 Normalized (a) $\overline{u'u'}/U_\infty^2$ distribution and (b) $\overline{v'v'}/U_\infty^2$ distribution for AFT-G1, AFT-G2, AFT-RSM-G1 and AFT-RSM-G2 transition models (see Figure 6.4 for legend) and experimental data by (∘) Parnaudeau et al. (2008), (□) Lourenco and Shih (1993) and (△) Ong and Wallace (1996) . 96
6.8 (a) C_p and (b) C_f distribution for AFTDDES-G1, AFTDDES-G2 and AFTDDES-G3 transition models for validation case at $Re_D = 3900$. . . . 98
6.9 Mean normalized streamwise velocity $\overline{U}/U_\infty$ at centerline downstream of the cylinder surface. 99
6.10 Normalized (a) $\overline{U}/U_\infty$ distribution and (b) $\overline{V}/U_\infty$ distribution for AFTDDES-G1, G2 and G3, transition models (see Figure 6.9 for legend) and experimental data by (∘) Parnaudeau et al. (2008), (□) Lourenco and Shih (1993) and (△) Ong and Wallace (1996) 100
6.11 Mean-variance of streamwise velocity fluctuations $\overline{u'u'}/U_\infty^2$ at centerline downstream of the cylinder surface. 101
6.12 Normalized (a) $\overline{u'u'}/U_\infty^2$ distribution and (b) $\overline{v'v'}/U_\infty^2$ distribution for AFTDDES-G1, G2 and G3 transition models (see Figure 6.9 for legend) and experimental data by (∘) Parnaudeau et al. (2008), (□) Lourenco and Shih (1993) and (△) Ong and Wallace (1996) 103

7.1 (a) C_p distribution with Achenbach (1968) experimental data at $Re_D = 1 \times 10^5$and (b) C_f distribution with experimental data by Cantwell and Coles (1983) and Kim (2006) along current predictions with SST, AFT, AFT-RSM, AFT-DDES, Langtry and Menter (2009) and Menter et al. (2015) model at $Re_D = 1.5 \times 10^5$. 111
7.2 Mean normalized streamwise velocity $\overline{U}/U_\infty$ at centerline downstream the cylinder surface. 112
7.3 Mean normalized Reynolds stress term $\overline{u'v'}/U_\infty^2$ at $x/D = 1$ downstream the cylinder surface. 114
7.4 Mean normalized variance of streamwise velocity fluctuations $\overline{u'u'}/U_\infty^2$ at $x/D = 1, 3, 7$ downstream the cylinder surface. 115
7.5 Mean normalized variance cross-stream velocity fluctuations $\overline{v'v'}/U_\infty^2$ at $x/D = 1, 3, 7$ downstream the cylinder surface. 116
7.6 Q criterion iso-surface representation of value $Q = 200$ for 3D computation using AFT. 117

7.7 Q criterion iso-surface representation of value $Q = 200$ for 3D computation using AFT-DDES. 117
7.8 (a) C_p distribution with Bursnall and Loftin (1951) experimental data at $Re_D = 3.5 \times 10^5$ and LES by Cheng et al. (2017) and Rodríguez et al. (2015) and (b) C_f distribution with LES predictions by Cheng et al. (2017) at $Re_D = 3.5 \times 10^5$. 121
7.9 Mean normalized streamwise velocity $\overline{U}/U_\infty$ at centerline downstream the cylinder surface. 124
7.10 Mean normalized variance of streamwise velocity fluctuations $\overline{u'u'}/U_\infty^2$ at centerline downstream the cylinder surface. 125
7.11 Mean normalized variance of streamwise velocity fluctuations $\overline{u'u'}/U_\infty^2$ at $x/D = 1, 3, 7$ downstream the cylinder surface. 126
7.12 Mean normalized variance of cross-stream velocity fluctuations $\overline{v'v'}/U_\infty^2$ at $x/D = 1, 3, 7$ downstream the cylinder surface. 127
7.13 Q criterion iso-surface representation of value $Q = 300$ for 3D computation using AFT-DDES. 127
7.14 (a) C_p distribution and (b) C_f distribution with experimental data by Roshko (1961) and Spitzer (1965) at $Re_D = 6.5 - 7.5 \times 10^5$ respectively along current predictions with SST, AFT, AFT-RSM, AFT-DDES, Langtry and Menter (2009) and Menter et al. (2015) model at $Re_D = 6.5 \times 10^5$. 132
7.15 (a) C_f distribution with Achenbach (1968) and Shih et al. (1993) experimental data at $Re_D = 8.5 \times 10^5$and (b) C_p distribution with experimental data by Achenbach (1968) and LES by Rodríguez et al. (2015) along current predictions with SST, AFT, AFT-RSM, AFT-DDES, Langtry and Menter (2009) and Menter et al. (2015) model at $Re_D = 8.5 \times 10^5$. 134
7.16 Mean normalized streamwise velocity (a) $\overline{U}/U_\infty$ at $Re_D = 6.5 \times 10^5$ and (b) $\overline{U}/U_\infty$ at $Re_D = 8.5 \times 10^5$ at centerline $y/D = 0$. 135
7.17 Mean normalized variance of streamwise velocity fluctuations (a) $\overline{u'u'}/U_\infty^2$ at $Re_D = 6.5 \times 10^5$ and (b) $\overline{u'u'}/U_\infty^2$ at $Re_D = 8.5 \times 10^5$ at centerline $y/D = 0$. 137
7.18 Mean normalized variance of streamwise velocity fluctuations $\overline{u'u'}/U_\infty^2$ at $x/D = 1, 3, 7$ downstream the cylinder surface. 138
7.19 Mean normalized variance of cross-stream velocity fluctuations $\overline{v'v'}/U_\infty^2$ at $x/D = 1, 3, 7$ downstream the cylinder surface. 139
7.20 (a) $Q_{criterion} = 500$ for AFT-DDES at $Re_D = 8.5 \times 10^5$ showing the vortical structures within the wake and (b) zoom of the $Q_{criterion} = 500$ close to cylinder surface to show the laminar separation bubble line across the span. 140
7.21 (a) C_D variation with Reynolds number using AFT, AFT-RSM and AFT-DDEs along Menter (1993), Langtry and Menter (2009), Menter et al. (2015) model predictions and literature data DES by Vaz et al. (2009), LES by Rodríguez et al. (2015) and experimental data by Schewe (1983) with $Tu = 0.4\%$, (b) C_D variation with Reynolds number using AFT, AFT-RSM and AFT-DDES along Menter (1993), Langtry and Menter (2009), Menter et al. (2015) model predictions and experimental data by Roshko (1961) with $Tu = 4\%$. 146

7.22 (a) St variation with Reynolds number using AFT, AFT-RSM and AFT-DDEs along Menter (1993), Langtry and Menter (2009), Menter et al. (2015) model predictions and literature data DES by Vaz et al. (2009), LES by Rodríguez et al. (2015) and experimental data by and Schewe (1983) with $Tu = 0.4\%$, (b) St variation with Reynolds number using AFT, AFT-RSM and AFT-DDES along Menter (1993), Langtry and Menter (2009), Menter et al. (2015) model predictions and experimental data by Schewe (1983) with $Tu = 4\%$. 147
7.23 (a) $-C_{p,min}$ variation with Reynolds number using AFT, AFT-RSM and AFT-DDEs along Menter (1993), Langtry and Menter (2009), Menter et al. (2015) model predictions and literature LES by Rodríguez et al. (2015) and Cheng et al. (2017). (b) ϕ_s variation with Reynolds number using AFT, AFT-RSM and AFT-DDEs along Menter (1993), Langtry and Menter (2009), Menter et al. (2015) model predictions and literature LES by Rodríguez et al. (2015) and Cheng et al. (2017). 150
7.24 (a) $-C_{p,b}$ variation with Reynolds number using AFT, AFT-RSM and AFT-DDEs along Menter (1993), Langtry and Menter (2009), Menter et al. (2015) model predictions and literature LES by Rodríguez et al. (2015) and Cheng et al. (2017) and (b) L_r/D variation with Reynolds number using AFT, AFT-RSM and AFT-DDEs along Menter (1993), Langtry and Menter (2009), Menter et al. (2015) model predictions and literature LES by Rodríguez et al. (2015) and Liu et al. (2019) 151

8.1 (a) The behaviour of H_{12} in terms of H_L for LES predictions at $Re_D = 1 \times 10^5$ and 5.3×10^5 and (b) the averaged correlation from two Reynolds numbers. 160
8.2 (a) The behaviour of k_v in terms of H_{12} for LES predictions at $Re_D = 1 \times 10^5$ and 5.3×10^5 and (b) the averaged correlation from the two Reynolds numbers. 161
8.3 (a) The behaviour of $Re_{\theta,cr}$ in terms of H_{12} for LES predictions at $Re_D = 1 \times 10^5$ and 5.3×10^5 and (b) the averaged correlation from two Reynolds numbers. 162
8.4 The behaviour of dn/dRe_θ in terms of H_{12} for LES predictions at $Re_D = 1 \times 10^5$ and 5.3×10^5. 163
8.5 (a) C_f predictions within the supercritical regime at $Re_D = 1.5 \times 10^5$ with the original AFT and modified version along Achenbach (1968) measurements $Re_D = 1.5 \times 10^5$ and (b) C_p with LES data by Kim (2006) and measurements by Cantwell and Coles (1983) 164
8.6 (a) γ contour and (b) $\tilde{n}$ for AFT with $N_{crit} = 9$ with averaged streamlines. 165
8.7 (a) γ contour and (b) $\tilde{n}$ for AFT with $N_{crit} = 15$ with averaged streamlines. 165
8.8 Velocity magnitude with averaged streamlines for laminar flow solution. . 166
8.9 (a) C_f predictions within the critical regime at $Re_D = 3.5 \times 10^5$ with the original AFT and modified version along Cheng et al. (2017) LES predictions at $Re_D = 3.5 \times 10^5$ and (b) C_p with LES data by Rodríguez et al. (2015), Cheng et al. (2017) and measurements by Bursnall and Loftin (1951) measurements 167

8.10 (a) C_f predictions within the supercritical regime at $Re_D = 8.5 \times 10^5$ with the original AFT and modified version along Achenbach (1968) measurements $Re_D = 8.5 \times 10^5$ and (b) C_p with LES data by Rodríguez et al. (2015) and measurements by Achenbach (1968) 168

List of Tables

4.1 Grid characteristics for TMW and AIAA families. 59
4.2 Grid characteristics for different y^+ distributions. 60

5.1 Primary dimensionless reattachment length (x_1/S) predictions for backward-facing step for different CFL using AFT, AFT-RSM and S-A at $Re = 1200$. 73
5.2 Grid characteristics of four different distributions for backward-facing step. 74
5.3 Predictions of x_1/S using AFT, AFT-RSM and S-A for grid sensitivity study for the backward-facing step. 74

6.1 Grid characteristics for AFT, AFT-RSM and AFT-DDES simulations for the validation case at $Re_D = 3900$. 89
6.2 Mean flow field characteristics at $Re_D = 3900$ for the validation. 105

7.1 Numerical resolutions and schemes for grid at different Reynolds numbers 109
7.2 Mean flow field characteristics at $Re_D = 1.5 \times 10^5$ for transitional URANS and literature data. 110
7.3 Mean flow quantities at $Re_D = 3.5 \times 10$ using transitional URANS and literature data. 129
7.4 Mean flow field characteristics at $Re_D = 6.5 \times 10^5$ and $Re_D = 8.5 \times 10^5$ for transitional URANS and literature data. 143

Nomenclature

C_D	Drag coefficient
C_f	Skin friction coefficient
C_p	Pressure coefficient
$-C_{p,b}$	Back pressure coefficient
$-C_{p,min}$	Minimum pressure coefficient
$\tilde{d}$	DDES length scale
$\tilde{d}_m$	Modified DDES length scale
D	Circular cylinder diameter, m
dn/dRe_θ	Growth rate of amplification factor
d_w	Wall distance
h	Height of the inlet channel, m
H	Height of the channel, m
H_{12}	Integral shape factor
H_L	Local shape factor
k	Turbulent kinetic energy, m^2/s^2
L_f/D	Dimensionless formation length
L_r/D	Dimensionaless recirculation length
$\tilde{n}$	Amplifcation Factor term
N_{crit}	Critical Amplification Factor
Q	Q criterion
Re	Reynolds number
Re_D	Reynolds number based on cylinder diameter
Re_Dh	Reynolds number based on hydraulic diameter of the channel
Re_v	Vorticity Reynolds number
Re_x	Reynolds number based on streamwise distance
Re_θ	Momentum thickness Reynolds number
$Re_{\theta,cr}$	Critical momentum thickness Reynolds number
S	Strain rate magnitude, s^{-1}
St	Strouhal number
Tu	Free-stream turbulence level, %
$\overline{U}$	Mean streamwise velocity, m/s
$\overline{u'u'}$	Variance of streamwise mean velocity fluctuations

u^+	Dimensionless velocity in terms of friction velocity
U_b	Bulk velocity
$-U_{min}$	Minimum velocity
$\overline{u'v'}$	Mean Reynolds stress
U_∞	Free-stream velocity, m/s
$\overline{V}$	Mean crossflow velocity
$\overline{v'v'}$	Variance of crossflow mean velocity fluctuations
x_i/S	Dimensionless distance of recirculation region with subindex "i"
y^+	Dimensionless wall distance
γ	Intermittency term
δ	Boundary layer thickness, m
ϵ	Dissipation term, m^2/s^3
θ	Momentum thickness,
μ	Dynamic viscosity, kg m/s
μ_t	Turbulent dynamic eddy viscosity, kg m/s
ν	Kinematic viscosity, m^2/s
$\tilde{\nu}$	Modified kinematic viscosity, m^2/s
ν_t	Turbulent kinematic eddy viscosity, m^2/s
ϕ	Angle from the front stagnation point, deg
ρ	Density, kg/m^3
σ_i	Diffusion coefficient in transport equations
τ_{ij}	Reynolds stress term
Φ_{ij}	Pressure-strain redistribution term
ϕ_{BL}	Length of the separation bubble
$\phi_{l,s}$	Laminar separation point
$\phi_{t,s}$	Turbulent separation point
Ω	Vorticity magnitude, s^{-1}
ω	Specific dissipation rate, s^{-1}
AIAA	American Institute of Aeronautics and Astronautics
AFT	Amplification Factor Transport model
AFT-DDES	Delayed Detached-Eddy simulation with Amplification Factor Transport model
AFT-RSM	Amplification Factor Transport coupled to Reynolds Stress Model
BFS	Backward-facing step
CFD	Computational Fluid Dynamics
CFL	Courant-Friedrichs-Lewy number
DES	Detached-eddy simulation
DDES	Delayed Detached-eddy simulation
LES	Large Eddy Simulation
S-A	Spalart-Allmaras Turbulence model
PISO	Pressure-Implicit with Splitting Operators
SIMPLE	Semi-Implicit Method for Pressure Linked Equations

SIMPLEC	Semi-Implicit Method for Pressure Linked Equations-Consistent
SST	Shear Stress Transport Turbulence Model
TMW	Turbulence Modelling Website
URANS	Unsteady Reynolds Averaged Navier-Stokes

Chapter 1

Introduction

1.1 General Background

The main goal of Computational Fluid Dynamics (CFD) and wind tunnel testing in the aeronautical industry is to predict accurately flight conditions and if possible, to accurately capture all the flow physics, i.e. transition, flow separation etc. Achieving such conditions is possible these days in facilities like the European Transonic Windtunnel (ETW) or the National Transonic Facility (NTF) in the USA. These facilities are cryogenic wind tunnels and they are therefore capable of matching Reynolds numbers in flight conditions. For example, Boeing, tested the validity of the measurements of flight performance in the wind tunnel to compare with flight testing as reported by Blackwell (2013). These facilities are designed for complex geometries or final designs but are prohibitively expensive for simpler tests. Thus, the use of simpler facilities, which are not capable of matching free-flight Reynolds numbers introduces potential errors when tripping boundary layer such as displaced shock positions, forced laminar separation bubbles, earlier separation position due to a mismatch between the boundary layer growth for both low and high Reynolds number conditions Blackwell (2013).

The transition position is highly dependent on the Reynolds number, as it is strongly related to the thickness and state of the boundary layer. Thus, in lower Reynolds number conditions or facilities, the transition is sometimes forced using a trip, which helps to match the high Reynolds number transition location. Determining the transition location is relatively easy for simple geometries. However, it becomes difficult for complex geometries, thus uncertainty is present about how appropriate the tripping location and size is. Furthermore, determining the transition location is just a part of the problem since the flow is essentially different to the high Reynolds number flow field downstream of the trip, as it is still under low Reynolds number conditions. Boundary layers will potentially be thicker than the real boundary layer which could lead to earlier separation positions than in the high Reynolds number case.

An example of potential errors is shown in Figure 1.1 for an airfoil profile. In the wind tunnel, where a low Reynolds number is achieved, the boundary layer is tripped at the same position as in-flight conditions. The larger Reynolds number at in-flight conditions however made the relative thickness of the boundary layer smaller, since the turbulent boundary layer thickness scales with $Re^{-1/5}$. Thus, the thinning of the boundary layer moves the shock separation in the streamwise direction closer to the trailing edge, while the thickening of the boundary layer for a lower Reynolds number induces an earlier separation. Consequently, readings of lift and drag coefficients will differ between the two cases.

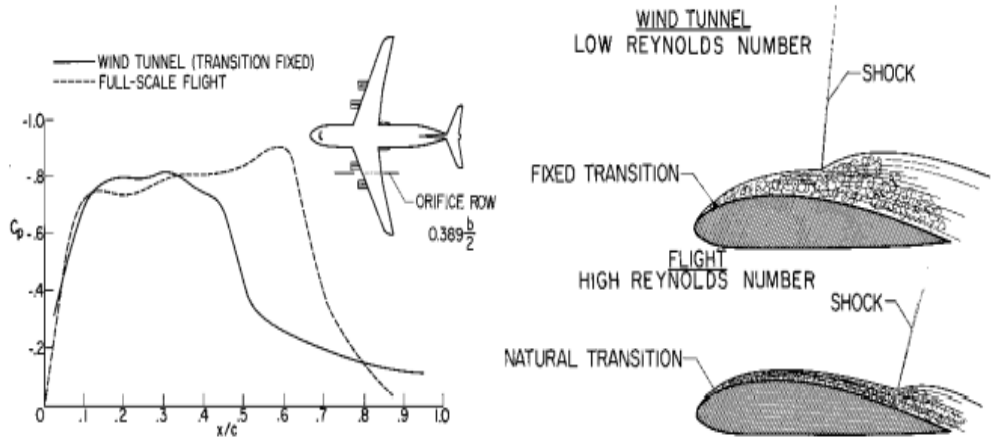

FIGURE 1.1: (a) Discrepancies in pressure distribution for a section of an airfoil profile and (b) boundary layer shock-induced separation discrepancies presented by Blackwell (2013) for low and high Reynolds numbers.

Differences presented in the paragraph above are also important for bluff bodies, specifically for flow past a circular cylinder at a high Reynolds number. That is the main interest and focus of this work. At high Reynolds numbers ($Re_D > 3.8 \times 10^5$), flow past a circular cylinder is characterized by undergoing boundary layer transition and separation over the cylinder surface. It is crucial to achieving an accurate estimation of these features for an appropriate description of the flow field. Figure 1.2 presents the behaviour of C_D and St as a function of Reynolds number for smooth circular cylinder and low freestream turbulence level, which is divided into four regimes. Sub-critical is characterised by a laminar flow followed by a laminar separation when the flow cannot withstand the pressure gradient. With an increased Reynolds number, the flow enters the critical regime where transition and separation occur over one side of the cylinder surface. This is characterised by the sharp drop of C_D, and symmetry between the two bubbles is achieved within the supercritical regime. A further increase of Reynolds number would lead to a completely turbulent boundary layer at the early stages of the upstream face.

Thus, to achieve a similar flow field to high Reynolds number conditions when testing

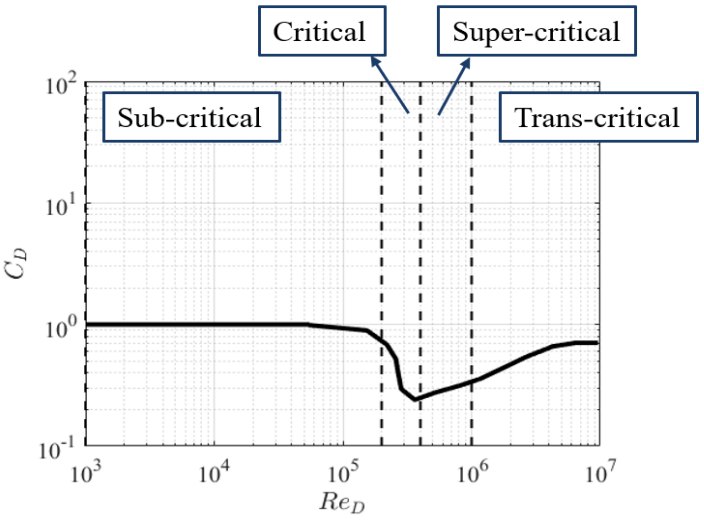

FIGURE 1.2: Drag coefficient distribution in terms of Reynolds number for flow past a circular cylinder and its regimes based on Schewe (1983) and Zdravkovich (1997) discussions.

at low Reynolds number conditions, the tripping of the boundary layer is still necessary. However, the question remains where to trip and according to what conditions. Tripping the boundary layer within the sub-critical regime to match transition with high Reynolds number conditions, could introduce enough disturbances to cause transition into a turbulent state before the laminar separation can occur or even introduce separation bubbles where there should be none as tripping experiments show between sub-critical regime Jenkins et al. (2006) and trans-critical Roshko (1961) experimental data, as shown in Figure 1.3. In addition, differences in the turbulent boundary layer thickness would lead the thicker boundary layer under the low Reynolds number conditions to an earlier separation, which was confirmed by Roshko (1961). Drag is underpredicted by approximately 0.1 with measurements by Roshko (1961). Consequently, there are always doubts about the validity of the trip location and its influence on the overall flow field, particularly when compared to numerical simulations.

The main motivation of this work is then to predict transition using CFD at high Reynolds numbers and correlate with wind tunnel tests at scale Reynolds numbers. The importance of CFD has become more significant with the increase in computational capability. The calculation of the transition point requires either experiments or expensive computations such as Direct Numerical Simulation (DNS) or Large Eddy Simulation (LES). Experiments to determine transition are highly dependent on test conditions and geometries, thus it is complex to get accurate empirical correlations for determining the transition location. On the other hand, DNS and LES simulations require a lot of computational resources and are massively time-consuming for high Reynolds numbers and industrial applications. However, recent research on Reynolds-averaged Navier-Stokes (RANS) approaches shows promising applications with less consuming

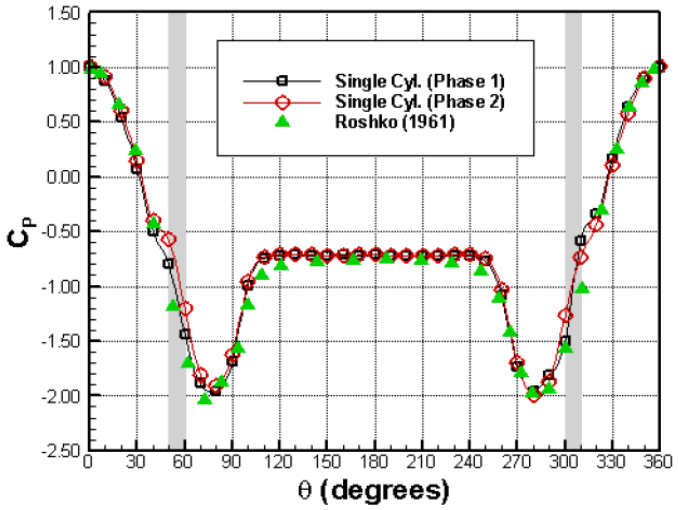

FIGURE 1.3: Pressure distribution on a single cylinder with transition trip by Jenkins et al. (2006)

estimations, though further verification and validation are still required as lastly discussed in the AIAA Transitional Modelling workshop held in Chicago during the AIAA Aviation Forum of 2022.

Before proceeding with the different models, transitional modelling aims to tackle natural and bypass transitions. Briefly, since both transition mechanisms will be described later in the literature review, the natural transition can be understood as a transition caused by the instability generated by the flow itself, with the development of linear instabilities into three-dimensional structures ending up in turbulent spots, while the bypass transition is triggered by external factors and "bypasses" all intermediate steps with the direct generation of turbulent spots. The natural transition occurs in environments with freestream turbulence levels below 1%, while bypass for turbulence levels above approximately 1%. This work is focused on the natural transition since its appearance is consistent with external aerodynamic conditions with a low turbulence environment for flow past a circular cylinder.

Transitional models can be divided into two groups: phenomenological and physics-based approaches. The former does not account for the physics of transition directly, as transition physics is hidden behind the use of empirical correlations based on turbulence intensity and pressure gradient. Models proposed by Langtry and Menter (2009) and Menter et al. (2015) are examples of phenomenological models, that are mostly focused on modelling bypass transition for turbomachinery applications although modifications can be done for a natural transition. Physics-based models aim to describe or quantify the development of instabilities during the pre-transitional stage to determine the transition onset. The laminar kinetic energy ($k - k_L - \omega$) or the amplification factor transport (AFT) are two different methods proposed by Mayle and Schulz (1997) and Coder and Maughmer (2014) respectively, which aim to solve natural transition.

As already introduced, a low turbulence environment is relevant to external aerodynamic conditions we are interested in this work for the analysis of transitional predictions for flow past a circular cylinder. The linear stability theory (LST) has been used in aeronautical applications since the establishment of the e^N method, independently proposed by van Ingen (1956) and Smith and Gamberoni (1956). Boundary layer codes coupled to Navier-Stokes equations were able to predict transition via the amplification factor. However, Coder and Maughmer (2014) implemented the AFT model as a RANS approach compatible to CFD codes, as any integration throughout the boundary layer to compute non-local variables is required because integral properties are estimated via local computations. For either intermittent or laminar kinetic energy approaches, the natural transition is predicted by employing a threshold function. Similarly to the e^N method, the latest version of the AFT model is also capable of providing transition predictions comparable to experiments for natural transition over a zero-pressure gradient flat plate and airfoil. Natural transition is also accounted by Langtry and Menter (2009) or Menter et al. (2015), but physics and upstream flow effects are avoided by the incorporation of empirical correlations. Conversely, the AFT model does not require empirical correlations to determine transition and accounts for upstream boundary layer history, thus making this model of interest for general applications in transitional flows.

1.2 Aims and Objectives

The $\gamma - Re_\theta$, γ, $k - k_L - \omega$ and AFT transitional models are widely tested on wings, blades, flat plates but a single study for circular cylinder using $\gamma - Re_\theta$ by Zheng and Lei (2016). With regards to the AFT model, most of the prior analysis are on airfoil-like or streamlined profiles but any study is available for transitional backward-facing step (only a single front-facing step in the validation process of $k - k_L - \omega$) and bluff bodies such as circular cylinder, as a gap of study, this is addressed in this thesis. Furthermore, in this thesis, the implementation of the AFT model in OpenFOAM, followed by its verification and validation, is presented as the model is not currently available in open source or commercial solvers. Ultimately, the use of Falkner-Skan similarity assumptions within the AFT correlations is another gap that is studied in this thesis, especially regarding the integral properties of the boundary layer compared to LES numerical results provided by the LES group at Barcelona Supercomputing Center.

Hence, the main aim of this project is to implement the AFT transitional model, and its variants with Reynolds Stress Model (AFT-RSM) coupling and Delayed Detached Eddy Simulation (AFT-DDES) hybridization, followed by the comparison to fully-turbulent approaches for backward-facing step and circular cylinder flow to demonstrate their improved performance throughout the transitional regime.

The key objectives of the thesis can be summarized in the following points:

- To verify and validate the implementation of the AFT and AFT-RSM model using natural transition experimental data for a zero-pressure gradient flat plate.
- To show performance improvement regarding laminar separating bubbles and laminar reattachment regions versus fully turbulent predictions for a backward facing step scenario throughout its transitional regime reported by Armaly et al. (1983).
- To validate transitional AFT, AFT-RSM and AFT-DDES models at $Re_D = 3900$ for flow past a circular cylinder.
- To demonstrate the improved performance using transitional methods like AFT, AFT-RSM and AFT-DDES for flow past a circular cylinder at sub-critical, critical and supercritical regimes. Specifically key flow features such as laminar separation, laminar separation bubble, transition, and turbulent separation that play an important role throughout circular cylinder regimes without the need of using pure LES or DNS.
- To demonstrate that differences regarding the correlations estimating boundary layer properties and the growth of disturbances can be a possibility to improve current predictions for AFT-based models for flow past a circular cylinder.

1.3 Layout of the Thesis

Before utilising the AFT model for complex analysis of the flow past a circular cylinder, the AFT model needs to be implemented into OpenFOAM and a verification and validation process is conducted for zero-pressure gradient flat-plate using AFT and its RSM coupling. Numerical schemes and grid analyses are carried out to understand the behaviour and gather good practice for the transition prediction with the AFT model in the OpenFOAM CFD package in Chapter 4.

As an intermediate step before simulating flow past a circular cylinder, a backward-facing step is used as a simple test case for separation and reattachment of laminar and transitional flow. In this case, a backward-facing step can be regarded as having the simplest geometry while retaining the rich flow physics manifested by separation, transition, reattachment, and diverse recirculating bubble lengths depending on the Reynolds number and the geometrical characteristics of the step and channel. In a backward-facing step, the flow is not subjected to any curvature change or variable pressure gradient. Another simplification to the circular cylinder flow is the fixed separation point at the step location. Thus, it permits an analysis of the AFT performance and its variants for separated transition and reattachment of laminar and turbulent boundary layers against the fully turbulent approaches in Chapter 5.

Chapter 7 discusses a novel transitional prediction for flow past a circular cylinder with the AFT, AFT-RSM and AFT-DDES models at transitional Reynolds number regimes

after the validation at $Re_D = 3900$ in Chapter 6. This chapter discusses the capability of the transitional models for predicting separation, transition, laminar separation bubble and turbulent separation over the cylinder surface. In this case, the flow is subjected to curvature and variable pressure gradients, which is different to a backward facing step, to determine the ability of the models to predict the rich flow physics in more complex scenarios.

From the analysis of the AFT model correlations for flow past a circular cylinder in Chapter 7, Chapter 8 presents an analysis of the differences between the original formulation of AFT correlations and results from LES prediction for flow past a circular cylinder. This chapter aims to extend these correlations used in the model for improved predictions for flow past a circular cylinder using data from published LES simulations for transition prediction via stability analysis and the laminar boundary layer state.

Chapter 2

Literature Review

2.1 Transition Mechanisms

Different transition mechanisms exist in nature. This section presents the main laminar to turbulent transition mechanisms: natural transition, bypass transition and separation-induced transition. Relaminarization, where from a turbulent state the flow recovers its laminar behaviour if the flow experiences a sufficiently large acceleration, is also discussed.

2.1.1 Natural Transition

The natural transition mechanism refers to a breakdown process of a laminar boundary layer that is excited by different types of growing instabilities that eventually force the transition from laminar to turbulent flow. Surface waviness, vibrations or weak disturbances lead the flow to primary instabilities, usually referred to as Tollmien-Schlichting waves for boundary layer and first observed by Tollmien (1931) and Schilichting (1931). It is well accepted that for the freestream turbulence level $Tu < 1\%$ instabilities within the laminar boundary layer develop into Tollmien-Schlichting waves as Mayle (1991) concluded. Primary instabilities are two-dimensional, linear, usually viscous and grow slowly until they are sufficiently large to trigger instabilities of streamwise periodic nature, which are so-called secondary instabilities as first experimentally observed by Schubauer and Skramstad (1947) and Liepmann (1943). Secondary instabilities grow rapidly into three-dimensional structures like spanwise periodic hairpin vortices, which develop further downstream causing the breakdown of the laminar boundary layer with the generation of turbulent spots as described by Klebanoff et al. (1962). These spots grow and coalesce into a fully turbulent boundary layer further downstream, as shown in Figure 2.1 and first observed by Emmons (1951).

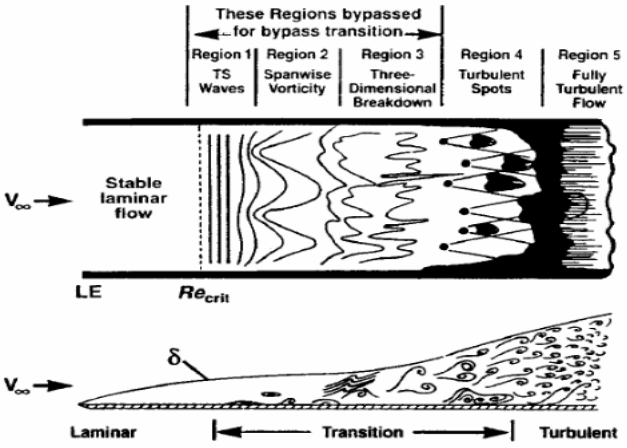

FIGURE 2.1: Transition process starting from T-S waves and finishing in fully-turbulent flow illustrated by White (2006)

The laminar breakdown process is slow and sensitive to all kinds of perturbations as it normally occurs under very low mean-flow turbulence levels i.e external aerodynamics. This makes the prediction in external aerodynamics very challenging. On the other hand, in turbomachinery flows, the disturbance levels are rather high, therefore the perturbations in the pre-transitional stage amplify and control the growth of the Tollmien-Schilichting waves. Turbomachinery flows are less sensitive to small perturbations because of the high level of freestream turbulence and more suitable to simple descriptions by correlations because of the highly turbulent environment.

2.1.2 Bypass Transition

Unlike boundary layers with low freestream turbulence, environments with sufficiently large disturbances, cause the primary and secondary instabilities to be bypassed (see Figure 2.1). In environments with high-freestream turbulence levels, streamwise elongated disturbances are induced in the near-wall region of an attached boundary layer.

Klebanoff (1971) is key in the study of bypass transition. It is considered pioneering as he first reported the presence of three-dimensional large fluctuations of low frequency inside the laminar boundary layer. These laminar fluctuations are referred to as Klebanoff modes and are shown as elongated structures called "streaks". DNS simulations by Jacobs and Durbin (2001) suggest that low-frequency perturbations in the freestream can penetrate deep within the laminar boundary layer originating the so-called Klebanoff modes. These modes are acted upon shear and grow in the flow direction. Jacobs and Durbin (2001) observed that the laminar fluctuations within the laminar boundary layer only exist in the streamwise velocity u and that its growth is proportional to the Re_x and T_u. Johnson and Ercan (1999) show the low-frequencies to be amplified up to 50 times the freestream value and the maximum amplification occurs at approximately $\delta/3$, confirming the deep penetration of the low-frequencies by Jacobs and Durbin (2001),

Andersson et al. (1999) and Luchini (2000). High-frequency fluctuations instead are unable to penetrate as deep, since they are damped by the laminar shear layer as observed by Jacobs and Durbin (2001).

Jacobs and Durbin (2001) showed that Klebanoff modes have slow-moving fluid relative to the mean flow, which causes the Klebanoff modes to rise to the upper part of the boundary layer. In the upper region of the boundary layer, shear sheltering has relatively little influence, and the Klebanoff modes are more receptive to freestream turbulence. The Klebanoff modes then break into turbulent spots, which spread laterally and grow longitudinally, eventually leading to a fully turbulent boundary layer. This similar transition onset was initially observed by Brandt and De Lange (2008) and later confirmed by Wu et al. (2017).

Most of the efforts have been put into understanding natural transition since the primary instabilities can be described with linear stability theory (LST) and therefore analytical solutions can be found. On the other hand, in bypass transition, correlations between large eddies and the pre-transitional boundary layer are pivotal. This analysis is challenging and requires high-fidelity numerical simulations such as LES or DNS, to precisely understand the bypass transition mechanisms.

2.1.3 Separation-Induced Transition

Under large adverse pressure gradients, the transport of streamwise momentum across the boundary layer is not sufficient to retain the laminar boundary layer attached and eventually the laminar boundary layer separates from the surface. After the separation, the transition is initiated at the laminar shear layer by inviscid Kelvin-Helmholtz instabilities originating spanwise vortices. As for the natural and bypass transition mechanisms, the instabilities break down to produce turbulent spots. Soon after the shear layer becomes turbulent which provides enhanced momentum mixing, the turbulent shear layer reattaches to the surface forming the so-called laminar separation bubble as discussed by Gaster (1969). The mixing properties of the reattached turbulent boundary layer are better than the laminar boundary layer, where the enhanced momentum transport allows the turbulent boundary to withstand greater pressure gradients. A transition of this type can occur behind a boundary layer trip and also throughout laminar separation of the boundary layer in an adverse pressure gradient as presented.

Conventionally, separation bubbles have been divided according to their length and their effect on the surface pressure distribution. The length of the bubble depends on the transition process over the free shear layer originated after separation, which essentially may involve all the stages presented for the natural transition.

Short bubbles have a local impact on the pressure distribution and act as to trigger transition (see Figure 2.2). In addition, short bubbles can be considered an effective way

to force turbulent flow and enhance the performance. On the other hand, long bubbles modify the overall pressure distribution and can lead to large losses in lift performance. The present difficulty is to predict if the bubble will be short or long as discussed by Malkiel and Mayle (1996).

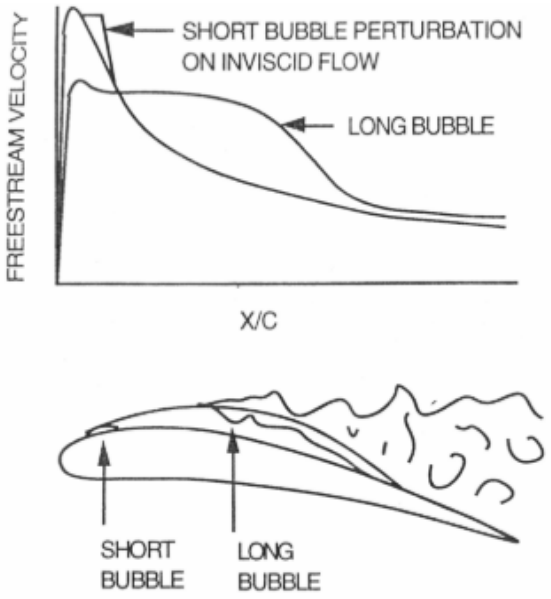

FIGURE 2.2: Long and short bubble effects on freestream velocity and wake Malkiel and Mayle (1996).

2.1.4 Reverse Transition

The three mechanisms discussed earlier explain how the transition to turbulent can be triggered in a laminar boundary layer. In this section, the relaminarization of the boundary layer is discussed. Unlike the separation-induced transition, where the laminar boundary layer separates because it cannot withstand the adverse pressure gradient, the reverse transition (or relaminarization process) occurs if the flow experiences a large favourable pressure gradient.

When a flow is under sufficient acceleration, the transition can be reverted and recover the pure laminar behaviour from a fully turbulent state, this is called relaminarization. This mechanism is present at the leading edge of the suction side and the trailing edge of the pressure side of most turbines. Mayle (1991) investigated this mechanism and proposed the pressure gradient parameter, $K = \nu/U_x^2(dU_x/dx)$. Mayle (1991) investigated the characterizations of the acceleration parameter and concluded that $K = 3 \times 10^{-6}$ was a limiting value. Hence, any turbulent boundary layer with an acceleration parameter above the limiting value may undergo relaminarization. However, if the acceleration diminishes below the limit, the laminar boundary layer may become fully turbulent again.

2.2 Flow Parameters Influencing Transition

2.2.1 Freestream Turbulence

The freestream turbulence levels (T_u) and the type of disturbances are of great importance to the laminar to turbulent breakdown process. As already discussed in Section 2.1, freestream turbulence is key to determine the type of transition. It is well established in the literature, as discussed by Mayle (1991), that below $Tu < 1\%$ natural transition occurs. As T_u increases, secondary instabilities are bypassed. This was initially observed by Morkovin (1969) and extensively analysed by Klebanoff (1971). Westin et al. (1994), Kendall (1997) and Jacobs and Durbin (2001) among others concluded that the variation of laminar fluctuations is proportional to the square root of distance and T_u. On the other hand, the transitional Reynolds number is inversely proportional to T_u.

The influence of the freestream turbulence is not only key in transition for attached boundary layers but also important in separation-induced transition. The nature of the disturbances will determine if the laminar separation bubble reattaches to the surface or if bubble bursting occurs, where a laminar separation bubble is intermittently appearing on the surface of the geometry forcing an asymmetric flow, i.e critical region for flow past a circular cylinder.

2.2.2 Pressure Gradient

Adverse pressure gradients accelerate the laminar to turbulent transition and promote separation of laminar attached boundary layers. On the other hand, favourable pressure gradients can be used as a mechanism to delay the transition. According to studies by Julien et al. (1969) and Jones and Launder (1972) among others, if the favourable pressure gradient is sufficiently strong it may even cause reverse transition or relaminarization of the turbulent boundary layer. In addition, Mayle (1991) concluded that the reverse transition may happen when the acceleration parameter reaches levels of 3×10^{-6} or higher.

2.2.3 Other types of Disturbances

In addition to the freestream turbulence level and pressure gradient, the existence of other types of disturbances that can be found in nature i.e. surface roughness, compressibility, surface curvature, flow unsteadiness and so on also influences the flow transition. Surface roughness can be a cause of bypass transition when sufficiently large. Roberts and Yaras (2005) studied the effect of separation-induced transition who concluded that the effect of the surface roughness is comparable to that of T_u, as well as the roughness distribution. Compressibility effects were studied by Boyle and Simon (1999)

among others concluded that modifications to the spot production rate are needed when $M > 2$. The effect of flow curvature apart from causing pressure gradients is not significant, however on concavely shaped surfaces, Gortler vortices may affect the transitional behaviour as studied by Schultz and Volino (2003). Flow unsteadiness can act as a subset of a bypass transition type since those high levels of turbulence in an oncoming wake will act as a high-turbulence disturbance. Wu and Durbin (1998) and Wu et al. (1999) demonstrated such behaviour with DNS simulations. Furthermore, imperfections in solid surfaces, films, and sudden changes in geometry can be also other disturbances to the boundary layer that can be found in industrial applications and real scenarios.

2.3 The intermittency γ concept

To identify the state of a flow i.e. laminar, turbulent or an intermediate laminar-turbulent state, the concept of intermittency term has become pivotal in transitional RANS models. This section introduces the origin of the intermittency concept and its very first assumptions for transition prediction. Following the origin of intermittency, its integration within computational methods is discussed via conditionally averaged methods and transport equations methods. At the end of this section, three state-of-the-art transitional RANS approaches are discussed.

2.3.1 Origin and Development of Intermittency

The intermittency concept was introduced by Emmons (1951) during a simple water-table analogy to supersonic flow at Harvard, as a student demonstration. The mechanics of transition to turbulence could be observed since the turbulent motion disturbed the surface of the thin layer of water. The disturbances originated from the turbulent spots were sketched by Emmons (1951) as shown in Figure 2.3.

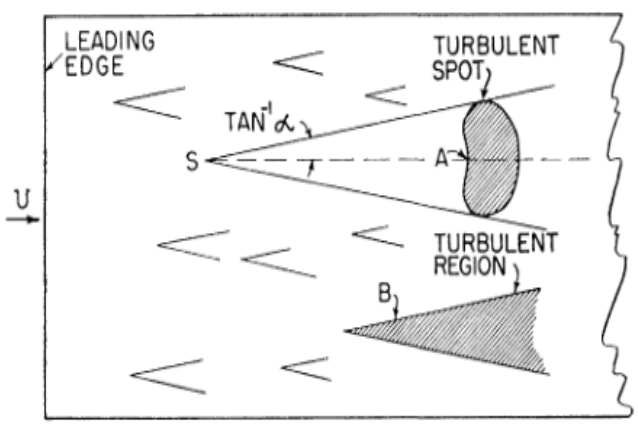

FIGURE 2.3: Illustration of the observations made by Emmons (1951)

According to Emmon's observations, these turbulent spots grew as they were washed along with the fluid. The approximate heart-shaped planform and size of the spot after a period of time is shown in Figure 2.3 (see annotated as A). These spots were observed to appear at random time instances and locations all over the plate (also referred to as continuous breakdown), but their frequency of appearance was strongly related to velocity and disturbance level. These observations led Emmons (1951) to conclude that turbulence in transition was essentially intermittent since any point of the plate was covered by laminar flow except the fraction of time when a turbulent spot passes through. As the spots grow and overlap downstream of the plate. The points in the downstream region are covered for a greater fraction of time by turbulent spots until the laminar boundary layer is continuously covered.

Based on prior observation, Emmons (1951) derived a statistical expression for intermittency (γ). The intermittency is defined as the fraction of time at any point (x, z) that is turbulent due to the growth and convection of the spots produced at (x_0, z_0, t_0). The equation proposed by Emmons (1951) is the following:

$$\gamma(x, z, t) = 1 - \exp \iiint_V g(x, z, t)\, dV \tag{2.1}$$

where $g(x, z, t)$ is the spot formation rate per unit time per unit area and dV is an infinitesimal volume in the propagation volume. The product $g\ dV$ denotes the probability that a turbulent spot is originated within the infinitesimal volume dV.

The complexity in Equation 2.1 is to define an expression for the spot formation rate. As the first assumption, the spot formation rate $g(x_0, z_0, t_0)$ was taken as a constant, independent of time and space, i.e. $g(x_0, z_0, t_0) = g$. Furthermore, the propagation volume region was considered a cone with straight generators as the spot propagation wedge was considered linear for constant pressure flows . Hence, the integral within the exponential in Equation 2.1 results in:

$$g \iiint dx_0\, dz_0\, dt_0 = g \int \frac{\sigma}{U}(x_0 - x)^2\, dx_0 \tag{2.2}$$

where σ is the dimensionless spot propagation parameter governed by geometrical characteristics and spot velocity ratio (refer to Appendix of Emmons, 1951 for further details). Substituting Equation 2.2 into Equation 2.1 leads to the expression

$$\gamma(x) = 1 - \exp\left[\frac{-\sigma g(x - x_t)^3}{3U}\right] \qquad (x > x_t) \tag{2.3}$$

where x_t denotes the transition onset location.

The initial assumptions made by Emmons (1951) regarding the linear propagation of the turbulent spots downstream of a plate were confirmed by Schubauer and Klebanoff (1956). However, differences between Emmons (1951), Schubauer and Klebanoff (1956) and later experimental work acquired by Dhawan and Narasimha (1958) suggested that the assumption of a "continuous breakdown" of turbulent spots after the transition onset was not accurate, i.e. $g(x_0, z_0, t_0) = g$. Dhawan and Narasimha (1958) observed that the spots were originated at a concentrated location at a finite distance from the leading edge of the flat plate, but randomly in time and spanwise location. Furthermore, experimental data showed that the turbulent spots stabilize the flow downstream of the transition onset and therefore the breakdown is unlikely. This stabilization of the turbulent flow was named initially by Schubauer and Klebanoff (1956) as the "calming effect".

Hence, Dhawan and Narasimha (1958) represented the "concentrated breakdown" of the spot propagation term by a Dirac Delta function centred at the transition onset which lead to the following intermittency equation

$$\gamma(x) = 1 - \exp\left[-\frac{n\sigma}{U}(x - x_t)^2\right] \quad (x > x_t) \tag{2.4}$$

where n is the spot production rate per unit time per unit spanwise distance. Equation 2.4 can be expressed in dimensionless form as

$$\gamma(x) = 1 - \exp\left[-\hat{n}\sigma(Re_x - Re_{xt})^2\right] \quad (x > x_t) \tag{2.5}$$

by introducing $\hat{n} = n\nu^2/U^3$, a dimensionless spot production parameter where ν is the kinematic viscosity.

This equation describes a very complex phenomenon but it is widely used because of its simplicity. However, the equation remains to be closed since it demands a description of the transition onset location and the spot production rate. Even though Equations 2.4-2.5 were derived for zero pressure gradient flows, it is found to produce fair predictions of many pressure gradient flows, as shown by Cutrone et al. (2007). However, a large number of experimental data have been gathered over the years to extend its validity for a wider range of scenarios, most of them being focused on bypass transition.

As the universal distribution by Dhawan and Narasimha (1958) shows that the transition onset has to be prescribed in the equation. Abu-Ghannam and Shaw (1980) gave one of the most extensively algebraic correlations for natural transition and low freestream turbulence levels on by-pass transition. An initial simple relation for the transition onset was proposed by Abu-Ghannam and Shaw (1980) only as a function of T_u for zero-pressure gradient flows expressed in Equation 2.6. The range of applicability was extended for pressure gradient flows by Abu-Ghannam and Shaw (1980) using a pressure

gradient parameter $f(\lambda_\theta)$ with $\lambda_\theta = (\theta^2/\nu)(dU/ds)$, where dU/ds is the acceleration along the streamwise direction at the edge of the boundary layer. Correlations are given in Equations 2.7 and 2.8 for completion given its relevance but full details can be found in the original paper. The inclusion of $f(\lambda_\theta)$ promotes early transition under the effect of an adverse pressure gradient and retarding the transition under the effect of a favourable gradient. The critical Reynolds number ($Re_{\theta,t}$) for zero-pressure gradient flows is

$$Re_{\theta t} = 163 + \exp(6.91 - Tu). \tag{2.6}$$

With the pressure gradient parameter, the critical Reynolds number reads as

$$Re_{\theta t} = 163 + \exp\left[f(\lambda_\theta) - \frac{f(\lambda_\theta)}{6.91}Tu\right] \tag{2.7}$$

with

$$f(\lambda_\theta) = \begin{cases} 6.91 + 12.75\lambda_\theta + 63.64\lambda_\theta^2 & \lambda_\theta < 0 \\ 6.91 + 2.48\lambda_\theta - 12.27\lambda_\theta^2 & \lambda_\theta > 0. \end{cases} \tag{2.8}$$

Ten years later Mayle (1991) gathered sufficient experimental data to propose a correlation for zero pressure gradient flows experiencing by-pass transition ($Tu > 1\%$). Mayle (1991) not only investigated the transition in attached boundary layers but also the transition onset on shear layers from separation-induced flows. Mayle (1991) derived correlations for the transition onset in the free shear layer originating from the boundary layer separation in steady freestream conditions. A distinction is made between short and long bubbles according to the Reynolds number at the separation point ($Re_{\theta,s}$). Initial correlations did not take into account the effect of freestream turbulent intensity. Mayle (1991) and Suzen et al. (2003) proposed correlations where the turbulence intensity level was taken into account for separated flow.

The last information that needs to be introduced into Narashima's universal distribution is how the turbulent spots propagate expressed with the product $n\sigma$. Mayle (1991) also proposed a simple correlation for the growth of intermittency in by-pass transition for attached boundary layers in zero pressure gradient conditions as a function of the freestream turbulence level. This initial correlation was extended for decelerating and accelerating flows using Gostelow et al. (1994) and Blair (1992a), Blair (1992b) studies respectively using a ratio to the zero-pressure gradient case. Steelant and Dick (1996) expressed this proportional factor in terms of the acceleration parameter (K) and T_u, which was later improved by Suzen et al. (2003).

2.4 Intermittency Integration

In most practical flows there exist regions that can be characterized as being either, laminar, transition or fully turbulent. The transitional regime can be considered a mixture of both laminar and turbulent behaviour. In the case of a flat plate, initially, the flow is laminar but as the flow develops downstream, the boundary layer will eventually undergo a transition to a turbulent state. The three characterizations coexist for example in a turbulent jet with undisturbed surroundings. The core of the jet is turbulent and the flow away from the core is laminar. Close to the edge of the jet, the flow is less obvious since the turbulent jet entrains laminar flow, and therefore a complex mixture of both flows is expected.

It is a common approach when computing these types of flows to use turbulent models tuned for a good performance in turbulent flows for the entire domain considered. The reason is that the nature of the flow is not known in advance. Even though, these approaches provide meaningful estimations, the nature of the flow that has undergone a transition to a turbulent state is different from a laminar flow. The complexity in CFD is to determine a procedure to treat laminar and turbulent flow separately.

2.4.1 Conditionally Averaged Flow Equations

As discussed, a transitional flow can be understood as a mixture of turbulent and non-turbulent regions. Hence, it can be described by a model, with intermittency to describe the probability that the turbulent phase is present. To describe the flow in that way, the conditional averaging of flow quantities and equations are necessary for turbulent and non-turbulent regions. Ultimately, in the transitional region both sets of conditioned equations, laminar and turbulent respectively, can be blended to provide a prediction.

Libby (1975) and Dopazo (1977) introduced the technique initially for the description of intermittency at the outer edge of boundary layers and mixing layers, but it can also be used for the transitional description of boundary layers and free shear layers. The idea behind the technique is to derive an analogue to the experimentalists technique of “conditional sampling”. This technique is based on splitting a measured signal of an arbitrary quantity into periods that are either laminar or turbulent so that the experimentalist can determine the properties of the flow during each phase.

This technique led Libby (1975) and Dopazo (1977) to propose two sets of conditionally averaged Navier-Stokes equations for the laminar and turbulent regions of the flow respectively and interaction terms between the two phases, requiring modelling. Kuan and Wang (1990) showed that the interaction term can be dropped as the fluctuations do not contribute significantly to the Reynolds stress term. The turbulent phase is commonly reproduced by a fully-turbulent model and the laminar fluctuations can be

modelled, however, ignoring the non-turbulent fluctuations produces good agreement with experimental data as shown by Vancoillie and Dick (1988). Furthermore, an intermittency equation is introduced to the system to discern the fraction of time the flow is turbulent or non-turbulent. For example, the total contribution of the Reynolds stress for conditioned equations can be expressed in three terms: the contribution of the turbulent Reynolds stress, the contribution of the laminar Reynolds stress and the last term including the effects of the turbulent-laminar interaction.

Vancoillie and Dick (1988) modelled the interaction terms with boundary layer approximations and applied the conditionally averaged flow equations to a flat plate case. The two sets of equations are combined with a fully-turbulent approach and the intermittency is described using Narashima universal distribution only for the streamwise direction.

Steelant and Dick (1996) extended this technique to the full Navier-Stokes equations. In a similar way to Vancoillie and Dick (1988), the conditioned equations were coupled to a fully-turbulent model and a generalised version of the Narahisma universal distribution so it took into account the intermittency at the outer edge of the boundary layer due to freestream eddies and the intermittency inside due to breakdown of turbulent spots.

Nonetheless, the use of a double set of equations considerably increases the computational effort, while the improvement is mostly in better predictions of fluctuating kinetic energy across the boundary layer but does not help much in shear stress predictions. This is due to the interaction term which is prominent halfway through the boundary layer and is the largest in the middle of the transition region, approximately. Furthermore, the interaction terms can be dropped as investigated by Kuan and Wang (1990) and the contribution of the laminar fluctuations is only significant at the early stages of the transition development and can be dropped out too. Therefore, despite the possibilities that it offers, the same level of performance can be achieved by multiplying the production term of the turbulence production or the turbulence eddy-viscosity with intermittency using algebraic models for transition prediction.

2.4.2 Algebraic Correlations

As an alternative to conditionally averaged flow equations, an algebraic transition model consists of an algebraic formula describing a relevant quantity controlling transition that is appended to a fully-turbulent model. The algebraic function is mostly introduced as a multiplier of the production and destruction terms of the turbulent kinetic energy or the eddy viscosity of a turbulence model. These algebraic models commonly describe adequate parameters along streamlines using Narashima's universal distribution or a similar correlation.

Cho et al. (1993) use a two-layer model where a one-equation model in the viscosity-affected near-wall region and the standard $k - \epsilon$ in the outer region of the flow. In this

case, the eddy-viscosity is modified using a similar exponential distribution to Dhawan and Narasimha (1958). A similar approach was used by Michelassi et al. (1999), where the algebraic transition model was coupled to the standard $k-\omega$ turbulence model modifying the eddy-viscosity.

The models by Kožulović and Lapworth (2009) and Fürst et al. (2013) modified the fully-turbulent models by multiplying the production and destruction term by γ. Kožulović and Lapworth (2009) utilize a similar intermittency distribution function to Dhawan and Narasimha (1958) with Abu-Ghannam and Shaw (1980) correlations. This algebraic model is coupled to the one-equation Spalart-Allmaras turbulence model, multiplying the production term of the modified eddy-viscosity equation with the intermittency value and the destruction term with the same value. The model proposed by Fürst et al. (2013) used a modified intermittency distribution and followed the same idea, multiplying the production and destruction term of the turbulent kinetic energy equation of the $k-\omega$ turbulence model. An example of the modified intermittency distribution by Fürst et al. (2013) is described by

$$\gamma = 0.5(\gamma_e + \gamma_i) + 0.5(\gamma_e - \gamma_i)\tanh\left(y/\delta - 1\right) \tag{2.9}$$

where γ_e is the intermittency of the freestream, which is 1 for a turbulent flow and 0 for a non-turbulent flow, γ_i is the intermittency in the interior of the boundary layer, determined with the Narasimha-formula in Equation 2.5, y is the distance to the wall and δ is the thickness of the boundary layer

Kožulović and Lapworth (2009) or Fürst et al. (2013) are representative algebraic transition models where the transition onset and growth of intermittency are determined using the correlations proposed by Mayle (1991), Abu-Ghannam and Shaw (1980) or modified versions of these correlations to predict the intermittency distribution. This way, the performance of streamwise algebraic correlations models is directly related to the quality of the transition correlations utilised.

The boundary layer momentum thickness is necessary for all the presented models is necessary to estimate the intermittency value. Cho et al. (1993) and Kožulović and Lapworth (2009) perform an integration of the momentum thickness across the boundary layer. The computation of non-local information is not an easy procedure because the edge of the boundary layer is not well defined in a Navier-Stokes environment due to massive parallelisation and the integration depends on the details of the implementation of the search algorithm. Difficulties to estimate non-local properties are exaggerated by current CFD methods based on unstructured grids and massive parallel decomposition, where the boundary layer can be split up between different CPUs, making an integration difficult.

On the other hand, Fürst et al. (2013) estimate the boundary layer momentum thickness using a scaled relation with the monotonic maximum of the vorticity Reynolds number. Since the vorticity Reynolds number (Re_V) is a local property, it can be easily computed at each grid point in an unstructured grid and parallel Navier-Stokes solver.

Regardless of the procedure to estimate any integral property to determine the transition onset, the streamwise algebraic methods only produce a streamwise intermittency distribution. However, these algebraic models can be generalised for multidimensional and unsteady predictions as it is introduced in the next section.

2.4.3 Intermittency Transport Equations

As discussed, a major drawback of the algebraic correlations is that they are one-dimensional, meaning that they are only valid along a streamline. However, an extension to a three-dimensional and unsteady formulation is possible with the starting point being the intermittency universal law proposed by Dhawan and Narasimha (1958). This section introduces the key steps of deriving an intermittency transport equation, which is extensively used in RANS transitional models.

Differentiating the intermittency distribution of Dhawan and Narasimha (1958) given in Equation 2.4 and using the following relations derived from Equation 2.4:

$$\frac{d\gamma}{dx} = 2\beta_\gamma^2(1-\gamma)(x-x_t) \tag{2.10}$$

$$\sqrt{-\ln(1-\gamma)} = \beta_\gamma(x-x_t) \tag{2.11}$$

where β_γ is defined by $\sqrt{n\sigma/U}$, results in the following expression for the rate of change of intermittency in the streamwise direction:

$$\frac{d\gamma}{dx} = 2\beta_\gamma(1-\gamma)\sqrt{-\ln(1-\gamma)} \tag{2.12}$$

This expression can be generalised using the convective derivative for steady flows as:

$$\overrightarrow{v}\cdot\nabla\gamma = u\ 2\beta_\gamma(1-\gamma)\sqrt{-\ln(1-\gamma)} \tag{2.13}$$

where $\overrightarrow{v}$ is the local velocity vector, u is the magnitude of the local velocity and U, in β_γ, is the magnitude of the velocity at the boundary layer edge as described by Dick and Kubacki (2017). A further generalisation is to introduce the unsteady term

of the material derivative, the F_{onset} function and the diffusion term to construct an intermittency transport equation:

$$\frac{D(\rho\gamma)}{Dt} = u\ \rho 2\beta_\gamma(1-\gamma)\sqrt{-\ln(1-\gamma)}\ F_{\text{onset}} + \frac{\partial}{\partial x_j}\left[\left(\mu + \frac{\mu_t}{\sigma_t}\right)\frac{\partial\gamma}{\partial x_j}\right] \tag{2.14}$$

The material derivative describes the rate of change of intermittency in time and space. The F_{onset} function acts as a trigger of the production term when the transition onset location is reached. It switches from zero to unity at the transition onset location allowing the turbulent kinetic energy production term to become active. The diffusion term allows a cross-stream intermittency distribution within the boundary layer.

It is common in most intermittency transport models to replace the second and fourth terms in the production term of Equation 2.14 with similar terms. The second factor in the production term of the intermittency transport equation, $\sqrt{-\ln(1-\gamma)}$, is proportional to $\sqrt{\gamma}$ and γ, in the range of 0 to 0.35 and the range of 0.35 to 0.95 respectively from pure mathematical analysis. Therefore, this term can be replaced by $\sqrt{\gamma}$ and γ, or a combination of both as suggested by Dick and Kubacki (2017).

The fourth factor in the production term of the intermittency transport equation, uU/ν, has dimensions of rotation or shear rate. The ratio of the factor to S or Ω depends on the dimensionless thickness of the boundary layer and the shape of the boundary layer. This dependency is commonly incorporated via the F_{onset} function or the F_{length} function.

Ultimately, it is common to find a destruction term (E_γ) in the intermittency transport equation to dampen any spurious turbulence that might be produced within the laminar boundary layer before transition. Thus, all prior modifications lead to a most common intermittency transport equation in Equation 2.15. This equation is very similar to the general intermittency transport equation discussed in Chapter 3 in Equation 3.10.

$$\frac{D(\rho\gamma)}{Dt} = F_{\text{length}}\rho S(1-\gamma)\sqrt{\gamma}F_{\text{onset}} - E_\gamma + \frac{\partial}{\partial x_j}\left[\left(\mu + \frac{\mu_t}{\sigma_t}\right)\frac{\partial\gamma}{\partial x_j}\right] \tag{2.15}$$

The following subsections introduce representative examples that are widely used in literature for transition modelling. The intermittency transport equation is pivotal to reproducing the laminar and transition region, coupled with one of the standard fully-turbulent models.

2.5 Transitional Flow Modelling

2.5.1 Local-Correlation-Based $\gamma - Re_\theta$ Model

The $\gamma - Re_\theta$ model is a local correlation-based transition model first introduced by Menter et al. (2002) and later improved by Menter et al. (2006) and Langtry and Menter (2009). The local approach to estimating integral properties of the boundary layer allows the transition model to be fully-compatible with CFD solvers and allows parallelization on unstructured grids as discussed by Menter et al. (2002). The $\gamma - Re_\theta$ model aims to solve bypass transition for the attached boundary layer in high freestream turbulence and separated boundary layers at low freestream turbulence.

This is a four-equation model, conformed by the standard $k - \omega$ turbulence approach proposed by Menter (1994) plus two extra equations, an intermittency transport (γ) and a transition momentum thickness Reynolds number transport equation ($\overline{Re_{\theta t}}$). The intermittency transport equation is as:

$$\frac{D(\rho\gamma)}{Dt} = P_\gamma - E_\gamma + \frac{\partial}{\partial x_j}\left[\left(\mu + \frac{\mu_t}{\sigma_t}\right)\frac{\partial \gamma}{\partial x_j}\right], \tag{2.16}$$

where the production and destruction terms are given as

$$P_\gamma = c_{a1} F_{length} \rho S (1 - c_{e1}\gamma)\sqrt{\gamma F_{onset}} \tag{2.17}$$

$$E_\gamma = c_{a2} F_{turb} \rho \Omega (c_{e2}\gamma - 1)\gamma. \tag{2.18}$$

The intermittency transport equation takes a similar form as Equation 2.15. In this case, the F_{onset} function acts as a trigger for the intermittency production and F_{turb} sustains the turbulence production outside laminar regions. The F_{length} function controls the transition length and acts as a proportional ratio with the S magnitude to the term (uU/ν), as discussed in Subsection 2.4.3. The length of the transition is based on empirical functions as $F_{length} = f(\overline{Re_{\theta t}})$ published in Langtry and Menter (2009). Details regarding the calibration constants ($c_{a1}, c_{e1}, c_{a2}, c_{e2}$ and σ_t), and the formulation of F_{turb}, F_{onset} and F_{length} can be found in the former reference.

The transition momentum thickness Reynolds number ($Re_{\theta t}$) is estimated using a modified empirical correlation by Abu-Ghannam and Shaw (1980) as a function of $Re_{\theta t} = f(Tu, \lambda_\theta)$ published in Langtry and Menter (2009). The idea behind $\overline{Re_{\theta t}}$ transport equation is to diffuse $Re_{\theta t}$ to the interior of the boundary layer via a generalised diffusion term to transform a non-local property at the edge of the boundary layer into

a local variable that can be computed at every point of the grid. The $\overline{Re_{\theta t}}$ transport equation is defined as

$$\frac{D(\rho\overline{Re_{\theta t}})}{Dt} = P_{\theta t} + \frac{\partial}{\partial x_j}\left[\left(\mu + \frac{\mu_t}{\sigma_{\theta t}}\right)\frac{\partial\overline{Re_{\theta t}}}{\partial x_j}\right]. \tag{2.19}$$

The source term $P_{\theta t}$ forces the freestream values of $\overline{Re_{\theta t}}$ to be equal to $Re_{\theta t}$ while it turns to zero within the boundary layer. The reader is referred to Langtry and Menter (2009) for full details regarding the formulation of the source term. As already mentioned, the $Re_{\theta t}$ is diffused to the interior of the boundary layer via $\overline{Re_{\theta t}}$ to estimate the critical momentum thickness Reynolds number ($Re_{\theta c}$) via empirical correlations $Re_{\theta c} = f(\overline{Re_{\theta t}})$ published in Langtry and Menter (2009).

The transitional equations are coupled to the standard $k-\omega$ SST approach multiplying the turbulent kinetic energy production and destruction term with the intermittency scalar. Therefore, there will be no presence of turbulence until the intermittency production is activated, in other words, until the transition onset condition is reached according to the empirical correlations.

As discussed earlier, the quality of the transition correlations determines the performance of the model. The use of correlations from Abu-Ghannam and Shaw (1980) provides good performance for a range of different pressure gradients and freestream turbulence levels as demonstrated by Langtry et al. (2006) and Langtry and Menter (2009) under flat-plate, turbomachinery and aeronautical test cases. Despite the good performance, the boundary layer history is not taken into account by Abu-Ghannam and Shaw (1980) correlations since the maximum pressure gradient is present at the transition point. A major deficiency of the model is the lack of Galilean invariance due to the use of the streamline direction when computing the freestream turbulence. This limits the model to work only on stationary walls with respect to the coordinate system of the simulation.

2.5.2 Local-Correlation-Based γ Model

The γ-model aims to simplify the $\gamma - Re_\theta$ model and address the lack of Galilean invariance present in the estimation of T_u at the edge of the boundary layer. The goal of this model is the same as the $\gamma - Re_\theta$ model, to solve bypass transition for attached boundary layers in high freestream turbulence levels and separated boundary layers at low freestream turbulence levels with only the intermittency transport equation in Equation 2.16 coupled to $k-\omega$ SST model.

Menter et al. (2015) proposed to estimate the $Re_{\theta c}$ with local formulations for the T_u and λ_θ, therefore the $\overline{Re_{\theta t}}$ transport equation can be avoided. Furthermore, the model recovers the Galilean invariance due to the use of the value of turbulence kinetic

energy (k), wall distance (d_w), ω and wall-normal velocity gradient over the wall-normal direction instead of the magnitude of local velocity. Details about this new formulation can be found in Menter et al. (2015).

The complexity of the $Re_{\theta c}$ correlation was also tackled by Menter et al. (2015). Instead of $Re_c = f(\overline{Re_{\theta t}})$, this model estimates $Re_c = f(Tu, \lambda_\theta)$ with similar results to Abu-Ghannam and Shaw (1980) correlations, except for strongly favourable pressure gradients where Mayle (1991) criteria was used for calibration. Three controlling constants were introduced, two constants to control the limits and the third constant controls the rate of decrease of the critical momentum thickness Reynolds number as the turbulence intensity increases. Furthermore, since the transition momentum thickness Reynolds number transport equation and its scalar are eliminated, Menter et al. (2015) approached the F_{length} correlation to a constant value. The formulation and calibration of the modified correlations are given in detail in the former reference.

These modifications simplify the model considerably and address the lack of Galilean invariance from $\gamma - Re_\theta$ model. In terms of performance, it is shown in Menter et al. (2015) that flat-plate tests compare to $\gamma - Re_\theta$ results. Aeronautical tests show a good agreement with experimental data and also with prior results achieved using $\gamma - Re_\theta$. For turbomachinery applications, overall, the γ model predicts a slightly later transition on the suction side and is somewhat closer to DNS data than $\gamma - Re_\theta$. However, since the same correlations are in use, the lack of boundary layer history effects is still present.

Amplification Factor Transport Model

As opposed to the prior $\gamma - Re_\theta$ and γ-models, the motivation of the AFT model is to solve the natural transition mechanism incorporating the linear stability theory in a manner that is compatible with massively parallelised unstructured CFD solvers. Details of the model will be discussed in more detail in Chapter 3, however, a brief explanation is given here for the evolution of the model throughout the years and its rationale.

Mainly, the e^{N} theory proposed independently by Smith and Gamberoni (1956) and van Ingen (1956) is not appropriate to be incorporated into current CFD solvers as it requires prior knowledge with regard to the geometry and mesh topology. Furthermore, the e^{N} theory involves non-local operations that are also difficult to incorporate in massively parallelised unstructured CFD solvers.

Gleyzes et al. (1985) and Drela and Giles (1987) shed light on the field with a simplified method for the e^{N}. This method tracks the maximum amplitude of the most-amplified frequencies while assuming linear growth and locally self-similar boundary layer development. Conversely to $\gamma - Re_\theta$ and γ transition models, the current formulation of the Amplification Factor Transport model does not predict the length of transition.

As shown in Figure 2.4, each solid line describes the spatial amplification curve for a given frequency and velocity profile. The spatial amplification curves are computed by solving the spatial instability via the Orr-Sommerfeld equation using Falkner-Skan velocity profiles for a range of shape factors and unstable frequencies. The dashed line describes the envelope of the most-amplified frequencies in terms of the momentum thickness Reynolds number. As presented in Figure 2.4, a linear approximation can be produced for the envelope of most amplified frequencies, where the growth rate of the amplification factor is estimated for a given shape factor. Hence, the growth rate of the amplification factor at any given point can be expressed as a differential equation in terms of the spatial coordinate.

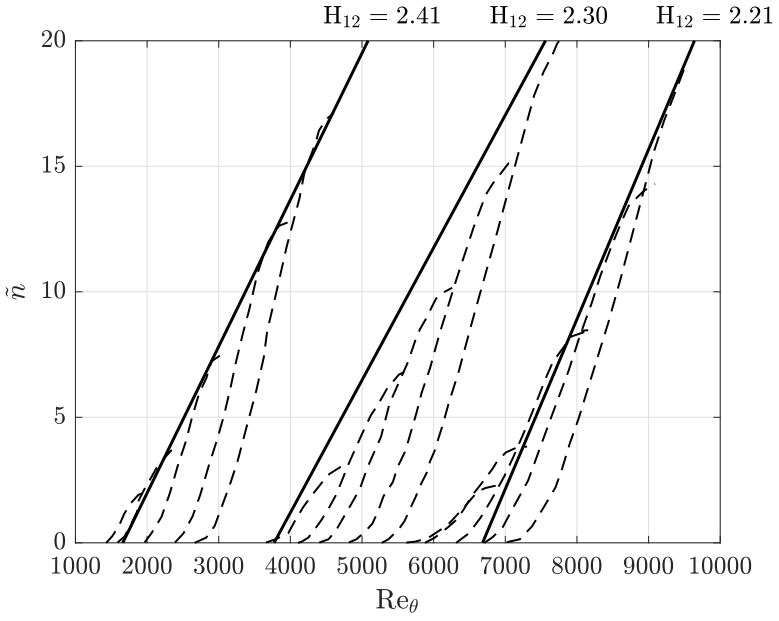

FIGURE 2.4: Digitalized Orr-Sommerfeld spatial amplification curves for different frequencies (dashed line) along the envelope of the growth-rate $\tilde{n}$ (solid line) versus the momentum thickness Reynolds number (Re_θ) from Gleyzes et al. (1985). Both terms are presented for three shape factors as denoted in the top side.

Drela and Giles (1987) expressed the growth rate in terms of the spatial coordinate using the chain rule with two terms. The rate of change of the amplification factor in terms of the momentum thickness Reynolds number and its spatial rate of change. Three terms conform the variation of momentum thickness Reynolds number over the spatial coordinates; two terms are originally given by Drela and Giles (1987) to describe the growth of momentum thickness (θ) for the Falkner-Skan boundary layer. The third term was introduced originally by Coder and Maughmer (2014) and later improved by Coder (2017, 2018, 2019) relating the local flow velocity and wall effects to the local vorticity along the focus of maximum values of the local shape factor.

In addition to the amplification factor transport, the model uses an intermittency transport equation. As presented in section 2.4.3, the F_{onset} acts as a trigger of the intermittency production term. In this case, the F_{onset} is constructed as a ratio of the current

amplification factor to a critical amplification factor value. Therefore, when the ratio reaches unity, the transition onset occurs.

The AFT model is the primary model used in this work, with an extension using Reynolds Stress Model and a DDES hybridization to introduce transition prediction onto the DDES approach. The AFT model is chosen instead of the physics-based approach $k - k_L - \omega$ since the buffeting problem remains not completely understood and the simplicity of the AFT formulation compared to laminar kinetic energy models. On the other hand, the AFT model is chosen ahead of two Menter's models, $\gamma - Re_\theta$ and γ, because it is a physics-based model that intends to resolve or quantify pre-transitional physics to determine transition, via linear stability theory that has been proven to be valid for aeronautical applications for more than 50 years, rather than constructing complex transitional correlations for a vast number of conditions such as different Reynolds numbers, turbulence levels and pressure gradients. In addition, pressure gradient history is not considered by such constructions, as the transition is assumed to occur always at the location of the maximum pressure gradient. As opposed to Menter models, the amplification factor model considers the upstream boundary layer history via the estimation of the mostly amplified frequencies, therefore responding better to pressure gradients with a transition condition based on the simple relation proposed by Mack (1977).

2.5.3 Laminar Fluctuation Energy Method

The laminar fluctuation energy method is a physics-based model, based as its name indicates on the analysis of the laminar fluctuation energy on the pre-transitional stage of the boundary layer.

In the pre-transitional region, the boundary layer mean velocity profile is laminar. However, as the freestream turbulence is increased, the mean velocity profile is distorted with a decrease in momentum in the outer region and an increase in the inner region. This behaviour can be observed even for T_u as low as approximately 1%. High-amplitude streamwise fluctuations originate and can reach intensities several times larger than freestream turbulence level as measured by Dryden (1939). These streamwise fluctuations eventually break down leading to a bypass transition of the boundary layer.

Experiments carried out by Volino and Simon (1997) under moderate and at high freestream turbulence and analyses by Leib et al. (1999), evinced that the peak energy of wall-normal velocity fluctuations (v') in the freestream occurred at the same low-frequency as the peak of streamwise velocity fluctuations (u') within the boundary layer. Bradshaw (1994) named this behaviour the splat mechanism. The splat mechanism explains the cause of the u' fluctuations appearing inside the boundary layer (Bradshaw, 1994 and Volino, 1998). According to Bradshaw (1994), the v' compresses

the boundary layer momentarily as a large-scale eddy passes by, forcing the speed to increase from the outer region closer to the wall. The wall-normal fluctuation is redirected by the wall to u' inside the boundary layer leading to disturbance amplification without involving turbulence diffusion. It can also be understood as large-scale eddies brought to rest at the wall due to the non-slip condition, instigating its energy to be addressed tangentially. Note these fluctuations shall not be confused with the turbulent fluctuations as they are structurally dissimilar.

Mayle and Schulz (1997) introduced the laminar kinetic energy equation to reproduce the behaviour of the pre-transitional fluctuations in the streamwise direction. As discussed above, the "splat mechanism" differs from typical turbulence production. Furthermore, as the "splats" are likely to occur only for eddies with large scales relative to the wall distance, the turbulence energy spectrum can be divided into wall-limited and non-wall-limited sections in the near-wall region, or what is the same large-scale eddies that contribute to the production of non-turbulent fluctuations and small-scale eddies that contribute to turbulent production, respectively. The cut-off eddy size is determined by the effective turbulent length scale.

The magnitude of k_l represents the magnitude of the non-turbulent streamwise fluctuations. The laminar kinetic energy transport equation differs from the standard turbulent kinetic energy transport equation since it lacks the shear-stress/strain related production term. In this case, the source term is formed by a pressure-diffusion correlation. This magnitude develops over the pre-transitional stage and local transition parameters are implemented that depend on the turbulence energy, the effective length scale and the fluid viscosity based on experimental measurements by Andersson et al. (1999). As transition conditions are accomplished, the energy is transferred to the turbulent kinetic energy transport equation k_t. After the transition region, the model predicts a fully-turbulent boundary layer with a small amount of laminar kinetic energy in the viscous sub-layer.

This is an eddy-viscosity model conformed by three transport equations: the laminar kinetic energy transport equation k_l, turbulent kinetic energy transport equation k_t and specific turbulent kinetic energy dissipation rate ω. The model has not been extensively validated for general geometries except for flat plate tests and turbine blade scenarios. Initial results present a good sensitivity to the freestream turbulence and produce fair results. However, it is still uncertain its validity to predict transition under the effects of pressure gradient and separation at low T_u levels, specifically below 1%.

2.5.4 LES and DNS for Transition

LES and DNS are suitable methods for transition prediction. In essence, DNS can accurately predict the laminar flow breakdown, the development of turbulent spots and

ultimately transition to fully-turbulent flow. As opposed to RANS, DNS solves the time-dependent Navier-Stokes equations without Reynolds averaging. Consequently, there is no need to use a turbulence model for turbulence closure.

DNS requires a fine grid to resolve all eddies down to the smallest scales of the turbulence spectrum. This requirement significantly increases the computation cost by an order of approximately $Re^{9/4}$ for a steady state problem and Re^3 when time is taken into account for unsteady flow, which is still too costly for high-Reynolds number scenarios.

To reduce the computational costs associated with DNS, researchers developed the concept of Large Eddy Simulations to transitional flows. In LES only the large-scale eddies are resolved, while the small-scale eddies are modelled so the grid requirements are alleviated. Small-scale eddies are modelled using a subgrid-scale model similar to the eddy viscosity approach such as the one proposed by Smagorinsky (1963). The main problem when using LES to predict transition is that it is very sensitive to the choice of the Smagorinsky constant to calibrate the subgrid-scale model proposed by Smagorinsky (1963). The dynamic sub-grid scale model by Germano et al. (1991) adjusts the Smagorinsky constant dynamically as the calculation progresses. One of the advantages that the dynamic sub-grid scale model brings is that the sub-grid eddy viscosity is zero in laminar boundary layers, as the resolved turbulence stress vanishes. This is believed to help predict transitional flows, however, the dynamic sub-grid scale model is not the complete solution as shown by Michelassi et al. (2003) for low-pressure turbine blades, because there are still quantitative differences with DNS results regarding the transition point and the difficulty to represent the fine scales fluctuations and turbulent spots as it is suggested in the publication.

2.5.5 Summary of Transitional Modelling Methods

The current available transitional models have been presented along with high-fidelity approaches such as DNS and LES that can predict the smaller structures within the boundary layer and free shear layers triggering transition. These former two methods, for high Reynolds number cases, are not easily accessible yet as the grid requirements escalate with a factor of 9/4 with Reynolds number to capture the smaller structures. However, both methods have demonstrated their potential to provide good predictions for experimental data for transitional scenarios.

As more accessible methods, the transitional approaches have become a rising possibility for explicit transition prediction. Transitional modelling can be currently divided into two big groups: phenomenological models and physics-based models. Phenomenological, as has been discussed, aims to construct complex empirical correlations from observations and a vast set of experiments for the determination of the transition onset. Examples are Langtry and Menter (2009) and Menter et al. (2015), which are ruled by

the quality of the transitional correlations. These models have shown good results for flat-plate experiments with different pressure gradients, as the basis of their correlations. Predictions on streamlined bodies along with one test for different Reynolds numbers for flow past circular cylinder have shown promising results, despite numerical instabilities and regions that are not predicted and bypassed at high Reynolds number, i.e trans-critical resembles a super-critical behaviour.

Physics-based models, as opposed to the prior group, aim to solve the evolution of the pre-transitional disturbances within the boundary layer to determine the onset of transition. The $k - k_L - \omega$ model is based on the laminar kinetic energy idea, which aims to determine the evolution of laminar instabilities. The model has shown promising results for flat plate analysis and streamlined airfoils nonetheless, the understanding of the "buffeted layer" proposed in the $k - k_L - \omega$ model is not yet fully understood and requires further insight.

On the other hand, the AFT model aims to use the linear stability theory to estimate natural transition, used for more than 50 years in aeronautical applications, within the CFD environment and it is the primary model used in this work. The amplification factor is computed locally, thus considering the upstream boundary layer effects and therefore a better transition response to variable pressure gradients to the phenomenological model's correlations. The method has proven valid for flat plate and aeronautical applications, such as streamlined airfoil profiles. This method does not require transition correlations but only the computation of the turbulence levels, which is also required in phenomenological models along the complex transitional correlations. Furthermore, the model is constructed using the chain rule, which is rather simpler than both the phenomenological model and all relations necessary for the $k-k_L-\omega$ model, which still requires further understanding of the ´´buffet layer" physics and description. Thus, AFT is considered an interesting option with discussed benefits to other available methods that can be exploited and improved for transitional prediction.

2.6 Backward Facing Step

Backward-facing step flow is a simple geometry that manifests a rich flow physics regarding flow separation, reattachment and separation bubbles depending on the Reynolds number and geometry characteristics of the channel. Several experimental measurements have been performed since the 80s, with the major interest to identify the growth of the reattachment length in terms of Reynolds number. Here, we present the major findings regarding flow physics, of available experimental data and numerical predictions for backward facing with an expansion ratio of $H/h \sim 2$, which is characteristic of Armaly et al. (1983) geometry test case, which is a well-reported configuration in literature.

2.6.1 Review of experimental studies

The key measurements provided by Armaly et al. (1983) are considered state-of-the-art regarding the flow physics involved within the backward-facing step with Re_{D_h}. From experimental observation of the results, Armaly et al. (1983) proposed a division in three regimes according to the flow physics of the primary recirculating length (x_1) with Re_{D_h}: laminar, transitional and turbulence. Figure 2.5 tags the separation bubbles for backward-facing step flow, while their behaviour in terms of Reynolds number is shown in Figure 2.6, where the three aforementioned regions are identified.

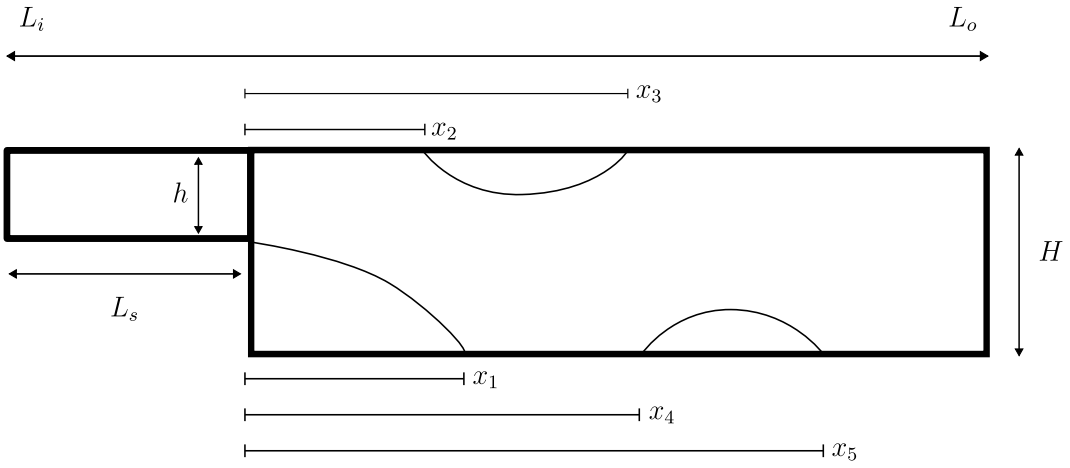

FIGURE 2.5: Schematic domain for backward-facing step and recirculating regions.

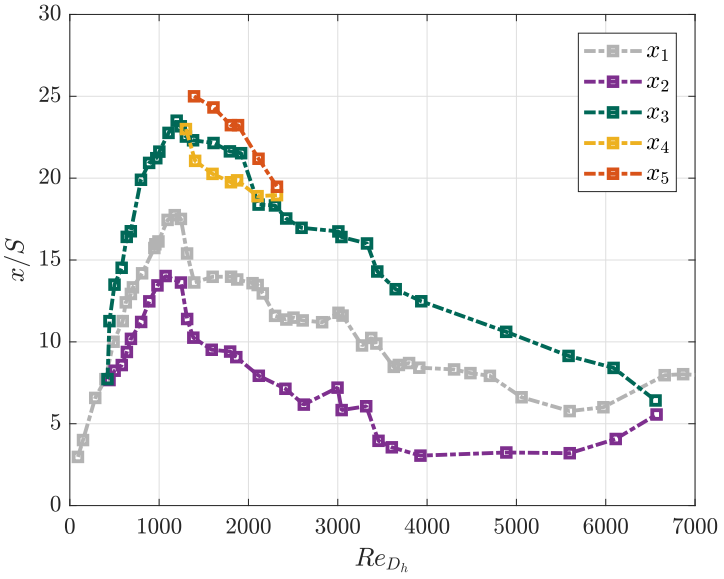

FIGURE 2.6: Dimensionless recirculation regions (x/S) in terms of Reynolds number based on the hydraulic diameter of the channel (Re_{D_h}) reported in experiments by Armaly et al. (1983).

Throughout the laminar region, the primary recirculation length growths with the increase of Reynolds number, with the appearance of the secondary bubble due to the

adverse pressure gradient at the step. The three-dimensional behaviour becomes prominent with the appearance of the secondary bubble. The interaction between the structures emanating from the primary recirculation region and secondary bubble causing the laminar to turbulent transition, due to the Kelvin-Helmholtz structures. Within the transitional regime, a third bubble is reported by Armaly et al. (1983). As Reynolds increases the recirculation lengths reduces their dimension for x_1 and x_2 as the flow becomes fully turbulent. At the end of the transitional regime, the secondary bubble is already vanished and the primary recirculation length is almost constant.

- Laminar regime

Experimental data reveal that the laminar regime is characterized by the stretching of the primary recirculating length (x_1) mainly, but the growth is not linear. The secondary recirculating bubble appears at approximately $Re_{D_h} = 400$ and is also stretched with the increase of Re_{D_h}. The appearance of the secondary bubble (x_2) is caused by the sudden expansion after the step and was first reported by Armaly et al. (1983). Its appearance is strongly related to the expansion ratio and backward-facing step geometry. The growth of the recirculating length in terms of Reynolds number is also proven by Denham and Patrick (1974) and Mouza et al. (2005), with the measurements on a laminar flow in a similar geometry. Experimental work done by Lee and Mateescu (1998) also presents the growth of x_1 in terms of Re_{D_h}, but with an initial linear growth. The growth is maintained generally up to $Re_{D_h} = 1200$, except for experiments carried out by Lee and Mateescu (1998), that this region is extended until about $Re_{D_h} = 1400$, as the growth of the primary recirculating length is slower and more linear.

Measurements by Armaly et al. (1983) at different positions over the spanwise length, revealed that near the step, the flow was three-dimensional at approximately $Re_{D_h} = 400$. The flow three-dimensionality is increased with the Reynolds number due to the interaction between the upper bubble and the main reattachment length. For Re_{D_h}, it was demonstrated with measurements that the flow was essentially two-dimensional all the spanwise length.

The growth is maintained generally up to $Re_{D_h} = 1200$, except for experiments carried out by Lee and Mateescu (1998), which is extended until about $Re_{D_h} = 1400$, as the growth of the primary recirculating length is slower and more linear.

- Transitional regime

The transitional regime is considered to begin as x_1 shows a sharp decrease with the increase of Re_{D_h} until approximately a Reynolds number of 5500. That is accompanied by a reduction of the x_2 until the similar Re_{D_h} and the appearance of a tertiary separation bubble further downstream of the main reattachment length. This tertiary bubble was first reported by Armaly et al. (1983) and also decreases in length with the increase of Re_{D_h} until it vanishes at about $Re_{D_h} = 2300$. This was later confirmed by DNS.

Experimental work by Lee and Mateescu (1998) shows the onset of the transitional regime to be delayed at approximately $Re_{D_h} = 1400$ and extended up to $Re_{D_h} = 2800$, the largest Reynolds number tested. The additional bubble on the lower side is not captured by Lee and Mateescu (1998) measurements. While Mouza et al. (2005) only present the behaviour of x_1, which agrees with Armaly et al. (1983) measurements.

Measurements along the spanwise length by Armaly et al. (1983) at Re_{D_h} show a strong three-dimensional behaviour within the transitional regime. Armaly et al. (1983) showed how the position of the primary reattachment length dictates the position of the onset of the secondary bubble. This was confirmed with regard to their behaviour along the span, where if x_1 increases, x_2 increases too. The length of the secondary bubble behaves contrarily to former parameters, i.e. x_1 and x_2 are moved downstream, the length of the bubble is shortened and vice versa.

- Turbulent regime

With the increase of Re_{D_h}, the secondary bubble disappears and the primary recirculation length rises ever so slightly until resembling a constant behaviour as Armaly et al. (1983) reported. This agrees with experimental values reported by Mouza et al. (2005) and prior experiments by Abbott and Kline (1962) at a higher Reynolds number. The constant behaviour within the turbulent regime was also confirmed by Moss et al. (1979), however, the larger the expansion ratio is, the larger is the primary reattachment length within the turbulent regime.

The plateau achieved at high Reynolds number regimes within the turbulent region was also confirmed by Durst and Tropea (1981), who studied the primary reattachment length decency to Reynolds number and expansion ratio.

2.6.2 Review of numerical studies

The first DNS for fully turbulent backward-facing step analysis was carried out in the late 90s by Le et al. (1997), with an expansion ratio of 1.2. However, it was not until Biswas et al. (2004) and Schäfer et al. (2009), that a DNS to study the BFS flow transition from laminar to turbulent was performed. The growth of x_1 with the increase of Reynolds number, predicted by DNS from Biswas et al. (2004), agrees with Armaly et al. (1983) as well as the appearance of the secondary bubble. Furthermore, it confirms the three-dimensional for $Re_{D_h} > 400$. At the end of the transitional regime $Re_{D_h} = 6000$, predictions by Schäfer et al. (2009), confirms the presence of the secondary bubble at this Reynolds number and its agreement with the length of x_1 , and the secondary bubble measured by Armaly et al. (1983). DNS simulations provide insight about the vortical structures interactions with the main flow and recirculating bubbles. Furthermore, it shows the interaction of the primary and the secondary bubble observed by Armaly et al.

(1983). A fully turbulent DNS with an expansion ratio of 2 was performed by Pont-Vílchez et al. (2019). The constant plateau right after the transitional region is confirmed and in good agreement with Armaly et al. (1983) experimental data. In addition, they analyse the vortical Kelvin-Helmholtz structures emanating from the shear layer after the separation point, to provide a deeper insight into the flow physics.

Rani et al. (2007) study the transitional region for backward-facing step using an LES approach at $Re_{D_h} = 2000$, apart from demonstrating the strong dependence of reattachment lengths to Reynolds number. It provides an insight into the interaction between vortical structures emanating from secondary bubble and primary reattachment length, concluding that the development of the Kelvin-Helmholtz structures leads to a transition to a fully developed turbulent flow. Choi et al. (2016) also showed agreement for the primary reattachment length at an angle of 90° and an expansion ratio of 2, although any further insight is given. Similarly happens for DDES predictions. Spalart et al. (2006) present a prediction comparing DES and DDES for the Driver and Seegmiller (1985) case, higher aspect ratio than Armaly et al. (1983) and fully turbulent case. Simulations for a similar case are carried out by Wang et al. (2014), which shows the possibility to describe turbulent flow with DDES although the transitional regime is avoided and no further insight on transitional flow is given.

To the author's knowledge, only Medina and Early (2014) have performed a test for aft-facing step flow using URANS transitional model $k - k_L - \omega$. This work presents a two-dimensional analysis using the AFT model, throughout the three big already described regimes to determine the strengths and weaknesses of using transitional modelling AFT approach than high fidelity approaches. Ratha and Sarkar (2015) reported an analysis throughout the three regions using $k - \epsilon$. Predictions show the consistent shortening of the primary reattachment length and secondary bubble, reaching a constant behaviour in the early stages of the transitional regime as if the flow field was completely turbulent.

2.6.3 Summary

Major findings were reported by Armaly et al. (1983) with the identification of three different regimes dependent on the Reynolds number and in this case for an expansion ratio of approximately 2. These regimes are confirmed by DNS, as well as the appearance of a tertiary laminar bubble. Three-dimensional behaviour of the flow is also reported by measurements and confirmed by either DNS or LES simulations from $Re_{D_h} \sim 400$ approximately. Few attempts to identify the transitional effect have been done, especially simulations by Rani et al. (2007) report insight into the main cause of the transitional behaviour. Fully turbulent analyses are performed with LES and DDES as discussed, showing the capability to provide a better description of the physics within the recirculating region but any transitional analysis is reported.

Most RANS methods are focused on producing studies on the fully turbulent regime. Ratha and Sarkar (2015) produced a complete analysis throughout the whole spectrum of Reynolds numbers, over the three different regimes, showing the shortening of the primary and secondary bubbles, without the prediction of the tertiary bubble. This work aims to present a complete analysis using the transitional AFT and AFT-RSM models for the laminar, transitional and turbulent regime to demonstrate the improved predictions that transitional models can bring for backward-facing step flow.

2.7 Flow past a circular cylinder

The analysis of bluff-body transitional flow and specifically flow past a circular cylinder is the main interest of this project, as already discussed. Flow past a circular cylinder is known to exhibit a different range of physical phenomena that are interesting to the scientific community. Existing experimental and numerical analyses are discussed in the following paragraphs.

2.7.1 Review of experimental studies

Roshko (1961) first divided the behaviour of the flow past a circular cylinder into four big regimes depending on Reynolds number based on cylinder diameter (Re_D), where some of them are internally dividend in sub-regimes. Bear in mind that this is an idealized solution for a disturbance-free flow. Regions are sub-critical, critical, super-critical and trans-critical. Zdravkovich (1997) considered the position of the separation point the key feature to classify the particular state of the flow past a circular cylinder. This explanation is done by reflecting on the four big groups initially proposed by Roshko (1961) and shown in Figure 1.2.

- Laminar and Transition in the wake regime

With the increased Reynolds number, the flow develops from not having a separation, passing through a steady and stable state with a closed wake to an unsteady behaviour following the wake transition. At approximately $Re_D = 1000 - 2000$ the flow is observed to first become turbulent, due to Kelvin-Helmholtz instability of the two shear layers separating from the cylinder, as Prasad and Williamson (1997) discussed. Above this Reynolds number, the turbulence in the wake flow strengthens and gradually moves closer to the cylinder base with the increased Re_D. This marks the onset of shear-layer transition within the sub-critical regime.

- Sub-critical regime

As introduced, the sub-critical regime coincides with the transition in the shear layers identified by Zdravkovich (1997). It is commonly called sub-critical, referring to the fact

that the boundary layer remains laminar up to and beyond the separation position over the cylinder surface. In this state, the free shear layers are the ones determining the behaviour of the flow in the near wake. Zdravkovich (1997) named the typical structures of this regime transition eddies. A general tendency regarding the transition on the shear layers for increasing Re_D, accompanied by a reduction of the recirculating length and increasing drag coefficient because of the transition eddies moving gradually closer to the back of the cylinder.

Further increasing the Re_D shows a constant behaviour for C_D and fluctuating lift and drag by Zdravkovich (1997) due to the stagnation of transition. This was confirmed by Weidman (1968) as well since he found the pressure minima for the cylinder surface between $Re_D = 10^4 - 10^5$ are practically similar to the increase of Reynolds number. Measurements performed by Achenbach (1968), Cantwell and Coles (1983) confirmed the laminar separation and a rather constant behaviour of C_D within the upper sub-critical range as shown in Figure 1.2.

- Critical regime

As Reynolds increases, the transition advances in the free shear layers until it reaches the separation location. This triggers a complex interaction between separation and transition, at about $Re_D = 2 \times 10^5$ but somewhat arbitrary in literature due to its high sensitivity to experimental conditions and uncontrolled perturbations. However, the main characteristic is the sharp fall of the drag, as shown in Figure 1.2, due to a narrowing of the wake and a gradual movement of the separation downstream the cylinder surface with the increase of Reynolds number. The length of the formation eddy is stretched and the roll-up of shear layers occurs further downstream. Initial pressure surface measurements within this region were performed by Fage and Falkner (1931), Giedt (1951) and Bursnall and Loftin (1951).

With the subtle increase in Reynolds number, a single laminar separation bubble can appear on one side of the cylinder surface, while the opposite side retains the sub-critical behaviour as first identified by Bearman (1969) and later on by Achenbach and Heinecke (1981). Analysis of such asymmetric behaviour was performed by Schewe (1983) in detail. He concluded that these phenomena "lies in the behaviour of the boundary layer", with the occurrence of perturbations or fluctuations inherent in the boundary layer and the freestream causing the single bubble initially. Thus, once the reattachment happens for the single bubble, there is an acceleration on one side and a deceleration on the other, delaying the appearance of the second bubble on the opposite side. Therefore, as Reynolds number is ever so slightly increased, the increased acceleration on the opposite side (decelerated when single bubble forms) causes the second laminar separation bubble to occur. At this point, the drag is minimum, and the Reynolds number is so-called critical Reynolds number, marking the beginning of the supercritical regime. The specific side where the initial single bubble appears is not clear yet since measurements by

Bearman (1969) and Farell and Blessmann (1983) reveal different behaviour. Furthermore, the Reynolds number occurrence remains to be fully established as Schewe (1983), Zdravkovich (1997) and Achenbach (1968) determine different Reynolds numbers for the onset of the critical region.

- Super-critical regime

Hence, this region is characterised by two separation bubbles with a delayed turbulent separation. Schewe (1983) investigated a constant vortex shedding with maximum values of $St = 0.48$ with narrow band lift fluctuations. Throughout the whole region, the mean drag can be considered constant, although a small rise is observed. Measurements by Roshko (1961), Achenbach (1968), Schewe (1983) and Shih et al. (1993) confirmed the supercritical behaviour with the stabilization of the two laminar separation bubbles and the almost constant value of C_D and St over this regime.

- Trans-critical regime

With the further increase of Reynolds number, the suppression of vortex shedding marks the beginning of the trans-critical regime. In this regime, the drag coefficient is essentially constant, after the rise between the transition from the super-critical regime. This means the position of the separation point is almost constant. Transition in this case will move gradually towards the stagnation point until the flow can be considered completely turbulent as measurements carried out by Roshko (1961) demonstrate.

2.7.2 Review of numerical studies

As discussed, experiments with increased Re_D become sensitive to many effects such as tunnel blockage, surface roughness, turbulence levels and uncontrolled perturbations. Thus, numerical simulations could potentially avoid some of these effects and therefore provide a clearer insight into the physics of flow past a circular cylinder.

DNS predictions are available for $Re_D = 3900$, at intermediate sub-critical regime, and up to $Re_D = 10^4$ by Dong et al. (2006). However, this Reynolds number is well below the drag-crisis regime, and consequently further away from supercritical and trans-critical regimes. With the increased Re_D, the grid requirements escalate very rapidly to be accessible for DNS predictions. Alternatives available at the sub-critical regime are LES predictions such as Kim (2006),Cheng et al. (2017), Breuer (2000) and DDES simulations by Liu et al. (2019) and D'Alessandro et al. (2016).

In the critical region, wall-resolved and wall-modelled methods have been used by Catalano et al. (2003), Rodríguez et al. (2015), and Cheng et al. (2017) in the study of flow over a circular cylinder. Travin et al. (1999) produced predictions using a DES approach at the the critical regime and further deep within the trans-critical region ($Re_D = 3.6 \times 10^6$) and Liu et al. (2019) up to $Re_D = 3.6 \times 10^5$ in the critical regime.

As discussed by Cheng et al. (2017), there have been few efforts in closing the gap between the current accessible range to DNS simulations and high Reynolds numbers. To the author's knowledge, only two have attempted to close that gap with wall-resolved LES simulations that are Cheng et al. (2017) and Rodríguez et al. (2015), with results at $Re_D = 6.5 - 8.5 \times 10^5$. One of the aims of this work is to close the gap with the use of a DDES hybridisation of a RANS transitional approach using AFT methodology for transition prediction in the near wall region and the recovery of LES behaviour away from the walls, rather than a fully turbulent assumption of the boundary layer in the near wall region.

Transitional URANS approaches are currently another possibility for the circular cylinder predictions. To the author's knowledge only Vaz et al. (2009) and Zheng and Lei (2016) have presented analyses for flow past a circular cylinder using Menter et al. (2015). In these publications, results show promising results only from skin friction and surface pressure perspective, but the critical regime analysis is missing, as well as comparisons to available DDES, LES and experimental. Furthermore, the validity of downstream results over the cylinder surface are doubtful, while still predicting a fall of C_D in the super-critical regime. Another aim of this work is to present an insight description not only from a surface perspective but also from a wake perspective using AFT transitional approach, from sub-critical to trans-critical and demonstrate the enhanced predictions to Menter models, including the critical regime.

2.7.3 Summary

From the experimental review, there is a general agreement regarding the four big regimes shaping the flow dynamics for flow past a circular cylinder: sub-critical, critical, super-critical and trans-critical.

The laminar boundary layer development and the laminar separation are well established in the literature regarding sub-critical flow physics. Available measurements performed throughout the sub-critical regime, either mid or upper region of the same, agree with the drag coefficient, shedding frequency and lift fluctuations, and literature data do not show a large scatter data. The initial rise and stall of the drag coefficient measures, once the transition is in a constant location downstream within the shear layers, and the constant shedding frequency is identified overall.

In the critical regime, the key finding is the deep investigation by Schewe (1983) of a single laminar separation bubble mode followed by the establishment of a second laminar separation bubble with a mild increase of the Reynolds number. Nonetheless, there is scatter data regarding the side of the single bubble appearance and the Reynolds number of the onset of the critical region. The general conclusion for that scatter is the sensitivity

of this regime to differences in experimental conditions and uncontrolled disturbances affecting the boundary layer and free shear layers.

Supercritical and trans-critical key findings are the symmetric recovery with the occurrence of the second separation bubble and its disappearance at a sufficient Reynolds number, respectively. Measurements available on both regimes are in agreement, although at trans-critical regime, measurements of drag coefficient and Strouhal number show differences in value while presenting the same tendency.

Numerically, only two publications analyse the performance of Menter et al. (2015) from a surface behaviour perspective with the lack of information on the critical regime and wake behaviour. DDES by Liu et al. (2019) are carried out up to $Re_D = 3.6 \times 10^5$ showing the fall of C_D at the critical regime. Wall-resolved LES simulations provide an insight into the asymmetric bubble, confirming experimental observations, as well as for the supercritical regime, with the recovery of symmetric flow with the occurrence of the second bubble. Travin et al. (1999) demonstrate the agreement with transition occurring at the upstream face at trans-critical regime $Re_D = 3.6 \times 10^6$. Regarding transitional URANS just the work done using $\gamma - Re_\theta$ mode is available, missing the critical region and presenting numerical instabilities in the results. Hence, this work aims to present a deep analysis using transitional AFT, which is a much simpler model than Menter et al. (2015) approach, along with transitional DDES at high Reynolds numbers.

Chapter 3

Amplification Factor Transport Model

In this Chapter, the Amplification Factor Transport model details are given. The base definition of the AFT is a contribution published in Coder and Maughmer (2014). However, the author's contribution in this thesis is the implementation of the model into OpenFOAMv1912 and the modification of the intermittency equation, which is reverted from $\ln(\tilde{\gamma})$ (as expressed in Coder, 2017) to γ. With regards to the extension of the AFT model with a Reynolds Stress Model closure is also a contribution, as well as the implementation into OpenFOAMv1912. The chapter implements and discusses the contribution in Coder and Ortiz-Melendez (2019) for the incorporation of AFT into DDES hybrid approaches.

3.1 Amplification Factor Transport Model

A wide range of turbulence models are available for fully-turbulent flows using Reynolds-averaged Navier-Stokes (RANS) simulations. However, they are not suitable for laminar boundary-layer or transition to turbulence prediction. To incorporate transition prediction different techniques have been proposed and applied in the industry. Empirical transition criteria as the work by Abu-Ghannam and Shaw (1980) or Gostelow et al. (1994), the e^{N} method by van Ingen (1956) and transport equation-based approaches. Out of all of the transitional methods compatible with current CFD methodologies, the AFT model, proposed by Coder and Maughmer (2014), is appealing as it estimates the actual amplification of the Tollmien-Schilichting waves via a scalar transport equation and accounts for the upstream boundary layer history, therefore responding better to pressure gradients than models by Langtry and Menter (2009) and Menter et al. (2015). The model has been mainly validated for flow over flat-plate and airfoil-like geometries with moderate curvature. The main goal of the following chapters is to assess and

demonstrate the performance of the transitional AFT model, and the improvements of different modifications to the original AFT model for flat-plate, backward-facing step and most extensively for flow past a circular cylinder at high-Reynolds number, where the separation point is not fixed and the curvature is not moderate.

The AFT model introduces correlations to compute the variation of the amplification factor ($\tilde{n}$) in terms of the momentum-thickness Reynolds number (Re_θ) for a fixed integral shape factor, defined as the displacement-thickness to the momentum-thickness ratio ($H_{12} = \delta_1/\theta$) at every point in the flow. In the current AFT model, the $\tilde{n}$ correlations were introduced by Drela and Giles (1987) from the analysis of Falkner-Skan similarity velocity profiles. Moreover, the current AFT model determines the flow stability purely based on the critical Reynolds number. All these correlations depend on the estimation of the momentum thickness Reynolds number and the integral shape factor, which are estimated via proportionality functions with the local shape factor defined in Equation 3.5 and the vorticity Reynolds number defined as

$$Re_{\mathrm{v}} = \frac{S d_w^2}{\nu + \nu_t} \tag{3.1}$$

where d_w is the wall distance, S is the strain rate magnitude, ν refers to kinematic viscosity and ν_t refers to turbulent eddy viscosity.

The original AFT model proposed by Coder and Maughmer (2014), capable of producing a transition estimation with the description of the envelope of linearly amplified instabilities within the boundary layer via the amplification factor ($\tilde{n}$), reads as

$$\frac{\partial \widetilde{n}}{\partial t} + \frac{\partial u_j \widetilde{n}}{\partial x_j} = \Omega F_{\mathrm{crit}} F_{\mathrm{growth}} \frac{\mathrm{d}\widetilde{n}}{\mathrm{d}Re_\theta} + \frac{\partial}{\partial x_j}\left[\frac{1}{\sigma_n}(\nu + \nu_t)\frac{\partial \widetilde{n}}{\partial x_j}\right]. \tag{3.2}$$

$$F_{\mathrm{growth}} = D(H_{12})\frac{1 + m(H_{12})}{2} l(H_{12}) \tag{3.3}$$

$$F_{\mathrm{crit}} = \begin{cases} 0, Re_V < Re_{V,cr} \\ 1, Re_V \geq Re_{V,cr} \end{cases} \tag{3.4}$$

The AFT equation given above is dominated by the production term (first term on the right-hand side of Equation 3.2), which controls the rate of amplification of the most unstable frequencies in terms of Re_θ. Drela and Giles (1987) proposed a correlation for $\mathrm{d}\bar{n}/\mathrm{d}Re_\theta$ based on similarity velocity profiles together with the correlation for the critical Reynolds number $Re_{\theta,\mathrm{cr}}$ as shown Equations 3.7 and 3.8 in terms of an integral shape factor H_{12}.

Since the AFT model does not compute any integral boundary-layer property to ensure the model is compatible for parallel CFD solvers, H_{12} is estimated via the local shape factor (H_L). The local shape-factor H_L is based on the work of Menter et al. (2015) on the evaluation of a local boundary-layer shape factor or the pressure-gradient parameter and is defined as.

$$H_L = \frac{d_w^2}{\nu}\frac{\mathrm{d}U_y}{\mathrm{d}y}, \tag{3.5}$$

where $\mathrm{d}U_y/\mathrm{d}y$ denotes the gradient of the wall-normal velocity in the wall-normal direction. H_L is computed everywhere but its maximum value (approximately in the middle of the boundary layer) is the one used to establish the correlations, as originally proposed by Coder and Maughmer (2014). This H_L estimation is related to the integral shape factor H_{12} from Falkner-Skan similarity profiles as defined in Equation 3.6.

$$H_{12} = 0.376960 + \sqrt{\frac{H_L + 2.453432}{0.653181}}. \tag{3.6}$$

$$\frac{\mathrm{d}\widetilde{n}}{\mathrm{d}Re_\theta} = 0.028(H_{12}-1) - 0.0345\exp\left[-\left(\frac{3.87}{H_{12}-1} - 2.52\right)^2\right] \tag{3.7}$$

$$\log_{10}(Re_{\theta,\mathrm{cr}}) = 0.7\tanh\left(\frac{14}{H_{12}-1} - 9.24\right) + \left(\frac{2.492}{(H_{12}-1)^{0.43}}\right) + 0.62 \tag{3.8}$$

The F_{growth} function encapsulates the effects of the growing boundary layer over separation bubbles by the use of two empirical correlations proposed by Drela and Giles (1987) based on solutions from the Falkner-Skan similarity profiles. F_{crit} is a function that determines if the local boundary layer is capable of containing instabilities, switching on or off the production of $\tilde{n}$. The function k_{v} describes the proportionality of the two Reynolds numbers Re_{v} and Re_θ from Falkner-Skan similarity profiles. Since the AFT model does not compute the momentum thickness at any point, k_{v} is needed to estimate the momentum-thickness Reynolds number. The proportionality function is defined as

$$k_{\mathrm{v}} = 0.4036H_{12}^2 - 2.5394H_{12} + 4.3273 \;\text{ where }\; Re_{\mathrm{v}} = k_{\mathrm{v}}Re_\theta. \tag{3.9}$$

The vorticity Reynolds number defined in Equation 3.1 can be computed at every single point in the domain, so if it is larger than its critical value, the F_{crit} function equals unity. Otherwise, it will remain zero and no unstable modes will be amplified within the boundary layer. Figure 3.1 shows the behaviour of k_v, dn/dRe_θ and $Re_{\theta,cr}$ in terms of the integral shape factor for completeness. The AFT model is coupled to a fully-turbulent

approach, specifically the Spalart-Allmaras turbulence model proposed by Spalart and Allmaras (1994), via the following intermittency (γ) transport equation

$$\frac{D\gamma}{Dt} = c_1 S F_{onset}(1-\gamma) + c_2 \Omega F_{turb}(c_3\gamma - 1) + \frac{\partial}{\partial x_j}\left[\left(\nu + \frac{\nu_t}{\sigma_\gamma}\right)\frac{\partial \gamma}{\partial x_j}\right] \tag{3.10}$$

$$F_{\text{onset}} = \max\left[\min(\tilde{n}/N_{crit}, 2.0) - \max[1-(\nu_t/3.5\nu)^3, 0]\right] \tag{3.11}$$

$$F_{\text{turb}} = \exp[-(\nu_t/2\nu)^4] \tag{3.12}$$

where S is the magnitude of strain rate, ω is the vorticity magnitude and c_1, c_2, c_3 and σ_γ are calibration constants inherited from Menter et al. (2015) with values 100, 0.06, 50 and 1.0 respectively. The F_{onset} triggers the production of intermittency depending on the $\tilde{n}$ to N_{crit} ratio. The F_{turb} term ensures that intermittency is not destroyed within a turbulent boundary layer.

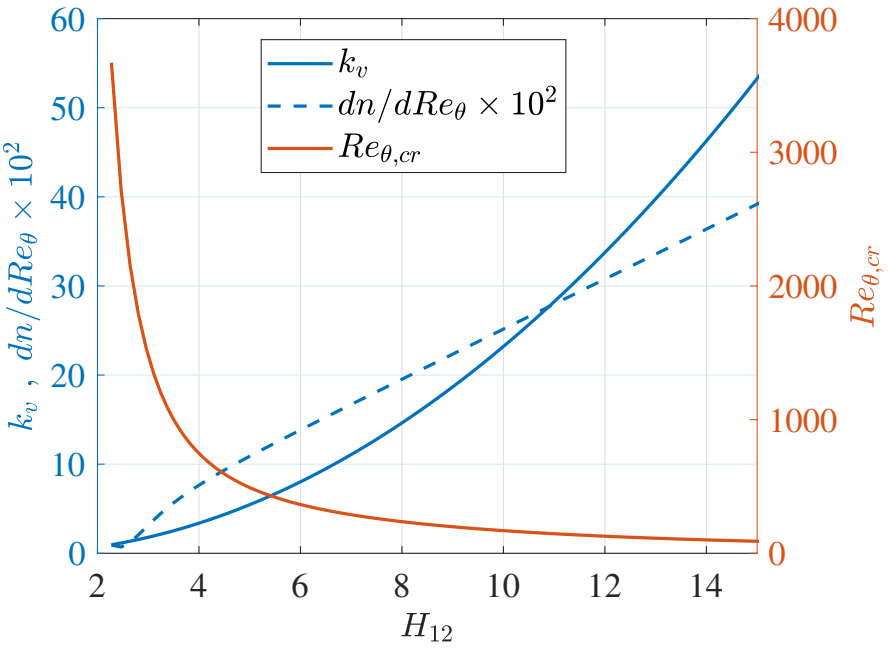

FIGURE 3.1: Variation of the k_v, dn/dRe_θ and $Re_{\theta,cr}$ factors in terms of the H_{12}.

The coupling is performed using a modified f_{t2} function from the original Spalart and Allmaras (1994) turbulence model as

$$f_{t2} = c_{t3}(1-\gamma) \tag{3.13}$$

where c_{t3} is a calibration constant with a value 1.2 which comes from the original Spalart and Allmaras (1994) fully-turbulent approach. This term ensures stability for regions of zero eddy viscosity and it is present in both production and destruction terms. When $\tilde{\nu}$ is close to zero, the production term becomes negative and provides stable laminar solutions. Its effect on the destruction term is to cancel in fully-turbulent layers without affecting the stability of laminar flows. The rest of the details regarding Spalart and Allmaras (1994) model can be found in the publication.

These four correlations are pivotal for the prediction of the transition onset. As discussed, this set of four correlations is based on Falkner and Skan (1931) velocity profiles. This may have a negative influence on flow past a circular cylinder at high-Reynolds number predictions. The shortcomings of these correlations are discussed in the following chapters. Ultimately, the last chapter presents a study of how these four correlations compare to relations achieved from LES simulations for flow past a circular cylinder. Furthermore, new correlations are proposed and their performance for different high-Reynolds regimes for flow past a circular cylinder is discussed.

To proceed with the implementation details first it is important to understand a bit the structure of OpenFOAM source code. OpenFOAM is constructed following the bases of Object-Oriented Programming (OOP), hence for the different methods like RANS, LES or DNS, the code is divided into "namespaces" that are divided into classes which refer to specific models like SST, S-A or $k-\omega$ SST-DDES among others. In addition, the structure of OpenFOAM is simplified via templates that can be used as a starting point to complete new implementations or modifications to the solver.

In this case, the process starts using the template from the already implemented Spalart-Allmaras model. The fully turbulent approach does not have implemented the f_{t2} function, so a method had to be defined and the term incorporated into the corresponding term of its transport equation. As in the example in Figure 3.2, all the methods to compute the values of F_{crit}, F_{growth} are implemented in the same way following the C++ syntax.

```
//Transitional Flow function

template<class BasicTurbulenceModel>
tmp<volScalarField> aft19<BasicTurbulenceModel>::ft2
(

) const
{
    return Ct3_*(1.0-gamma());
}
```

FIGURE 3.2: Definition of f_{t2} method in OpenFOAM C++ code.

Following the properties of the model, all the calibration constants must be declared and defined. OpenFOAM implements parsers to do such procedures. As the turbulence

model is declared in the OpenFOAM environment, a method inside the "read()" function named "$readIfPresent()$" is called, which will automatically read the values from the default defined in the source code or the values defined in the OpenFOAM case property file. An example of the definition of a calibration constant is shown together and the shape of the function "$read()$".

In addition, the new physical properties γ and $\tilde{n}$, are defined as the calibration constants but in this case, the properties of the method are different as shown in Figure 3.3.

```
gamma_
(
    IOobject
    (
        "gamma",
        this->runTime_.timeName(),
        this->mesh_,
        IOobject::MUST_READ,
        IOobject::AUTO_WRITE
    ),
    this->mesh_
),
```

FIGURE 3.3: Definition of γ variable in OpenFOAM C++ code.

The last important part is to define the new transport equations for the new model, in this case, the AFT. An example of the definition of the $\tilde{n}$ transport equation is shown in Figure 3.4.

```
volScalarField Pgamma1 = c1_ * S * gamma_ * Fonset;
volScalarField Pgamma2 = c2_ * Omega * gamma_ * Fturb;


//-Solve intermittency equation
tmp<fvScalarMatrix> gammaEqn
(
  fvm::ddt(alpha, rho, gamma_)
+ fvm::div(alphaRhoPhi, gamma_)
- fvm::laplacian(alpha*rho*DgammaEff(), gamma_)
==
  alpha*rho*Pgamma1
- fvm::Sp(alpha*rho*Pgamma1, gamma_)
+ alpha*rho*Pgamma2
- fvm::Sp(alpha*rho*c3_, gamma_)
);

gammaEqn.ref().relax();
solve(gammaEqn);
bound(gamma_, dimensionedScalar("0", dimensionSet(0, 0, 0, 0, 0), 0.0));
```

FIGURE 3.4: Definition of γ transport equation in OpenFOAM C++ code.

3.2 Transitional Amplification Factor Transport with Reynolds Stress Model

To this point, the pivotal equations for the original AFT transitional model is discussed. The method uses a fully-turbulent Spalart and Allmaras (1994) model based on eddy-viscosity closure. This section discusses the advantages and disadvantages of the eddy-viscosity closure and proposes the use of a Reynolds Stress Model for improved predictions along the AFT transitional model.

The transitional framework from the original AFT alone only provides information about the state of the boundary layer. As discussed at the beginning of this section, the intermittency scalar has to be blended with a turbulent closure model, which will be fully recovered when the criteria for the transition onset are fulfilled.

Currently, the original transitional AFT presented in the first section of this chapter uses the Spalart-Allmaras turbulent approach. However, there are other versions of the model with the use of the Shear Stress Transport turbulent approach proposed by Menter (1993). These turbulence models use the Boussinesq hypothesis by Boussinesq (1903) as a closure approach which is not ideal for predicting different types of flow-fields, such as flow with sudden changes in mean strain rate, flow over curved surfaces, anisotropy of the normal stresses.

3.2.1 Reynolds Stress Model

The Boussinesq hypothesis is based on the postulation made by Boussinesq (1903) that the momentum transfer caused by turbulent eddies can be modelled with an eddy viscosity term. This assumption is a direct analogy with how the momentum transfer caused by the molecular motion in a gas is described by molecular viscosity. In a sheared flow, the lower particles are accelerated by the faster-moving fluid located above. This interaction generates a net transport of momentum to the lower particles. In a general case, it can be said that the momentum is transported in the direction of the velocity gradient.

Thus, the Boussinesq hypothesis assumes that the turbulent shear stress is proportional to the trace-less mean strain rate tensor. The eddy-viscosity has been proven to provide good predictions for a wide range of scenarios by different turbulent models. However, the application of such linear relation leads to failure in certain areas as:

- flows with sudden changes in mean strain rate;
- flow over curved surfaces (streamline curvature);
- flow in systematic rotation;

- the prediction of the anisotropy of the normal stresses;
- the prediction of the return to isotropy.

In addition to the above five points discussed by Wilcox (1994) and Pope (2000), experimental evidence reveals that the history flow effects for τ_{ij} persist for long distances, thus compromising the validity of a single linear relationship between the Reynolds stress tensor and the mean strain-rate tensor. Thus, a possibility is to use a higher-order method to predict the Reynolds stress tensor.

The Reynolds stress equation model is a second-order moment closure that avoids the computation of a single eddy-viscosity term for all the components of the tensor and the individual components of the Reynolds stress tensor are directly computed. The use of the Reynolds stress model addresses some of the shortcomings introduced by the use of Boussinesq hypothesis, however, the exact equation requires modelling for the dissipation, pressure-strain rate and turbulent transport terms. The following paragraphs discuss the improvement compared to the use of eddy-viscosity closure from the analysis of the exact equation for the Reynolds stress tensor in Equation 3.14.

$$\frac{\partial \tau_{ij}}{\partial t} + U_k \frac{\partial \tau_{ij}}{\partial x_k} = -\tau_{ik}\frac{\partial U_j}{\partial x_k} - \tau_{jk}\frac{\partial U_i}{\partial x_k} + \epsilon_{ij} - \Pi_{ij} + \frac{\partial}{\partial x_k}\left[\nu \frac{\partial \tau_{ij}}{\partial x_k} + C_{ijk}\right] \tag{3.14}$$

where the dissipation, the pressure-strain redistribution and the turbulent transport term read as

$$\epsilon_{ij} = 2\nu \overline{\frac{\partial u_i'}{\partial x_k}\frac{\partial u_j'}{\partial x_k}} \tag{3.15}$$

$$\Pi_{ij} = \overline{\frac{p'}{\rho}\left(\frac{\partial u_i'}{\partial x_k} + \frac{\partial u_j'}{\partial x_k}\right)} \tag{3.16}$$

$$\rho C_{ijk} = \rho \overline{u_i' u_j' u_k'} + \overline{p' u_i'}\delta_{jk} + \overline{p' u_j'}\delta_{ik}. \tag{3.17}$$

It can be seen from the analysis of the exact equation for the Reynolds stress tensor that a second-order approach for the Reynolds stress tensor description will include effects of flow history with the presence of convection and diffusion of τ_{ij}. Additionally, the time scales unrelated to mean flow time scales are present with the dissipation and turbulent-transport terms, which leads to a better prediction of the flow history than eddy-viscosity closure models.

The streamline curvature and system rotation are more realistically represented too with the use of a second-order approach for describing the Reynolds stress tensor τ_{ij}.

This is due to the presence of the convection and production term for the Reynolds stress tensor, which responds automatically to such effects qualitatively better than eddy-viscosity closures.

From the analysis of Equation 3.14, it can also be said the Reynolds stress equation for each component should not predict the normal stresses to be equal when the mean strain-rate vanishes, since their relationship is not linear as for the eddy-viscosity closures. In fact, the values of the normal stresses will depend on other flow processes.

The dissipation, turbulent transport and pressure strain terms could be modelled with different approaches. One of these approaches is the well-known SSG-LRR Reynolds stress model proposed by Eisfeld et al. (2016). The fundamental idea behind the SSG-LRR-ω is to combine the ϵ-based SSG model to utilise the pressure-strain correlation and the insensitivity provided by ϵ to the initial conditions of ω, along with the LRR model in the near-wall region, which is based on the ω-equation being capable to provide accurate predictions in the near-wall region.

The dissipation rate in Equation 3.15 is commonly modelled following Kolmogorov's hypothesis of local isotropy at the smallest scales of turbulence for high-Reynolds number flows, where the dissipation occurs. To compute the isotropic dissipation rate, the ω equation as for the Shear Stress Transport is used. Note that the assumption of local isotropy is not completely correct in the near wall region where the behaviour is essentially anisotropic. However, the incorporation of the dissipation term for each component of the Reynolds stress tensor τ_{ij} would lead to a better description of flow history effects.

Another term in the second-order approach of SSG-LRR that helps in the improved description of flow history effects and that requires modelling is the turbulent transport term in Equation 3.17. The spatial redistribution of the Reynolds stress tensor due to fluctuating velocity field and pressure fluctuations is commonly modelled using a simple gradient diffusion term. This is the case with the SSG-LRR Reynolds stress model.

The last term for the closure of the SSG-LRR Reynolds stress model or any second-order approach is the pressure-strain term in Equation 3.16. This term is where most of the efforts are focused by the researchers since its function is crucial for the description of the Reynolds stress tensor behaviour. This term is also referred to as the pressure-strain redistribution term and it serves to distribute the energy among the components of the Reynolds stress tensor. In a turbulent boundary layer, redistribution of energy is as dominant as production and dissipation terms.

As discussed by Pope (2000), in the energy budget of the streamwise Reynolds stress R_{11} for a turbulent boundary layer, the redistribution is as significant as the dissipation term, since it removes energy at twice the rate of dissipation. This energy deduction is balanced by the production of energy for the streamwise normal Reynolds stress. For

the wall-normal and span-wise normal Reynolds stresses, the production is negligible but the dissipation is significant. In this case, the energy balance is achieved by the redistribution term. Essentially, energy is transferred from the dominant axis to the other two directions of the normal stress. Regarding the energy budget distribution for the cross Reynolds stress terms, the behaviour is similar to wall-normal and span-wise but in this case, the redistribution term balances the production term because dissipation is negligible. The redistribution term also addresses a shortcoming of the Boussinesq hypothesis which is the return to isotropy with the presence of the term including the behaviour of self-interaction of the fluctuating field. These explanations show the important role that the redistribution term plays in the Reynolds stress equation and the need to propose correct modelling.

The SSG-LRR Reynolds stress model divides the modelling of the pressure-strain-rate term into two parts. The first part, often referred to as the rapid-strain term, aims to model the behaviour of the redistribution of energy throughout all the components of the Reynolds stress tensor due to the interaction between the fluctuating field with the mean velocity field. The second part of the term is referred to as the slow-strain pressure term and is responsible for the redistribution of energy for the return to isotropy due to the self-interaction of the fluctuating field.

3.2.2 Transitional AFT with Reynolds Stress model

The original AFT transitional framework consists of a two-equation model formed by an intermittency transport equation and the AFT equation. These of two equations in the original model are coupled to the Spalart-Allmaras fully-turbulent approach via the intermittency transport equation. Similarly, the SSG-LRR Reynolds stress model is coupled in this work to the transitional framework via the intermittency transport equation modifying some of the present terms in the Reynolds stress equation. The coupling will allow the SSG-LRR Reynolds stress model to produce a laminar solution until the transition criteria are fulfilled. From the transition onset onward, the SSG-LRR Reynolds stress model will produce a transitional region until the fully-recovery of the fully-turbulent behaviour of the Reynolds stress model. Three terms must be modified: the production of the Reynolds stress, the dissipation of the Reynolds stress and the pressure-strain term.

The production term represents the work done of the mean velocity gradients to the Reynolds stresses and can be computed directly without any modelling required. Essentially, this term accounts for the transfer of kinetic energy from the mean flow to the fluctuating velocity field. Hence, in essence, it sustains the turbulence generation transferring energy from the largest-scale eddies to the small-scale eddies. This description of the physical behaviour for the production term is valid for a fully-turbulent flow field. In a laminar region, experimental results revealed that the contribution of the production

term of Reynolds stress is negligible. Thus, the transitional SSG-LRR approach needs to eliminate the contribution of the production term within the laminar region. After the transition onset, the production term starts to recover its relevance due to the appearance of the interactions between the mean flow and the growing fluctuating velocity field. To achieve this behaviour, the new production term for the SSG-LRR Reynolds Stress Model is

$$P_{t,SSGLRR} = \gamma P_{o,SSGLRR} \tag{3.18}$$

where subscript $'t'$ indicates the term for the transitional SSG-LRR model and subscript $'o'$ indicates the original term in Equation 3.14, in this case, the production term.

As a consequence of the Reynolds stress production term being negligible within the laminar region, is that how the dissipation terms behave within that region. Essentially, since there is no transfer of kinetic energy from the mean flow to the fluctuating velocity field, there is not any fluctuating velocity being fed and consequently a nonexistent dissipation at this scale. Thus, similarly to the new production term, the new dissipation term is multiplied by intermittency to neglect its activation during the laminar regime as

$$E_{t,SSGLRR} = \min(\gamma, 1) E_{o,SSGLRR} \tag{3.19}$$

where subscript "t" indicates the term for the transitional SSG-LRR model and subscript "o" indicates the original modelled dissipation term in Eisfeld et al. (2016). The min factor is used as a safeguard to recover the fully-turbulent dissipation term in case γ exceeds 1 due to numerical instabilities.

Furthermore, due to the negligible contribution of the Reynolds stresses within the laminar region, there is not any possible distribution of energy from the streamwise fluctuating velocity towards the rest of the directions. Consequently, the contribution of the pressure-strain term is negligible during the laminar region but it regains its relevance beyond the transition onset point. Hence, the new pressure-strain term is multiplied by the intermittency term to achieve the behaviour discussed above and reads as

$$\Pi_{t,SSGLRR} = \gamma \Pi_{o,SSGLRR} \tag{3.20}$$

where subscript $'t'$ indicates the term for the transitional SSG-LRR model and subscript $'o'$ indicates the original modelled transport term in Eisfeld et al. (2016). The rest of the details of the model are inherited from the original SSG-LRR-ω.

The final form of the AFT-RSM consists of the intermittency (γ) transport equation as Equation 3.10, the amplification factor transport ($\tilde{n}$) equation as Equation 3.2, the Reynolds stress (τ_{ij}) transport equation in Equation 3.14 from Eisfeld et al. (2016) with modifications from Equations 3.18-3.19 and Equation 3.20 and the specific dissipation rate (ω) transport equation in Eisfeld et al. (2016).

The transitional AFT-RSM model is used in this work for predictions on a zero-pressure gradient flat-plate, backward-facing step flow and flow past a circular cylinder at high Reynolds numbers. The first case verifies and validates the implementation of the Reynolds Stress Model extension coupled with transitional AFT for a zero-pressure gradient flat plate where a natural transition occurs. Furthermore, Chapter 4 compares predictions to the AFT model presented in previous paragraphs and experimental data by Schubauer and Skramstad (1947). Chapter 5 uses the transitional AFT-RSM to predict laminar, transitional and turbulent regimes and validate its results against the original AFT and experimental data. Ultimately, Chapter 6 presents estimations using AFT-RSM for flow past a circular cylinder and its improved performance to fully turbulent methods and AFT, and further insight from a surface and wake perspective.

3.3 Transitional Delayed Detached Eddy Simulation Amplification Factor Transport Model

As introduced earlier in Section 2.5.4, the idea behind the use of RANS/URANS transitional models is to avoid resolving the complete spectrum of turbulence using DNS techniques or most of the turbulence spectrum via LES approaches down to the wall. On the other hand, RANS due to the averaging of all the scales are modelled and for the URANS, only the unsteady mean flow, i.e scales that are comparable to the geometry of the flow are resolved, whereas the rest of the scales are modelled.

RANS/URANS simulations have been shown to be useful in a wide range of flow typologies. As turbulent scales are modelled in RANS/URANS methods, this yields to inaccurate for some types of flows. In addition, the standard form of the S-A model becomes overly dissipative in wakes and separated flow regions as a result of the wall distance being the relevant length scale and approaching infinity. Examples are the bluff-bodies flows, where the wake consists of unsteady, large turbulent structures or flows with large separation regions. In fact, as discussed in Section 3.1, the main goal of this work is to produce predictions for the laminar, transitional and turbulent regimes of a backward-facing step, where a major part of the flow field is covered by a big separated region and predictions for bluff-body flow, specifically for flow past a circular cylinder.

Therefore, the use of a DES approach, introduced by Spalart et al. (1997), is an alternative to retain the RANS/URANS transitional prediction of the amplification factor

transport in the near wall region, while switching to LES when the turbulent scale exceeds the grid dimension. This hybridisation alleviates the demand for fine grid resolution in the near-wall region in comparison to fully-LES approaches down to the wall, in particular for high-Reynolds flows. Thus, the near-wall region is modelled instead of being fully resolved and thus a coarser grid is used.

Common shortcomings of the original DES formulation are the modelled stress depletion and grid-induced separation. Different improvements have been proposed to address the early switching from RANS to LES mode in attached flow regions. The DDES formulation proposed by Spalart et al. (2006), is a modified version of the original DES that aims to delay the switching to LES mode when grid spacing is smaller than the boundary layer thickness. In this case, the switching function depends not solely on the grid spacing but also on eddy-viscosity. The Improved Delayed Detached Eddy Simulation (IDDES) proposed by Shur et al. (2008) also aims to delay the switching to LES mode in attached flows. However, depending on the grid dimensions, it can work on a DDES approach or a wall-modelled LES.

The original DDES length scale by Spalart et al. (2006) is defined as

$$\tilde{d} = d_w - f_d \max(0, d_w - C_{DES}\Delta) \tag{3.21}$$

d_w is the wall distance, f_d is the delaying function defined as $f_d = 1 - tanh[(8r_d)^3]$, designed to be 1 in the LES region and 0 elsewhere. The r_d term is borrowed from the S-A turbulence model by Spalart and Allmaras (1994), which includes the molecular and turbulent viscosity information to delay the switching mechanism in boundary layers. C_{DES} is the DES constant and Δ is a grid-based length scale.

For transitional DDES approaches, the behaviour of the r_d function needs to be reassessed to ensure that the intended behaviour still occurs for different flow regimes viz. attached or separated and laminar or turbulent. In the attached turbulent boundary layers, r_d is equal to 1 in the log layer and approaches infinity in the viscous sub-layer, forcing the solution to remain on the RANS behaviour. At the near-wall region, the r_d reflects a constant-stress behaviour. In separated turbulent flows, the r_d is smaller than 1 due to the wall distance tending to infinity, thus the model switches to LES behaviour as Spalart et al. (2006) present.

In the attached laminar boundary layers, r_d does not resemble a constant stress behaviour, however, it is the inverse of the vorticity Reynolds number. Consequently, r_d can approach very small values within the laminar boundary layer and the switch would behave as an LES approach, which would lead to unintended behaviours. Therefore, the DDES length scale needs to be redefined to include the RANS behaviour for attached laminar boundary layers. Coder and Ortiz-Melendez (2019) propose a change

that includes intermittency (γ) to prevent the already discussed DDES logic in laminar boundary layers. This new scale is defined as

$$\tilde{d_m} = d_w - \min(\gamma, 1) f_d \max(0, d_w - C_{DES}\Delta). \tag{3.22}$$

The factor term $\min(\gamma, 1)$ ensures the recovery of $\tilde{d} = d_w$ for laminar regions ($\gamma = 0$). The minima function ensures γ never exceeds 1 so the DDES length scale is originally recovered for separated and turbulent flows.

For the implementation of the DDES, the implementation for the original AFT can be followed but then change the namespace to LES and the name of the model to AFTDDES. Then, only the length scale is required to be modified as discussed in the paragraphs above. The implemented method with the new definition of the length scale is shown in Figure 3.5.

```
template<class BasicTurbulenceModel>
tmp<volScalarField> AFT19DDESXGamma<BasicTurbulenceModel>::dTilda
(
    const volScalarField& chi,
    const volScalarField& fv1,
    const volTensorField& gradU
) const
{

    volScalarField gLim(min(this->gammaInt_, 1.0));

    return max
    (
        this->y_
      - gLim*fd(mag(gradU))
       *max
        (
            this->y_ - this->CDES_*this->delta(),
            dimensionedScalar("zero", dimLength, 0)
        ),
        dimensionedScalar("small", dimLength, SMALL)
    );
}
```

FIGURE 3.5: Definition of $\tilde{d_m}$ in OpenFOAM C++ code.

The transitional AFT blended with LES is presented in Chapter 6 for flow past a circular cylinder. It is validated for a Reynolds number based on the diameter of the cylinder (Re_D) equal to 3900, since it is probably the most extensively benchmarked case for circular cylinder flow. Following the surface and wake analysis, the transitional DDES model is used for predictions at sub-critical ($Re_D = 1.5 \times 10^5$), critical ($Re_D = 3.5 \times 10^5$), and super-critical ($Re_D = 8.5 \times 10^5$) regimes for flow past circular cylinder. This work aims to demonstrate the superior performance of URANS transitional models and improved predictions against DDES, where turbulent models are used within the RANS region.

3.4 Summary

This chapter has presented the implementation process of the original AFT, including the changes performed to the intermittency equation for Finite Volume Methods. This change in the intermittency equation has any effect on the implementation, as the interpretation of the values for γ are only in the positive range.

With regards to the extension of the AFT model with a Reynolds Stress Model closure, the author's contribution to the modification of production, destruction, and transport terms of the Reynolds Stress Equation have been discussed along the shortcomings introduced by the eddy-Boussinesq hypothesis. Furthermore, the final form of the model is given along with a description of the implementation process.

Ultimately, the discussion and implementation process for the hybridization of the AFT using a DDES approach is presented. Including the analysis of the r_d term behaviour and a small sketch for the understanding in which regions AFT and LES are activated.

Chapter 4

Zero Pressure Gradient Flat Plate

This chapter presents a verification and validation of the AFT and AFT-RSM models described in the previous chapter. Since there is still a lack of verification data to compare with, the results achieved by Coder (2019) for a set of five nested grids using OVERFLOW are compared with the current implementation. Coder (2019) discussed the lack of convergence for this grid family, as transition shifts downstream as the grid is refined and the maximum value of $\tilde{n}$ increases. However, predictions are presented to compare behaviours. Along the Turbulence Modelling Website (TMW) nested grids, predictions are also carried out for the set of five nested grids proposed in the AIAA Transition Workshop. Details are given in Table 4.1.

Experimental data of Schubauer and Klebanoff (1956) for a flat plate is used to validate the transitional methods. This experiment consists of a zero-pressure gradient flat plate with low free-stream turbulence. The initial boundary layer developing over the flat plate is laminar and eventually undergoes a natural transition.

It is well known that different turbulence models exhibit different behaviours to minimum wall-normal resolution. A sensitivity study is presented before the verification and validation with the use of a given grid in Table 4.2. Furthermore, the influence of N_{crit} is studied.

Hence, this chapter aims to verify and determine the sensitivity of transitional AFT and transitional AFT-RSM models for different sets of meshes and to validate the models by comparing them with experimental results by Schubauer and Skramstad (1947).

4.1 Details of numerical simulation

4.1.1 Simulation domain and boundary conditions

The computational domain consists of a rectangle box as shown in Figure 4.1. The minimum height of the domain is given by the AIAA Transition Workshop grid family, $L_y = 0.5$ m, which is considered to be sufficiently large to avoid any influence on the boundary layer. The family of TMW grids have a height of $L_y = 1$ m. The length of the rectangle is $L_x = 2.3$ m, extending from $-0.3 < L_x < 2$ m. The length of the flat plate is $L = 2$ m, where a no-slip boundary condition is applied. There upstream region before the leading of the flat plate has a length of 0.3 m ($L_y = -0.3$ m), and a symmetric is applied. It is used to stabilize the flow before it reaches the leading edge of the "no-slip" surface. A uniform velocity profile at the inlet face is applied with "fixedValue" of 50.1 $\mathrm{m\,s^{-1}}$, and a "fixedValue" equal to zero is set for the outlet face in OpenFOAM. Ultimately, the top surface is set to "symmetryPlane".

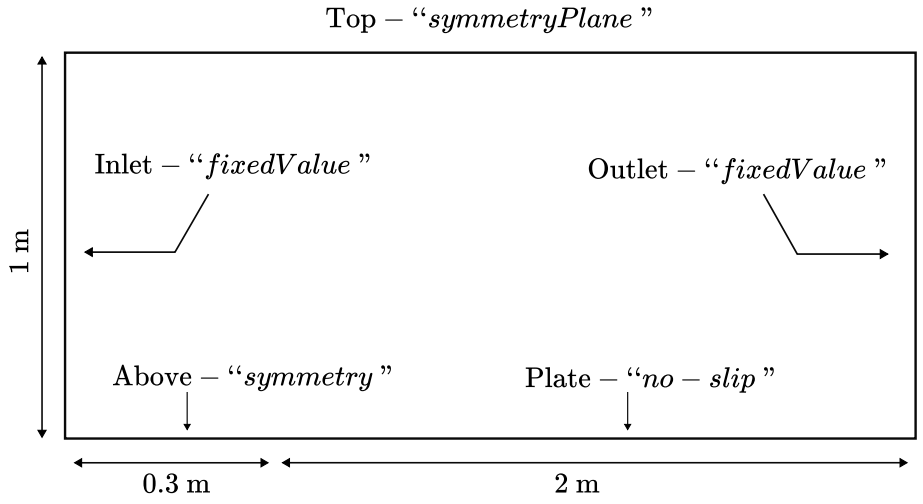

FIGURE 4.1: Domain and Boundary conditions for the zero-pressure-gradient flat plate case. (Figure not to scale)

The experiments performed by Schubauer and Klebanoff (1956) achieved a unit Reynolds number of 3.34×10^6 halfway the plate length ($L = 1$ m). Thus, the non-dimensional parameter defining the flow, in this case, is $Re_L = \frac{U_\infty L}{\nu}$. The free-stream velocity (U_∞) is set to 50.1 $\mathrm{m\,s^{-1}}$, with a kinematic viscosity (ν) of 1.5×10^{-5} $\mathrm{m^2/s}$ and measured free-stream turbulence level of $Tu = 0.03$ %.

4.1.2 Design of the grids

The two grid families used in this section. The TWM grids were created for analysis of fully-turbulent flat-plate flow without pressure gradient. The mesh is clustered near the leading edge of the solid surface and grows until $x = 0.97$ m. This growth is denoted as

TABLE 4.1: Grid characteristics for TMW and AIAA families.

TMW					AIAA				
$N_x \times N_y$	N_x-wall	Max. Er_x	$\Delta_{y_{\min}}$	Max. Er_y	$N_x \times N_y$	N_x-wall	Max. Er_x	$\Delta_{y_{\min}}$	Max. Er_y
545×385	449	1.017	5×10^{-7}	1.03	705×384	513	1.019	1.25×10^{-6}	1.0245
273×193	225	1.035	1×10^{-6}	1.063	353×193	257	1.038	1.25×10^{-7}	1.05
137×97	117	1.07	2×10^{-6}	1.13	177×97	129	1.07	2×10^{-7}	1.1
69×49	57	1.13	4×10^{-6}	1.27	89×49	65	1.16	4×10^{-7}	1.21
35×25	29	1.26	8.3×10^{-6}	1.62	45×25	33	1.35	8.3×10^{-7}	1.46

the maximum expansion ratio in the streamwise direction ER_x in Table 4.1. The first cell height is denoted as $\Delta y_{\min}$ and the maximum expansion ratio in the wall-normal direction is denoted as ER_y. The main issue with this mesh is that the position of the constant expansion ratio falls within the transition position. Therefore, depending on ER_x different solutions are shown. In fact, Coder (2019) showed a lack of convergence for the two coarser grids, while partly converging for the finest grid.

The AIAA Transitional Modelling grids, referred to henceforth as AIAA, are generated for testing transition modelling in ERCOFTAC cases T3A and T3B mainly. However, they have also been used for T3A- experiment, which consists of a natural transition at low Tu. The main problem of this grid family is that the nodes along the solid wall gradually grow. This family of meshes are used to confirm TMW behaviours.

4.1.3 Numerical schemes

The SIMPLEC method was used for all flat-plate simulations. The simulation convergence was assessed using residual values in this case, the solution was considered converged when residuals fall below 1×10^{-6} as shown in Figure 4.2. Transition scalars, $\tilde{n}$ and γ are limited to an 80% change relative to the variable value at the prior step, which is different to 50% suggested by Denison and Pulliam (2018) to keep the stability of the solver. Second-order upwind schemes were used for momentum, transition and turbulent properties, as Coder (2019) employs after stabilizing the simulation with first-order schemes. Second-order upwind discretization, employing upwind interpolation weights, with an explicit correction based on the local cell gradient defined by Warming and Beam (1976). $\tilde{n}$ is bounded within $[-0.5, 20]$ and γ within $[0, 1]$ for stability as suggested by Denison and Pulliam (2018).

4.2 Zero Pressure Gradient Flat Plate Verification and Validation

4.2.1 Sensitivity to wall-normal grid distribution

This section investigates the impact of the y^+ at the wall on the transition onset and the fully-turbulent recovery for seven different y^+ distributions with the AFT and the

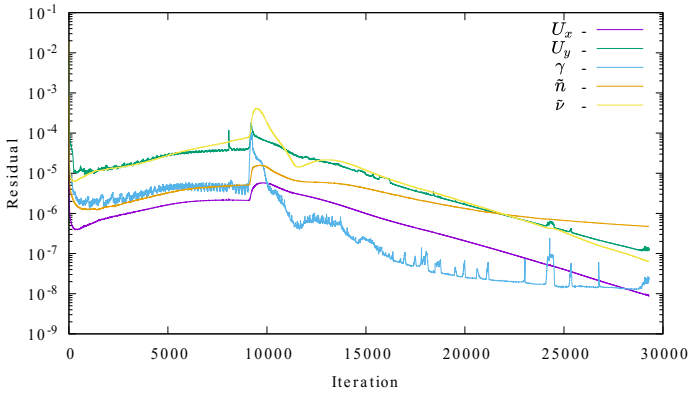

FIGURE 4.2: Residuals behaviour of AFT for SIMPLEC method using finest grid from AIAA family grid.

extended RSM models. Table 4.2 gathers the characteristics for the seven different y^+ conditions, along with the stretching factor and the y^+ average over the full flat plate. In addition, Figure 4.3 shows the y^+ distribution over the flat plate for all grids given in Table 4.2. To isolate the y^+ effect the streamwise resolution was kept unchanged. The plate is covered with 300 points which are distributed in a constant resolution in the streamwise direction of 6.6×10^{-3} m.

TABLE 4.2: Grid characteristics for different y^+ distributions.

Case	$N_x \times N_y$	$\Delta_{y_{\min}}$ [m]	ER_y	y^+
1	300×97	0.5×10^{-6}	1.13952	0.03
2	300×97	1×10^{-6}	1.13054	0.07
3	300×97	2×10^{-6}	1.12157	0.13
4	300×97	4×10^{-6}	1.11262	0.26
5	300×97	8×10^{-6}	1.10366	0.50
6	300×97	16×10^{-6}	1.09470	1.60
7	300×97	32×10^{-6}	1.08570	2.10

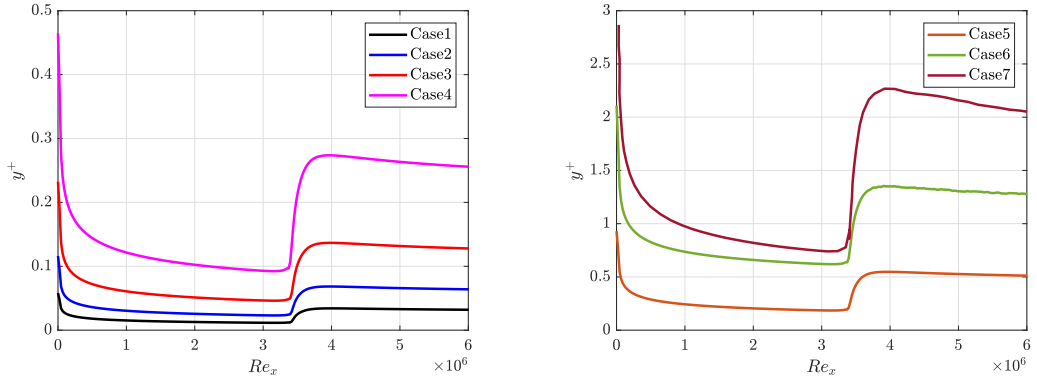

(a) y^+ distribution for Cases 1 to 4 in terms of Re_x. (b) y^+ distribution for Cases 5 to 7 in terms of Re_x.

FIGURE 4.3: The y^+ distribution for a zero-pressure-gradient flat plate cases given in Table 4.2.

For the AFT model, Figure 4.4 shows that agreement is achieved for cases 1 to 5, in terms of laminar behaviour, transitional region and within the fully-turbulent recovery. These cases retain a y^+ lower than unity while, as can be seen from Table 4.2, cases 6 and 7 are the only scenarios that have an average y^+ above unity. Cases 6 and 7 as shown in Figure 4.4(a), produce an earlier transition onset from the rest of the cases but retain a good agreement with the rest over the laminar region. Specifically, the coarsest y^+ configuration triggers earlier transition onset than case 6. During the transition, the peak of skin friction is over-predicted by cases 6 and 7, as well as throughout the fully-turbulent recovery where both cases show no convergence with the rest of the cases 1-5 and overpredicting the C_f. Hence, when using the AFT model, the first point of the wall shall have y^+ below unity in light of the presented results.

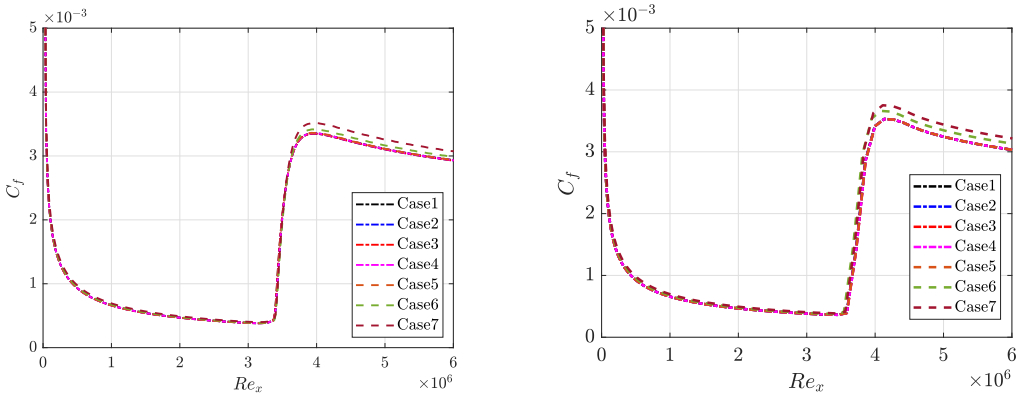

(a) AFT model

(b) AFT-RSM model

FIGURE 4.4: The y^+ impact on C_f for the transitional AFT and AFT-RSM models.

The effect of the y^+ distributions in the near-wall for cases presented in Table 4.2 is shown in Figure 4.4(b) for the transitional AFT-RSM. As can be seen, cases 1 to 5 show a convergence in the complete prediction. The agreement is good within the laminar region, transition and turbulent region when y^+ in the wall region falls within unity.

Case 6, which has the 2$^{\text{nd}}$ coarsest y^+ distribution, maintains the C_f prediction of the laminar boundary layer with good agreement with the rest of the solutions. At the transition onset, the solution does not perfectly match the same position as the rest of the finest cases. This behaviour is also found for the coarsest y^+ distribution. For the fully-turbulent region, the two coarsest distributions (cases 6 and 7) show an overprediction of the C_f peak at the very beginning of this region. As the fully-turbulent boundary layer develops over the flat plate, case 6 shows a reduced overprediction for the C_f compared to case 7. On the other hand, when compared to the rest of the cases, cases 6 and 7 overpredict the C_f predicted by grids 1 to 5.

4.2.2 N_{crit} effect

As already discussed, the N_{crit} is estimated using the Mack (1977) relationship and it is dependent on Tu. Hence, as this scalar is imposed by the user, it is necessary to validate its behaviour. N_{crit} is inversely proportional to Tu. Thus, the lower turbulent the environment is, the larger N_{crit} is and a later laminar to turbulent transition is predicted. Figure 4.5-4.6 shows the impact of different N_{crit} factors on the base model AFT and the AFT-RSM respectively. Furthermore, both Figures shows how the maximum value of transport $\tilde{n}$ is increased as the transition condition with regard to Tu is modified. The agreement between the AFT and AFT-RSM is good, however, AFT-RSM has shown to be sensitive to ν_t/ν and ω since it controls the decaying rate of Tu.

As mentioned, the predictions achieved using AFT and AFT-RSM are similar as Figures 4.5-4.6 show. When using the $N_{\text{crit}} = 5$ the differences between both models are negligible. It can be seen in $1 \times 10^6 < Re_x < 2 \times 10^6$ that $\tilde{n}$ behaves similarly in both models and the growth of the amplification factor term is almost the same for $Re_x > 2 \times 10^6$. For $N_{\text{crit}} = 9$ the results show similar contour behaviour with the AFT-RSM showing a larger region with larger values of $\tilde{n}$. This is in agreement with the slight delayed transition location discussed when comparing AFT and AFT-RSM with different y^+ values in Figure 4.4.

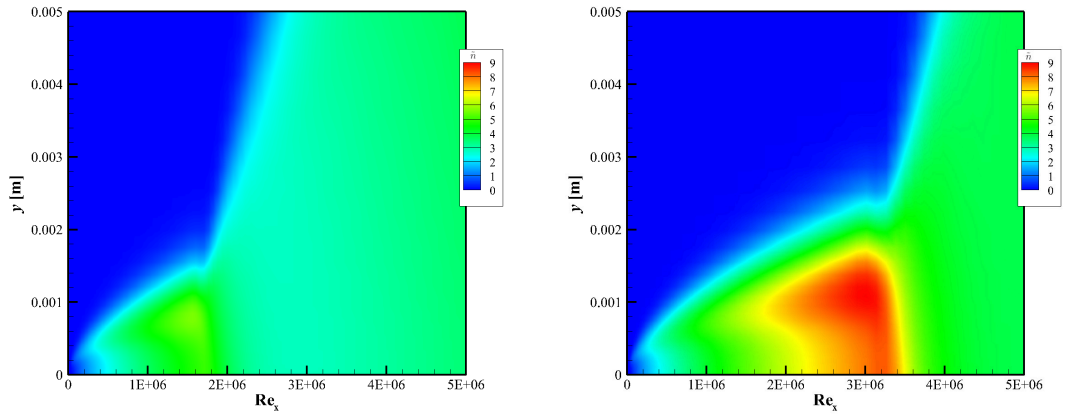

(a) $\tilde{n}$ for $N_{\text{crit}} = 5.0$

(b) $\tilde{n}$ for $N_{\text{crit}} = 9.0$

FIGURE 4.5: Maximum value of $\tilde{n}$ varying N_{crit} at 5 and 9 for AFT transition model using TMW 137×97 Grid.

4.2.3 Verification of the AFT and AFT-RSM models

This section aims to demonstrate the correct implementation of both the AFT and AFT-RSM models within OpenFOAM using a set of nested grids from two families.

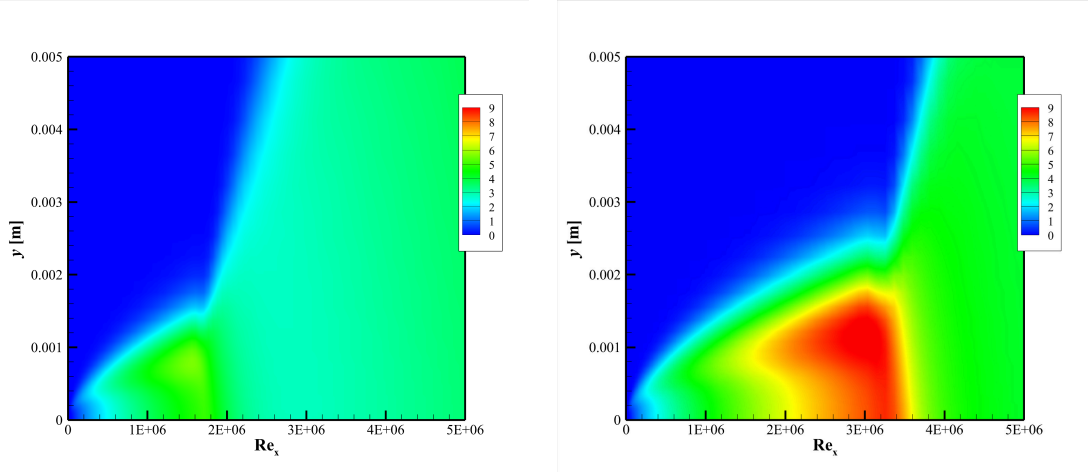

(a) $\tilde{n}$ for $N_{\text{crit}} = 5.0$ (b) $\tilde{n}$ for $N_{\text{crit}} = 9.0$

FIGURE 4.6: Maximum value of $\tilde{n}$ varying N_{crit} at 5 and 9 for AFT-RSM transition model using TMW 137×97 Grid.

Figure 4.7(b) shows the behaviour for the set of TMW grids with $N_{crit} = 10.3$. This value is chosen according to analyses by van Ingen (1956), that reports the boundary layer has fully transitioned from laminar to turbulent flow at a specific N_{crit}. The two coarsest grids by TMW show a lack of transition prediction due to an insufficient number of points in the streamwise direction. As the grid is refined from 137×97 to 545×385, the transition point is shifted downstream as a difference to the behaviour observed in Coder (2019), where he notices a lack of convergence due to the coupling of γ and $\tilde{\nu}$. In this case, the original equation from Menter et al. (2015) is utilised, and any convergence problem is observed during simulations. Furthermore, as the grid is refined, predictions of C_f in both regions, laminar and turbulent, show a trend of convergence, as the two finest grid overlap in Figures 4.7-4.8.

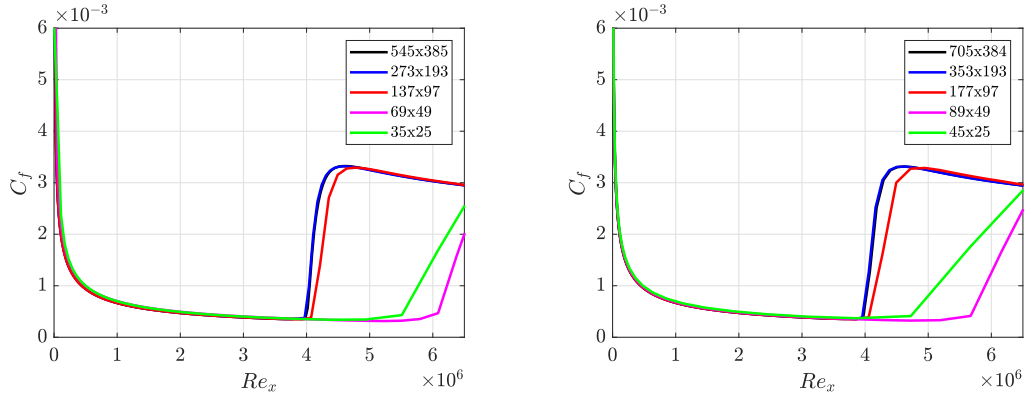

(a) TMW Grid (b) AIAA Grid

FIGURE 4.7: Validation of transition prediction using AFT for TMW and AIAA Grid families with $N_{crit} = 10.3$.

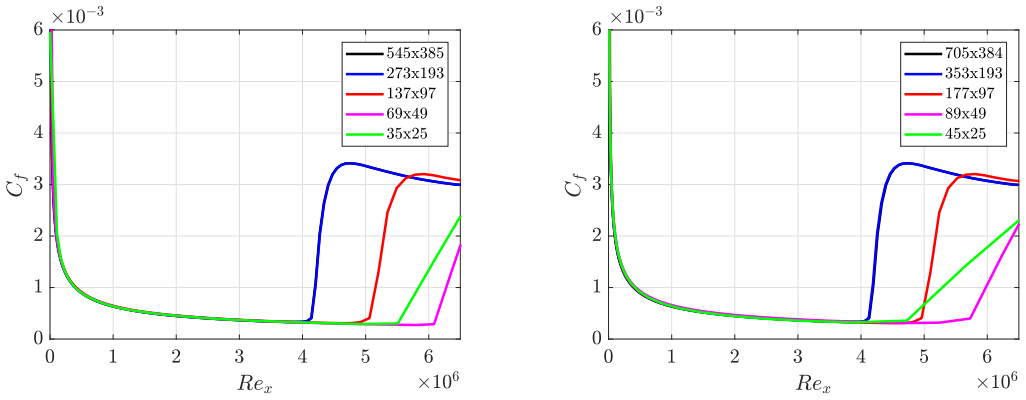

(a) TMW Grid (b) AIAA Grid

FIGURE 4.8: Validation of transition prediction using AFT-RSM for TMW and AIAA Grid families with $N_{crit} = 10.3$.

This convergence is also shown when using the AIAA Grid family. The two coarsest meshes present a similar behaviour with a lack of transition convergence. Grids varying from 177×97 to 705×385 grids indicate good convergence as the transition is shifted downstream. With the refinement, the transition point and C_f values during the laminar and turbulent stages go towards the same results as shown in Figure 4.7(b).

The behaviour for AFT-RSM is shown in Figure 4.8 for TMW and AIAA Grid families. The observed behaviour validates its implementation into OpenFOAM as both AFT and AFT-RSM provide similar results regarding transition. AFT-RSM shows a consistent difference in the transition prediction to AFT of approximately $Re = 1 \times 10^5$. The AIAA Grid family predicts similar results for the three finest meshes. Two coarsest meshes for TMW and AIAA still show a lack of convergence as before. Grid 137×97 TMW also shows a lack of convergence when using AFT-RSM, and the same behaviour is observed for AIAA with the increased number of points (40) in streamwise direction in 177×97 AIAA Grid. The two finest grids 545×385 and 705×384 (black and blue line almost completely overlapped), for TMW and AIAA respectively, show similar transition predictions, laminar and turbulent C_f values with the increased refinement.

Figure 4.9 and 4.10 show the distribution of $\tilde{n}$ and H_{12} for AFT and AFT-RSM using 545×385 TMW Grid. Distributions are shown to be fairly similar and show a good resemblance to what can be observed in Coder (2019). Note Coder (2019) presents results with Grid 137×97 and here Grid 545×385 is used. For $\tilde{n}$, there is a growth until its maximum value, in this case, $\tilde{n} = 10.3$, which agrees with the maximum N_{crit}. Beyond the packet of maximum $\tilde{n}$, it gradually decays as expected from linear stability theory. Furthermore, outside the boundary layer, the values of amplification are null as expected. The vertical self-similarity of H_{12} can be noticed upstream transition as a consequence of the use of H_L. Approximately at the transition point, it can be seen how the integral shape factor undergoes a streamwise oscillation until the turbulent flow

is settled down. This effect is due to the transport of momentum near the wall as the turbulent boundary layer is formed. This effect leads to negative H_L values forcing H_{12} to reach such small figures. This is in agreement with the behaviour observed by Coder (2019).

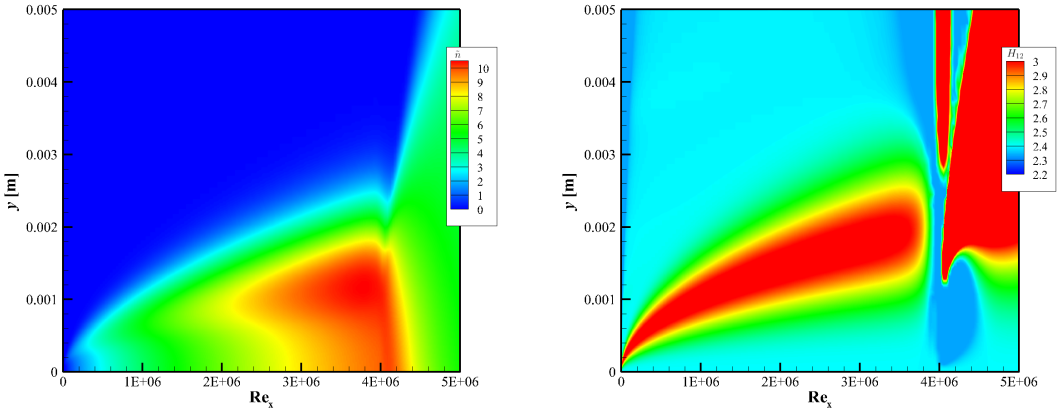

(a) $\tilde{n}$ (b) H_{12}

FIGURE 4.9: Distribution of $\tilde{n}$ and H_{12} for AFT transition model using TMW 545×385 Grid.

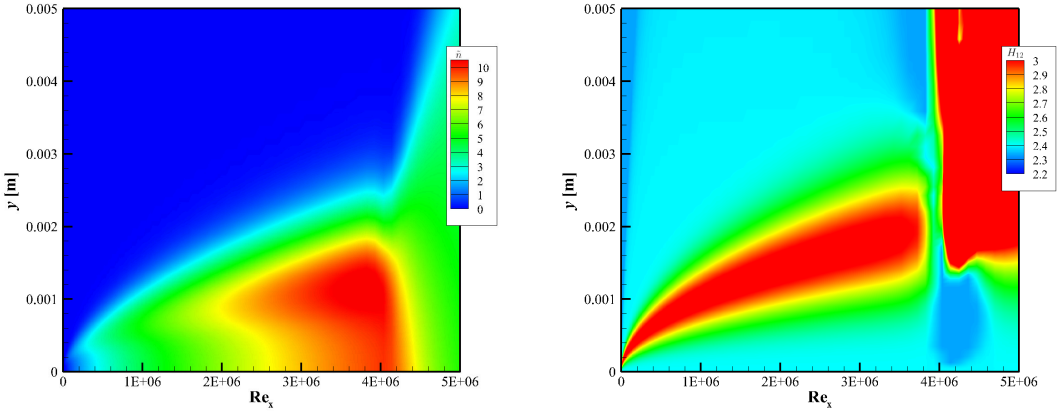

(a) $\tilde{n}$ (b) H_{12}

FIGURE 4.10: Distribution of $\tilde{n}$ and H_{12} for AFT-RSM transition model using TMW 545×385 Grid.

Ultimately, velocity profiles within the laminar and turbulent regions are shown in Figure 4.11 to verify the AFT and AFT-RSM behaviour. Two Reynolds number are chosen for this verification, $Re = 1 \times 10^6$ and 4.5×10^6, falling within the laminar and turbulent region respectively. As shown both models do predict laminar and turbulent profiles where it is expected. The characteristic shape-factor difference between both can be readily seen in Figure 4.11(a) for the AFT and Figure 4.11(b) for AFT-RSM. Note the small kink in the turbulent profile predicted by AFT-RSM. This is because

$Re = 4.5 \times 10^6$ falls at the end of the transition zone, where the profile is not yet a fully-developed turbulent profile, as confirmed in Figure 4.13(b).

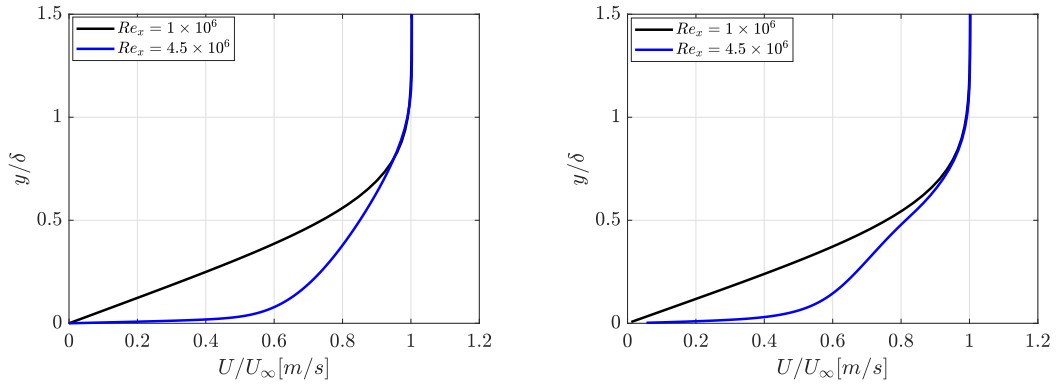

(a) AFT 137x97 Grid

(b) AFT-RSM 137x97 Grid

FIGURE 4.11: Velocity profiles at laminar and turbulent regions of the flow with AFT and AFT-RSM transition models using TMW 545×385 Grid.

4.2.4 Validation for AFT and AFT-RSM

In this section, the AFT and AFT-RSM predictions are compared to experimental data by Schubauer and Skramstad (1947) and other CFD results with a variety of models. Furthermore, theoretical behaviours for laminar and turbulent C_f and u^+ are used to establish the capability of the model to reproduce physics. Transitional AFT and AFT-RSM results are always using $N_{crit} = 10.3$ unless the contrary is stated in the legends.

Figure 4.12(a) compares the AFT and AFT-RSM against the experimental data from Schubauer and Skramstad (1947) and theoretical C_f predictions for laminar and turbulent boundary layers. When using $N_{crit} = 10.3$, transition onset is expected to occur at the end of the transition, as this was measured by Van Ingen (2008). As can be seen, the AFT and AFT-RSM agree with that and predict the transition approximately at the end of the experimental transition region by Schubauer and Skramstad (1947). As shown in the verification, there is a consistent difference regarding the transition prediction between AFT and AFT-RSM. In addition, at the end of the transition prediction, the AFT-RSM shows a slightly larger C_f peak than AFT. The agreement with the theoretical C_f predictions is good. The laminar region agrees perfectly with Blasius theoretical $C_f = 0.664/\sqrt{Re_x}$. Turbulent theoretical prediction by Prandtl $C_f = 0.027/Re_x^{1/7}$ shows an agreement when the turbulent flow has developed for a certain distance.

Predictions for AFT and AFT-RSM are presented along with other transitional methods in Figure 4.12(b). Compared to Coder (2019) current predictions fall closer to the end of the transition region measured by Schubauer and Skramstad (1947). On the other hand, phenomenological models produce a fair prediction but there is no physics involved since

it is all experimental-based. Furthermore, even though they introduce a term to control the transition length, results do show a similar prediction to AFT models without any controlling term. In fact, using $N_{crit} = 8.22$ and 9, which are the values measured by Van Ingen (2008) that indicate the onset of transition and the average value for typical aeronautical applications, matches the behaviour of $\gamma - Re_\theta$ and γ model respectively. These behaviours show the potential of AFT models (physics-based), on predicting transition using $\tilde{n}$ to represent the disturbance amplification within the laminar boundary layer without any transition correlation as a difference to $\gamma - Re_\theta$ and γ models. The former two models require experimental evidence to construct the correlations for transition prediction i.e the critical Reynolds number, the transition Reynolds number, the momentum thickness of the boundary layer as a boundary condition and the length parameter of the boundary layer. In addition, the AFT is a transition model to exploit since it takes into account the boundary-layer history as a difference to phenomenological models where the need for experiments for each scenario would be required.

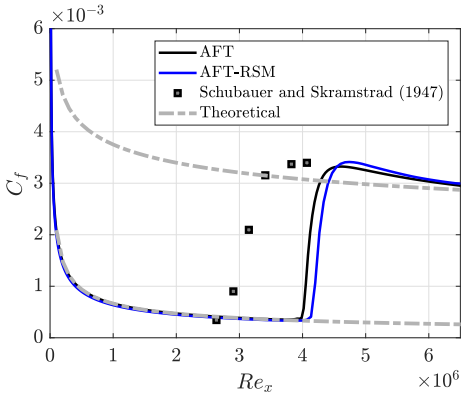

(a) AFT and AFT-RSM model using $N_{crit} = 10.3$

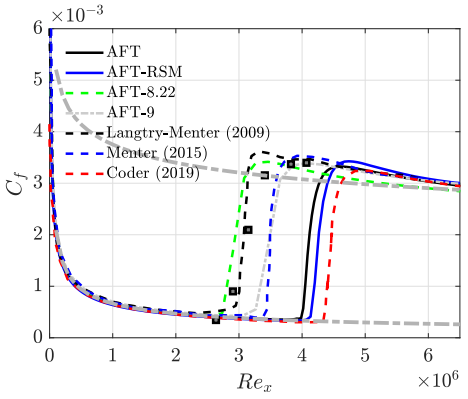

(b) AFT using $N_{crit} = 8.22$, 9, 10.3, identified as AFT-8.22, AFT-9 and AFT respectively, and AFT-RSM using $N_{crit} = 10.3$

FIGURE 4.12: C_f distribution for AFT and AFT-RSM transition model using TMW 545 × 385 Grid with experimental data and γ, $\gamma - Re_\theta$ models, theoretical C_f and experimental data by Schubauer and Skramstad (1947).

To close the validation section, velocity profiles in terms of y/δ and U/U_∞ and dimensionless wall distance y^+ vs dimensionless velocity u^+ are shown in Figure 4.13. This is a continuation of the verification process presented in the prior section. However, this time the velocity profiles are compared to theoretical laminar and turbulent dimensionless profiles. Blasius theoretical profile in Figure 4.13(a) is in agreement with the velocity at $x = 0.3$ m predicted by the transitional AFT. Turbulent profile in Figure 4.13(b) shows the development within the inner region following perfectly the $u^+ = y^+$. Log-law region is also in good agreement with the predictions of both transitional models and lastly reaches the outer region, which also resembles the typical defect layer or wake-law.

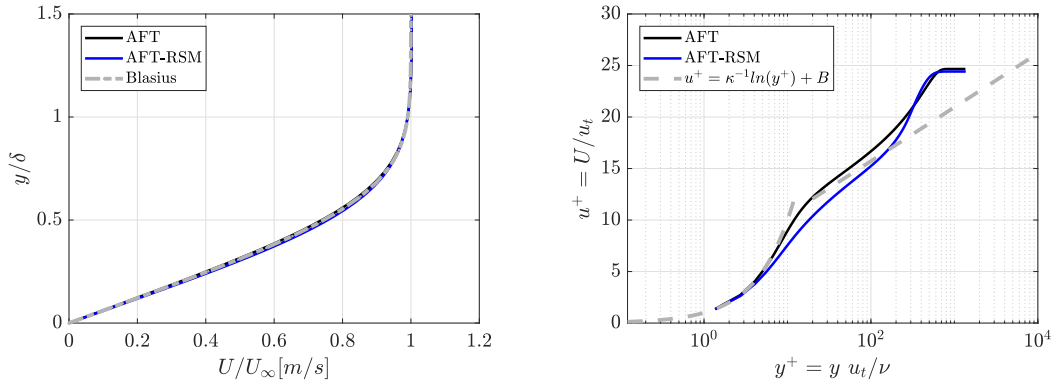

(a) Laminar profiles

(b) Turbulent profiles

FIGURE 4.13: Dimensionless velocity profiles for AFT and AFT-RSM transition model using TMW 545×385 Grid compared to Blasius and Law of the wall theoretical predictions.

4.3 Summary

This chapter have presented the verification and validation for the implementation of the transitional AFT and AFT-RSM models into the OpenFOAM CFD package.

Verification consisted of an initial analysis of the N_{crit} impact on the transition position and the sensitivity of the model to the wall grid resolution. The critical amplification limits the growth of the instabilities within the boundary layer, thus the smaller its value is, the earlier the transition onset occurs. On the other hand, if the N_{crit} value is increased, a delay in the transition should occur. This behaviour is confirmed for both AFT and AFT-RSM models. In the verification process, two families of nested grids were tested, from the Turbulence Modelling Website and AIAA Transitional Workshop. It has been shown that with the continuous refinement of both families of grids, transition onset point, laminar skin friction prediction and turbulent skin friction tend to the same position. Contours plots regarding $\tilde{n}$ and H_{12} discussing the similarities with the implementation reported by Coder (2019). Furthermore, a verification of the boundary layer nature is also presented using two different boundary layer velocity profiles at two different positions, where the laminar and turbulent behaviour of the boundary layer were confirmed.

The validation process consisted of a comparison to experimental data regarding the natural transition for zero pressure gradient flat plate reported by Schubauer and Skramstad (1947). Additionally, it is validated against the implementation carried out by Coder (2019) and compared to other transitional methods. According to experimental measurements, Van Ingen (2008) concluded that under the current conditions the end of transition occurs at approximately $N_{crit} = 10.3$, while the onset of transition is approximately estimated with a $N_{crit} = 8.22$. Coder (2019) suggested using the value at the end of the transition since the model does not have any function controlling the length of it.

The results presented, demonstrate that the current implementation can be considered validated for the three following reasons:

- Transition onset when using $N_{crit} = 8.22$ agrees with the onset of transition predicted by measurements.
- The transition positions physically agree with the end the transition region of the measurements by Schubauer and Skramstad (1947) when using $N_{crit} = 10.3$ suggested by Van Ingen (2008).
- The standard value used for aeronautical applications under low turbulence levels $N_{crit} = 9$, also demonstrates the transition prediction to be approximately within the middle of the experimental measurements. This is consistent with the description of the physics of the model.

These three results guarantee a correct physical description of the transition position, which is validated with experimental data by Schubauer and Skramstad (1947). Therefore, for the following results, the well-established averaged value for transition prediction of $N_{crit} = 9$ is used. In addition, it is convenient to maintain a wall grid resolution of $y^+ \leq 1$, so the transition onset, laminar and turbulent skin friction prediction are not degenerated. The expansion ratio in both directions should be $ER \leq 1.05$ and the number of points over the streamwise direction are going to be evaluated with sensitivity analysis for each flow field configuration.

Chapter 5

Backward Facing Step

In this section numerical solutions of two-dimensional laminar, transitional, and turbulent flow over a backward-facing step (BFS) at high Reynolds numbers are presented for AFT, AFT-RSM and S-A.

As already discussed, a major interest of this thesis is to study the performance of the AFT transitional model and its variants for a specific type of bluff body such as the flow past a circular cylinder at high Reynolds numbers, while most prior studies up to date have been performed on streamlined bodies such as airfoil-like geometries.

Separation, transition, and reattachment of the boundary layers, along with large recirculating regions are encountered in the flow over a circular cylinder throughout the different regimes depending on the Reynolds number. In this case, a backward-facing step can be regarded as having the simplest geometry while retaining rich flow physics manifested by flow separation, flow transition, flow reattachment and diverse recirculating bubbles depending on the Reynolds number and the geometrical characteristics of the step and channel. In a backward-facing step, the flow is not subjected to any curvature change and variable pressure gradient. Another of the simplifications to circular cylinder flow is the fixed separation point at the step location. Thus, it permits to analyze the AFT performance and its variants for separated transition and reattachment of laminar and turbulent boundary layers against fully-turbulent approaches and demonstrate their better performance throughout laminar and transitional regimes.

5.1 Details of numerical simulation

5.1.1 Simulation domain and boundary conditions

The geometry of the flow problem was chosen in accordance to the experimental setup of Armaly et al. (1983) sketched in Figure 5.1. The expansion ratio is defined by Armaly

et al. (1983) as $H/h = 1 + S/h$, by the ratio of the channel height H downstream of the step to the channel height h of the inflow channel, where S denote the height of the step. In this case, the expansion ratio H/h is the same as Armaly et al. (1983), $H/h = 1.9423$.

Upstream and downstream of the step, the computational domain has an extension of 0.8 m, respectively. The inlet section is at $x = -0.1$ m, and the end of the domain at $x = 0.7$ m, with the step located at $x = 0.2$ m from the origin denoted by O in Figure 5.1. The origin is located at 0.1 m from the inlet surface. The length of the settling region is denoted by $L_s = 0.2$ m/s. According to the literature, a well-established agreement is that a distance of five times the channel height h upstream of the step is sufficient to avoid the backward influence of the inlet for the predicted results past the step as shown by Biswas et al. (2004).

The upper and lower channel walls, including the step, are treated as solid walls, and the no-slip condition is applied. At the outlet of the computation domain ($x_e = 0.7$ m), a zero gradient condition is applied. At the inlet of the computational domain ($x_i = -0.1$ m) a fixed velocity condition is applied with appropriate turbulent values according to the Re number with $Tu = 0.05\%$.

The non-dimensional parameter describing the different regimes of the backward-facing step flow is the Reynolds number based on the bulk velocity (U_b) and hydraulic diameter of the channel ($D_h = 2h$), which is equivalent to twice its height. Thus, Re_{D_h} is defined as

$$Re = Re_{D_h} = \frac{U_b 2h}{\nu}. \tag{5.1}$$

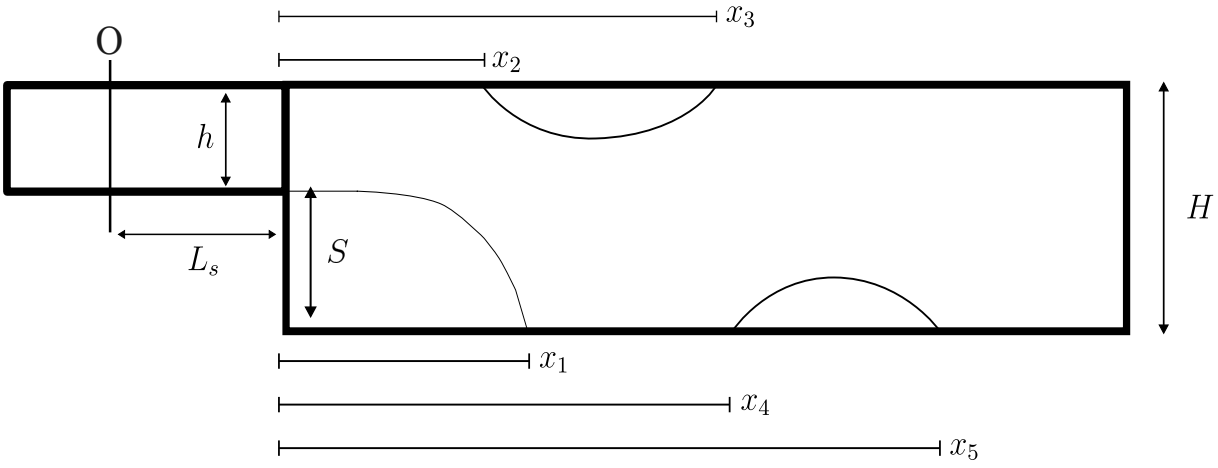

FIGURE 5.1: Schematic domain for backward-facing step and recirculating regions. (Figure not to scale)

5.1.2 Numerical properties

The SIMPLEC algorithm is used to provide an averaged solution as an initial condition to speed up the necessary time required by the time-dependent solver to avoid the transient solution until the flow field is established within the geometry. PIMPLE is used to solve the unsteady flow field, which combines PISO and SIMPLE. The PIMPLE algorithm, in this case, is set to 2 inner loops, where the Poisson and continuity equations are solved, while the maximum of iterations in the outer loop is set to 15, which is reduced according to the residual control with values of 5×10^{-3} and 1×10^{-4} for pressure and velocity respectively. Second-order upwind schemes are used for momentum, transitional and turbulent variables after stabilizing the simulation for one flow-through time with first-order schemes. Similar to the flat plate, transition scalars are limited to 80% change relative to the variable value at the prior step. The solution is advanced 9 flow-through times with second-order schemes before sampling for 10 flow-through times until a constant velocity behaviour at the centre of the domain is observed, assuming a converged solution.

A second-order implicit scheme is used for time integration, although the appropriate time step should be determined to resolve the physics of the flow and maintain the computational efficiency. Predictions for the recirculating length (x_1) with different Courant-Friedrichs-Lewy CFL = $\Delta t U_\infty / \Delta x$ are given in Table 5.1 at $Re = 1200$. As can be seen, differences go down to the third decimal place from the smallest to the third-largest CFL number. The largest CFL = 2, produces an overprediction of the primary recirculating region x_1. This behaviour is shown to be consistent for all the models presented in Table 5.1. Overall, the two transitional models compare well with experimental results by Armaly et al. (1983), which report a $x_1/S \approx 14.35$. Furthermore, the S-A predictions evinced a shortened x_1, which is shortened due to the turbulence production and resembling a fully-turbulent behaviour as discussed in the following paragraphs. Hence, a CFL = 0.9 is used as it shows negligible differences to other x_1 predictions when CFL < 1.

TABLE 5.1: Primary dimensionless reattachment length (x_1/S) predictions for backward-facing step for different CFL using AFT, AFT-RSM and S-A at $Re = 1200$.

CFL	AFT	AFT-RSM	S-A	Armaly et al. (1983) Exp.
0.4	14.222	14.291	6.141	17.63
0.6	14.224	14.293	6.142	
0.9	14.225	14.293	6.143	
2	14.571	14.591	6.303	

5.1.3 Design of the grids

The backward-facing step flow is solved using URANS methods. Four different grid resolutions were tested initially to carry out a sensitivity analysis at $Re = 7000$. The

grids are numbered from the finest to coarsest as 1 to 4, respectively.

The grids vary in the minimum wall spacing as well as the grid spacing in the streamwise and wall-normal direction, given in Table 5.2. The domain before the step is divided by 40 nodes from the coarsest to 80 points for the finest case, clustered at the extremes. Downstream of the step, the region is discretized with 75 points to 400 points, from the coarsest to finest grid respectively. The stretching ratio past the step varies from 1.10 to 1.02 for the finest grid. At the outflow, the grid spacing is about 7 times the step height for the coarsest and approximately 1 time the step height for the finest grid.

In the wall-normal direction, grids are discretized with 30 to 60 points before the step and 60 to 120 points past the step, from coarsest to finest respectively in both cases. These grids distributions result in a minimum wall spacing of $\Delta y_{\min} = 1 \times 10^{-4}$ m for the coarsest mesh and $\Delta y_{\min} = 1 \times 10^{-5}$ m for the finest configuration.

TABLE 5.2: Grid characteristics of four different distributions for backward-facing step.

Grid	Nx_p [1]	Nx_a [2]	Ny_p	Ny_a	ER_x	ER_y	$\Delta y_{\min}$ [m]
1	40	75	30	60	1.10	1.10	1×10^{-4}
2	50	100	40	80	1.07	1.07	8×10^{-5}
3	80	200	50	100	1.04	1.05	2×10^{-5}
4	80	400	60	120	1.02	1.02	1×10^{-5}

[1]Subscript "p" refers prior the step location.
[2]Subscript "a" refers after the step location.

Table 5.3 shows the results for the four presented grid discretizations at $Re = 7000$. It gives the primary recirculating dimensionless length (x_1/S) estimation for the three different models, as is common in the literature.

Transitional AFT and AFT-RSM for $Re = 7000$ show an underestimation of the primary reattachment dimensionless length x_1 for the coarsest mesh. This is a consequence of the $y^+ > 1$ at the inlet and outlet channel, combined with an insufficient number of grids in the streamwise direction past the step. The underprediction is also shown by S-A, however, it falls closer to converged results when using grid 3 or finer. For the rest of the grids, excluding the coarsest, there is a good agreement between the two finest grids. Hence, according to prior results, grid 3 is utilised as the baseline grid for the simulations performed over the backward-facing step at different Reynolds numbers in this section.

TABLE 5.3: Predictions of x_1/S using AFT, AFT-RSM and S-A for grid sensitivity study for the backward-facing step.

Grid	AFT	AFT-RSM	S-A	Armaly et al. (1983) Exp.
1	4.489	5.918	7.142	7.91
2	5.714	6.122	7.550	
3	6.122	6.530	8.160	
4	6.122	6.530	8.160	

5.2 Results and Discussion

In this section, the results for the AFT transitional model, its RSM extension and S-A are presented and discussed for Armaly et al. (1983) test case. The description and discussion of the results are divided into three according to the flow regimes discussed and classified by Armaly et al. (1983): laminar region ($Re < 1200$), transitional ($1200 < Re < 6600$) and turbulent ($Re > 6600$) regimes, as discussed in Literature Review following Armaly et al. (1983) measured data. Furthermore, the different recirculating regions and bubbles used for the analysis are identified in Figure 5.1.

5.2.1 Laminar Region - $Re < 1200$

The laminar region extends up to $Re < 1200$ and it is characterized by the increase of the reattachment length (x_1) of the main recirculating region with Reynolds number as shown in the experimental data by Armaly et al. (1983) in Figure 5.2. Together with the experimental data by Armaly et al. (1983) and 2D laminar predictions by Erturk (2008), numerical results for the transitional AFT and AFT-RSM are presented for different Reynolds numbers. As shown in Figure 5.2, the AFT and AFT-RSM models demonstrate good agreement for the recirculation length x_1 over the laminar region up to approximately $Re = 400$. The transitional AFT and AFT-RSM models show similar results within the laminar region, however the former always predicts a slightly larger reattachment length.

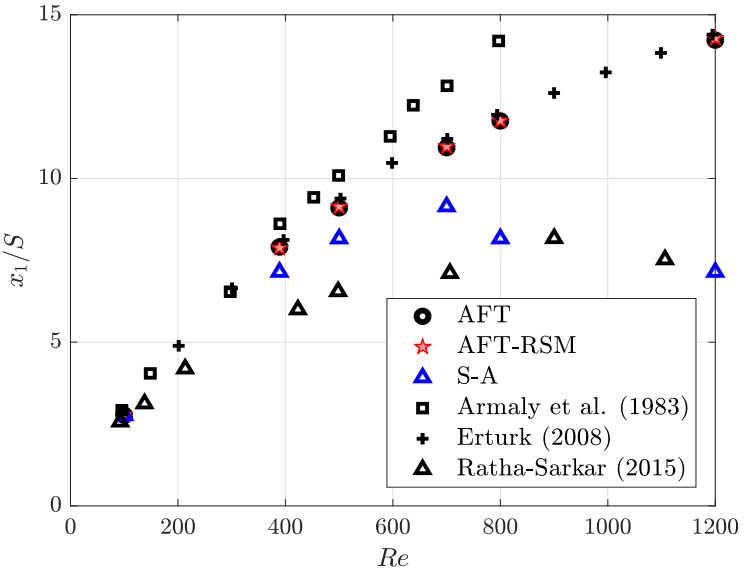

FIGURE 5.2: Predictions of x_1/S throughout the laminar region using AFT, AFT-RSM and S-A, including experimental data by Armaly et al. (1983), laminar DNS simulations by Erturk (2008) and $k-\epsilon$ simulations by Ratha and Sarkar (2015).

Figure 5.3 and Figure 5.4 show the developing profiles at $Re = 100$ and 389 for the AFT, AFT-RSM and S-A models. The agreement is good for the three models at $Re = 100$. The maximum inlet velocity achieved at the step agrees well with experimental data although a small defect of velocity (U) of approximately 2% is observed in the prediction for the three models. The development of the profiles is similar throughout the separation and reattachment. At $x/S = 2.55$, the three computations show an almost attached velocity profile as a difference from the experimental data by Armaly et al. (1983), confirming the reduced x_1/S dimensions. Ultimately, the three profiles are in agreement with the experimental velocity profile at location $x/S = 12.04$. The agreement with experimental profiles at $Re = 389$ is good. Both AFT and AFT-RSM show superior predictions while a shortened recirculating region is predicted by S-A. Differences using S-A become prominent beyond $x/S = 3.57$. Furthermore, the quasi-developed and fully-developed profile within the expansion region of the domain shows a velocity defect when compared to pure laminar profiles predicted by AFT and AFT-RSM as can be observed at locations $x/S = 11.84$ and 13.57. The primary cause of these differences is the production of turbulence due to the strain rate (S) in the mean velocity profile when it separates, which is the main source of turbulence production. Conversely, for the transitional models, the production is suppressed as $\gamma = 0$.

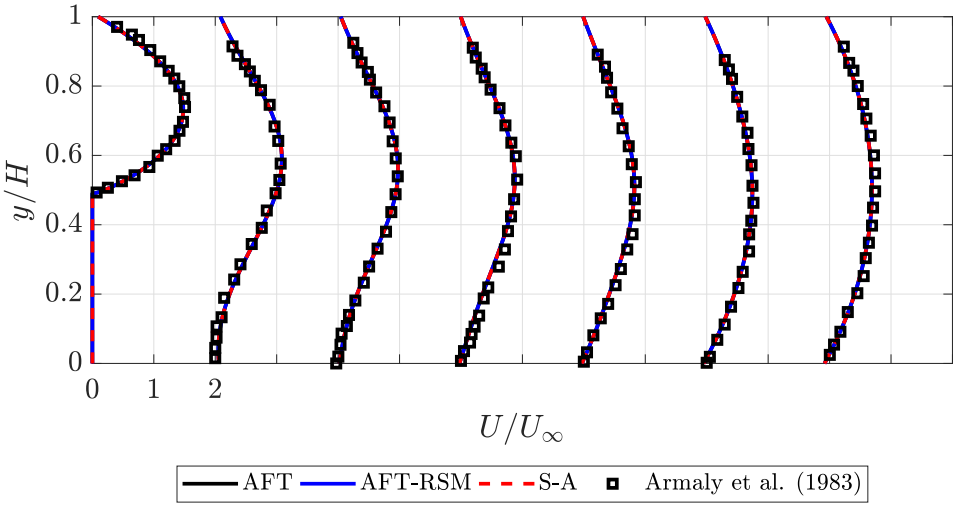

FIGURE 5.3: Normalized velocity profile predictions at $Re = 100$ for AFT, AFT-RSM and S-A, including experimental data by Armaly et al. (1983) at positions $x/S = 0,\ 2.55,\ 3.06,\ 3.57,\ 4.18,\ 6.12,\ 12.04$.

The S-A fully turbulent approach produces sensible results with a fair agreement to experimental data from Armaly et al. (1983) and computations by Erturk (2008). Nonetheless, as the secondary recirculating bubble is formed ($Re > 400$), the flow becomes three-dimensional and forcing the x_1/S to depart from the growth predicted from laminar results obtained by Erturk (2008). The S-A model under-predicts the length of the reattachment for $Re > 400$. This under-prediction scales with Reynolds number in the

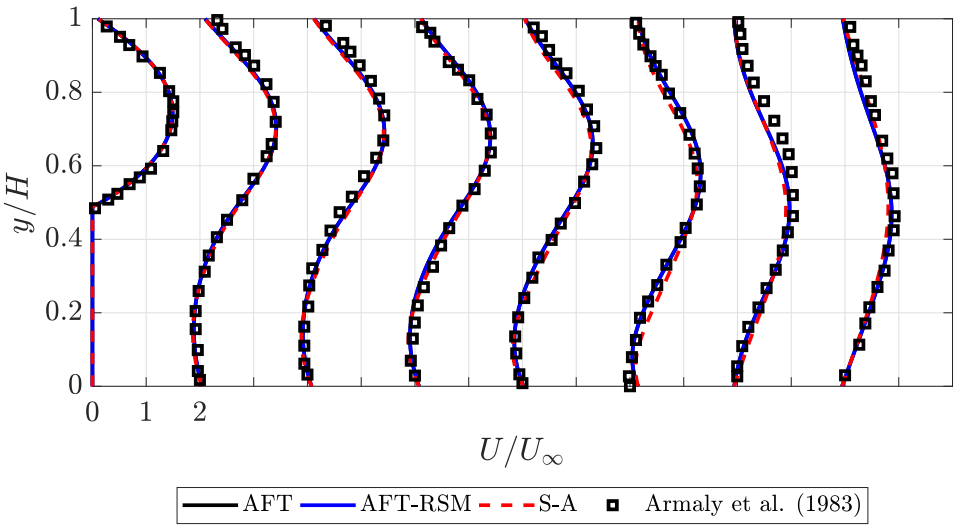

FIGURE 5.4: Normalized velocity profile predictions at $Re = 300$ for AFT, AFT-RSM and S-A, including experimental data by Armaly et al. (1983) at positions $x/S = 0,\ 2.55,\ 3.06,\ 3.57,\ 4.18,\ 6.12,\ 8.52,\ 11.84,\ 13.57$.

laminar region as Figure 5.2 shows. The departure from AFT and AFT-RSM transitional models and 2D simulations by Erturk (2008) is in good agreement with turbulent predictions by Ratha and Sarkar (2015) using $k - \varepsilon$.

For $Re > 400$ the transitional AFT and AFT-RSM follow perfectly the results from two-dimensional laminar simulations presented by Erturk (2008). The departure from the experimental results by Armaly et al. (1983) is due to the three-dimensional flow induced by the secondary bubble. Both transitional AFT and AFT-RSM predict the appearance of the secondary recirculating bubble on the upper wall for $Re > 400$. The formation of the secondary recirculating length is due to the adverse pressure gradient seen by the laminar boundary layer on the upper wall. The start (x_2) and the end (x_3) of the secondary recirculating region scale with Reynolds number as shown in Figure 5.5. This is in agreement with experimental and laminar predictions as shown. Transitional AFT and AFT-RSM provide fair predictions for x_2 and x_3, following the tendency predicted by the laminar simulations performed by Erturk (2008) in both cases. The largest difference can be found for x_3 at $Re = 1200$, where AFT-RSM does produce a longer secondary reattachment bubble. In addition, the length of the secondary recirculating bubble also scales with Re in AFT and AFT-RSM, which is in good agreement with experimental and two-dimensional laminar data. The shortened recirculation length behaviour observed with the S-A approach follows neither experimental nor two-dimensional laminar data. Nonetheless, the results in $400 < Re < 1200$ range are consistent with turbulent predictions presented by Ratha and Sarkar (2015) except for the rate of increase of x_3.

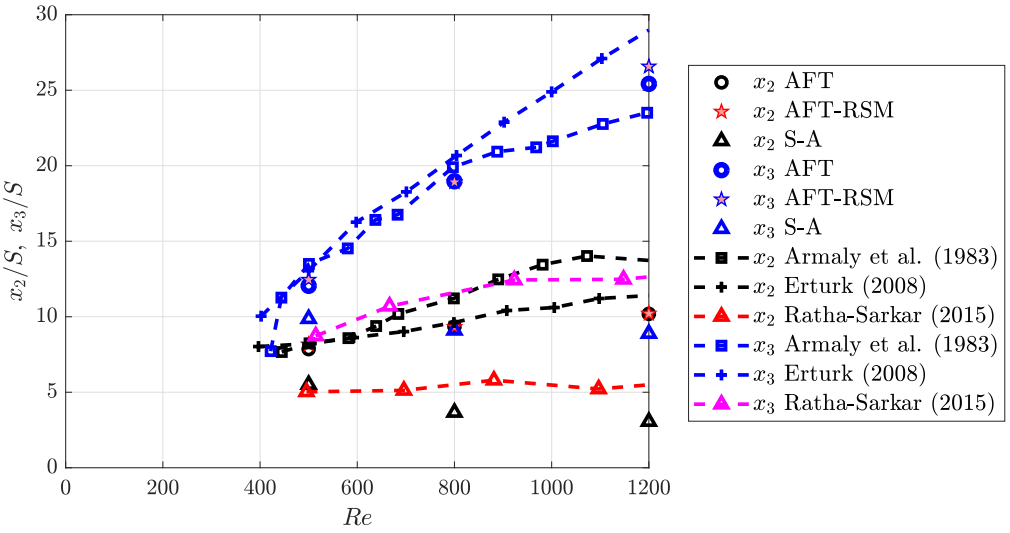

FIGURE 5.5: Predictions of x_2/S and x_3/S throughout the laminar region using AFT, AFT-RSM and S-A, including experimental data by Armaly et al. (1983), laminar DNS simulations by Erturk (2008) and $k-\epsilon$ by Ratha and Sarkar (2015).

5.2.2 Transitional Region - $1200 < Re < 6600$

The transitional regime is characterised by first, a sharp decrease of the main reattachment length (x_1/S) as shown in Figure 5.6 by Armaly et al. (1983) results. A gradual decrease is continuous down to approximately $Re = 5500$, then a small increase is observed followed by a plateau region from $Re = 7000$ characterising a fully-turbulent regime beyond the former value as reported by Armaly et al. (1983) measurements. The length of the secondary recirculating region $x_3/S - x_2/S$ also diminishes with the Re number as shown in Figure 5.6 and Figure 5.7. In this region, an additional tertiary recirculating bubble appears downstream of the main separation region at the step. The tertiary recirculating region is sketched in Figure 5.1 and denoted by x_4/S and x_5/S. To avoid confusion, note these are denoted with x_2/S and x_3/S in the original publication by Armaly et al. (1983).

Figures 5.6, 5.7 and 5.8 show the behaviour of the different recirculating regions with the Re number throughout the transitional regime and in the lower turbulent regime ($Re \approx 7000$). At a first glance, the AFT and AFT-RSM models show sensitivity to the transitional regime, with the reduction in all recirculating regions showing a similar trend to experimental data. Conversely, the S-A decreases rapidly at the early stages of the transitional regime and reaches a constant behaviour.

The transitional AFT and transitional AFT-RSM show a better description of the physics over this region than S-A and fully-turbulent $k-\varepsilon$ predictions by Ratha and Sarkar (2015). In fact, solutions are very similar for both transitional models, which reinforces the conclusions of a proper implementation shown in Chapter 4. At the early stages of the transitional regime, there is a sudden decrease of the primary dimensionless

recirculating length x_1/S, resembling the behaviour presented by Armaly et al. (1983). The AFT-RSM predicts an ever so slightly larger x_1/S which is consistent with the behaviour observed throughout the laminar regime. As the Re number is increased, x_1/S is shown to be reduced for AFT and AFT-RSM in Figures 5.6-5.7 respectively. Predictions compared to experimental data by Armaly et al. (1983) are consistently underpredicted. Conversely, the S-A predictions show x_1/S to increase for $Re > 4000$ in the transitional region until it reaches its fully-turbulent behaviour for $Re > 6600$.

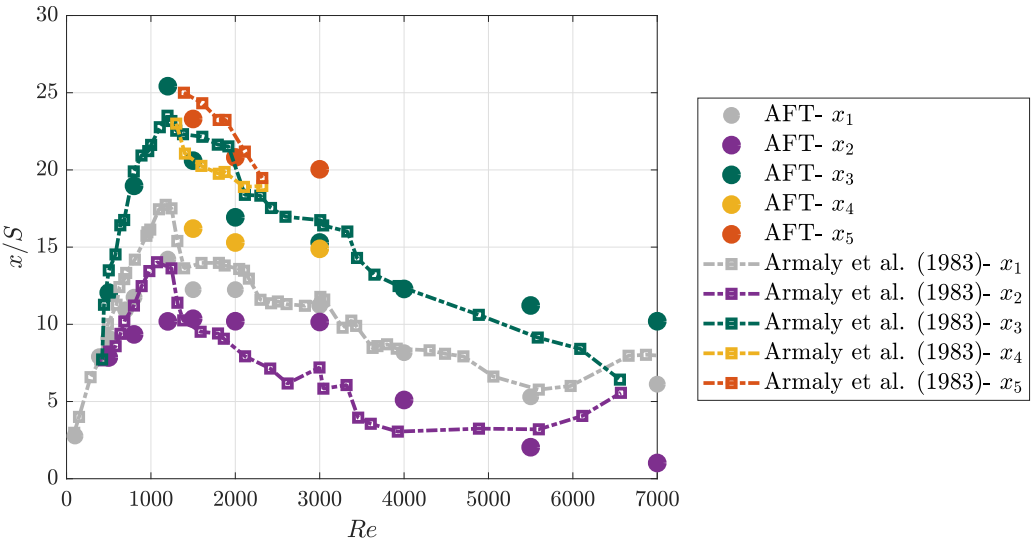

FIGURE 5.6: Predictions of x_i/S where $i = [1, 5]$ throughout laminar, transitional and turbulent regime for AFT, including experimental data by Armaly et al. (1983).

The secondary recirculating region is predicted by both transitional methods as well as for the turbulent S-A approach. This is the only additional recirculating region predicted by the S-A approach. Predictions with S-A show the length of the secondary recirculating region to diminish until $Re \approx 3000$. For $Re > 3000$, the secondary recirculating length increases until it vanishes beyond $Re > 6600$, where only the primary recirculating is predicted, which is in agreement with Armaly et al. (1983). Nonetheless, there is an evident underprediction of $x_1/S, x_2/S$ and x_3/S within the transitional regime, as shown in Figure 5.8. This behaviour is consistent with Ratha and Sarkar (2015) fully-turbulent predictions.

Figure 5.9 shows the velocity profile at $Re = 1200$. At this Re number, only two recirculating regions are predicted by the transitional AFT and AFT-RSM models, as well as by S-A fully-turbulent approach. The AFT and AFT-RSM show good agreement in the proximity of the step. Differences regarding the primary recirculating region are visible in positions $x/S = 12.24$ and 15.31. The x_1/S is shorter for AFT and AFT-RSM compared to Armaly et al. (1983) data as shown in Figure 5.6-5.7. This is confirmed by the velocity profiles at $x/S = 12.24$ and is even more evident with the positive component at the proximity of the lower wall in the velocity profile at

$x/S = 15.31$. The separation point of the secondary recirculating region x_2/S is also shown to occur before the experimental data. This is confirmed by the velocity profiles at the proximity of the upper wall at $x/S = 12.24$ and 15.31. Ultimately, at $x/S = 26.53$ the delayed reattachment of x_3/S can be noticed at the proximity of the upper wall. The experimental data show a more developed profile than AFT and AFT-RSM. The fully-turbulent approach shows how x_1/S reattaches before $x/S = 10.2$. On the upper wall, the early separation and reattachment is visible respectively at $x/S = 6.12$ and $x/S = 10.20$, where the flow is already reattached.

Transitional AFT and AFT-RSM models predict the secondary as well as the tertiary recirculating region throughout the transitional region. The secondary recirculating region for transitional models predicts a diminishing length from $1200 < Re < 3000$. The position x_2/S is shown to be constant, as the primary recirculating region. The position of x_3/S moves upstream with the increased Re. For $Re > 3000$, with the reduction of x_1/S, the x_2/S diminishes as well. The reattachment position of the secondary recirculating length continues moving upstream until the end of the transitional regime. The length is shown to increase during the second half of the transitional regime as opposed to experimental data. As shown in Figure 5.7, the AFT-RSM shows a consistent overprediction of the positions compared to AFT.

The tertiary recirculating region is predicted between $1500 < Re < 3000$ only by AFT and AFT-RSM, which are superior to fully-turbulent S-A model predictions. This is consistent with fully-turbulent predictions by Ratha and Sarkar (2015). Armaly et al. (1983) experimental data shows a rapid upstream movement of the tertiary recirculating length as the Re is increased between $1200 < Re < 2400$. Its length is shown to be constant until it vanishes. Transitional AFT and AFT-RSM predict a decrease in the length of the tertiary of the recirculating region. The position of x_4/S is consistently predicted before x_3/S as experimental data shows. The position of x_5/S is also predicted to be located always downstream of the position of x_3/S, which agrees with Armaly et al. (1983) data.

The transitional region demonstrates the capability of AFT and AFT-RSM to undergo transition on the primary and secondary recirculating regions as Re is increased. This is shown by the upstream displacement of x_1/S, x_2/S and x_3/S over the transitional region. Thus, not only demonstrate that for a fixed separation region the performance of AFT and AFT-RSM is superior to fully-turbulent approaches but also the capability of the model to laminarly separate, undergo transition and reattach without a fixated position separation position. This behaviour, leads to think that the transitional model will be able to improve predictions for flow past a circular cylinder, as the boundary layer undergoes similar changes. Ultimately, everything that has been discussed is performed without any transitional correlation as a difference to γ or $\gamma - Re_\theta$ models.

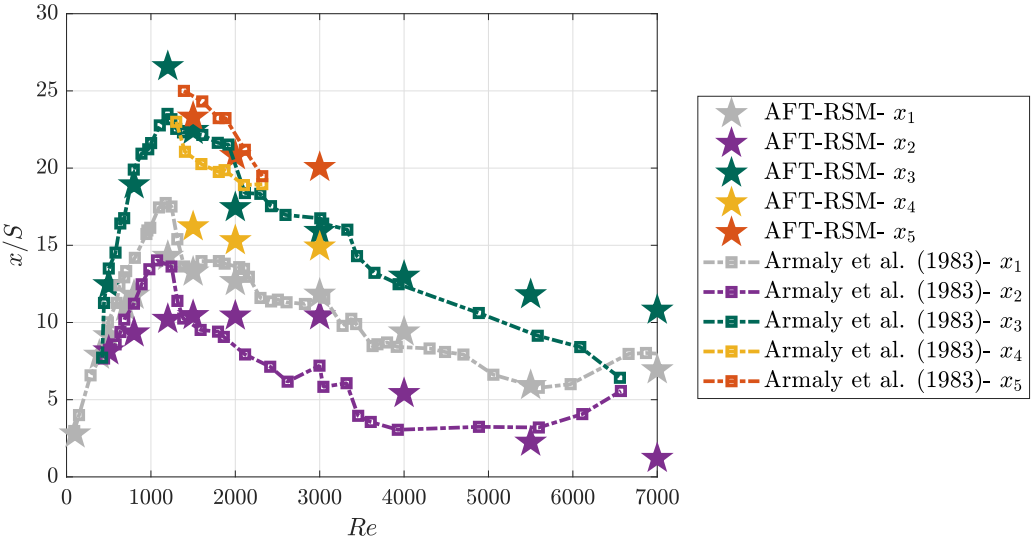

FIGURE 5.7: Predictions of x_i/S where $i = [1, 5]$ throughout laminar, transitional and turbulent regime for AFT-RSM, including experimental data by Armaly et al. (1983).

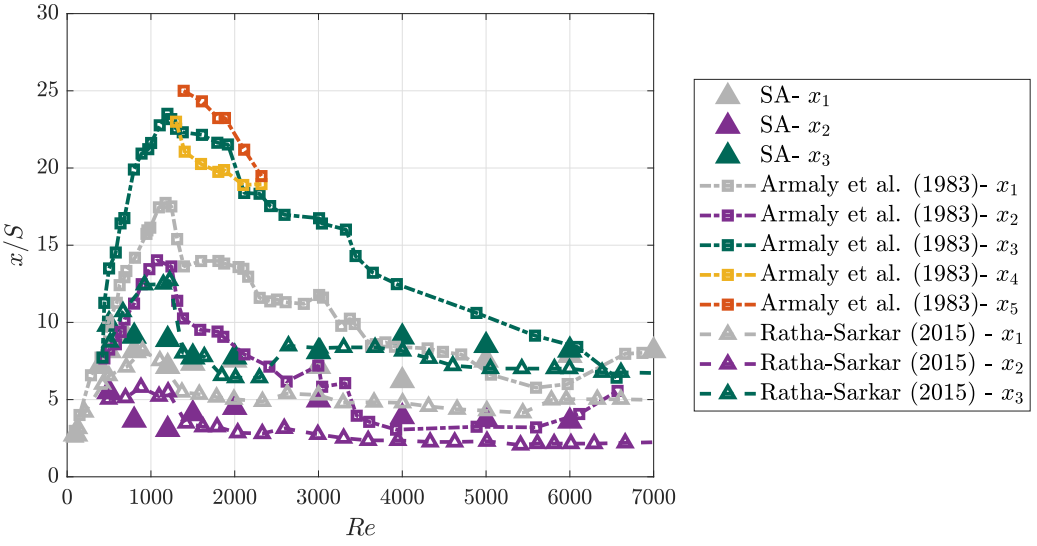

FIGURE 5.8: Predictions of x_i/S where $i = [1, 5]$ throughout laminar, transitional and turbulent regime for S-A, including experimental data by Armaly et al. (1983) and $k-\epsilon$ by Ratha and Sarkar (2015).

5.2.3 Turbulent Region - $Re > 6600$

Performance of the AFT and AFT-RSM in the turbulent region is characterised by a simulation at $Re = 7000$. In this region the primary reattachment length is considered constant. In this region, the secondary recirculating region disappears. As Figures 5.6 and 5.7 show, the secondary recirculating region is still being predicted by the transitional models at $Re = 7000$. Furthermore, the x_1/S is underpredicted by AFT and AFT-RSM. This is a consequence of the presence of the secondary recirculating region

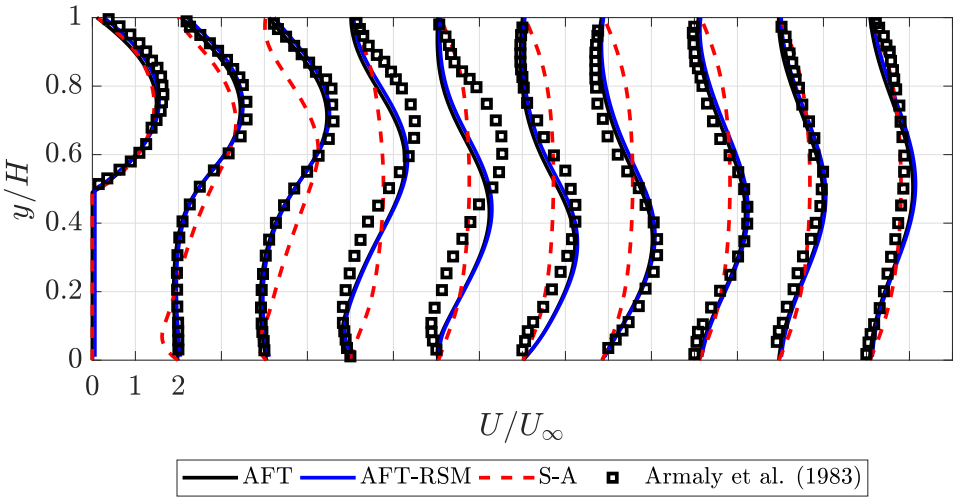

FIGURE 5.9: Velocity profile predictions at $Re = 1295$ for AFT, AFT-RSM and S-A, including experimental data by Armaly et al. (1983) at positions $x/S = 0,\ 3.06,\ 6.12,\ 10.2,\ 12.24,\ 15.32,\ 18.37,\ 22.45,\ 24.49,\ 26.53$.

at this Re number, as it forces the primary separated flow to deviate, producing an earlier reattachment.

The main problem that can be observed when using AFT and AFT-RSM is the nature of the flow at the step location. The flow is still laminar as indicated by γ as shown in Figure 5.10 for the AFT model, thus it being susceptible to separate on the upper wall vicinity due to the inability to withstand the adverse pressure gradient of the expansion. The primary recirculating region is shown to be fully-turbulent as $\gamma = 1$, however, the upper wall is laminar until it separates. In contrast to the transitional approaches, the S-A is already fully turbulent at the step, with a turbulent boundary layer on the upper wall capable of withstanding the pressure gradient due to the expansion ratio.

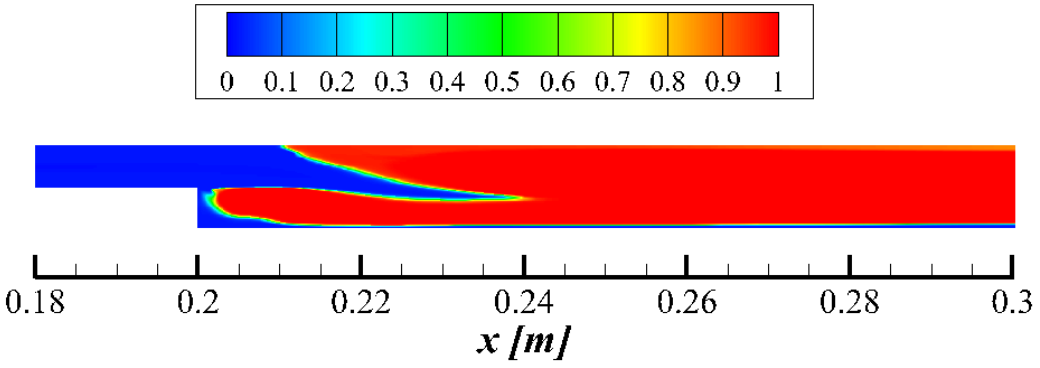

FIGURE 5.10: Distribution of γ at $Re = 7000$ using transitional AFT model.

The S-A continues predicting a constant recirculating length for x_1/S. This turbulent behaviour is exhibited since the latter stages of the laminar region as shown in Figure 5.2. Hence, the length is still $x_1/S \approx 8$ at $Re = 7000$, which is superior to the predictions observed by transitional methods for the turbulent region. Contrary to the laminar and transitional regions where it has been demonstrated that AFT and AFT-RSM are superior.

5.3 Summary

An analysis of the backward facing step flow has been presented in this Chapter, for an expansion ratio of 1.94, throughout the laminar, transitional and turbulent region, as described by Armaly et al. (1983) using transitional AFT and AFT-RSM along with the S-A turbulence model.

It has been demonstrated how the transitional approach improves predictions compared to fully turbulent approaches, as the one presented by Ratha and Sarkar (2015) using $k - \epsilon$ turbulence model. There are improvements over the laminar region, where the fully turbulent model shortens the reattachment length of the primary recirculating region and the secondary bubble and in a similar manner within the transitional region. Both transitional AFT and AFT-RSM, give sensible predictions in the laminar and transition regions as discussed, predicting longer reattachment lengths. AFT-RSM consistently predicts an elongated length for x_1, x_2 and x_3. The tertiary bubble is present downstream of the main recirculating region for transitional predictions using AFT and AFT-RSM. However, their dimensions are overestimated.

The dimensions of x_1, x_2 and x_3 regions have shown to increase with Reynolds number for transitional models up to approximately $Re_{D_h} = 1200$, showing the capability to predict laminar separation bubbles, separation and reattachment situations. For the turbulent approach, the growth with Reynolds number is approximately up to $Re_{D_h} = 800$ for x_1 and x_3, while x_2 shows a concave behaviour with Reynolds number up to $Re_{D_h} = 2000$ that is completely different from measurements.

When studying the turbulent region, it is shown how fully turbulent model performance is superior to transitional AFT and AFT-RSM. Even though that happens at approximately the middle of the transitional region as Figure 5.8 shows. In addition, the length of the secondary bubble is almost constant while measurements reveal to shrink. That also is shown by transitional AFT and AFT-RSM, however, the secondary bubble does not disappears at $Re_{D_h} = 6600$ as it is still predicted within the turbulent region at $Re_{D_h} = 7000$.

Hence, we can conclude that the transitional AFT and AFT-RSM improve predictions over the laminar and transitional regime to fully turbulent approaches. The performance for both transitional models is similar, although the AFT-RSM provides larger x/S values the improvements are not that significant. Nevertheless, it shows promising behaviour for the use of transitional models in more complex flow fields such as flow past a circular cylinder. However, there are questions regarding its behaviour when the flow is expected to be fully turbulent as in $Re_{D_h} > 6600$.

Chapter 6

Validation at $Re_D = 3900$ for a circular cylinder flow

Chapter 4 and Chapter 5 have demonstrated a successful implementation of the AFT and AFT-RSM model into the OpenFOAM computational fluid dynamics package. As discussed in the former chapter, the AFT-based models have demonstrated the superior a performance given compared to fully-turbulent approaches regarding the estimation of recirculating length and the appearance of separation bubbles within the transitional regime for backward step flow, where the pressure gradient and main separation point are fixed.

This chapter aims to perform a grid sensitivity analysis to validate the performance of two-dimensional simulations using the transitional AFT and AFT-RSM models and three-dimensional simulations for the hybrid AFT-DDES model for flow past a circular cylinder. The validation is performed at $Re_D = 3900$ as it is a really well-benchmarked case that can be found in the literature. The flow past a circular cylinder, as opposed to the backward-facing step, has a variable pressure gradient and a separation that is not static.

The discussion is divided in three: pressure coefficient and skin-friction coefficient, a wake velocity analysis and the study of the behaviour of the turbulence intensities at six different position within the wake. Before proceeding with the result section, the domain, boundary conditions and the numerical properties of the simulations are described.

6.1 Details of numerical simulations

6.1.1 Simulation domain and boundary conditions

The geometry of the flow problem is a circular cylinder of diameter $D = 0.05$ m. The chosen domain has a circular topology, exemplified in Figure 6.1 to ensure mesh orthogonality. As it is discussed extensively in literature i.g. Cheng et al. (2017), the domain extends upstream (L_i) and downstream (L_o) the circular cylinder a distance of $\pm 15D$. This dimension is sufficient to avoid interactions with the flow-filed in the proximity of the cylinder surface and a sufficient distance for the wake to develop. The blockage ratio is 3.33%, which is sufficiently below 6% to have any impact on the drag and pressure predictions, as discussed by West and Apelt (1982).

The non-dimensional parameter describing the different regimes of the flow field is the Reynolds number based on the freestream velocity (U_∞) and the diameter D of the circular cylinder, defined as

$$Re_D = \frac{U_\infty D}{\nu}. \tag{6.1}$$

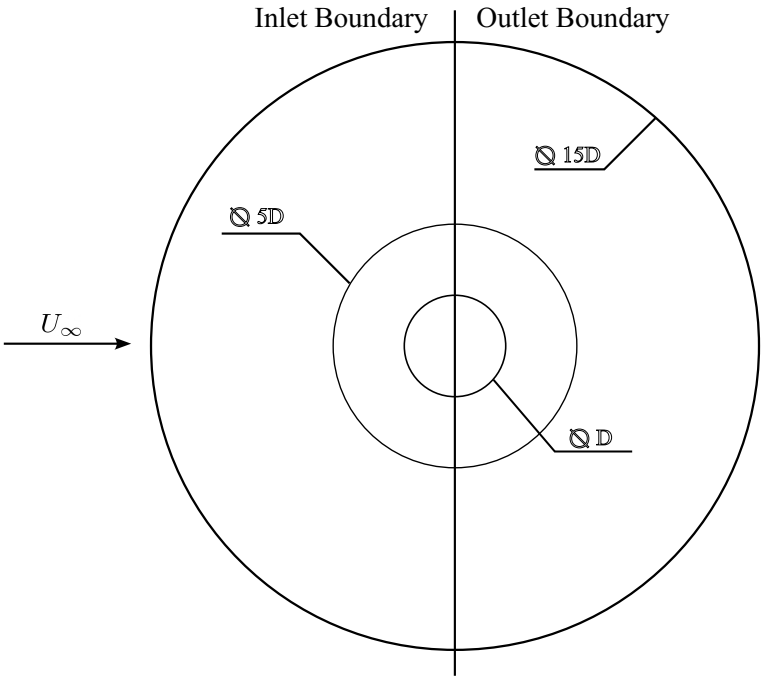

FIGURE 6.1: Schematic domain for circular cylinder simulation case including the inner cylinder for the wake refinement of $5D$. (Figure not to scale)

The upstream boundary is set to uniform velocity inlet and the downstream boundary is set to "zero- gradient" condition. At the connection point between the inlet and outlet boundary there is any numerical effect, as the "zero-gradient" condition ensures any spurious data as shown in Figure 6.2 as an example. The cylinder surface is treated

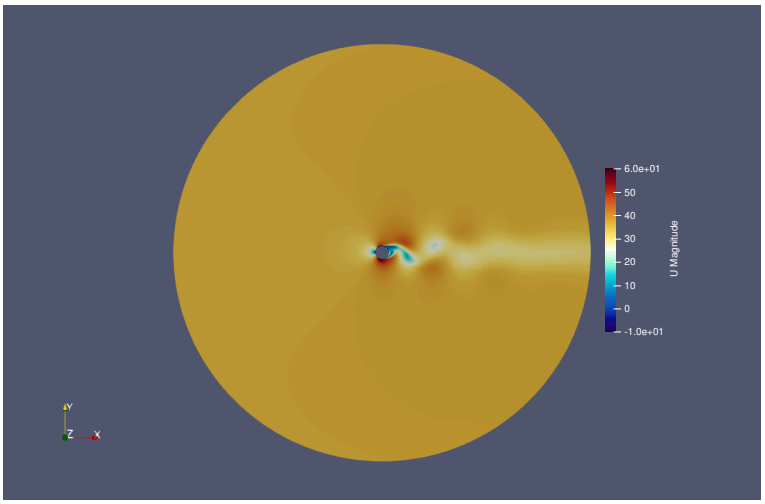

FIGURE 6.2: Example of instantaneous velocity magnitude contour plot for circular cylinder flow at $Re = 1.5 \times 10^5$ to show that any spurious data is generated with the joint forward facing and backward facing boundaries of the domain.

as a solid surface and therefore is set to a no-slip condition. Front and back surfaces are set to "empty" for two-dimensional simulations, while to simulate cylinders with an infinite span, periodic boundary conditions are imposed in the spanwise direction in three-dimensional simulations.

In this case, the interest is to simulate the flow past a circular cylinder under low-freestream turbulence conditions of approximately $Tu \approx 0.05\%$. Values of R_{ii}, ω and N_{crit} are set according to the boundary conditions presented in Section 3.1 for the AFT-RSM. The turbulent viscosity ratio for transitional methods is set $\tilde{\nu}/\nu = 0.1$ for AFT, DDES-SA and AFT-DDES and $\nu_t/\nu = 5$, for AFT-RSM as discussed in Chapter 2.

6.1.2 Numerical properties

For URANS, a second-order upwind scheme (UW) is used for the spatial discretization of momentum, transitional and turbulence equations. The momentum equations in the DDES are spatially discretized using a second-order interpolation scheme limited Linear (CD). This model is a total variation diminishing (TVD) interpolation method, which combines the upwind and centered schemes to minimize diffusion inherited by the upwind scheme and retain stability within the simulation, as discussed by Mockett et al. (2009). It is reported in the literature that second-order upwind for scale-resolving methods has a significant numerical dissipation due to the upwind nature of the scheme. Gradients are discretized using a second-order scheme. A second-order implicit temporal discretization is used for URANS and DDES simulations, allowing stable and accurate predictions using large CFL numbers. Dimensionless time step ($\tilde{\Delta t} = \Delta t U_\infty / D$) is given in Table 6.1 and Table 7.1 for $Re = 3900$ and a range of Reynolds numbers respectively. All dimensionless time-step ensures a CFL number below 2.

The pressure-velocity coupling is solved using the PIMPLE algorithm, which is a combination of the SIMPLE (Semi-Implicit Method for Pressure Linked Equations) and PISO (Pressure Implicit with Splitting of Operators) algorithms. Specifically, in each time step, the SIMPLE algorithm is applied, while between different time steps, the PISO algorithm applies Greenshields and Weller (2022). For such specific cases, the number of inner loops is set to 3, with a non-orthogonal correction of 2 as a default scenario. The outer loop is set to a maximum of 25 iterations that is reduced as the residual control is set to 1×10^{-3} and 1×10^{-4} for pressure and velocity respectively, with the relaxation factors as discussed in Chapter 4.

6.2 Validation - $Re_D = 3900$

Before proceeding with the analysis of the upper-sub-critical, critical and super-critical regimes, new predictions at $Re_D = 3900$ using AFT, AFT-RSM and AFT-DDES are discussed. This will serve first, to determine a baseline mesh, from where the following Reynolds number grids are constructed, and secondly, as a validation case for the current wall-transition resolved DDES code in OpenFOAMv1912.

Near-wall and near-wake measurements are available in the literature. Norberg (1994) reported pressure coefficient measurements over the surface while Lourenco and Shih (1993) and Parnaudeau et al. (2008) presented experimental results for mean velocity, variance and covariance profiles in the near-wake region at six different locations up to $x/D = 10$. Discrepancies are found in the mean velocity profile inside the recirculation bubble. Ma et al. (2000) reported that mean velocity converges to a U-shape for $L_z = \pi D$, but to a V-shape for $L_z = 2\pi D$, which is consistent with numerical simulations by Parnaudeau et al. (2008) and D'Alessandro et al. (2016), however, there is not yet a clear answer for such behaviour.

Here, we choose the experimental data by Parnaudeau et al. (2008) and Lourenco and Shih (1993), and LES predictions by Cheng et al. (2017), Kravchenko and Moin (2000) to compare with. The two-dimensional predictions for AFT and AFT-RSM are discussed first, followed by the analysis of the results obtained by the AFT-DDES model applied to a three-dimensional flow field. The discussion is divided into three sections: the surface pressure and skin friction, the wake velocity and finally the recirculating and turbulence intensities.

6.2.1 Transitional URANS

The transitional URANS sensitivity to AFT and AFT-RSM is studied using two different grid distributions, as given in Table 6.1: 120×160 (AFT-G1 and AFT-RSM-G1) and 240×220 (AFT-G2 and AFT-RSM-G2) number of points for the radial and angular

directions. The coarser mesh (AFT-G1 and AFT-RSM-G1) is the same as the one used by Breuer (2000) at a higher Reynolds number, while the second mesh provides the same resolution in radial and angular directions as used by many simulations in literature, i.e. Cheng et al. (2017), Liu et al. (2019) and Breuer (2000). In all cases, y^+ is maintained below 1, as concluded in Chapter 4 for a good laminar and turbulent skin friction prediction. Furthermore, the mean flow characteristics discussed in the following paragraphs are given in Table 6.2.

TABLE 6.1: Grid characteristics for AFT, AFT-RSM and AFT-DDES simulations for the validation case at $Re_D = 3900$.

Run	Grid $N_r \times N_\theta \times N_z$	Domain $L_i \times L_o \times L_z$	Model	Δt	Scheme
AFT-G1	120×160	$15D \times 15D$	AFT	0.004	UW
AFT-G2	240×220	$15D \times 15D$	AFT	0.004	UW
AFT-RSM-G1	120×160	$15D \times 15D$	AFT-RSM	0.004	UW
AFT-RSM-G2	240×220	$15D \times 15D$	AFT-RSM	0.004	UW
AFTDDES-G1	$160 \times 160 \times 30$	$15D \times 15D \times 3D$	AFT-DDES	0.004	CD
AFTDDES-G2	$160 \times 160 \times 60$	$15D \times 15D \times 3D$	AFT-DDES	0.004	CD
AFTDDES-G3	$256 \times 256 \times 60$	$15D \times 15D \times 3D$	AFT-DDDES	0.004	CD

A: Surface pressure (C_p) and skin friction (C_f)

The surface pressure coefficient at $Re_D = 3900$ is shown in Figure 6.3(a). The two grids produce similar results for AFT and AFT-RSM. The pressure coefficient shows a reduction over the upstream face of the cylinder, as the flow is accelerated, until reaching its minimum value. The minimum pressure coefficient ($C_{p,min}$) indicates the extension of the favourable pressure gradient region from the stagnation point. Thus, an increased favourable pressure gradient region, and a lower minimum pressure ($C_{p,min}$), leads to delayed separation of the boundary layer. In this case, AFT-G1 and AFT-G2 predict a $-C_{p,min} = 1.68$, and AFT-RSM-G1 and AFT-RSM-G2 predict a $-C_{p,min} = 1.65$. The smallest value of $-C_{p,min}$ predicted by AFT-RSM-G1 and AFT-RSM-G2, is in agreement with its earlier separation location, as given in the next paragraph using C_f. Following the flow separation, one can see how there is a sharp decrease in the pressure coefficient from approximately $\phi = 130°$ to the aft-part of the cylinder surface. This represents a pair of counter-rotating vortices, due to the reattachment of the flow as shown by the skin friction coefficient C_f in Figure 6.3(b), between $\phi = 130° - 180°$.

The C_f predictions for the current runs are shown in Figure 6.3(b). The prediction for AFT-G1 and AFT-G2, and AFT-RSM-G1 and AFT-RSM-G2, are similar throughout the upstream face. The C_f profiles show that AFT-G1 and AFT-G2 predict a laminar separation $\phi_{l,s} = 99°$, while AFT-RSM-G1 and G2, predict an earlier separation at $\phi_{l,s} = 97°$. Beyond the separation location, the C_f resembles a plateau region until the counter-rotating vortex produces an attached region since the C_f becomes positive again at $\phi = 130°$ until $\phi = 180°$ for all runs.

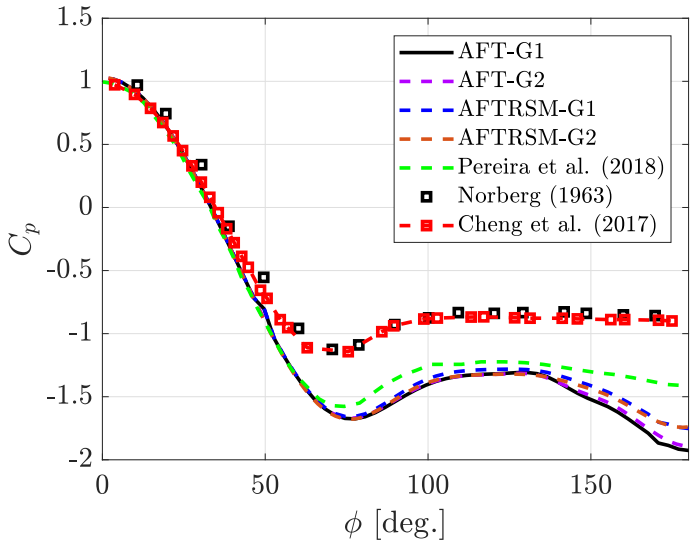

(a) C_p

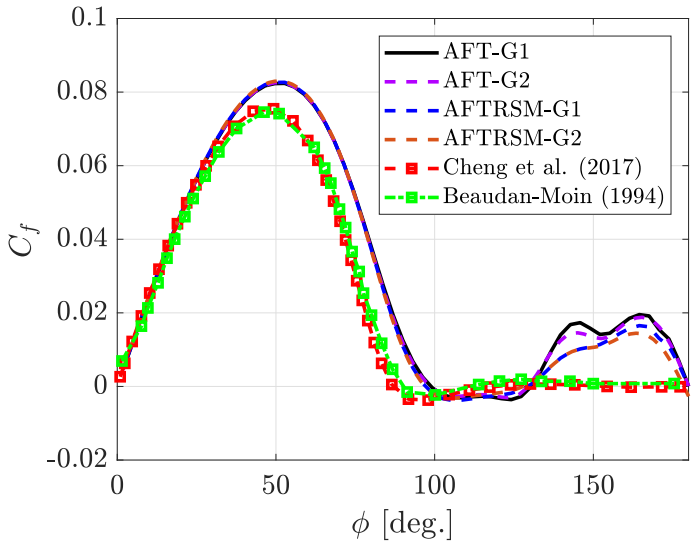

(b) C_f

FIGURE 6.3: (a) C_p and (b) C_f distribution for AFT-G1, AFT-G2, AFT-RSM-G1 and AFT-RSM-G2 transition models for validation case at $Re_D = 3900$.

Experimental results by Norberg (1994) and LES simulations by Cheng et al. (2017) are included in Figure 6.3(a) for comparison. It is readily seen that the favourable pressure gradient region predicted in the literature data is smaller than predicted by all transitional URANS cases. Norberg (1994) and Cheng et al. (2017) report a $-C_{p,min} \approx 1.14$, while AFT-G1 and AFT-G2 predict a larger $-C_{p,min}$ by 47% and AFT-RSM-G1 and AFT-RSM-G2 predict a larger $-C_{p,min}$ too, by 44%. The limitations of the two-dimensional URANS models, using even transitional approaches, to resolve the turbulent structures downstream of the separation have a direct impact on the separation point, and on the C_p prediction. The delay of separation and the increased $-C_{p,min}$ were also

seen in the URANS predictions by Pereira et al. (2018).

After the separation, the plateau pressure value between $\phi = 100° - 130°$, is also observed to be lower than literature in Figure 6.3(a). AFT-G1 and G2, predict a $C_p = -1.31$ and the two grids for AFT-RSM predict a $C_p = -1.32$, which is approximately 52% smaller than Norberg (1994) and Cheng et al. (2017). This is consistent with the three-dimensional URANS prediction by Pereira et al. (2018), where the difference to Norberg (1994) is 33.6% over the plateau region of the C_p after separation. The pressure rise is related to the proximity of the core of the two-symmetric counter-rotating vortices to the aft-part of the cylinder surface. This is also consistent with observations within the wake by Pereira et al. (2018). Lastly, a sharp decrease is observed for G1 and G2 with AFT and AFT-RSM, which is not captured by Norberg (1994) or Cheng et al. (2017). The three-dimensional URANS prediction by Pereira et al. (2018) shows a similar sharp decrease of the C_p, which is milder than the one predicted by the current simulations. With the increase of the modelled to the resolved kinetic energy ratio, the sharp decrease disappears, as the three-dimensional structures generated in the shear layer can be resolved by LES but not with two-dimensional or three-dimensional URANS predictions. Thus, this confirms the inability of the URANS to resolve certain turbulent structures within the wake in two-dimensional and three-dimensional cases. In fact, LES simulations with a short spanwise domain resemble the same behaviour as reported by Cheng et al. (2017).

Predictions of C_f are compared to LES results by Kravchenko and Moin (2000) and Cheng et al. (2017). The C_f prediction over the upstream face for G1 and G2 with AFT and AFT-RSM show an agreement up to $\phi = 40°$. Beyond that angle, the maximum C_f is overpredicted by 9%, compared to the results of Beaudan and Moin (1994) and Cheng et al. (2017). Laminar separation prediction is delayed by 9° and 12.5° using AFT-G1 and AFT-G2, while AFT-RSM-G1 and AFT-RSM-G2, delay the separation by 7° and 10.5°, compared to Beaudan and Moin (1994) and Cheng et al. (2017) respectively.

B: Wake velocity

Predictions of the mean streamwise velocity along the centerline within the wake are shown in Figure 6.4. Recirculation length (L_r/D) is determined as the distance from the aft-part of the cylinder to the position where the mean velocity at the centerline recovers to zero, $\overline{U}/U_\infty = 0$. The AFT-G1 and AFT-G2 predictions show a similar distribution of the velocity, with a rise of velocity after a recirculating length $L_r/D = 0.18$ until approximately $x/D = 2$. AFT-RSM-G1 and AFT-RSM-G2 predict a similar $L_r/D = 0.30$, which is 15% larger than the AFT model for both grids. Beyond that point, the velocity does not recover gradually and shows a wavy behaviour instead from $x/D = 6$, for all current URANS simulations. This is a consequence of the narrowing and widening of the wake downstream of the back of the cylinder. As seen in Figure 6.4,

differences with the data in the literature are large, and the reasons are discussed in the following paragraph.

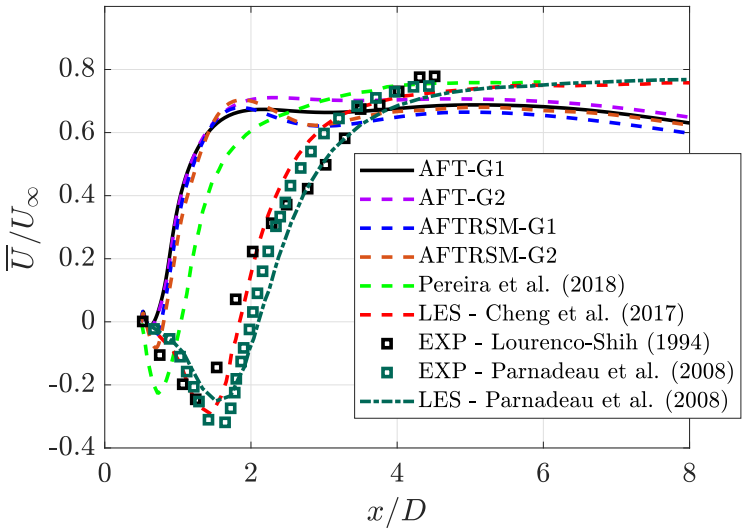

FIGURE 6.4: Mean normalized streamwise velocity $\overline{U}/U_\infty$ at centerline downstream the cylinder surface.

Experimental work done by Parnaudeau et al. (2008) ($L_r/D = 1.56$) and Lourenco and Shih (1993) ($L_r/D = 1.19$) are presented along with LES by Cheng et al. (2017) ($L_r/D = 1.34$) and Parnaudeau et al. (2008) ($L_r/D = 1.61$). Shortened $L_r/D = 1.19$ from PIV measurements by Lourenco and Shih (1993) are attributed to experimental error and an early transition of the shear layer as discussed in Kravchenko and Moin (2000). AFT-G1 and AFT-G2, predict a L_r/D shorter by $x/D = -1.1$, and AFT-RSM-G1 and AFT-RSM-G2, predict a L_r/D shorter by $x/D = -0.89$ to Lourenco and Shih (1993), while 1.38 and 0.89 to experimental measurements by Parnaudeau et al. (2008) respectively. The error to the LES simulation by Cheng et al. (2017) is $x/D = -1.16$ and $x/D = -1.04$ for AFT, and AFT-RSM, respectively. Thus, the shortening of the recirculating length in URANS predictions is a cause of the unresolved shear layer that triggers its earlier transition, as discussed by Kravchenko and Moin (2000). Consequently, the turbulent eddies are brought closer to the back of the cylinder. This is consistent with the predictions of Pereira et al. (2018), where $L_r/D \approx 0.5$ is largely underpredicted even in three-dimensional simulations when using URANS models.

Figure 6.5(a) and Figure 6.5(b) show mean streamwise ($\overline{U}$) and mean crossflow velocity ($\overline{V}$), respectively, at six different positions downstream of the cylinder ($x/D = 1.06$, $x/D = 1.54$, $x/D = 2$, $x/D = 4$, $x/D = 7$ and $x/D = 10$). The AFT and AFT-RSM with G1 and G2 predict a similar behaviour for $\overline{U}$, where the velocity defect within the wake can be observed around $y/D = 0$ at all locations, with its consequent velocity recovery at the centerline. Figure 6.5(b) shows an anti-symmetric behaviour for all URANS simulations when predicting $\overline{V}$. This is physically expected as two-symmetric

counter-rotating vortices occur within the wake. From the current predictions, no noticeable differences can be observed in the $\overline{U}$ and $\overline{V}$ data.

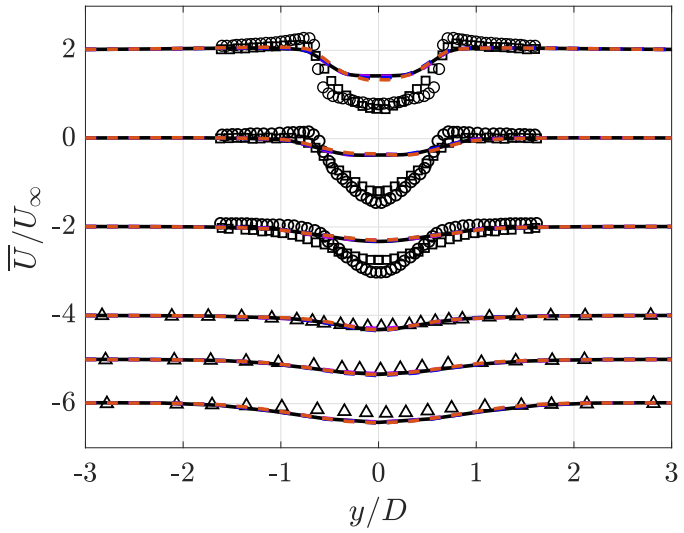

(a) $\overline{U}$

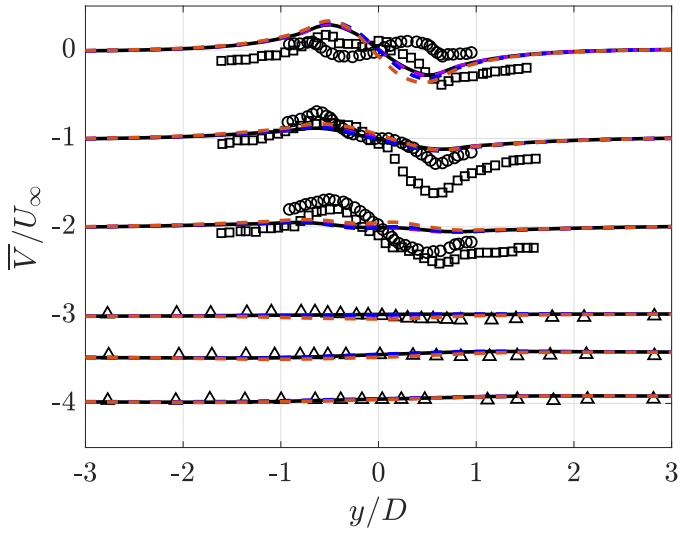

(b) $\overline{V}$

FIGURE 6.5: Normalized (a) $\overline{U}/U_\infty$ distribution and (b) $\overline{V}/U_\infty$ distribution for AFT-G1, AFT-G2, AFT-RSM-G1 and AFT-RSM-G2 transition models (see Figure 6.4 for legend) and experimental data by (○) Parnaudeau et al. (2008), (□) Lourenco and Shih (1993) and (△) Ong and Wallace (1996) .

Experimental data by Lourenco and Shih (1993) and Parnaudeau et al. (2008) are shown for $\overline{U}$ and $\overline{V}$ along with all current predictions. Two different shapes can be observed in Figure 6.5(a). The U-shape mean streamwise profile is measured in Parnaudeau et al. (2008) but V-shape is measured in experiments by Lourenco and Shih (1993). As discussed for shortened L_r/D by Lourenco and Shih (1993), Beaudan and Moin (1994) attributed this to experimental error, and an early transition of the shear layer

as discussed in Kravchenko and Moin (2000). However, Ma et al. (2000) examined this contradiction by performing DNS simulations with different spanwise domains. The mean velocity from Ma et al. (2000) converges to V-shape with $L_z = 2\pi D$ but to a U-shape using $L_z = \pi D$. Recent research by Lysenko et al. (2012) and D'Alessandro et al. (2016) suggest that a V-shaped profile is observed in flow fields, which have a short recirculating length, which is in agreement with what it is observed with the use of AFT and AFT-RSM in two-dimensional simulations.

The two-dimensional predictions when using AFT and AFT-RSM in grids G1 and G2 show a V-shape velocity profile in the near wake, with the largest deficit in velocity at $x/D = 1.54$, compared to experimental data by Lourenco and Shih (1993) and Parnaudeau et al. (2008). Predictions using AFT and AFT-RSM with G1 and G2, show a maximum deficit at the mentioned position of 70% and 76% to Lourenco and Shih (1993) and Parnaudeau et al. (2008), respectively. This large difference is a consequence of the shortened wake predicted by two-dimensional AFT and AFT-RSM with G1 and G2. As the mean velocity streamlines have already closed the pair of two-counter rotating vortices way earlier than $x/D = 1.06$, the flow-field is closer to zero than Lourenco and Shih (1993) and Parnaudeau et al. (2008) in this same position. Thus, further downstream the differences are much smaller as can be easily seen, with a fair agreement of approximately 9% when compared to Ong and Wallace (1996) for $x/D > 4$.

For the $\overline{V}$ behaviour, as already discussed, differences between Lourenco and Shih (1993) and Parnaudeau et al. (2008) are also shown, especially in the near wake for $x/D = 1.06 - 1.54$. Beyond the near-wake region, it is shown that both measurements show the same behaviour. Figure 6.5(b) shows how all predictions, resemble the Lourenco and Shih (1993) behaviour more than Parnaudeau et al. (2008), as occurred for $\overline{U}$. The asymmetric behaviour is not predicted by any of the current simulations. AFT-G1 and AFT-G2 show an anti-symmetric behaviour with the peak being overpredicted by almost twice from Lourenco and Shih (1993) at $x/D = 1.06$. This shifts downstream, as it is underpredicted by 15% at $x/D = 2$. Further downstream, differences are about $8 - 10\%$ to Ong and Wallace (1996). The error reduction is consistent with analyses of $\overline{U}$.

C: Turbulence intensities

AFT and AFT-RSM with G1 and G2 predict a peak in the variance of the streamwise velocity fluctuations as shown in Figure 6.6. This peak is related to the distance from the base of the cylinder where the vortices are shed as discussed by D'Alessandro et al. (2016). AFT-G1 and AFT-G2 predict the same peak value of $\overline{u'u'} = 0.1025$, while AFT-RSM-G1 and AFT-RSM-G2 predict the same value of $\overline{u'u'} = 0.1139$. Furthermore, the position of such peak is further downstream predicted by AFT-RSM ($L_f/D = 0.8925$), than AFT ($L_f/D = 0.8035$). This behaviour is consistent with predictions achieved for L_r/D with AFT-RSM, which were discussed earlier in the wake velocity section.

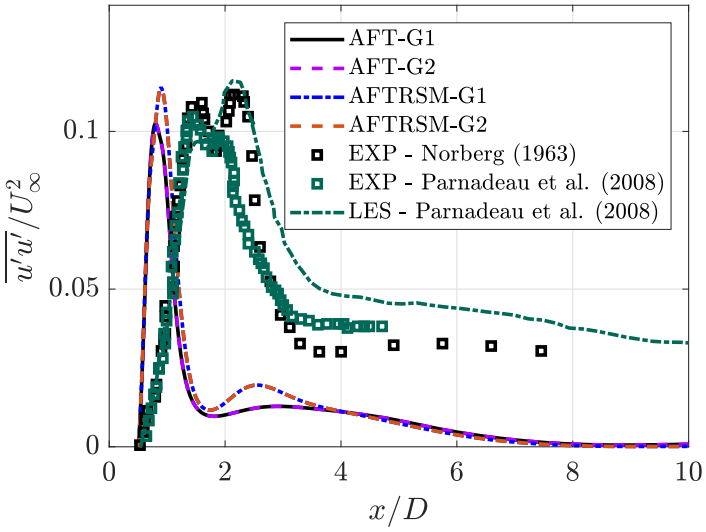

FIGURE 6.6: Mean variance of normalized streamwise velocity fluctuations $\overline{u'u'}/U_\infty^2$ at centerline downstream of the cylinder surface.

Experimental data by Norberg (1994), Parnaudeau et al. (2008) and LES by Parnaudeau et al. (2008) are shown along with the AFT and AFT-RSM predictions. Qualitatively, it is observed in Figure 6.6 that none of the URANS simulations predicts the two peaks observed in experiments by Norberg (1994) and Parnaudeau et al. (2008). The primary peak, with the largest value, is related to the vortex shedding and the secondary peak is believed by Norberg (1994) to be caused by a longitudinal vortex. However, Parnaudeau et al. (2008) report that the link between the second peak and vortical effects is unclear. LES prediction only shows the peak associated with the vortex shedding, as well as AFT and AFT-RSM with grids, G1 and G2. In this case, the peaks are located further upstream than in the experiments and LES given in Figure 6.6. This is a cause of the short recirculating length predicted by 2D AFT and AFT-RSM with grids G1 and G2, as already discussed in the paragraphs above. Downstream of the peak we can see the reduction of the $\overline{u'u'}$, which may be related to the dissipation of the upwind nature of the numerical scheme utilised for URANS simulations.

Figure 6.7(a) and Figure 6.7(b) show the mean-variance of the streamwise and transverse velocity fluctuations. Predictions of the AFT and the AFT-RSM with both G1 and G2 meshes are in agreement regarding the behaviour exhibited from the near cylinder to further downstream up to $x/D = 10$. In the plot there are 4 lines but AFT-G1 and G2 are coincident, as well as AFT-RSM-G1 and G2. Two peaks for $\overline{u'u'}$ are predicted by the current simulations, that are related to the vortex shedding process. Since the recirculation length predicted by the current simulations is shorter than the value in the literature, as presented in Figure 6.7(a), the flow field between the two prominent peaks approaches to zero, as at $x/D = 1.06$ the shedding has already occurred. When compared to measurements by Lourenco and Shih (1993) and Parnaudeau et al. (2008), one can see the tendency follows better the first set of experiments in the near wake,

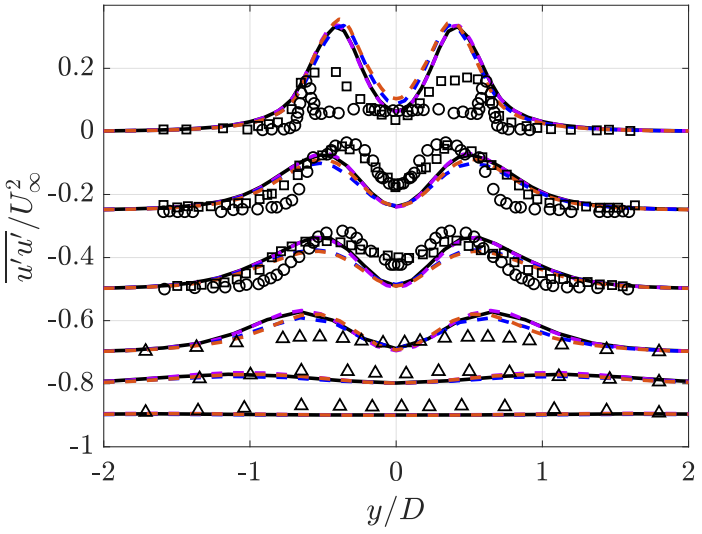

(a) $\overline{u'u'}$

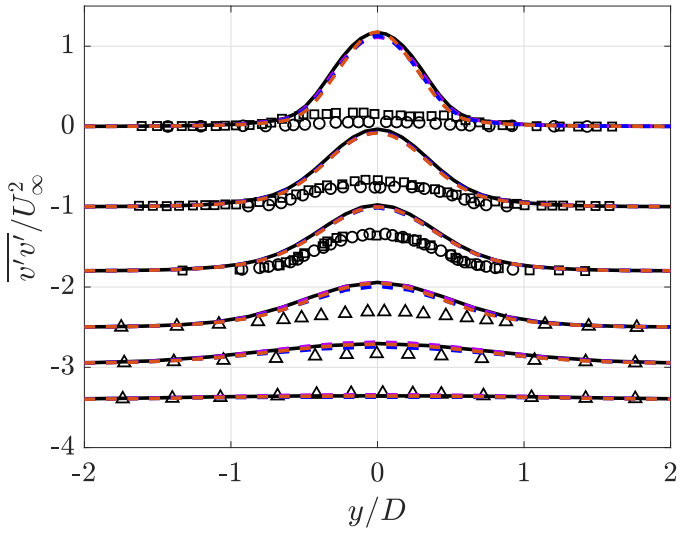

(b) $\overline{v'v'}$

FIGURE 6.7: Normalized (a) $\overline{u'u'}/U_\infty^2$ distribution and (b) $\overline{v'v'}/U_\infty^2$ distribution for AFT-G1, AFT-G2, AFT-RSM-G1 and AFT-RSM-G2 transition models (see Figure 6.4 for legend) and experimental data by (○) Parnaudeau et al. (2008), (□) Lourenco and Shih (1993) and (△) Ong and Wallace (1996) .

specifically at locations $x/D = 1.06$, $x/D = 1.56$ and $x/D = 4$. The difference in the peaks to Lourenco and Shih (1993) at the near wake ($x/D = 1.06$) is approximately 84%.

The mean-variance of the crosswise velocity fluctuations predicts a peak at the centerline for current predictions as expected, due to the vortex periodic shedding from the cylinder surface. The peak of $\overline{v'v'}$ gradually diminishes as flow moves away from the cylinder until the vortex shedding vanishes. Experimental data by Lourenco and Shih (1993)

and Parnaudeau et al. (2008) show a milder peak than AFT and AFT-RSM with G1 and G2, specifically from $x/D = 1.06$ to $x/D = 4$. Overprediction from the closest to the furthest position is large. The latest position at $x/D = 10$ shows a good agreement with experimental data, as the contribution almost vanishes.

6.2.2 Transitional DDES

The transitional DDES sensitivity is studied using two different grid distributions given in Table 6.1 with a central difference (CD) numerical scheme. The grids use 160×160 and 256×256 numbers of points for the radial and angular directions. The base mesh is similar to the used by Breuer (2000) with two different number of points along the spanwise direction, 30 (AFTDDES-G1) and 60 (AFTDDES-G2). With a refinement factor of about $\sqrt{2}$, grid $256 \times 256 \times 60$ (AFTDDES-G3) is a standard mesh used in literature by Cheng et al. (2017), D'Alessandro et al. (2016) amongst others, for this validation case at $Re_D = 3900$. Furthermore, in this case, the spanwise length is kept at $L_z = 3D$, as different literature (i.e. D'Alessandro et al., 2016, Cheng et al., 2017) showed that this is sufficient to develop the vortical structures, while shorter spanwise lengths alter the near-wake velocity and velocity fluctuation predictions.

A: Surface pressure (C_p) and skin friction (C_f)

Figure 6.8(a) shows predictions of surface pressure from DES calculations using AFT as the turbulence models. Differences in Figure 6.8(a) show the resolution in grids G1 and G2 to be insufficient. The $-C_{p,min}$ is smaller as the mesh is refined as AFTDDES-G2, as well as the $-C_{p,b}$. On the other hand, when increasing the resolution in the radial and angular directions from G2 to AFTDDES-G3, the $-C_{p,min}$ is reduced and the $-C_{p,b}$ too. AFTDDES-G3 falls closer to experimental results than G1 and G2 meshes, due to the refinement in the angular and radial direction. The $-C_{p,min}$ from G3 mesh is overpredicted by 10%, similarly to $-C_{p,b}$. Due to the lack of grid resolution in some of all the directions, AFTDDES-G1 and AFTDDES-G2 show an overprediction of minimum pressure coefficient and back pressure compared to literature data in Figure 6.8(a).

As $-C_{p,min}$ is reduced, the laminar separation point predicted by the current simulations moves upstream with positions: $\phi_{l,s} = 88$, $\phi_{l,s} = 87.5$, $\phi_{l,s} = 87$ degrees, respectively for AFTDDES-G1, AFTDDES-G2 and AFTDDES-G3 as shown in Figure 6.8(b). The small counter-rotating vortex is predicted at approximately from $\phi_{v,r} = 130^\circ$ to $\phi_{v,s} = 150^\circ$ for three meshes. It is also shown how the lack of resolution in radial, angular and spanwise directions does not have much of an effect at this Reynolds number on the C_f prediction. Nonetheless, the AFTDDES-G3 configuration shows the best agreement to Cheng et al. (2017) overall, and to Beaudan and Moin (1994) after separation. Predictions using AFTDDES-G1 and G2 are also in good agreement. However, the C_p is influenced by its lack of resolution in the radial, angular and spanwise direction. The

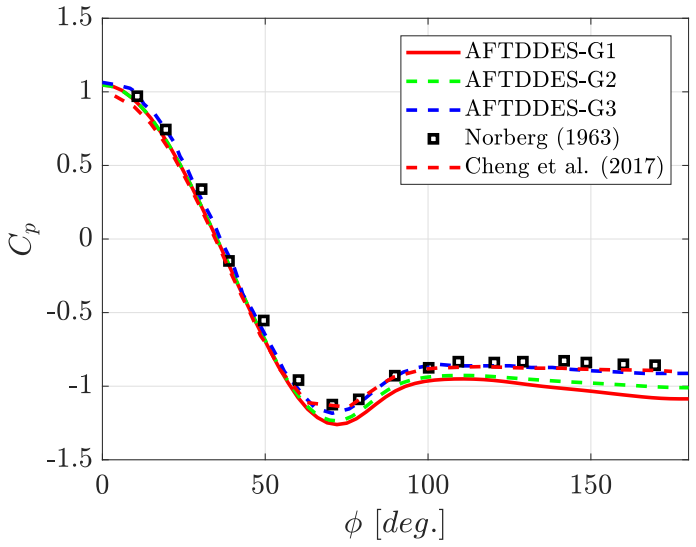

(a) C_p

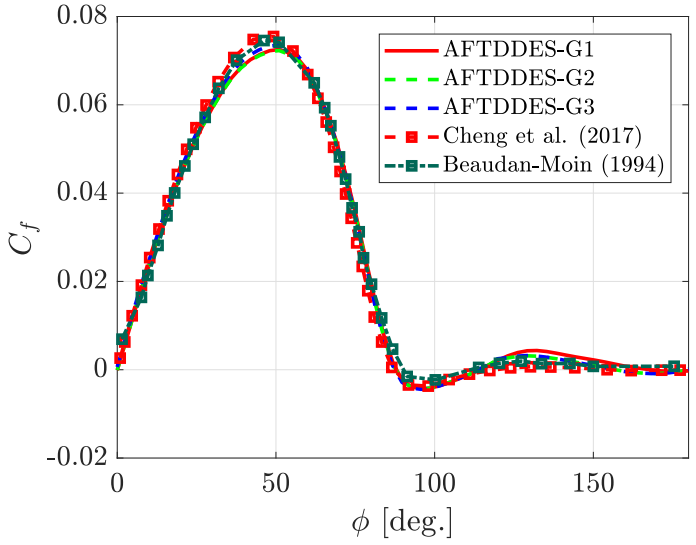

(b) C_f

FIGURE 6.8: (a) C_p and (b) C_f distribution for AFTDDES-G1, AFTDDES-G2 and AFTDDES-G3 transition models for validation case at $Re_D = 3900$.

predictions using three-dimensional AFT-DDES simulations show improvements compared to two-dimensional transitional AFT and AFT-RSM at this Reynolds number. Thus, reinforcing the idea that the correct prediction of the shear layer is pivotal for this low Reynolds number and throughout the sub-critical regime.

B: Wake velocity

Figure 6.9 shows predictions of centerline velocity profiles compared with reference data. The mesh AFTDDES-G1 produces a shortened $L_r/D = 1.0$, as discussed by Lysenko et al. (2012) and D'Alessandro et al. (2016). When increasing the spanwise resolution to

60 in the case of AFTDDES-G2, it is shown how the $L_r/D = 1.1$ is stretched compared to AFTDDES-G1. With AFTDDES-G3, the recirculating length is stretched down to $L_r/D = 1.43$. This behaviour is consistent with Lysenko et al. (2012) and D'Alessandro et al. (2016) as discussed earlier in the validation section of transitional URANS models.

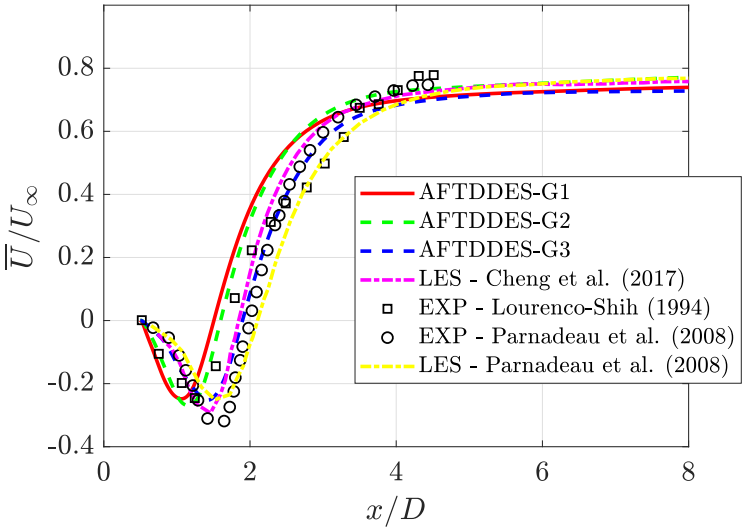

FIGURE 6.9: Mean normalized streamwise velocity $\overline{U}/U_\infty$ at centerline downstream of the cylinder surface.

Experimental data by Lourenco and Shih (1993) and Parnaudeau et al. (2008), and LES by Parnaudeau et al. (2008) and Cheng et al. (2017) are also shown in Figure 6.9. Predictions by AFTDDES-G1 and AFTDDES-G2 show a better agreement compared to Lourenco and Shih (1993). The insufficient spanwise resolution in AFTDDES-G1 reduces the L_r/D by roughly 9% and shows $U_{min} = -0.2482$ which is similar to Lourenco and Shih (1993). Improving the spanwise resolution for case AFTDDES-G2 stretches the L_r/D close to the value of $L_r/D = 1.1$ given by Lourenco and Shih (1993). The case AFTDDES-G3 shows an agreement with Cheng et al. (2017), while still producing a similar result to Parnaudeau et al. (2008) experimental $L_r/D = 1.56$ and LES predictions $L_r/D = 1.61$, with an $L_r/D = 1.43$. The minimum velocity for G3 is still underpredicted by roughly 25% to experiment and 1% to LES by Parnaudeau et al. (2008).

Similarly, the mean centerline velocity predictions from AFTDDES-G1 and AFTDDES-G2 follow the Lourenco and Shih (1993) behaviour, resembling a V-shape profile in the near wake, due to the insufficient resolution of the mesh. This is consistent with Lysenko et al. (2012) and D'Alessandro et al. (2016), as a short recirculating length resembles a V-shape profile as they reported. On the other hand, AFTDDES-G3 predicts a U-shape profile in the near wake location, $x/D = 1.06$, due to the stretched L_r/D compared to the other predictions. AFTDDES-G1, G2 retain the V-shape as we move further away from the cylinder surface, while AFTDDES-G3 develops into a V-shape profile, at the end of the formation length.

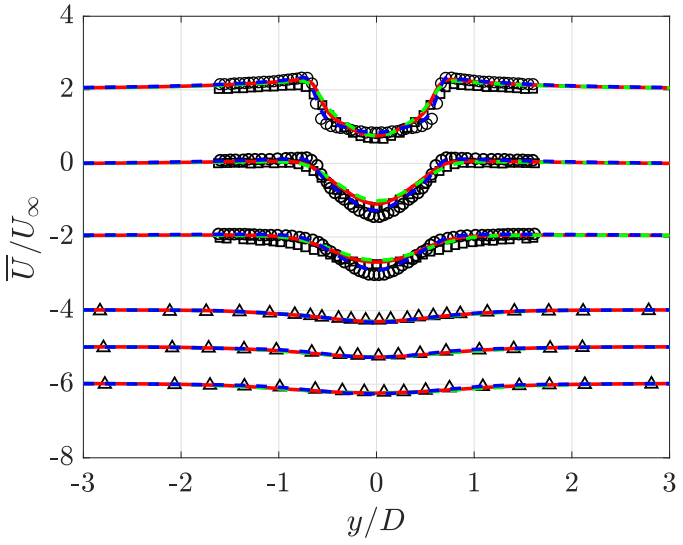

(a) $\overline{U}$

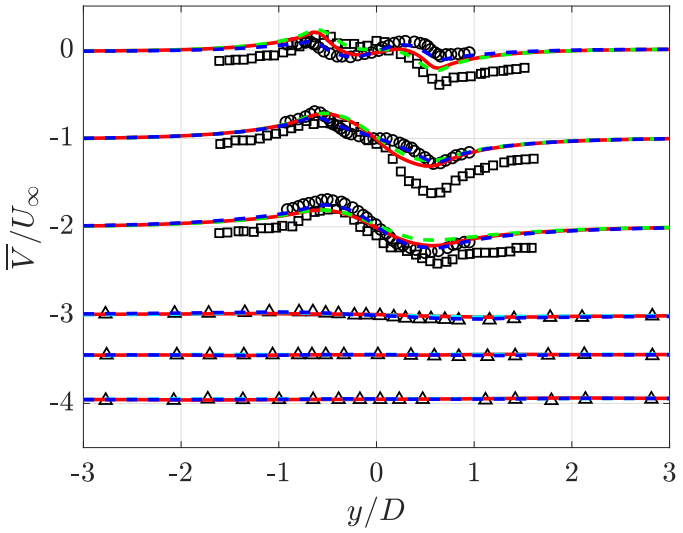

(b) $\overline{V}$

FIGURE 6.10: Normalized (a) $\overline{U}/U_\infty$ distribution and (b) $\overline{V}/U_\infty$ distribution for AFTDDES-G1, G2 and G3, transition models (see Figure 6.9 for legend) and experimental data by (○) Parnaudeau et al. (2008), (□) Lourenco and Shih (1993) and (△) Ong and Wallace (1996) .

AFTDDES-G1 and G2 show a maximum underprediction compared to Lourenco and Shih (1993) of approximately 14% in the near wake, that error diminishes downstream the wake down to approximately 3%. AFTDDES-G3 as described above, is consistent with Parnaudeau et al. (2008) measurements, underpredicting the defect of velocity by a maximum of 11% at $x/D = 1.56$ and diminishing to values of roughly 3% in the far wake.

The antisymmetric behaviour is shown for $\overline{V}$ with predictions AFTDDES-G1, G2 and

G3. The tendencies are still the same, G1 and G2 follow Lourenco and Shih (1993), while G3 agrees with Parnaudeau et al. (2008) measurements, at the two initial positions $x/D = 1.06$ and $x/D = 1.54$. For $x/D = 4$ both measurements show a similar tendency although Lourenco and Shih (1993) profile is asymmetric. Further away, the same behaviour as Ong and Wallace (1996) experimental data is predicted.

C: Turbulence intensities

Figure 6.11 shows the variance of the streamwise velocity fluctuation along the centerline downstream of the circular cylinder. The shorter L_r/D predicted by AFTDDES-G1 and G2 is consistent with the maximum peak of $\overline{u'u'}$. The longer L_r/D predicted by AFTDDES-G3 compared to G1 and G2, is consistent with the displaced peak of $\overline{u'u'}$ shown in Figure 6.11. Maximum value of $\overline{u'u'} = 0.1188$ for AFTDDES-G3, while reduced peak is predicted by AFTDDES-G1 and AFTDDES-G2, $\overline{u'u'} = 0.11,\ 0.1138$ respectively.

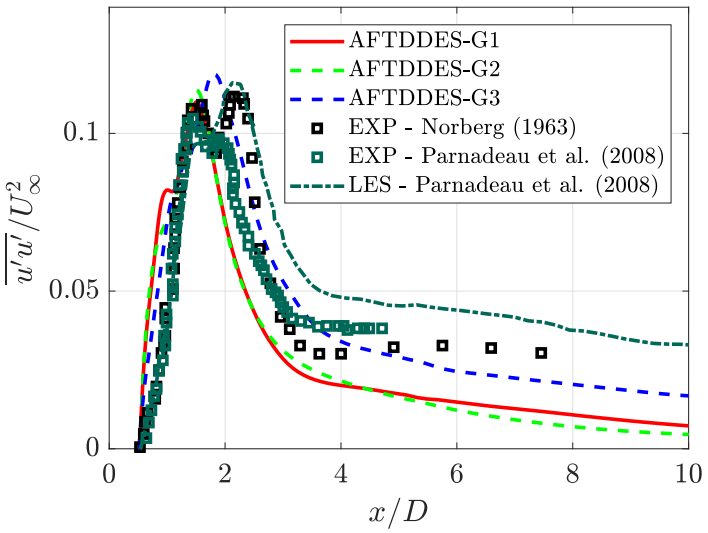

FIGURE 6.11: Mean-variance of streamwise velocity fluctuations $\overline{u'u'}/U_\infty^2$ at centerline downstream of the cylinder surface.

Here, AFTDDES-G3 shows better agreement to experimental data by Norberg (1994) ($\overline{u'u'}_{max} = 0.1117$) and LES predictions Parnaudeau et al. (2008) ($\overline{u'u'}_{max} = 0.116$), with a similar decay after the formation length. On the other hand, AFTDDES-G1 and G2 show the best agreement with measurements produced by Parnaudeau et al. (2008). Nonetheless, an explanation regarding the differences observed between measurements and LES by Parnaudeau et al. (2008) is not discussed in the publication, it might be attributed to experimental errors, as there is a mismatch between the peak and the L_r/D provided by their measurements. Furthermore, the L_r/D given in the LES by Parnaudeau et al. (2008) is overpredicted when compared to the experiment as given in Table 6.2.

Predictions with AFTDDESG1, G2 and G3 capture the two dominant peaks regarding the shedding process as shown in Figure 6.12(a). However, the AFTDDESG1, and G2, due to the lack of resolution and the initial short L_r/D estimation, show two thick peaks due to V-shape contribution from the mean velocity profile. The U-shape mean velocity profile predicted by AFTDDES-G3, is translated into two separated peaks, with a quiet flow field in between. As the flow develops into a V-shape profile as shown prior, the bulky peaks are predicted. Further downstream, close to the recirculating length, the flow at the centerline becomes agitated due to the end of the formation length. For $x/D \leq 4$ the agreement is good between AFTDDES-G1, G2 and G3.

As for the wake velocity analysis, AFTDDES-G3 shows a better agreement with Parnaudeau et al. (2008), while AFTDDES-G1 and AFTDDES-G2 show a better agreement with Lourenco and Shih (1993) measurements. In fact, the agreement by AFTDDES-G3 is really good that the maximum error in the defect of velocity estimation can be found at $x/D = 2.0$, and it is roughly 8%. Furthermore, the position of the peaks is coincident with the current prediction and experimental data. The refinement of AFTDDES-G2 improves the predictions compared to G1, as the defect of velocity falls closer to Lourenco and Shih (1993) measurements of approximately a maximum of 3% in the three closest positions.

The peak at the centerline resembled by transitional URANS models is also predicted by AFTDDES estimations of $\overline{u'u'}$ as shown in Figure 6.12(b). The AFTDDES-G2 shows improvements over AFTDDES-G1 of even a 10%, at $x/D = 1.54$ and $x/D = 2$. Further downstream than $x/D = 4\%$, the peak at the centerline diminishes its intensity with differences in predictions for G1, G2 and G3 of a 5% maximum $y/D = 0$.

AFTDDES-G1 and G2 show a closer behaviour to Lourenco and Shih (1993), which is consistent with all the parameters analysed prior to this point. On the other hand, AFTDDES-G3 agrees well with the behaviour of Parnaudeau et al. (2008) in the near wake region. The maximum difference to Parnaudeau et al. (2008) by AFTDDES-G3 is approximately 9% at $x/D = 1.06$, diminishing to 3% further downstream the wake. The maximum overprediction of the peak value for $\overline{v'v'}$ compared to Lourenco and Shih (1993) by AFTDDES-G1 and G2, is approximately 15% and 21%, respectively. The error diminishes as the flow field moves downstream, with a minimum of 3% in the far-wake region ($x/D \geq 4$) compared to experimental measurements by Ong and Wallace (1996).

6.2.3 Summary

From the sensitivity analysis, we have observed that increasing angular resolution below 2 degrees does not provide any benefit when using AFT and AFT-RSM. Similar effects are observed when analysing the wake velocity and turbulence intensities, and were due

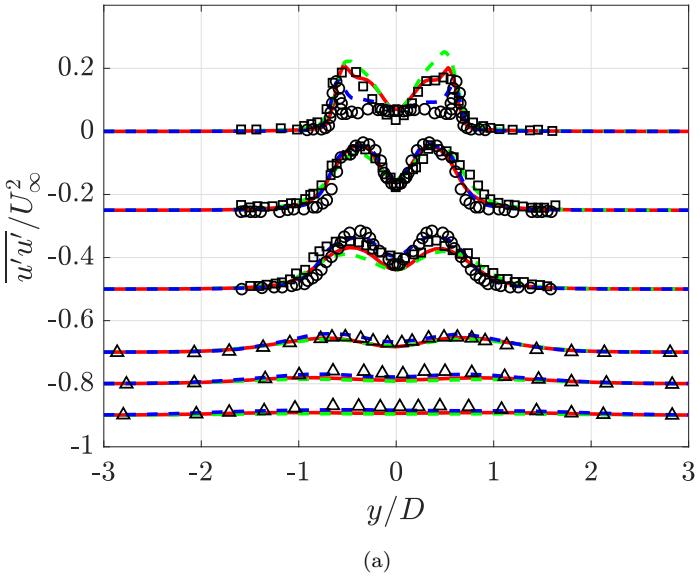

(a)

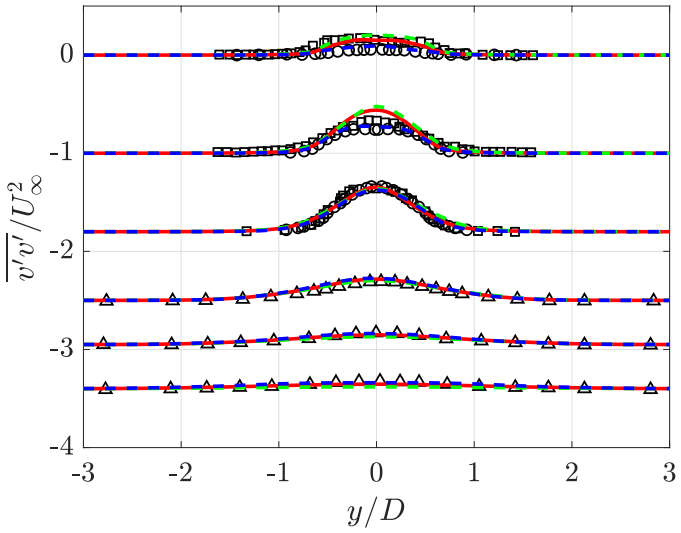

(b)

FIGURE 6.12: Normalized (a) $\overline{u'u'}/U_\infty^2$ distribution and (b) $\overline{v'v'}/U_\infty^2$ distribution for AFTDDES-G1, G2 and G3 transition models (see Figure 6.9 for legend) and experimental data by (○) Parnaudeau et al. (2008), (□) Lourenco and Shih (1993) and (△) Ong and Wallace (1996) .

to the two-dimensional simulation and the subsequent shortened recirculating length. Predictions are consistently similar to Lourenco and Shih (1993), which is expected as discussed in prior paragraphs, and also studied in literature by Lysenko et al. (2012), Beaudan and Moin (1994) and Kravchenko and Moin (2000). Downstream at $x/D = 4$, in the far-wake, the agreement falls by approximately 5% compared to the experimental data by Ong and Wallace (1996).

On the other hand, the increased resolution given by G2 and G3 when validating AFT-DDES makes a difference compared to the coarser mesh G1, especially in the wake description. The lack of resolution by AFTDDES-G1 produces a sharp drop in C_p and a delayed laminar separation. However, this effect is not relevant to the most refined case, AFTDDES-G3 when analysing C_p or C_f over the cylinder surface.

The improvement is evident in the near-wake to the cylinder surface. The lack of resolution in G1 and G2 produces a V-shape. As a consequence, all predictions by AFTDDES-G1 and G2 follow the tendency of measurements by Lourenco and Shih (1993) measurements. With a common resolution used in literature by many authors for DDES and LES, such as D'Alessandro et al. (2016) or Cheng et al. (2017) among others, predictions using AFTDDES-G3 fall close to Parnaudeau et al. (2008) experimental data and LES by Cheng et al. (2017). Furthermore, the boundary layer predicted here is laminar until separation, as a difference to standard turbulent DDES, as shown and discussed in the following Chapter 7.

Hence, the grid configuration of AFT-G2 and AFT-RSM-G2 is going to be used as the baseline for two-dimensional simulations. Even though differences are not significant to AFT-G1 and AFT-RSM-G1, we want to keep consistency with the AFTDDES-G3 grid configuration. Evidently, the grid configuration given in AFTDDES-G3 is used as the baseline mesh for three-dimensional analyses because of its agreement with well-established experimental data by Parnaudeau et al. (2008) and also to LES in literature, than AFTDDES-G1 and AFTDDES-G2.

As demonstrated the results obtained from 2D simulations differ from 3D runs. The first reason is the inability of the transitional model using RANS in the 2D simulations to predict the shear-layer transition that occurs at this Reynolds number, as a difference to the following analyses, where the transition occurs for an attached boundary layer over the cylinder surface, leading to improved predictions in such conditions. Conversely, the 3D simulation with the use of the hybrid AFT-DDES activates the LES behaviour once the laminar boundary layer separates, which predicts smaller turbulent scales interaction and therefore the shear-layer transition prediction is enhanced compared to 2D simulations.

TABLE 6.2: Mean flow field characteristics at $Re_D = 3900$ for the validation.

Case	$-U_{min}/U_\infty$	$-C_{p,min}$	$-C_{p,b}$	L_r/D [1]	L_f/D [2]	$\overline{u'u'}/U_\infty^2$	$\phi_{l,s}$ [deg.]
AFT-G1	0.6177	1.68	1.91	0.18	0.8035	0.1025	99
AFT-G2	0.6175	1.68	1.91	0.18	0.8035	0.1025	99
AFT-RSM-G1	0.6766	1.65	1.745	0.3	0.8925	0.1139	97
AFT-RSM-G2	0.6756	1.65	1.745	0.3	0.8925	0.1139	97
AFTDDES-G1	0.2482	1.261	1.086	1	1.498	0.11	88
AFTDDES-G2	0.2694	1.235	1.01	1.1	1.5	0.1138	87.5
AFTDDES-G3	0.2533	1.184	0.9129	1.43	1.804	0.1188	87
Literature Data							
Exp-Parnadeau et al. (2008)	0.3187	-	-	1.56	1.445	0.1047	-
LES-Parnadeau et al. (2008)	0.251	-	-	1.61	2.124	0.116	-
Cheng et al. (2017)		1.143	0.8996	1.34	-	-	86
Lourencho-Shih (1993)	0.2457			1.19	-	-	-
Norberg (1963)	-	1.125	0.8571	-	2.152	0.1117	-
Beaudan-Moin (1994)	-	-	-	-	-	-	90

[1] L_r/D is defined as the distance from the cylinder rear end to the saddle point formed at the wake.

[2] L_f/D is defined as the distance between the cylinder centroid and the peak of the squared streamwise velocity.

Chapter 7

Performance of AFT models at different Reynolds number regimes

This chapter studies the performance of the transitional AFT and AFT-RSM models for two-dimensional simulations and the AFT-DDES for three-dimensional scenarios. The analysis is performed throughout sub-critical, critical, and super-critical regimes for flow past a circular cylinder.

Chapter 5 has demonstrated the superior performance given by transitional methods to fully-turbulent approaches regarding the estimation of recirculating length and the appearance of separation bubbles within the transitional regime for backward-facing step flow, where the pressure gradient and main separation point are fixed.

The main objective is to demonstrate the superior performance of URANS transitional AFT and AFT-RSM against fully turbulent approaches from a skin-friction perspective, surface pressure coefficient, and wake analysis as a continuation of the simulations performed in Chapter 6 at $Re_D = 3900$, where the transitional AFT and AFT-RSM have demonstrated the capability of reproducing the laminar boundary layer at the upstream face of the cylinder. Even though the initial predictions in the wake are not good as shown in Chapter 6 , these models are tested at higher Reynolds numbers because of the transition occurring in an attached boundary layer, rather than in a separated one, which has shown to be not feasible for the models to predict correctly.

In this Chapter, the study of the flow at sub-critical, critical and super-critical regimes is presented, at $Re_D = 1.5 - 3.5 - 8.5 \times 10^5$ respectively. The AFT and AFT-RSM are tested at a higher Reynolds number than the Reynolds numbers used in Chapter 6 to demonstrate their capabilities in predicting transition in attached boundary layers as

a difference to transition in the shear-layers as already shown. Predictions with AFT-DDES are presented to demonstrate the capability to substitute turbulent RANS/DDES approaches since the laminar prediction of the boundary layer plays an important role throughout the sub-critical, critical and super-critical stages. To finalise the analysis, an overall perspective of the improvement when using transitional methods to fully-turbulent approaches is given for the Reynolds number effect.

Furthermore, unless stated otherwise, when referring to terms such as $\overline{U}$, $\overline{V}$, Reynolds stress term, variance of cross-stream velocity fluctuations and variance of streamwise velocity fluctuations, it denotes the normalized value either by U_∞ or U_∞^2 for the Reynolds stress and variance terms.

7.1 Sub-critical - $Re_D = 1.5 \times 10^5$

In this section, predictions at a sub-critical Reynolds number of $Re = 1.5 \times 10^5$ are discussed in this Chapter. The sub-critical regime is characterised by a laminar separation over the cylinder surface. Predictions using transitional AFT and AFT-RSM models are compared to AFT-DDES, as well as other transitional methods such as $\gamma - Re_\theta$ and γ models of Langtry and Menter (2009) and Menter et al. (2015) respectively, LES by Kim (2006) and measurements by Cantwell and Coles (1983) and Achenbach (1968). Mean flow characteristics that are discussed in the following sections are given in Table 7.2.

7.1.1 Mesh and computational setup

The grid characteristic used for this Reynolds number is given in Table 7.1. Note the mesh used for the URANS 2D cases are the same in the plane $x - y$. This specific grid is refined by a factor of $\sqrt{2}$ in the radial and angular direction to the mesh utilised for the validation case at $Re_D = 3900$. The number of points in the angular direction is between the resolution utilised by DDES grids by Liu et al. (2019) and higher resolution due to the pure LES simulations by Rodríguez et al. (2015) and Cheng et al. (2017). In the radial direction the number of nodes is similar to sub-critical meshes by Cheng et al. (2017), as well as the resolution in the spanwise length with $N_z = 96$ planes, resulting in a resolution of $\Delta z \approx 1.5 \times 10^{-2}$ m. The spanwise length is $L_z = 3D$, as discussed by Cheng et al. (2017) for the full sub-critical regime. The y^+ values are always kept approximately $y^+ \approx 1$ as learnt in Chapter 4.

7.1.2 Prediction of the flow-field

A: Surface pressure (C_p) and skin friction (C_f)

TABLE 7.1: Numerical resolutions and schemes for grid at different Reynolds numbers

Case	Grid $N_r \times N_\theta \times N_z$	L_z	$\tilde{\Delta}t$	Scheme 2D	Scheme 3D	$\Delta\theta$ [deg.]	Δz [m]
1.5×10^5	$256 \times 256 \times 96$	$3D$	0.05	UW	CD	1.4	1.5×10^{-2}
3.5×10^5	$320 \times 320 \times 128$	D	0.06	UW	CD	1.125	3.9×10^{-3}
6.5×10^5	450×450	–	0.05	UW	-	0.8	–
8.5×10^5	$450 \times 450 \times 192$	D	0.05	UW	CD	0.8	2.6×10^{-3}

Figure 7.1(a) shows predictions of C_p using the AFT, AFT-RSM and AFT-DDES along with other transitional models compared with literature data such as Cantwell and Coles (1983) and Kim (2006). The pressure reduction over the upstream surface is similar for the URANS transitional models but the minimum pressure coefficient is different, as well as the angular position where the minimum is achieved. AFT predicts a $-C_{p,min} = 1.826$ and AFT-RSM predicts a $-C_{p,min} = 1.624$, which is about 11% smaller. On the other hand, the minimum position is shifted downstream for the AFT approximately by 5° compared to the AFT-RSM minimum position at $\phi_{C_{p,min}} = 75°$. This difference is believed to be influenced by the downstream flow. For the AFT the streamlines are rather curved at about 90° which is a consequence of a reduced adverse pressure gradient, while for the AFT-RSM, the streamlines are more aligned to the freestream flow, thus observing a larger expansion, caused by a greater adverse pressure gradient that would lead to an earlier separation than AFT. This is consistent with observations in Figure 7.1(b), where the C_f predicted by AFT and AFT-RSM shows an earlier separation for AFT-RSM than AFT. The 3D prediction using AFT-DDES shows a reduced $-C_{p,min} = 1.39$ at about $\phi = 72°$, thus leading to an earlier separation as it is confirmed in Figure 7.1(b) by the C_f.

Over the plateau region of C_p, approximately between $\phi = 120 - 150°$, differences are about 10%, while the AFT still produces this sharp decrease in C_p from $\phi = 160°$. This sharp decrease is consistent with the shortened recirculation region that will be discussed in the following section, and with the observations at $Re_D = 3900$. Consequently, the AFT predicts a higher back pressure $-C_{p,b} = 1.29$ as vortical structures are brought closer to the cylinder surface, than AFT-RSM $-C_{p,b} = 0.911$. Hence, the wake prediction using AFT-DDES should be better than AFT. In fact, a longer recirculating length is expected, as the plateau region is predicted after the flow separation as expected. Since the AFT-RSM and AFT-DDES are similar over this plateau region, differences to AFT are approximately 10%.

When compared to measurements by Cantwell and Coles (1983), the AFT-DDES shows a better agreement than to LES predictions by Kim (2006). This has also been shown by Liu et al. (2019) DDES predictions. The overprediction of the $-C_{p,min}$ by AFT-DDES is roughly 11% to Cantwell and Coles (1983), while Kim (2006) predicts a value of $-C_{p,min} = 1.668$. Furthermore, the minimum pressure by Kim (2006) is located further downstream, which leads to an even more delayed separation point in their

TABLE 7.2: Mean flow field characteristics at $Re_D = 1.5 \times 10^5$ for transitional URANS and literature data.

Case	$-U_{min}/U_\infty$	$-C_{p,min}$	$-C_{p,b}$	L_r/D	$\pm\overline{u'v'}/U_\infty^2$	$\phi_{l,s}$ [deg.]
AFT	0.1264	1.826	1.295	0.35	0.1629	91
AFT-RSM	0.3245	1.624	0.911	0.73	0.083	87
AFT-DDES	0.1883	1.39	0.91	0.6	0.112	84
γ	-	1.843	2.124	-	0.1921	95
$\gamma - Re_\theta$	0.08982	1.798	1.634	0.3	0.214	89
SST	0.2275	2.091	1.103	0.49	0.1489	98
Literature Data						
Achenbach (1968)	-	-	-	-	-	78
Kim (2006)	-	1.668	1.343	-	-	-
EXP Cantwell Coles	-	1.236	1.249	0.48	-	-
LES Breuer	0.181	-	-	0.58	0.111	-

predictions. This is what happens to AFT and AFT-RSM, as both predictions are in better agreement with Kim (2006). AFT-RSM produces a similar prediction but AFT shows an even further delay in the minimum pressure location by about $\Delta\phi = 8°$ and a minimum value of $-C_{p,min} = 1.826$. With the drastic decrease due to the shortened recirculating length, the AFT predicts a similar $-C_{p,b}$ than the literature data given in Figure 7.1(a). On the other hand, the AFT-DDES and AFT-RSM underpredict back pressure values to experimental and LES data. Nonetheless, AFT-DDES predictions demonstrate an improvement to URANS methods and to fully turbulent models such as $k - \omega$ SST as can be observed due to its fully turbulent assumption.

Skin friction C_f over the upstream face for all model show similarities up to approximately $\phi = 55°$, where maximum differences are about 15.5% between AFT-DDES and SST fully turbulence models. After the maximum C_f peak, the reduction of skin friction presents differences that are similar for transitional models but overpredicted by the SST as shown in Figure 7.1(b). Beyond the maximum peak, the reduction region shows similar trends with maximum differences observed when the C_f crosses the zero value, indicating the separation point.

Predicted results of C_f given in Figure 7.1(b) show the delayed laminar separation ($\phi_{l,s}$) by the AFT at $\phi_{l,s} = 91$, while AFT-RSM moves the laminar separation upstream to $\phi_{l,s} = 87$ and finally the AFT-DDES to $\phi_{l,s} = 84$. Note that all three transitional models are capable of predicting laminar flow, as a difference to standard DDES approaches or wall-modelled LES, while requiring URANS grid characteristics rather than wall-resolved LES requirements. After the separation, the AFT-RSM does not show any reattachment of the flow, while AFT and AFT-DDES do predict one. The AFT shows a reattachment from $\phi = 150° - 180°$. On the other hand, AFT-DDES predicts a small reattachment between $\phi = 130 - 150$. This reattachment has been also observed in Travin et al. (1999) predictions between $\phi = 115 - 140°$.

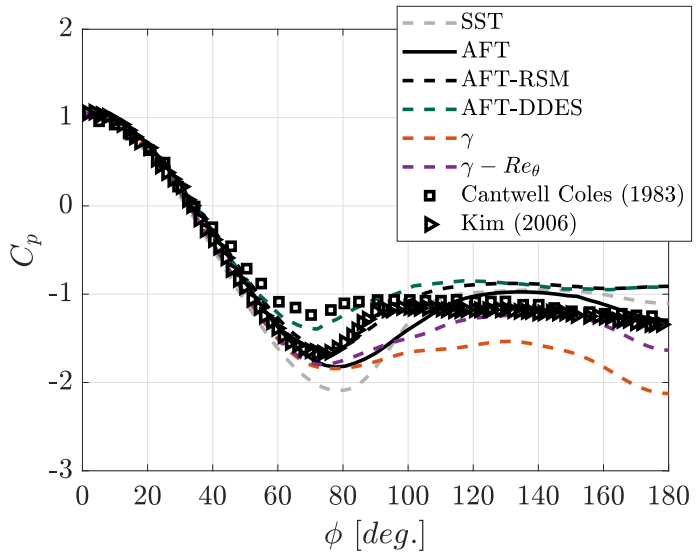

(a)

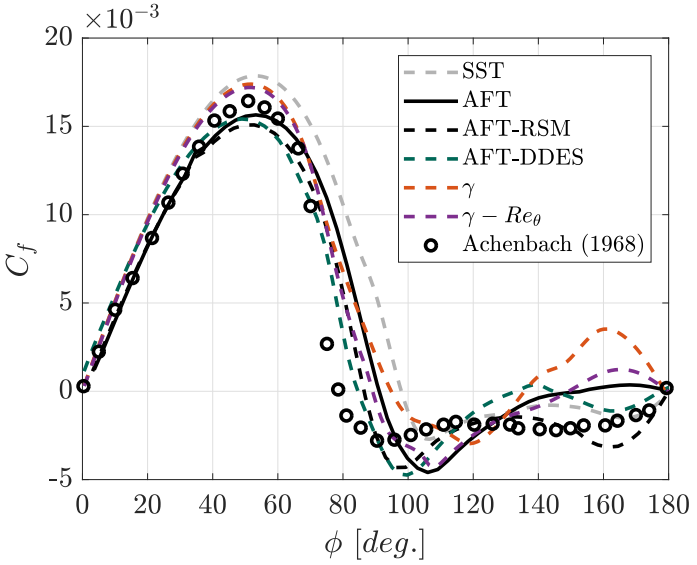

(b)

FIGURE 7.1: (a) C_p distribution with Achenbach (1968) experimental data at $Re_D = 1 \times 10^5$and (b) C_f distribution with experimental data by Cantwell and Coles (1983) and Kim (2006) along current predictions with SST, AFT, AFT-RSM, AFT-DDES, Langtry and Menter (2009) and Menter et al. (2015) model at $Re_D = 1.5 \times 10^5$.

Experimental data by Achenbach (1968) are also given in Figure 7.1(b), along with Langtry and Menter (2009) and Menter et al. (2015) transitional predictions. Transitional AFT, AFT-RSM and AFT-DDES underpredict the C_f at $\phi = 50°$ by about $6 - 10\%$. This is consistent with DDES results by Liu et al. (2019). The closest prediction of the laminar separation point is predicted by AFT-DDES, with a difference of about $\Delta\phi = 4°$. AFT-RSM and AFT delay the laminar separation to Achenbach (1968) by $\Delta\phi = 7°$ and $\Delta\phi = 11°$, respectively. When compared to fully-turbulent SST, one can see how the separation is delayed to about $\phi_{t,s} = 98°$, and the separation is

turbulent, as the subscript "t" indicates.

B: Wake velocity and mean flow field

Figure 7.2 shows the mean streamwise velocity at the centerline downstream of the wake for AFT, AFT-RSM and AFT-DDES. Overall except for the γ model, a recirculation length can be distinguished. AFT and AFT-RSM follow overall a similar tendency to experimental and LES data by Cantwell and Coles (1983) and Breuer (2000), while Menter models predict a sharp velocity recovery after crossing the zero velocity axis. The fully turbulent SST model also presents such sharp velocity recovery to freestream velocity. The transitional DDES shows the best agreement to the overall tendency of the velocity at the centerline as shown in Figure 7.2.

The shortened prediction of $L_r/D = 0.35$ by AFT is consistent with prior analysis at $Re_D = 3900$. As can be seen in Figure 7.2, AFT-DDES produces the intermediate of the values for the recirculating lengths $L_r/D = 0.6$ of the three models, and AFT-RSM stretches its value to $L_r/D = 0.73$, which is consistent with the discussion of the C_p behaviour in the section above. Furthermore, the wavy behaviour observed using AFT and AFT-RSM is not predicted anymore downstream the surface of the cylinder as the velocity is gradually recovered. The overprediction of L_r/D by AFT-RSM is also accompanied by an overprediction of U_{min}, with a value of about $U_{min} = -0.37$. AFT-DDES predicts a value of $U_{min} = -0.1883$ and AFT a reduced value of $U_{min} = -0.1264$.

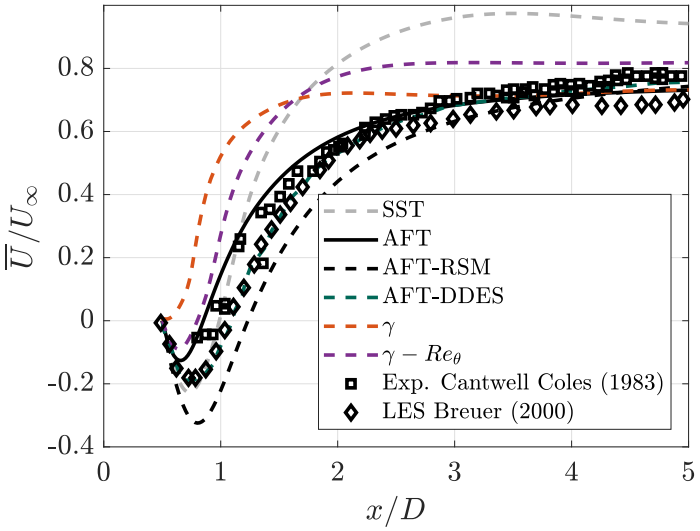

FIGURE 7.2: Mean normalized streamwise velocity $\overline{U}/U_\infty$ at centerline downstream the cylinder surface.

Data by Cantwell and Coles (1983) and LES by Breuer (2000) are used for comparison in here. Furthermore, the 2D fully turbulent SST prediction shows to produce a similar recirculating length $L_r/D = 0.49$ than Cantwell and Coles (1983) ($L_r/D = 0.5$), but its velocity recovery is faster than literature data for $x/D > 1$. It can be seen in Figure 7.2

how AFT, AFT-RSM and AFT-DDES perform better than SST for the wake velocity prediction, as the overall behaviour follows the tendency of Cantwell and Coles (1983) and Breuer (2000) data. AFT-DDES shows the best agreement to LES by Breuer (2000) with $U_{min} = -0.1883$ and $L_r/D = 0.6$. Far away from the cylinder surface the velocity recovery shows a wavy behaviour $x/D > 4$ for Breuer (2000), which might be related to an insufficient grid resolution, as other estimations in the literature show a gradual recovery such as Cantwell and Coles (1983) measurements, and DDES by Liu et al. (2019). AFT instead, underpredicts $-U_{min}$ by 30.1% to Breuer (2000), as Cantwell and Coles (1983) do not provide measurements for the minimum velocity. On the other hand, AFT-RSM overpredicts by 79% to Breuer (2000). Regarding the L_r/D, the estimation by AFT is underpredicted by about 30% and 41%, and AFT-RSM overpredicts L_r/D to Cantwell and Coles (1983) and Breuer (2000) by 52% and 26%, respectively.

From just a simple observation of Langtry and Menter (2009) and Menter et al. (2015), it can be observed how the performance of the AFT base model, (including AFT-RSM and AFT-DDES) is superior to these two models. The differences between Langtry and Menter (2009) to AFT are for $-U_{min}$ and L_r/D, roughly 28% and 15% respectively as given in Table 7.2, while the recovery velocity is completely different from expectations, as they show rapid velocity recovery.

C: Turbulence Intensities

Mean Reynolds stress, normalized by the freestream velocity, predictions for AFT, AFT-RSM and AFT-DDES are given in Figure 7.3 at $x/D = 1$, which is $0.5D$ away from the back of the cylinder. Overall it is shown in Figure 7.3 that the anti-symmetric behaviour is predicted by all transitional methods, including Menter models and SST, when compared to LES simulations reported by Breuer (2000).

It is shown in the figure, how the shortened recirculating length predicted by AFT is translated into the strength of the Reynolds stress peak, with an overprediction of almost 46% compared to A1 LES by Breuer (2000). Nonetheless, the location of the peaks is about $y/D = 0.29$. The peak position is displaced $\Delta(y/D) = 0.03$ by the AFT-RSM compared to AFT, although its maximum value is reduced to $\overline{u'v'}_{\max} = 0.083$, as the wake is stretched. AFT-DDES predicts a correct maximum value of the Reynolds stress ($\overline{u'v'}_{\max} = 0.112$) as well as the location of the peak $y/D = 0.4$. Here, one can see how the shortened recirculating length produces a smooth peak than AFT-RSM and AFT-DDES predictions, whose L_r/D is larger than AFT.

The peak of the Reynolds stress can give information about the distance from the centerline of the shedding location and its strength, thus it can give information about the wake too. As peaks fall closer to the centerline for AFT and AFT-RSM, it is possible to say that the wake is narrower than for AFT-DDES predictions. However, it is common to analyse the normalized $\overline{u'u'}$ or $\overline{v'v'}$ but data in the literature is not available.

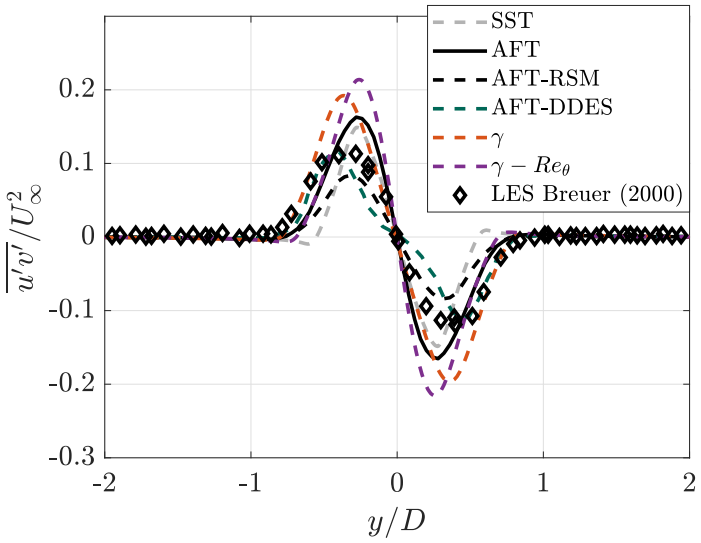

FIGURE 7.3: Mean normalized Reynolds stress term $\overline{u'v'}/U_\infty^2$ at $x/D = 1$ downstream the cylinder surface.

LES prediction by Breuer (2000) and DDES prediction by Liu et al. (2019) at a given Reynolds number is used for comparison to the current three transitional approaches. The agreement when using AFT-DDES to both LES and DDES is good. This is consistent with observations regarding the mean streamwise velocity variation along the centerline, in the section above. The capability of predicting turbulent structures has an impact on the estimations when compared to AFT and AFT-RSM. In addition, the performance shown by AFT-RSM is superior to SST, Langtry and Menter (2009), Menter et al. (2015) and AFT, where the error in the peak prediction is between $20 - 30\%$. Predictions by Langtry and Menter (2009) and Menter et al. (2015) show a large overprediction of the peak by about 73% and 93%, with the position of the peak being located at $y/D = 0.34$ and $y/D = 0.25$, instead of the expected $y/D = 0.4$ by Breuer (2000) and Liu et al. (2019). The overprediction of the peak value is consistent with the shortened L_r/D shown by these two models, as for AFT prediction.

Predictions for the variance of streamwise and cross-stream velocity fluctuations at three different positions $x/D = 1$, $x/D = 3$ and $x/D = 7$, are given in Figure 7.4 and Figure 7.5, respectively. As for the Reynolds stress description, a variety of behaviours can be observed from predictions, although the tendencies are generally sound in terms of the description of the two prominent peaks in the near-wake of $\overline{u'u'}$ and the main peak for $\overline{v'v'}$. These two different behaviours are consistent with those observed at $Re_D = 3900$.

As observed from the Reynolds stress predictions, differences between AFT and AFT-RSM are visible too. Although the trends are similar regarding the two peaks that are related to the shedding of the shear layers, the maximum peaks are around 45% different, with AFT maximum being $\overline{u'u'}_{\max} = 0.2$ and AFT-RSM being $\overline{u'u'}_{\max} = 0.11$.

Further away from the rear part of the cylinder the strength of the two peaks is reduced, reducing the differences as well.

The former behaviour is also observed for predictions of $\overline{v'v'}$ using AFT and AFT-RSM, where the maximum difference is found in the near-wake $x/D = 1$, and beyond that point, both models converge to an approximately similar solution. This is consistent with the behaviour observed at $Re_D = 3900$, where the difference between models diminishes as the analysis moves downstream the wake.

The differences observed in AFT-DDES predictions when compared to AFT and AFT-RSM are evident, however not as pronounced as the ones we observed with Menter models, the γ-model and the $\gamma - Re_\theta$ model that generally overpredicts the values for $\overline{u'u'}$ and $\overline{v'v'}$ as Figures 7.4-7.5 show.

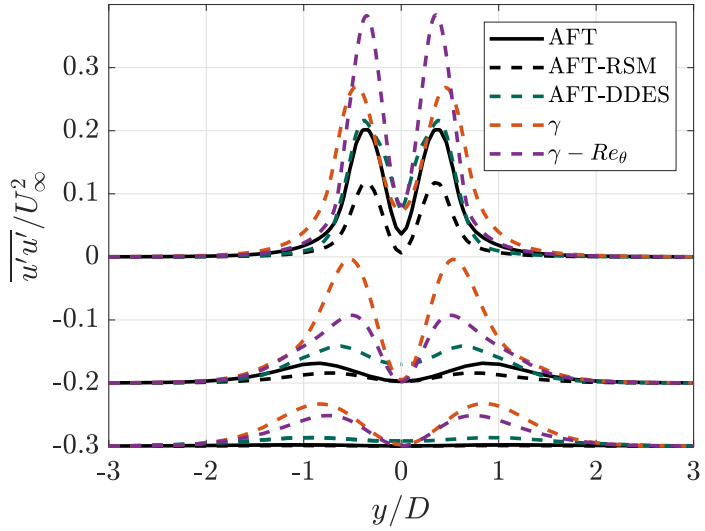

FIGURE 7.4: Mean normalized variance of streamwise velocity fluctuations $\overline{u'u'}/U_\infty^2$ at $x/D = 1, 3, 7$ downstream the cylinder surface.

Menter models show the two peaks of $\overline{u'u'}$ and the single peak for $\overline{v'v'}$. However, when compared to AFT, AFT-RSM and AFT-DDES (all AFT-based models) they overpredict the maximum values for both distributions. This is also consistent with predictions of Reynolds stress in Figure 7.3, where γ and $\gamma - Re_\theta$ overpredict the anti-symmetric peaks in the near-wake and beyond up to $x/D = 7$ predictions, as shown. Differences between the two Menter models diminish as the analysis moves downstream within the wake. Specifically, predictions of $\overline{u'u'}$ show maximum differences of 40%, while $\overline{v'v'}$ at $x/D = 1$ measures maximum differences of about 31%.

D: Instantaneous flow-field

In this Section D, a three-dimensional simulation using the URANS AFT base model is presented along the AFT-DDES case. The grid utilised for the three-dimensional AFT simulation is given in Table 7.1, with the same spanwise length. The main aim in

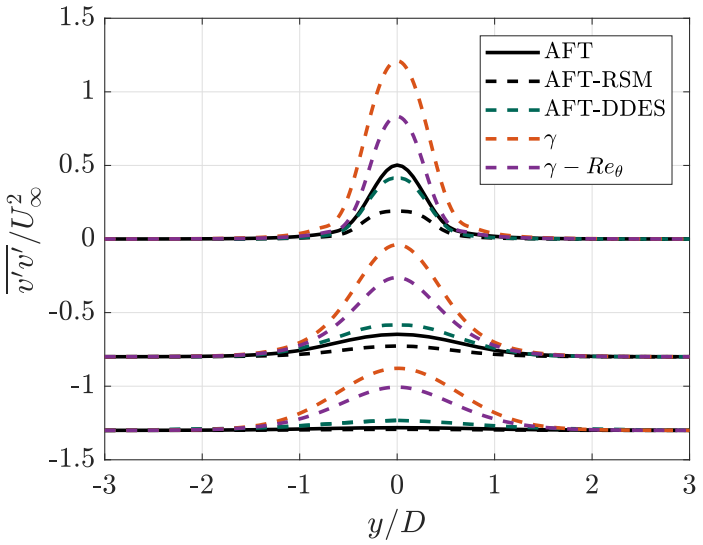

FIGURE 7.5: Mean normalized variance cross-stream velocity fluctuations $\overline{v'v'}/U_\infty^2$ at $x/D = 1, 3, 7$ downstream the cylinder surface.

showing these structures is to demonstrate the difference in the instantaneous flow-field structures predicted when averaging all the structures or modelling only the smallest scales. Figure 7.6 and Figure 7.7 represent the vortical structures with $Q = 200$ 1/s^2 for three-dimensional computations using AFT and AFT-DDES respectively.

From a visual perspective, the AFT structures are close to being approximately two-dimensional, from the vicinity of the cylinder surface to the furthest position downstream within the wake. On the other hand, the variety of structures resolved by the use of AFT-DDES are identified in Figure 7.7 compared to the AFT prediction in Figure 7.6. Specifically, the description of the shear-layer is superior to AFT, thus being able to capture its transition to turbulent and therefore producing a better estimation of the wake than pure transitional URANS methods.

As coherent structures are predicted by the AFT-DDES, AFT does not have the capability to provide any insight into the turbulent cascade. With the averaging of the Navier-Stokes equations, only the mean turbulent structure is predicted as shown in Figure 7.6. These observations, from a qualitative point of view, are consistent with prior analyses where AFT-DDES improves results obtained using AFT or AFT-DDES.

7.1.3 Summary

As analysed, we have shown simulations using the transitional AFT, AFT-RSM and AFT-DDES over circular cylinder flow at the sub-critical region. The base model AFT has a superior performance to fully turbulent approach SST and the γ and $\gamma - Re_\theta$ transitional approaches of Langtry and Menter (2009) and Menter et al. (2015).

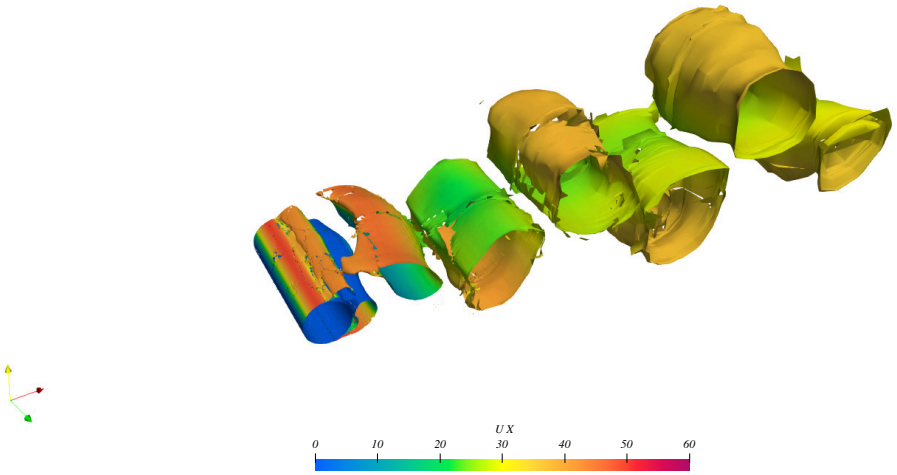

FIGURE 7.6: Q criterion iso-surface representation of value $Q = 200$ for 3D computation using AFT.

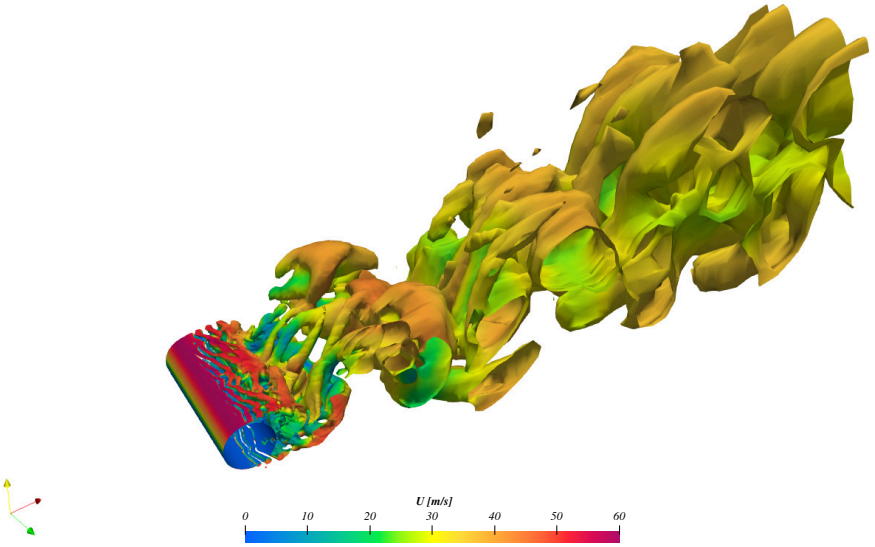

FIGURE 7.7: Q criterion iso-surface representation of value $Q = 200$ for 3D computation using AFT-DDES.

The capabilities of predicting a laminar boundary layer of the transitional turbulence models improve the laminar separation position for two-dimensional predictions over SST as shown in Figure 7.1(b). In fact, at this Reynolds number, AFT-RSM shows better predictions than AFT overall which is attributed to the largest eddy separation to the back of the cylinder surface. The three-dimensional AFT-DDES estimations show to be superior to two-dimensional URANS transitional models, not only from a surface perspective but evidently from a wake analysis perspective too. This is mainly due to the resolved large scales by the LES mode away from the wall, while retaining transitional capabilities in the wall. This is even more apparent in the sub-critical range as the

transition occurs over the separated free shear layer, where the transitional models are not fit for that specifically. Therefore, switching to LES mode in the far wall when using AFT-DDES helps to determine this and consequently, a correct prediction of the L_r/D is given. The instantaneous flow field for three-dimensional AFT and AFT-DDES shows the superior description of the vortical structures by the AFT-DDES approach to AFT, which is predicted to be essentially two-dimensional even with three-dimensional configuration.

Hence, we have demonstrated that AFT, AFT-RSM and AFT-DDES models show better results than existing predictions with Langtry and Menter (2009) and turbulent SST by Menter (1994) which is novel as it has not been demonstrated before for flow past circular cylinder. Furthermore, the improvements when using AFT-DDES are intrinsic to shear layer prediction and turbulent structures within the wake, which have an impact on the flow field topology affecting from the separation location to the recirculating length.

7.2 Critical - $Re_D = 3.5 \times 10^5$

This Reynolds number is chosen as it is characteristic of the asymmetric flow in the critical regime and simulations by Rodríguez et al. (2015) and Cheng et al. (2017) can be used for comparison. At this $Re_D = 3.5 \times 10^5$, it is common to observe under a low turbulence environment a single laminar separation bubble on one side, while the opposite side resembles sub-critical behaviour with laminar separation as discussed in Chapter 2.

This section discusses the results at $Re_D = 3.5 \times 10^5$ using the pressure and skin-friction coefficient over the cylinder surface, wake velocity, turbulence intensities and instantaneous flow field. In this region, wake measurements are not available in the literature regarding the wake velocity and turbulence intensities, therefore a novel insight is provided for the behaviour of AFT-based models along with SST and Menter transitional models. All the mean flow quantities are given in Table 7.3 for all transitional models and literature data used in the section.

7.2.1 Mesh and computation setup

With the increase of Reynolds number, the spanwise length is reduced to $L_z = D$ as detailed in Table 7.1. This is adopted as a consequence of the analyses by Cheng et al. (2017) and Rodríguez et al. (2015), where it is discussed that the domain can be reduced due to the presence of smaller turbulent eddies (with the increased Reynolds number) around the separation region than in sub-critical regime.

The radial direction is distributed with $N_r = 320$ points as the angular direction. The resolution is improved to DDES performed by Liu et al. (2019), with a resolution of

$\Delta\theta \approx 1.125°$. In the spanwise direction, the number of planes is $L_z = 128$ giving a resolution of the same order as Liu et al. (2019) and Rodríguez et al. (2015), and a reduced resolution compared to Cheng et al. (2017). Hence, these characteristics ensure a similar resolution in all directions to prior DDES simulations by Liu et al. (2019) in this regime.

7.2.2 Predictions of the flow-field

A: Surface pressure (C_p) and skin friction (C_f)

Results of C_p and C_f are shown in Figure 7.8(a) and Figure 7.8(b), respectively. As can be seen, the transitional predictions by AFT and AFT-RSM are similar overall, although differences are found in $-C_{p,min}$ and $-C_{p,b}$. In general, both show a laminar separation bubble with a reattachment region. Ultimately, turbulent separation is predicted by AFT and AFT-RSM after reattachment at approximately $94 - 93°$ respectively, resembling a super-critical-like regime on both sides of the cylinder without any sign of asymmetric flow. Prediction with AFT-DDES shows similar behaviour to full URANS methods, where the flow is symmetric too. Conversely, $\gamma - Re_\theta$ and γ resemble a sub-critical-like flow field without any laminar separation bubble, which is attributed to the transition correlations. This influences the nature of the separation which is laminar for Menter models while AFT and AFT-RSM models predict a turbulent separation after the small separation region predicted at approximately 90°.

The main differences between AFT and AFT-RSM are observed for C_p and also for C_f around 70°. The difference in $-C_{p,min}$ is observed, with AFT-RSM underestimating by 2% the value of AFT. These small differences are attributed to numerical differences, as C_f prediction shows in Figure 7.8(b). Further downstream, at about 90°, the C_p predicted by the URANS transitional models by AFT and AFT-RSM show a small disruption of the C_p, which is attributed to the appearance of a rather small laminar separation bubble. The following paragraphs give details about the dimensions of the laminar separation bubble when analysing the C_f profile. Pressure recovery to the back face of the cylinder is almost coincident for both models, but the values at 180° differ by approximately 15% which may be attributed to the position of the recirculation eddies. Pressure is lower further away from the cylinder and higher close to the cylinder as discussed in Chapter 6.

The C_p behaviour of $\gamma - Re_\theta$ and γ show similar behaviour to AFT and AFT-RSM, although the γ model underpredicts the $-C_{p,min}$ by 10%, as well as the $-C_{p,b}$ by 9%. Furthermore, another difference is that there is no evidence of a laminar separation bubble is observed from the C_p profile, as is confirmed by the C_f discussion later in this section. Thus, resembling a sub-critical-like behaviour within the critical regime. The AFT-based models show a closer prediction with the prediction of the laminar separation

bubble, in this case on both sides of the cylinder. Thus, the separation is fully laminar for Menter models while AFT-based models predict a turbulent separation which falls in better agreement to the physical behaviour discussed by Bearman (1969).

The AFT-DDES behaviour is similar to AFT as shown in Figure 7.8(a), for U_{min} and the pressure recovery to the $-C_{p,b}$. In this case, this behaviour is expected due to the use of the AFT model in the near-wall region with the hybridisation of the model. Although minimal changes can be observed especially on the skin friction prediction. Furthermore, the interaction between transition and separation is not expected because of the use of AFT in the RANS region. Consequently, a symmetric flow is predicted although improvements in the wake are expected because of the LES mode away from the wall.

LES simulations by Cheng et al. (2017) and Rodríguez et al. (2015), along with measurements by Bursnall and Loftin (1951) are also given in Figure 7.8(a) for comparison. Qualitatively, the main difference observed is the increment of $-C_{p,min}$ and the position of the minimum pressure that is displaced downstream, which leads to a delayed laminar separation compared to URANS transitional models, AFT and AFT-RSM. In fact, this is confirmed by the location for the three literature measurements regarding the $-C_{p,min}$ position, 83°, 85° and 85° to Rodríguez et al. (2015), Bursnall and Loftin (1951) and Cheng et al. (2017) respectively. Differences between LES simulations can be attributed to grid characteristics. Underprediction by AFT and AFT-RSM is about 11%, 18% and 15% to Rodríguez et al. (2015), Cheng et al. (2017) and Bursnall and Loftin (1951), plus 2% to prior percentages for AFT-RSM, respectively.

The behaviour of the AFT-DDES is similar over the cylinder surface to that predicted by the AFT model. Thus, the differences to LES data by Rodríguez et al. (2015) and Cheng et al. (2017) are about the same order, as to the experimental data reported by Bursnall and Loftin (1951), since predictions are practically similar, except for the $-C_{p,b}$. However, we see an improvement compared to pure DDES reported by Liu et al. (2019) on the $-C_{p,min}$ prediction. Although the separation point is approximately 10° upstream than Liu et al. (2019), which is consistent with sub-critical behaviour.

Regarding Menter models (γ and $\gamma - Re_\theta$ models), differences are similar to the AFT and AFT-RSM, except for the $-C_{p,min}$ using the γ model, as the reduction to literature data is about $9 - 10\%$ more than AFT predictions for the three cases respectively.

On the upstream face, the tendencies are generally in good agreement, although there are significant differences at about $\phi = 55°$, which coincides with the maximum value of C_f. Predictions using AFT and AFT-RSM do not show significant differences as results are almost coincident, however, an overprediction of about $6 - 7\%$ compared to $\gamma - Re_\theta$ and AFT-DDES respectively is observed. On the other hand, γ and SST predict a larger overprediction by 4% to AFT-based models and $\gamma - Re_\theta$ and AFT-DDES by 11%.

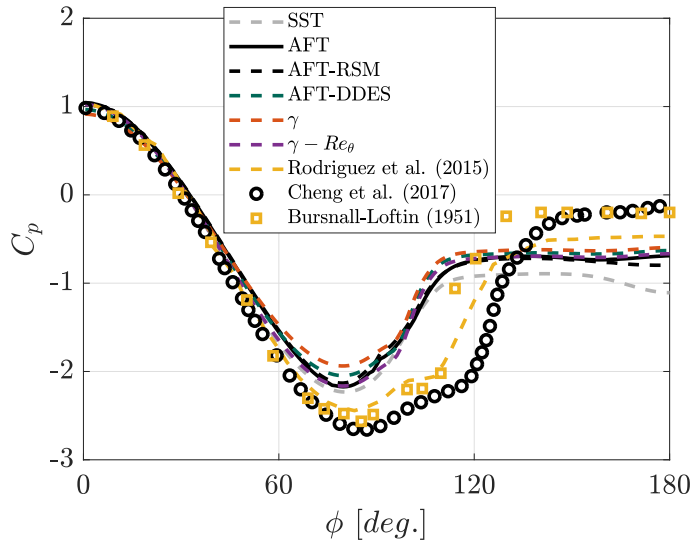

(a)

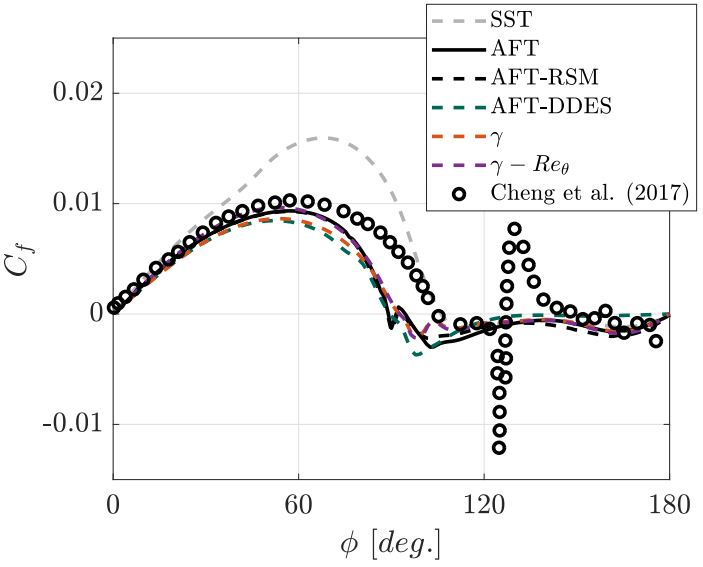

(b)

FIGURE 7.8: (a) C_p distribution with Bursnall and Loftin (1951) experimental data at $Re_D = 3.5 \times 10^5$ and LES by Cheng et al. (2017) and Rodríguez et al. (2015) and (b) C_f distribution with LES predictions by Cheng et al. (2017) at $Re_D = 3.5 \times 10^5$.

Beyond that point, differences can be identified by analysing the laminar separation position.

As C_f shows, AFT and AFT-RSM predict the laminar separation $\phi_{l,s}$ at about $\phi = 88.9°$ and $\phi = 88.6°$, respectively. This is consistent with the reduced $-C_{p,min}$ and the ever so slightly displacement of its location downstream compared to AFT-RSM, leading to a delayed separation. The length of the laminar separation bubble is about $\Delta\phi_b = 2°$. This bubble is rather small and the reattachment region is rather small too, roughly

2°, followed by the separation of the flow at about $\phi_{t,s} = 94.5°$ and 93.4° by AFT and AFT-RSM.

The γ and $\gamma - Re_\theta$ models predict a C_f such as the one observed in the sub-critical region at $Re_D = 1.5 \times 10^5$, as opposed to AFT-based models which capture a laminar separation bubble expected in this regime. This is consistent with observations already discussed in the C_p profiles. The laminar separation is about $\phi_{l,s} = 92.5°$, which is $\Delta\phi = 3.5 - 4°$ off from AFT and AFT-RSM. It is believed to be attributed to the empirical correlations used in the model, that does not consider any pressure gradient history of the boundary layer.

The AFT-DDES model, in this case, predicts a small bubble within this regime. In fact, a sub-cricital behaviour is resembled by the AFT-DDES with a laminar separation at about $\phi_{l,s} = 89.5°$. Discrepancies might be attributed to numerical differences as also discussed by Cheng et al. (2017) and Rodríguez et al. (2015), where in some scenarios they found the bubble and in others they do not. Once the flow separates from the surface, there is no reattachment downstream of the cylinder surface, which is in agreement with Cheng et al. (2017) predictions and Liu et al. (2019) using DDES.

The C_f predicted by Cheng et al. (2017) reported the laminar separation at approximately $\phi_{l,s} = 106°$. Separation predicted by URANS AFT and AFT-RSM show an earlier transition and consequently an earlier reattachment, although as discussed it may be understood as the sub-critical regime. The laminar separation is still resembling the position of the sub-critical regime at about 90°. The turbulent separation is different as AFT and AFT-RSM separate at about $\phi_{t,s} = 94.5°$ and 93.4° respectively, while Cheng et al. (2017) predict a turbulent separation at approximately $\phi_{t,s} = 150°$.

As discussed when analysing the C_p profiles by γ and $\gamma - Re_\theta$, the suggested sub-critical behaviour is consistent with the prediction of C_f. In this case, Figure 7.8(b) shows an offset to literature data by Cheng et al. (2017) of approximately 16°. This difference is consistent with the incapability of the model to predict any interaction between separation and transition in the cylinder surface.

B: Wake velocity

Figure 7.9 gives a novel insight into the streamwise velocity behaviour throughout the centerline of the wake for transitional AFT, AFT-RSM and AFT-DDES along with fully turbulent SST and transitional models by Langtry and Menter (2009) and Menter et al. (2015).

The AFT and AFT-RSM models predict a similar behaviour for the streamwise velocity within the wake as shown in Figure 7.9, with a difference in the $-U_{min}$ of approximately 15%. The gradual velocity recovery is similar too and reaching a value of about $\overline{U}/U_\infty = 0.8$ at $x/D = 5$. Here, it can be seen how the $L_r/D = 0.6$ predicted by AFT is stretched when compared to the sub-critical region, as expected with the turbulent eddies moving

downstream the wake and rolling up (see Chapter 2). On the other hand, as discussed, the AFT-RSM ($L_r/D = 0.59$) behaviour in this regime can be considered sub-critical still, since the change in the topology and length of the recirculating length is almost similar to its sub-critical behaviour.

When compared to 2D simulations using Langtry and Menter (2009) and Menter et al. (2015), it can be seen how $L_r/D = 0.73$ is stretched from the sub-critical regime with the increased Reynolds number. However, these two models are still showing a very rapid recovery of velocity downstream the cylinder surface than AFT-based models including AFT-DDES, which switches to LES away from the wall.

The AFT-DDES model predicts a similar performance to Liu et al. (2019) with a recirculating length of approximately $L_r/D \approx 1.1$, which is stretched compared to the rest of the transitional models using two-dimensional simulations, although differences are not extremely large. Minimum velocity $U_{min} \approx -0.3519$ which is similar to Menter models in this case. The gradual recovery of the velocity is observed as expected.

Liu et al. (2019) predict a $L_r/D \approx 1.13$, with a minimum velocity of $U_{min} = -0.3519$ and an expected gradual velocity recovery until its freestream velocity is away from the aft-part of the cylinder surface. AFT and AFT-RSM models show a shortened L_r/D of approximately 50%. This may find an explanation due to the early transition of the shear layer. The γ and $\gamma - Re_\theta$ models, in this case, show a shortened L_r/D of approximately 44%, which may be attributed as well to an early transition of the shear layer resembling a sub-critical-like behaviour.

The fully turbulent approach is still showing a reduced recirculation length, which is comparable to the sub-critical L_r/D result. It is also expected that as Reynolds number is increased, the turbulent approach is able to better predict the flow field, as we approach a fully turbulent regime. Nonetheless, this is not the case for the critical regime, as transition still plays an important role as discussed in Chapter 2.

C: Turbulence Intensities

The behaviour of $\overline{u'u'}$ at the critical regime for AFT, AFT-RSM and AFT-DDES is given in Figure 7.10. The analysis of the stresses behaviour using AFT-based models for circular cylinder flow is novel to the authors' knowledge. Furthermore, SST and Langtry and Menter (2009) and Menter et al. (2015) are also given for comparison. With the stretching of the wake, the formation length is consequently stretched too, as identified in Figure 7.10 with the location of the peaks compared to the sub-critical regime.

As discussed within $Re_D = 3900$ section, the peak of $\overline{u'u'}$ is related to the shedding process, which gives information about the formation length. In Figure 7.10, it can be seen the overprediction of the variance for the streamwise velocity fluctuations using the fully turbulent SST model, where the wake is completely turbulent once it separates. On the other hand, one can see the reduction in the peak of $\overline{u'u'}$ when using transitional

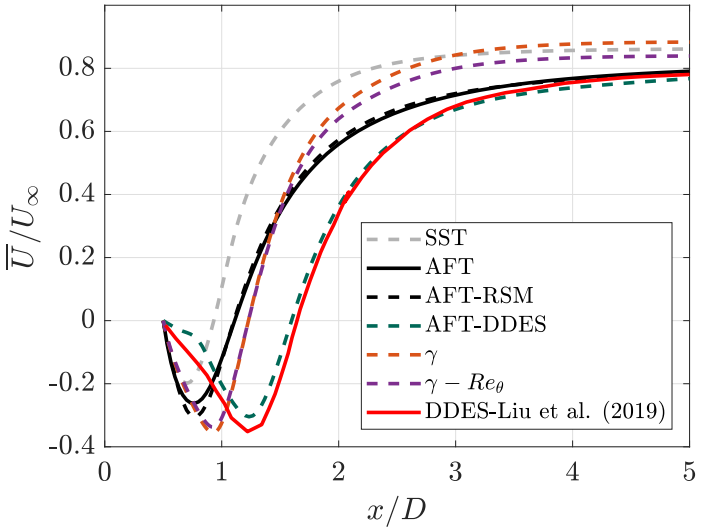

FIGURE 7.9: Mean normalized streamwise velocity $\overline{U}/U_\infty$ at centerline downstream the cylinder surface.

models to 1/3 of the fully turbulent prediction and 1/2 of the AFT-DDES prediction to URANS transitional models as given in Table 7.3.

The peak location is in agreement for AFT-RSM, γ and $\gamma - Re_\theta$ models, while only $\gamma - Re_\theta$ differs by about 13% regarding the maximum value of $\overline{u'u'}$. Furthermore, it is consistently slightly larger than L_r/D discussed in previous Section **B**. On the other hand, the position of the peak is displaced downstream when using AFT model at the location of $x/D = 1.22$ and a peak value of $\overline{u'u'}_{\max} = 0.01643$.

With the stretched L_r/D predicted by the AFT-DDES, that shows agreement with DDES within the wake of Liu et al. (2019), the peak of $\overline{u'u'}/U_\infty^2 = 0.04392$ is predicted downstream compared to the rest of transitional models at $x/D \approx 1.63$. Furthermore, the peak of the variance of the streamwise velocity fluctuations is shown to be under-predicted by the URANS transitional models, which is possibly linked to the width of the wake, as it is discussed by Rodriguez and Lehmkuhl (2021).

Predictions within the wake for $\overline{u'u'}$ and $\overline{v'v'}$ are given in Figures 7.11-7.12 using AFT-based transitional models and Menter models, γ and $\gamma - Re_\theta$ at $x/D = 1$, $x/D = 3$ and $x/D = 7$. Overall, the two peaks for the streamwise fluctuations and the main peak for the cross-wise fluctuations are predicted by all the models. Consistent with to prior analyses, the two peaks reduce their strength as the flow-field moves downstream as happens to the primary peak of $\overline{v'v'}$.

Results with AFT and AFT-RSM show similarity in the predictions for both $\overline{u'u'}$. Mild differences in the near-wake $\overline{u'u'}$ peaks are observed of about 6%, reducing this to 1% downstream the wake at location $x/D = 7$. The two large values of the peaks are

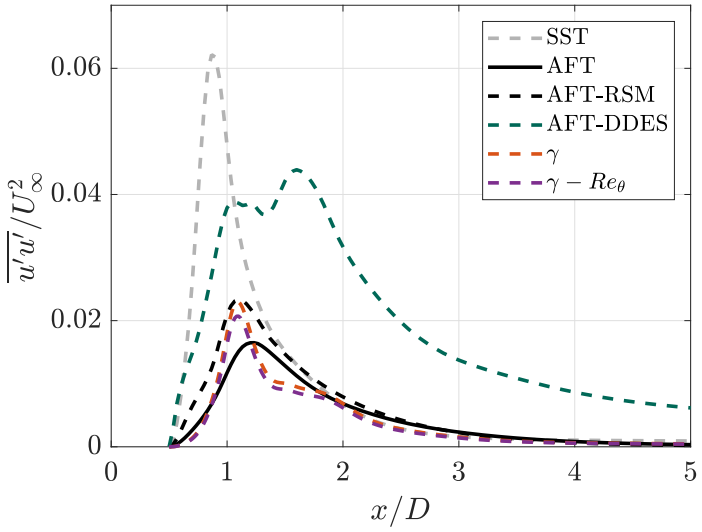

FIGURE 7.10: Mean normalized variance of streamwise velocity fluctuations $\overline{u'u'}/U_\infty^2$ at centerline downstream the cylinder surface.

attributed to the separation of the shear layers, allowing larger structures to interact and therefore produce stronger interactions.

On the other hand, when compared to AFT-DDES, both URANS transitional models show an overprediction of the peaks around $40\% - 46\%$ in the near-wake. Further downstream of the wake, at $x/D = 7$, the error is about 5%. Figure 7.11 shows how the value of $\overline{u'u'}$ over the centerline at $x/D = 1$ is larger than predictions given by AFT and AFT-RSM, as shown in the analysis for streamwise velocity fluctuations over the centerline of the wake in Figure 7.10.

Both Menter models, γ and $\gamma - Re_\theta$, show similarities in the behaviour predicted by AFT and AFT-RSM for the prediction of $\overline{u'u'}$. Two prominent peaks, which are related to shear layers that diminish as the flow moves downstream, are overpredicted compared to AFT-based models. At location $x/D = 7$, the differences to AFT and AFT-RSM are readily visible with an overprediction of the two peaks. This overprediction also occurs for $\overline{v'v'}$ as it is discussed in the following paragraphs.

Similar to $\overline{u'u'}$, the prediction by AFT and AFT-RSM is similar for $\overline{v'v'}$, where small differences of about 7.8% are found in the maximum peaks at each location, as shown in Figure 7.12. As the flow moves downstream the wake, these differences in the predictions diminish to approximately 1.5%.

For the AFT-DDES, it can be seen how the peak is smaller in the near-wake and becomes agitated as the recirculation region forms, followed by another reduction of its value as can be seen at location $x/D = 7$. It can be seen how the predictions by AFT and AFT-RSM show stronger interaction between the cross-stream velocity fluctuations, as both predictions close the formation length at approximately $x/D = 1.09 - 1.2$ respectively.

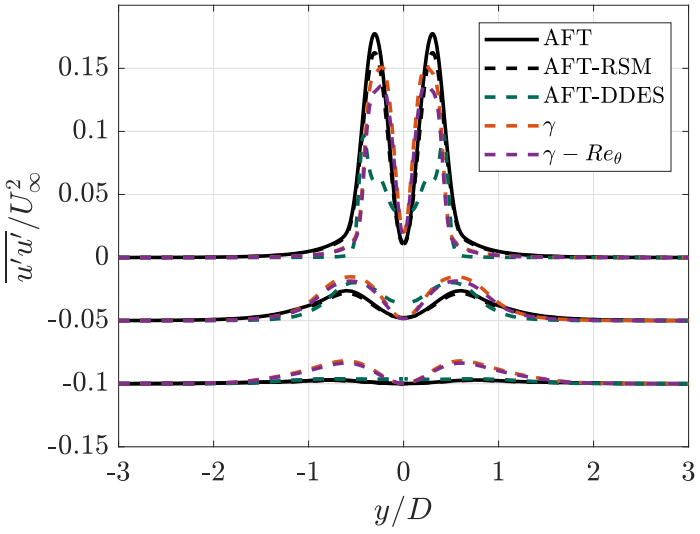

FIGURE 7.11: Mean normalized variance of streamwise velocity fluctuations $\overline{u'u'}/U_\infty^2$ at $x/D = 1, 3, 7$ downstream the cylinder surface.

For the AFT-DDES, the near-wake strength is shown to be reduced but increased at location $x/D = 3$, as the formation length is closed at approximately $x/D = 1.6$. Maximum differences between URANS AFT-based models and AFT-DDES are found in the near-wake position, while the differences diminish downstream of the wake.

The description of $\overline{v'v'}$ by γ and $\gamma - Re_\theta$ is also shown in Figure 7.12. As can be seen, in the near-wake at location $x/D = 1$, the estimation is in agreement with AFT and AFT-RSM, however further downstream the maximum value is largely overpredicted. This behaviour is not related to the closure of the formation length as it retains the strength down to $x/D = 7$. It can be concluded here that there is an excessive production of fluctuations in both Menter models, that is related to an overproduction of the eddy-viscosity in the model.

D: Instantaneous flow-field

From an instantaneous point of view using AFT-DDES in Figure 7.13, it can be seen how the length of the wake is elongated when compared to sub-critical regime, that is discussed in Figure 7.2. In this case three-dimensional AFT simulation is not presented as the main aim is to present two-dimensional simulations with URANS approaches. Furthermore, it can be seen how the vortical structures have diminished in dimension. As discussed, the spanwise dimension is reduced compared to the sub-critical regime, from $L_z = 3D$ to $L_z = D$.

The elongated wake is also shown qualitatively in the Q-criterion representation of a similar Reynolds number ($Re_D = 3.8 \times 10^5$) by Rodríguez et al. (2015). However, in their LES the asymmetric behaviour is captured with a single laminar separation bubble being predicted by LES. Instantaneous information reported by Cheng et al. (2017) at

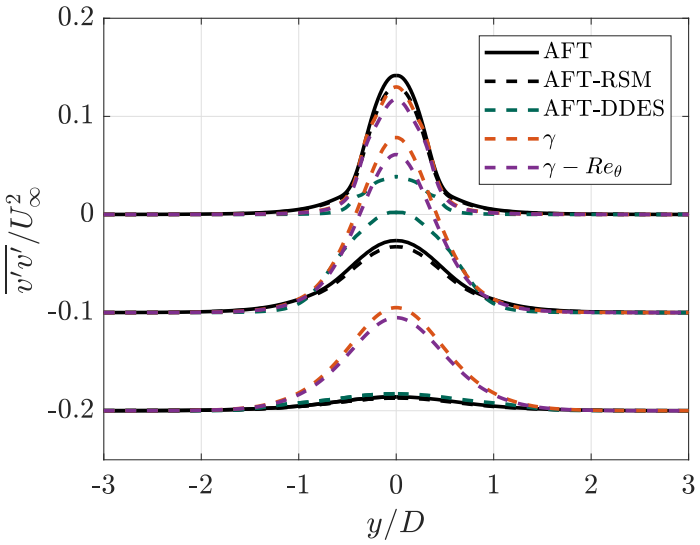

FIGURE 7.12: Mean normalized variance of cross-stream velocity fluctuations $\overline{v'v'}/U_\infty^2$ at $x/D = 1, 3, 7$ downstream the cylinder surface.

$Re_D = 3.5 \times 10^5$, also presents the appearance of a single laminar separation bubble over the upper surface of the circular cylinder.

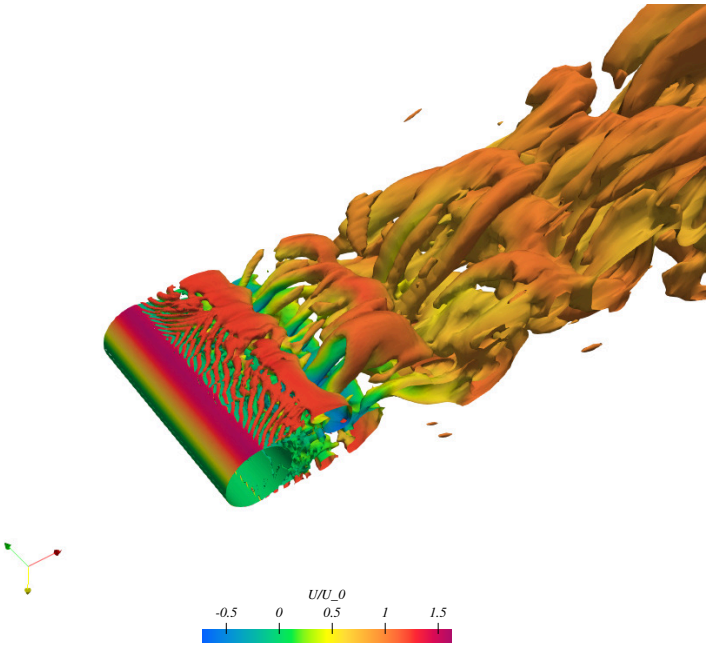

FIGURE 7.13: Q criterion iso-surface representation of value $Q = 300$ for 3D computation using AFT-DDES.

7.2.3 Summary

In summary, the most significant findings are:

Transitional models show improvements over fully turbulent models from a surface perspective and within the wake. Results using DDES transitional models show similar results to Liu et al DES simulations over the cylinder surface and within the wake compared to fully turbulent and full URANS transitional models.

Differences in transitional prediction between URANS AFT-based transitional models and Menter models have been observed. Specifically, the AFT-based model predicts a laminar separation bubble while Menter models, $\gamma - Re_\theta$ and γ predict a sub-critical behaviour over the cylinder surface.

The differences between the AFT and AFT-RSM models are not significant from on-surface, wake velocity and turbulence intensities. As discussed both predict a laminar separation bubble and their dimensions are similar too as given in Table 7.3. In addition, the minimum pressure falls closer to experimental and numerical data from literature than Menter models and the nature of the separation is turbulent. The improvement compared to the fully turbulent model is clear not only from the analysis of C_p and C_f over the surface, but also from a wake perspective where the recirculation length is significantly short.

AFT-based models predict a laminar separation bubble which is in agreement with LES simulations by Cheng et al. (2017) and Rodríguez et al. (2015). Nonetheless, the flow field is still symmetric. On the other hand, the sub-critical-like behaviour by Menter models shows no significant changes regarding surface features to $Re_D = 1.5 \times 10^5$. Recirculating length predicted by URANS transitional models is consistently underpredicted compared to literature data, as well as the variance of the streamwise velocity fluctuations. AFT-DDES does not show any asymmetric flow but the wake description is in good agreement with Liu et al. (2019) data.

TABLE 7.3: Mean flow quantities at $Re_D = 3.5 \times 10$ using transitional URANS and literature data.

Case	U_{min}/U_∞	$-C_{p,min}$	$-C_{p,b}$	L_r/D	L_f/D	$\overline{u'u'}/U_\infty^2$	$\phi_{l,s}$ [deg.]	$\phi_{t,s}$ [deg.]	ϕ_{BL} [deg.]
AFT	0.2637	2.174	0.688	0.6	1.2	0.01643	88.9	94.5	2.4
AFT-RSM	0.3057	2.131	0.7952	0.59	1.09	0.0229	88.6	93.4	3
AFT-DDES	0.3048	2.046	0.6305	1.1	1.6	0.04392	89.5	-	-
γ	0.3552	1.937	0.5969	0.73	1.097	0.02294	92.5	-	-
$\gamma - Re_\theta$	0.3376	2.174	0.6671	0.73	1.09	0.0207	92.5	-	-
SST	0.1991	2.307	0.9869	0.433	0.8667	0.06216	-	100	-
Literature Data									
Liu et al. (2019)	0.3519	-	-	1.138	-	-	-	-	-
Rodriguez et al. (2015)	-	2.443	0.4693	-	-	-	-	-	-
Cheng et al. (2017)	-	2.658	0.1284	-	-	-	106	150	-
Bursnall and Loftin (1951)	-	2.564	0.1989	-	-	-	-	-	-

7.3 Super-critical - $Re_D = 6.5 - 8.5 \times 10^5$

As discussed in Chapter 2, throughout this region the symmetry of the flow field is recovered with the appearance of a second laminar separation bubble on the cylinder surface. As previous results show, the transitional models play an important role in estimating these two features on each side of the cylinder while the fully-turbulent approaches cannot. After the drag crisis, the recovery of the symmetry flow brings back stable behaviour.

Before proceeding with the discussion of the results, note that Table 7.4 gathers all the mean flow properties at $Re_D = 6.5 \times 10^5$ and $Re_D = 8.5 \times 10^5$ using transitional models and also the relevant literature data analysed and discussed in the following paragraphs. Note that AFT-DDES simulation is performed at $Re_D = 8.5 \times 10^5$, as the super-critical regime is expected to be a quasi-steady regime. At $Re_D = 6.5 \times 10^5$ full URANS transitional models are presented using a second-order upwind scheme as identified in Table 7.1 for completing the analysis and confirming the quasi-steady prediction throughout this regime, where as the AFT-DDES model is only applied to 8.5×10^5 as the behaviour is expected to be similar at 6.5×10^5.

7.3.1 Mesh and computation setup

The grid properties for $Re_D = 6.5 - 8.5 \times 10^5$ are given in Table 7.1. The two grids are similar for the super-critical regime with an increased resolution compared to critical regime grid characteristics. The spanwise length is maintained to $L_z = D$, which is the length utilised by Cheng et al. (2017) in their simulations following the discussion from the sub-critical regime. The number of points in the spanwise domain is $N_z = 192$, which gives a resolution of approximately $\Delta z = 2.6 \times 10^{-3}$ m which is similar to the critical regime, in an analogy to Cheng et al. (2017) grid construction.

The radial and angular direction have 450 points, which is increased in a factor of $\sqrt{2}$ to critical regime radial and angular direction to ensure a sufficient resolution for the super-critical prediction within the wake. As the resolution is increased to $\Delta\theta = 0.8°$ from the critical regime where results are in good agreement with DDES by Liu et al. (2019), it is considered to be sufficient for the description of the super-critical regime as an analogy to the maintained resolution by Cheng et al. (2017) in their LES simulations between $Re_D = 3.5 \times 10^5$ and $Re_D = 8.5 \times 10^5$.

7.3.2 Predictions of the flow-field

A: Surface pressure (C_p) and skin friction (C_f) A1: $Re_D = 6.5 \times 10^5$

The predictions using AFT and AFT-RSM for C_p is shown in Figure 7.14(a). Predictions are similar between both models, although differences regarding the location and the value of the $-C_{p,min}$ are observed. In fact, the upstream location at 82° of the $-C_{p,min}$ by 1.5% compared to AFT, and its reduced value by 15.5% is consistent with the earlier separation observed in the skin friction predictions given in Figure 7.14(b). These differences are attributed to the different turbulence models used and therefore the wake effect to the upstream flow field. Further downstream of the laminar separation bubble, the pressure recovery becomes coincident at about 120° and the $-C_{p,b} \approx 0.5$.

Local correlation-based models, $\gamma - Re_\theta$ and γ by Langtry and Menter (2009) and Menter et al. (2015), show similar behaviour to the AFT model in predicting C_p. However, the γ-model does not show any plateau in the C_p profile that indicates a laminar separation bubble, which is confirmed by the C_f in Figure 7.14(b). Beyond 120°, the γ-model resembles a similar sharp decrease on the C_p that resembles behaviour observed at $Re_D = 3900$, with an increased $-C_{p,b}$ of twice the predicted value by the rest of transitional models. This might be attributed to simplified correlations from γ-model.

Roshko (1961) experimental data at $Re_D = 6.5 \times 10^5$ and Spitzer (1965) at $Re_D = 7.5 \times 10^5$ are given in Figure 7.14(a) for comparison. As shown, predictions using the transitional models over the upstream face agree well with the measurements. The minimum pressure coefficient is shown to be similar to AFT, γ and $\gamma - Re_\theta$, while AFT-RSM underpredicts its value due to the smallest LSB. The laminar separation bubble is shown to be delayed by Roshko (1961) and Spitzer (1965) compared to transitional predictions and therefore the $-C_{p,b}$ underprediction of the current simulations, either compared to Roshko (1961) or Spitzer (1965).

The laminar separation bubble can be observed in the C_f profiles, as crosses zero from positive to negative values for AFT and AFT-RSM, at approximately $\phi_{l,s} = 95°$ and $\phi_{l,s} = 92°$ respectively in Figure 7.14(a) and Figure 7.14(b), where any test data at this Reynolds number is available within the literature. The laminar separation bubble predicted by AFT is smaller than AFT-RSM, as the bubble length is $\phi_{BL} = 2°$ and $\phi_{BL} = 3°$ respectively. Following the laminar separation bubble, the boundary layer reattaches to the cylinder surface and develops a turbulent boundary layer until its complete separation for both AFT and AFT-RSM transitional models. The turbulent separation point is shown to be different for AFT and AFT-RSM as the turbulent approach is recovered. This is also consistent with C_p behaviour after a small disturbance of the profile indicating the LSB. The AFT transitional model predicts a turbulent separation point at $\phi_{t,s} = 115°$, while the transitional AFT-RSM model predicts an earlier turbulent separation point at approximately $\phi_{t,s} = 109°$.

At this Reynolds number, as shown in Figure 7.14(a) and Figure 7.14(b), the $\gamma - Re_\theta$ model predicts a similar length of the separation bubble to AFT-RSM, with a turbulent separation around the same angular position. On the other hand, the γ model shows

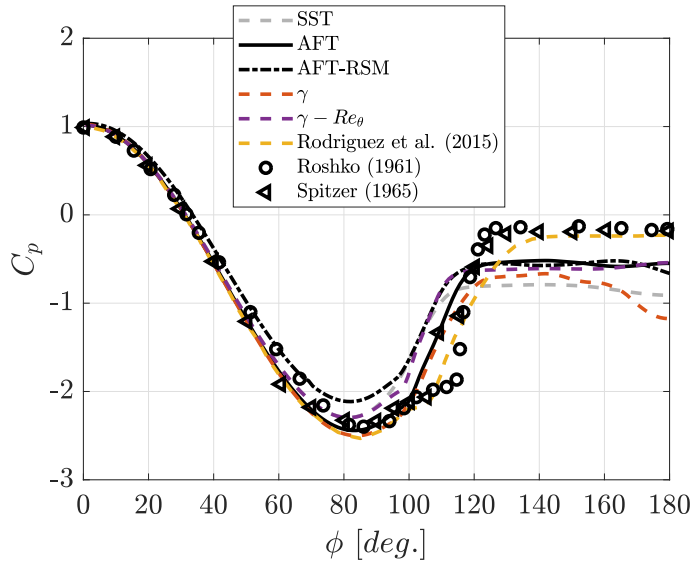

(a)

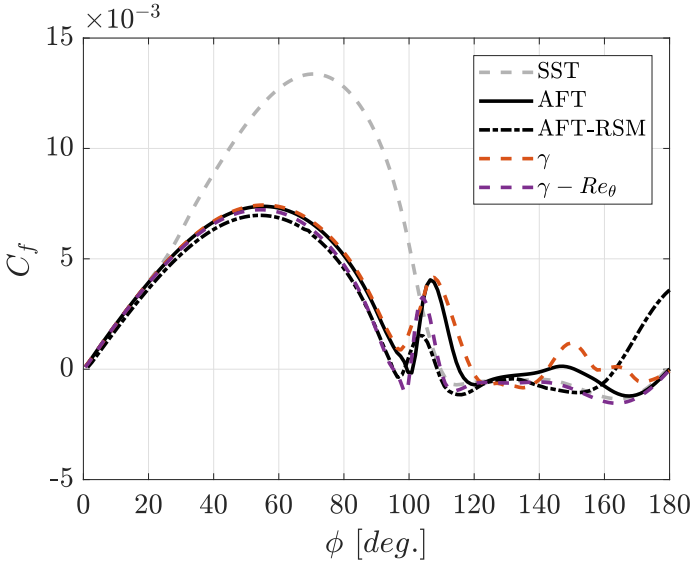

(b)

FIGURE 7.14: (a) C_p distribution and (b) C_f distribution with experimental data by Roshko (1961) and Spitzer (1965) at $Re_D = 6.5 - 7.5 \times 10^5$ respectively along current predictions with SST, AFT, AFT-RSM, AFT-DDES, Langtry and Menter (2009) and Menter et al. (2015) model at $Re_D = 6.5 \times 10^5$.

a closer prediction to the AFT model but without the appearance of the pure laminar separation, as the C_f never crosses the $C_f = 0$ axis and the transition occurs without any laminar separation at all. This shortcoming is also shown with the increased Re_D at 8.5×10^5.

Rodríguez et al. (2015) reported the laminar separation bubble on their LES simulations to be distributed at angles about $\phi \approx 100° - 110°$, which is approximately $\phi = 5° - 7°$ different downstream from the current URANS predictions. The laminar separation

bubble predicted by AFT is smaller than AFT-RSM, as the bubble length is $\phi_{BL} = 2°$ and $\phi_{BL} = 3°$ respectively, while Rodríguez et al. (2015) report a $\phi_{BL} \approx 8°$. In both cases, the separation point is moved upstream compared to literature data by Rodríguez et al. (2015) and Cheng et al. (2017), which is reported approximately $\phi_{t,s} = 148°$ throughout the super-critical regime.

A2: $Re_D = 8.5 \times 10^5$

With the increased Reynolds number, the behaviour of the flow field from a surface perspective is expected to be similar to $Re_D = 6.5 \times 10^5$. Figure 7.15(a) and Figure 7.15(b) show the C_p and C_f predictions respectively.

Similarities in the predictions using transitional models are observed. In fact, all of them are similar to the previous Reynolds number. The main difference is the peak of C_f when the turbulent flow reattaches after the laminar separation bubble. As in prior Reynolds, the laminar separation bubble is still rather small and the separation point is still at approximately $\phi_{l,s} = 97 - 99°$. The length of the bubble is approximately $\phi_{BL} = 2 - 3°$. Turbulent separation is also shown to be similar to $Re_D = 6.5 \times 10^5$ for the AFT case, as $\phi_{t,s} \approx 115°$ and AFT-RSM at $\phi_{t,s} = 109°$.

The $\gamma - Re_\theta$ model still shows similar behaviour to AFT-RSM, while the γ-model predicts a transition without any laminar separation bubble and a turbulent separation at about the same position as AFT predicts. This shortcoming seems to be consistent for the whole super-critical regime when using γ-model.

At this Reynolds number, the AFT-DDES prediction for C_p and C_f is shown. It is shown how the behaviour is similar to the AFT model, which includes the prediction of the laminar separation bubble over the cylinder surface. This is an approximation to the capabilities of pure LES, rather than turbulent assumptions of the near wall region when using standard DDES. In fact, it can be seen how the back pressure is closer to Rodríguez et al. (2015) data although differences are still about $\Delta C_{p,b} \approx 0.2$.

The laminar separation bubble using AFT-DDES is located at $\phi_{l,s} = 95°$ with a length of the bubble of $\phi_{BL} = 2°$. Experimental data by Achenbach (1968) does not report a bubble, as any $C_f = 0$ is shown in Figure 7.15(b). On the other hand, Rodríguez et al. (2015) and Cheng et al. (2017) report a laminar separation bubble $\phi_{l,s} \approx 148°$, with a length of approximately $\phi_{BL} \approx 8°$. Differences might be attributed to the use of correlations based on Falkner-Skan profiles over a flat plate, for the growth of the boundary layer momentum-thickness and the growth of instabilities throughout the boundary layer. Theses effects will be investigated in the last chapter of this thesis.

B: Wake velocity

In this section, the near wake is analysed using the streamwise velocity variation at the centerline downstream of the cylinder surface at $Re_D = 8.5 \times 10^5$. The behaviour

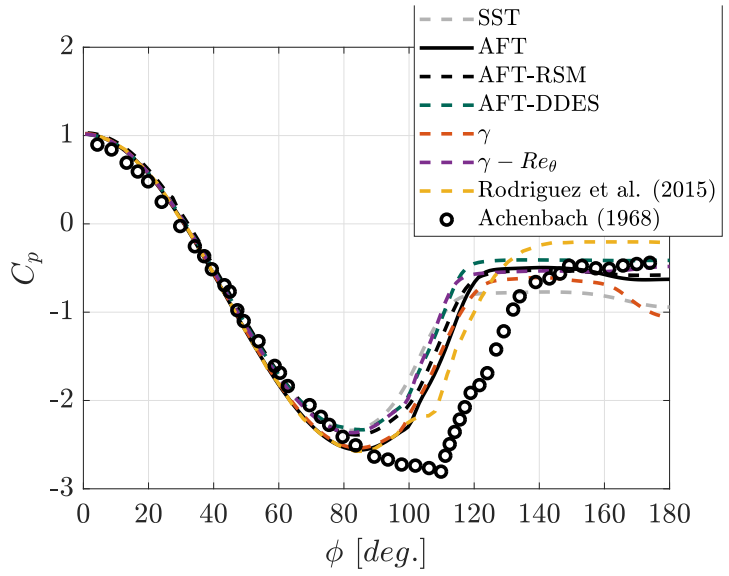

(a)

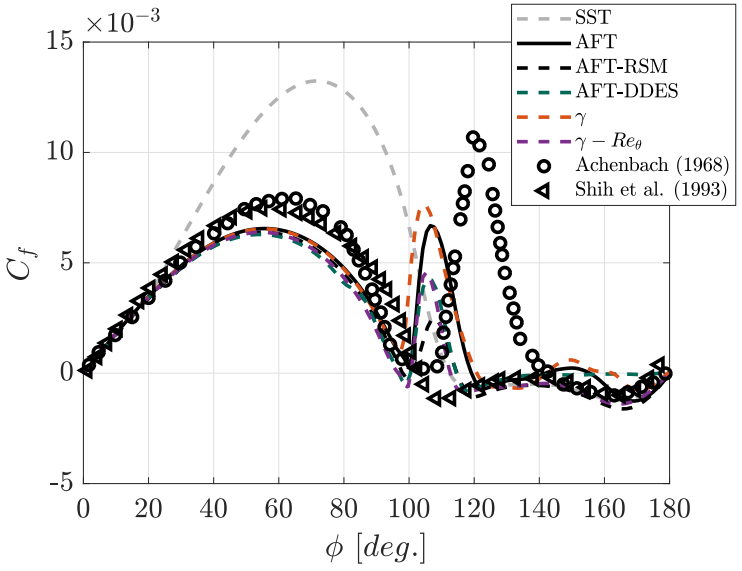

(b)

FIGURE 7.15: (a) C_f distribution with Achenbach (1968) and Shih et al. (1993) experimental data at $Re_D = 8.5 \times 10^5$and (b) C_p distribution with experimental data by Achenbach (1968) and LES by Rodríguez et al. (2015) along current predictions with SST, AFT, AFT-RSM, AFT-DDES, Langtry and Menter (2009) and Menter et al. (2015) model at $Re_D = 8.5 \times 10^5$.

at $Re_D = 6.5 \times 10^5$ for completeness in Figure 7.16(a), to justify the almost constant behaviour throughout the super-critical regime, as also discussed in the literature by Rodriguez and Lehmkuhl (2021). Physical behaviour expected within the super-critical regime from the critical regime is to reduce the length of the recirculating length L_r/D, as analysis by Rodríguez et al. (2015) and Rodriguez and Lehmkuhl (2021) reported.

Predictions using AFT and AFT-RSM models at $Re_D = 6.5 \times 10^5$ and $Re_D = 8.5 \times 10^5$, show a reduction to the critical values, respectively. Specifically, the prediction of AFT

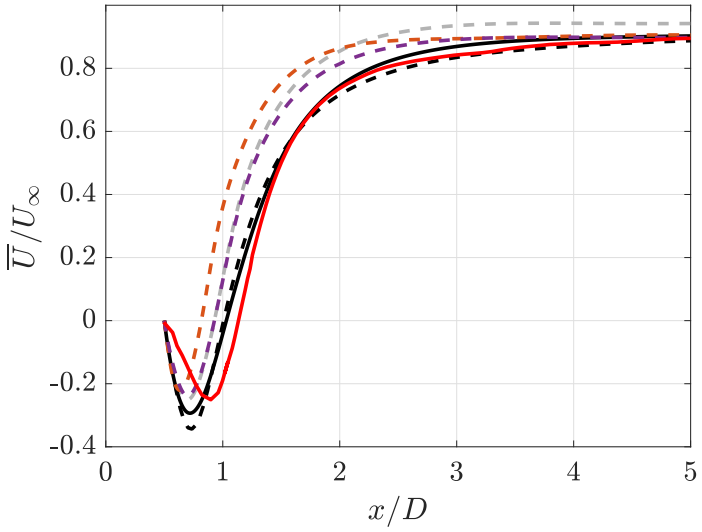

(a) $Re_D = 6.5 \times 10^5$

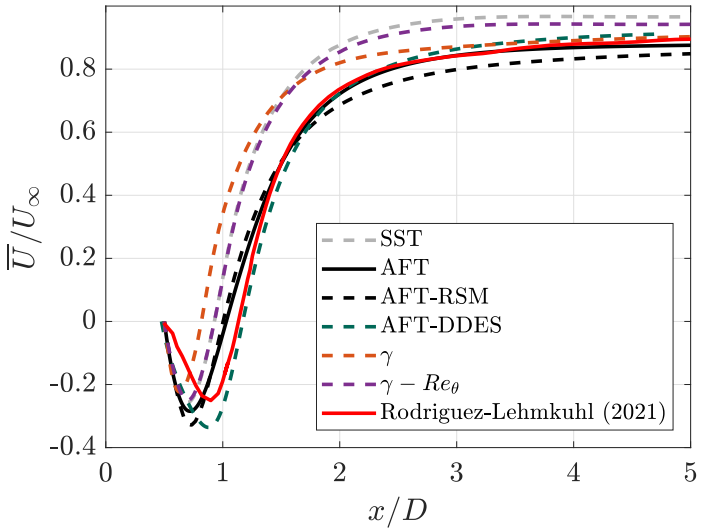

(b) $Re_D = 8.5 \times 10^5$

FIGURE 7.16: Mean normalized streamwise velocity (a) $\overline{U}/U_\infty$ at $Re_D = 6.5 \times 10^5$ and (b) $\overline{U}/U_\infty$ at $Re_D = 8.5 \times 10^5$ at centerline $y/D = 0$.

and AFT-RSM predict similar values, $L_r/D = 0.45$ and $L_r/D = 44$ respectively. The gradual velocity recovery is similar in trend to the sub-critical and critical regimes, except what was observed at $Re_D = 3900$, where a wavy behaviour was observed away from the cylinder surface. There are small differences regarding the $-U_{min}$ where AFT and AFT-RSM predict $U_{min} = -0.2847$ and $U_{min} = -0.328$ respectively. This difference is similar at $Re_D = 6.5 \times 10^5$, confirming the stable behaviour within super-critical regime by AFT and AFT-RSM.

The predictions by $\gamma - Re_\theta$ show a constant behaviour too regarding the wake velocity. Nonetheless, the value of $L_r/D = 0.425$ is shortened compared to AFT-based transitional

models, including literature data shown by Rodriguez and Lehmkuhl (2021). The γ model shows a shortened recirculating length compared to $\gamma - Re_\theta$. The flow field is different from a surface perspective and from a wake perspective too. In fact, the recirculating length is similar to SST predictions, where flow is considered fully turbulent from the inlet surface.

AFT-DDES shows a stretched $L_r/D = 0.614$ for both Reynolds numbers, which is about 26% longer than predictions using URANS. The velocity recovery to the freestream value is similar beyond $x/D = 0$ to AFT and AFT-RSM. Nonetheless, results do show similarities between the use of DDES and URANS transitional models.

LES prediction by Rodriguez and Lehmkuhl (2021) at $Re_D = 7.2 \times 10^5$ is given in Figure 7.16(b), with an $L_r/D = 0.57$. It shows to be similar to transitional URANS predictions using AFT, AFT-RSM and AFT-DDES. In Rodríguez et al. (2015) reports L_r/D at 6.5×10^5, 7.2×10^5 and 8.5×10^5 to be $L_r/D \approx 0.56 - 0.59$. Hence, the agreement is good with the AFT-based models as values are within $25 - 27\%$ of error. AFT-DDES shows a similar prediction to Rodriguez and Lehmkuhl (2021) profile given in Figure 7.16(b). The value predicted is about $L_r/D = 0.614$, which is approximately 6.3%, with a similar velocity recovery beyond $x/D = 0$.

C: Turbulence intensities

Analogous to the critical regime, the analysis of the variance of streamwise velocity fluctuations is given to analyze the near wake behaviour at the super-critical regime. Furthermore, it provides information about the formation length prediction for the different models.

The behaviour of $\overline{u'u'}$ at the critical regime for AFT, AFT-RSM and AFT-DDES is given in Figure 7.17(a) and Figure 7.17(b). This has not been reported before for AFT-based models. Along AFT, AFT-RSM, and AFT-DDES, the fully turbulent SST and transitional models by Langtry and Menter (2009) and Menter et al. (2015) are also given for comparison. In general, the location of the peaks are upstream compared to the sub-critical regime, and to critical values in Figure 7.10

With the increase of Reynolds number, the maximum values diminishes. This is consistent for all models presented in Figure 7.17. The agreement between AFT and AFT-RSM is consistent with the wake behaviour observed in Section **B**. The maximum peak value falls close to LES data by Rodriguez and Lehmkuhl (2021) ($\overline{u'u'}_{\max} = 0.35$) by an average of 22% and 44% for the two Reynolds numbers given.

Menter models show a much stronger peak, which may be attributed to the shortened recirculating length and wider wake, as the shear layers are more separated the interaction between each other in the formation zone is more intense. This is a consistent discussion with Rodriguez and Lehmkuhl (2021). Overprediction is about four times

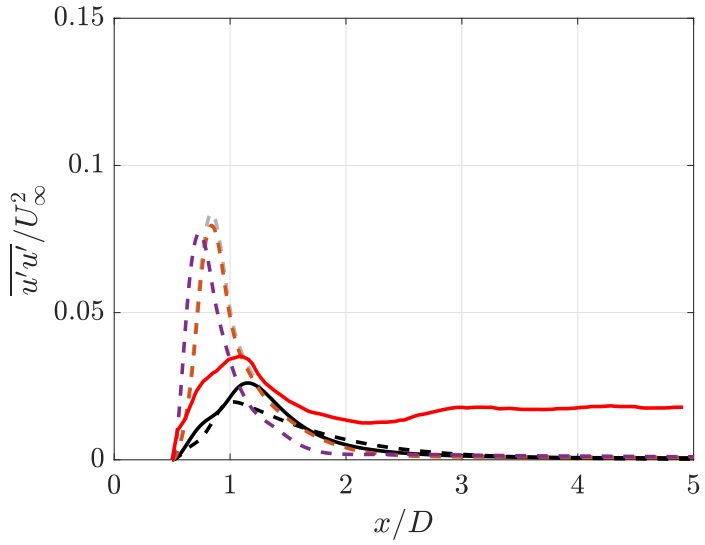

(a) $Re_D = 6.5 \times 10^5$

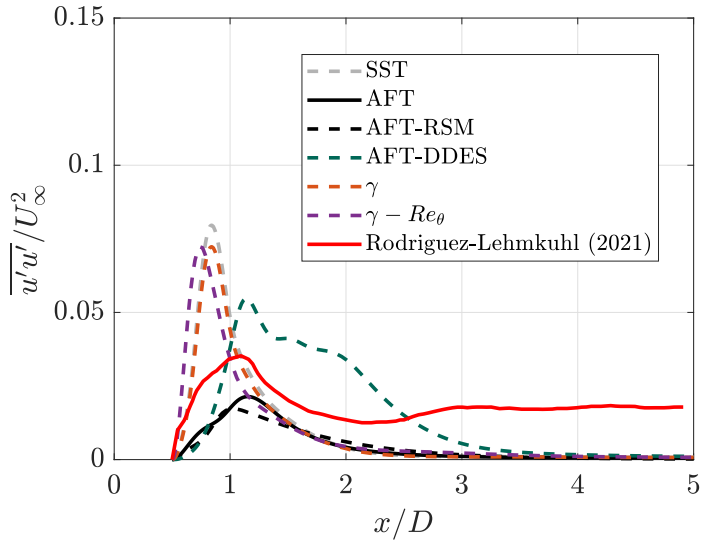

(b) $Re_D = 8.5 \times 10^5$

FIGURE 7.17: Mean normalized variance of streamwise velocity fluctuations (a) $\overline{u'u'}/U_\infty^2$ at $Re_D = 6.5 \times 10^5$ and (b) $\overline{u'u'}/U_\infty^2$ at $Re_D = 8.5 \times 10^5$ at centerline $y/D = 0$.

the peak value of AFT and AFT-RSM, while predictions for both Menter models are similar to fully turbulent SST model estimation.

The AFT-DDES shows consistent results regarding the peak estimation of the $\overline{u'u'}$ with its position being shifted downstream compared to Rodriguez and Lehmkuhl (2021) estimations. This is consistent too with the recirculating length estimation shown in Section **B**. In this case, demonstrates a similar performance to AFT and AFT-RSM predictions.

LES given by Rodriguez and Lehmkuhl (2021) only shows one peak at this regime, different to the two peaks observed in $Re_D = 3900$. As reported by Rodriguez and Lehmkuhl (2021), the maximum value is about $\overline{u'u'}_{\max}/U_\infty^2 = 0.035$, and the behaviour is similar to the previous analysis of the variance of the streamwise velocity fluctuations, it goes from zero right at the back of the cylinder to its maximum value, and then reduces its value further once the shedding vortex has been formed.

Predictions of $\overline{u'u'}$ and $\overline{v'v'}$ using AFT, AFT-RSM, AFT-DDES and Menter models, γ and $\gamma - Re_\theta$ at $Re_D = 8.5\times10^5$ are shown in Figure 7.18 and Figure 7.19, respectively for three different positions ($x/D = 1$, $x/D = 3$ and $x/D = 7$). Estimations using AFT and AFT-RSM are similar overall for $\overline{u'u'}$. The main two peaks are predicted practically with the same value of approximately $\overline{u'u'}_{\max} \approx 0.04$ and the value at $x/D = 1$ corresponds to the values that can be observed in Figure 7.17(b).

The AFT-DDES is shown to predict a stronger peak for $\overline{u'u'}$ at all three locations given in Figure 7.18 and Figure 7.12. The maximum value of $\overline{u'u'} = 0.013$ is in agreement with the value reported by Rodriguez and Lehmkuhl (2021). The strength is reduced downstream the wake, in fact the agreement is fair with AFT and AFT-RSM at $x/D = 3$ and $x/D = 7$.

Menter models, γ and $\gamma - Re_\theta$, both show an overprediction of the peaks for both $\overline{u'u'}$ and $\overline{v'v'}$. Both Menter models show similarities in their predictions. The two peaks for the streamwise velocity fluctuations are consistent with URANS AFT-based models and AFT-DDES, and the single peak for the cross-wise velocity fluctuations.

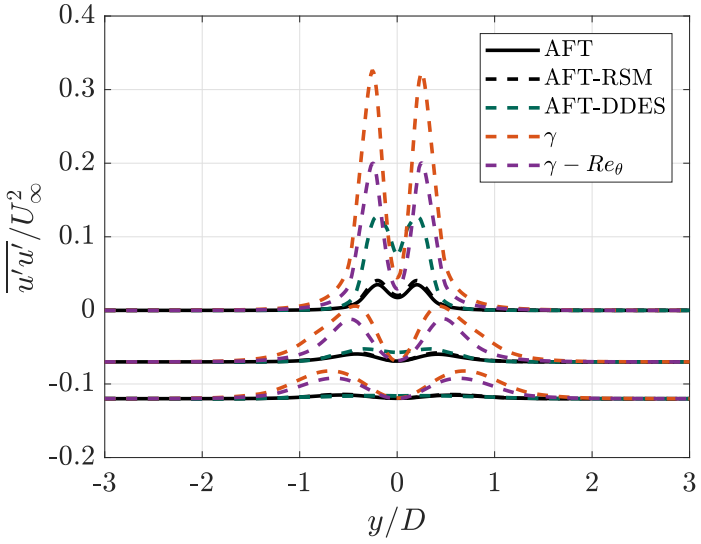

FIGURE 7.18: Mean normalized variance of streamwise velocity fluctuations $\overline{u'u'}/U_\infty^2$ at $x/D = 1, 3, 7$ downstream the cylinder surface.

A similar behaviour between AFT and AFT-RSM is shown in the prediction of $\overline{v'v'}$. The maximum peak diminishes as the flow moves downstream. This is the case as well for

the AFT-DDES, where the peak is stronger at the near-wake location $x/D = 1$, followed by a reduction at $x/D = 3$ and $x/D = 7$.

Differences between AFT-DDES and URANS AFT-based models are maximum at location $x/D = 1$ by 68% while diminishing down to 5% at the furthest measured position $x/D = 7$.

As a difference to URANS AFT-based models, the Menter models show large values for the peaks of approximately 0.5 and 0.23 for γ and $\gamma - Re_\theta$ respectively. This difference diminishes to about 35% at location $x/D = 7$. Predictions using γ and $\gamma - Re_\theta$ result in a difference to URANS AFT-based model of 79% and 84% to AFT-DDES.

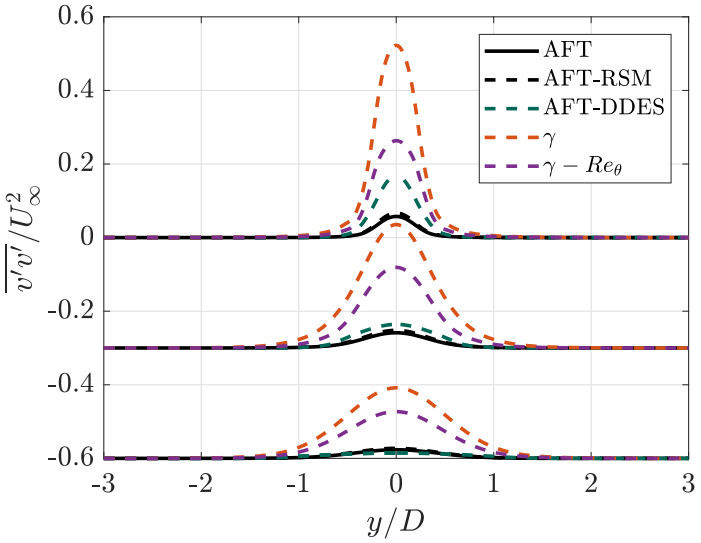

FIGURE 7.19: Mean normalized variance of cross-stream velocity fluctuations $\overline{v'v'}/U_\infty^2$ at $x/D = 1, 3, 7$ downstream the cylinder surface.

D: Instantaneous flow-field

The use of hybrid transitional-DDES shows that in the near-wall region the flow can be either laminar or turbulent depending on the transition conditions. A three-dimensional AFT simulation is not presented in this regime. In this case, the appearance of the two laminar separation bubbles is similar to the LES simulations close to the wall but with less intensive near-wall grid requirements. Time-spanwise-averaged data shows the prediction of two laminar separation bubbles over the cylinder surface in the skin-friction profile in Figure 7.15(b). The laminar separation bubble is also present as a small plateau in the C_p profile in Figure 7.15(a).

The vortical structures within the wake are shown in Figure 7.20, where lateral and zenith points of view are shown. From both, it can be seen that the recirculating length is shortened while the separation point is moved downstream. In fact, the laminar separation bubble line can be observed clearly in Figure 7.20(b) along the spanwise

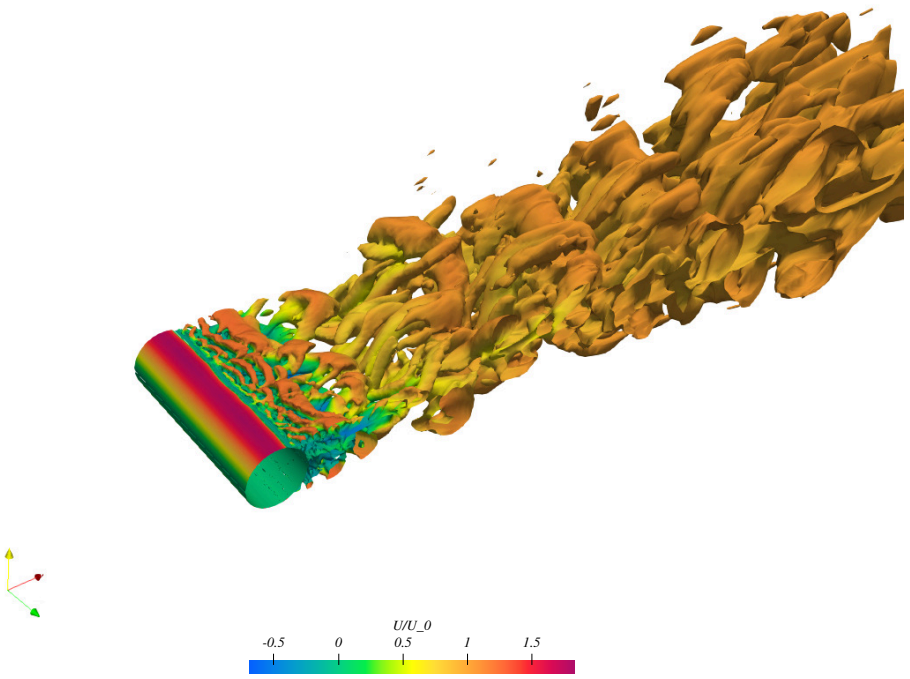

(a)

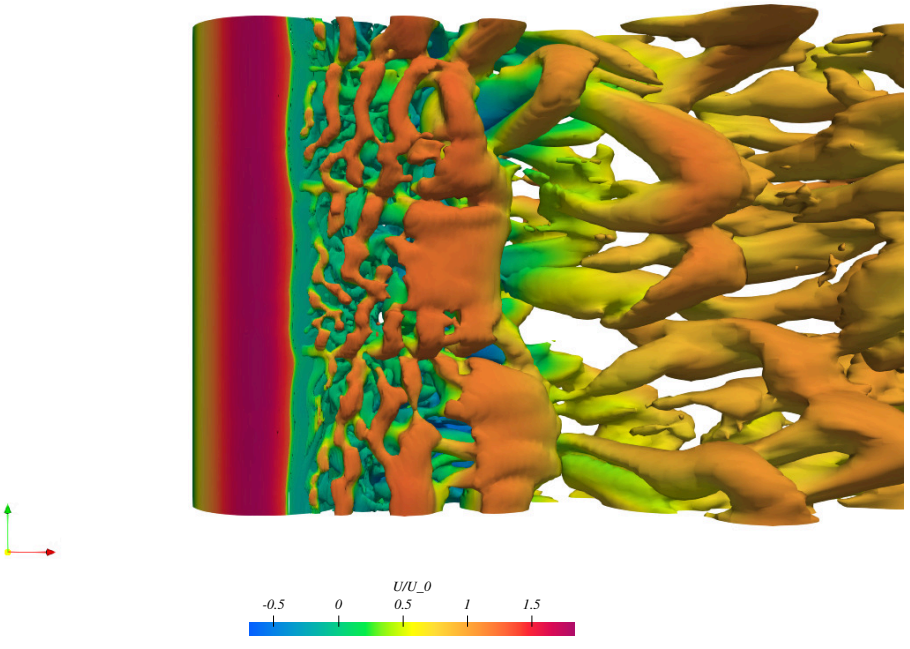

(b)

FIGURE 7.20: (a) $Q_{criterion} = 500$ for AFT-DDES at $Re_D = 8.5 \times 10^5$ showing the vortical structures within the wake and (b) zoom of the $Q_{criterion} = 500$ close to cylinder surface to show the laminar separation bubble line across the span.

length. Further downstream, the turbulent separation is observed with the formation of three-dimensional vortical structures, at approximately $\phi = 120°$.

Thus, the misprediction provided by the AFT is conserved within the near-wall region with the hybrid formulation. However, if transition prediction is improved with the use of refined transitional correlations as discussed in Chapter 8, the performance can become a closer alternative to LES. In this case, with a less intensive requirement in the near-wall region but retaining the LES performance away from the near-wall region.

7.3.3 Summary

This section demonstrates the superior performance of the AFT-based models, including the AFT-DDES to fully turbulent approaches when describing the flow features for flow past a circular cylinder at the super-critical regime. In addition, predictions by $\gamma - Re_\theta$ and γ models are introduced for comparison reasons.

It is evident from previous analysis that γ and SST cannot predict the laminar separation bubble in any of the two Reynolds numbers within the super-critical regime. This is considered to be attributed to the simplified correlations used in this model, which forces the production significantly earlier than separation occurs and therefore no laminar separation occurs, just on-surface transition. The original model proposed by Menter et al. (2015), referred to as $\gamma - Re_\theta$, has shown a better performance than its modified version. From a surface perspective, the performance is similar to AFT-RSM, while the base AFT shows the best fit to experimental and LES data presented in this section.

Within the wake, the AFT-based models show improved predictions by $\gamma - Re_\theta$ and γ as discussed when analysing wake velocity and turbulence intensities in Sections **B**, **C**. Menter models consistently predict a shortened recirculating length and formation length, consequently bringing eddies closer to the back of the cylinder surface.

Regarding the AFT-DDES, it is shown that the performance is similar to AFT in the near-wall predictions. However, it is important to comment on the capability of the hybrid model to introduce sensitivity to explicit transition prediction, which improves the physical description of the boundary layer over the cylinder surface to turbulent DDES and provides a closer behaviour to pure LES. Within the wake (away from the walls), with the recovery of the LES performance, the results show an improvement when compared to URANS transitional models.

Hence, not only the use of AFT shows promising results regarding two-dimensional simulations and the capability of flow description but, three-dimensional AFT-DDES also shows promising results for transitional prediction blended with LES. Accordingly, the transitional correlations may need to be revisited as discrepancies have been observed in the experiments by Achenbach (1968) and LES predictions by Cheng et al. (2017), Rodríguez et al. (2015) and Rodriguez and Lehmkuhl (2021). However, URANS transitional models show a clear improvement to fully turbulent SST predictions. The revision of these transitional correlations are performed in Chapter 8, where the behaviour of the

original correlations are compared to the behaviour given in laminar profiles predicted by LES at two different Reynolds numbers.

TABLE 7.4: Mean flow field characteristics at $Re_D = 6.5 \times 10^5$ and $Re_D = 8.5 \times 10^5$ for transitional URANS and literature data.

Case	$-U_{min}/U_\infty$	$-C_{p,min}$	$-C_{p,b}$	L_r/D	L_f/D	$\overline{u'u'}/U_\infty^2$	$\phi_{l,s}$ [deg.]	$\phi_{t,s}$ [deg.]	ϕ_{BL} [deg.]
$Re_D = 6.5 \times 10^5$									
AFT	0.2934	2.442	0.513	0.54	1.148	0.02608	99	115	2
AFT-RSM	0.3437	2.115	0.6471	0.5	1	0.01957	95	108.5	3
γ	0.2387	2.501	1.175	0.316	0.84	0.07963	-	119	-
$\gamma - Re_\theta$	0.221	2.297	0.513	0.428	0.7317	0.07692	95	109	4
SST	0.2504	2.297	0.9104	0.428	0.8417	0.08375	-	109	-
$Re_D = 8.5 \times 10^5$									
AFT	0.2847	2.561	0.6276	0.45	1.148	0.01728	99	115	2
AFT-RSM	0.3286	2.39	0.5791	0.44	1	0.02141	98	109	3
AFT-DDES	0.336	2.332	0.4138	0.614	1.14	0.051	95	115	2
γ	0.2234	2.537	1.052	0.31	0.84	0.072	-	120	-
$\gamma - Re_\theta$	0.2504	2.365	0.4828	0.425	0.735	0.072	97	113	3
SST	0.2568	2.338	0.9422	0.425	0.84	0.0796	-	112	-
Literature Data									
Rodriguez et al. (2021)	0.2507	2.575	0.2131	0.575	1.094	0.035	100-110	148	8
Cheng et al. (2017)	-	-	-	-	-	-	-	148	8
Achenbach (1968)	-	2.806	0.4404	-	-	-	-	-	-
Roshko (1961)	-	2.399	0.1815	-	-	-	-	-	-
Spitzer (1965)	-	2.336	0.1817	-	-	-	-	-	-

7.4 Mean Flow quantities at different Reynolds numbers

7.4.1 Drag coefficient C_D

As discussed in the introduction to this chapter, one of the main goals is to study the Reynolds effect for flow over a circular cylinder when using transitional methods versus fully-turbulent approaches. Predictions for typical Reynolds numbers over different flow regimes are compared for transitional and fully turbulent models. Figure 7.21 shows the C_D variation with the increase of Re_D up to $Re_D \approx 10^7$ with $Tu = 0.4\%$ and $Tu = 4\%$ respectively. Note the lines presented in the following figures are a visual aid for the reader to follow the behaviour of the transitional models. Experimental data by Roshko (1961) and Schewe (1983), DES by Vaz et al. (2009) and LES by Rodríguez et al. (2015) are presented along with the current computations.

The C_D is predicted to remain almost constant up to $Re_D = 1.5 \times 10^5$ for the URANS transitional models. As Reynolds number is increased the sharp decrease in C_D is observed followed by an almost plateau region over the super-critical regime by AFT and AFT-RSM. The γ-model and $\gamma - Re_\theta$ predict a continuous reduction of C_D at $Re_D = 8.5 \times 10^5$. Beyond that, at $Re_D > 10^7$, a continuous reduction in drag is still being predicted by URANS transitional models, including γ and $\gamma - Re_\theta$.

It can be seen how the performance using URANS transitional models is superior to fully turbulent SST prediction given in Figure 7.21, where the sensitivity to the critical and super-critical regimes is almost negligible. Beyond $Re_D > 10^7$, the fully turbulent model recovers its performance, showing agreement with the literature data.

The C_D predictions using AFT-DDES show a similar behaviour to URANS transitional methods. Throughout the sub-critical the behaviour is almost constant, followed by a sharp decrease within the critical region or drag crisis. With the continuous increase of Reynolds number at $Re_D = 8.5 \times 10^5$, the agreement is also good with URANS transitional models except for $\gamma - Re_\theta$. The difference with fully turbulent predictions is also readily visible in Figure 7.21. The sensitivity at the critical region is almost negligible, and similarly with the increased Reynolds number throughout the super-critical regime. Further predictions using AFT-DDES beyond $Re_D > 10^7$ are not performed in this thesis, but it can be considered future work to do.

The C_D is shown to remain almost constant up to $Re_D = 1.5 \times 10^5$ for the URANS transitional methods and the AFT-DDES models. This is consistent with prior DDES and LES predictions in the literature. Furthermore, transitional URANS and AFT-DDES agree with Zdravkovich (1997) observations regarding the "stabilization effect" throughout the sub-critical regime.

With the increase of Reynolds number, the wake narrows down and the separation point is displaced downstream stretching the recirculating length, inducing significant

changes to C_D results in a sharp decrease in C_D estimations. Transitional URANS and AFT-DDES demonstrate this sharp decrease in C_D and stretching of the L_r/D. This is consistent with Liu et al. (2019) DDES predictions, although this region is really sensitive to any numerical perturbation as discussed by Rodríguez et al. (2015) and Cheng et al. (2017). Conversely, the fully turbulent SST predicts a rather small change in comparison to the rest of the models and overpredicts C_D compared to literature data and transitional URANS models, as shown in Figure 7.21(a).

Flow begins to recover its symmetric behaviour in the super-critical region, as $C_{D,min}$ is reached. As Reynolds number increases, the flow field is relatively similar throughout the super-critical regime. AFT and AFT-RSM retain the plateau behaviour ($C_D \approx 0.4$ and $C_D \approx 0.3$ respectively), with an overpredicted C_D when compared to literature data. Both Menter models, the $\gamma - Re_\theta$ model and the γ-model still predicts a fall of C_D until approximately $Re_D = 8.5 \times 10^5$, which is consistent with the drastic change of L_r/D predicted by the two models within the super-critical regime. Langtry and Menter (2009) and Menter et al. (2015) keep reducing their C_D, while AFT and AFT-RSM keep a constant behaviour. Overall, Menter (1993) do not show significant sensitivity as the model demonstrates a moderate C_D reduction (consistent with the moderate change of L_r/D) until it reaches its fully-turbulent behaviour, where it recovers its performance.

7.4.2 Strouhal number St

The shedding frequency is presented in terms of the Strouhal number for the Reynolds number spectra. The Strouhal number is computed from the lift coefficient fluctuations using a fast Fourier transform.

Transitional URANS show a constant behaviour of the Strouhal number, which is approximately constant at about $St \approx 0.2$ for the whole sub-critical range as shown in Figure 7.22. This behaviour, is consistent with C_D predictions and L_r/D, where insignificant changes are observed. For the fully turbulent SST, the Strouhal number is consistently overpredicted within the sub-critical regime, and in fact it is almost constant throughout all circular cylinder regimes.

The constant behaviour of the Strouhal number is also predicted by AFT-DDES as shown in Figure 7.22. In fact, transitional URANS and AFT-DDES are in agreement overall throughout the sub-critical regime prediction for the Strouhal number. This is consistent with experimental data reported by Schewe (1983) ($St \approx 0.2$).

With the increase of the Reynolds number, within the critical regime, transitional URANS show an increase in the Strouhal number, that is in agreement with literature data by Liu et al. (2019) and Schewe (1983). Conversely, the fully turbulent prediction does not show any significant change from its sub-critical behaviour, where the value remains almost constant at approximately $St \approx 0.26$. The AFT-DDES shows a similar

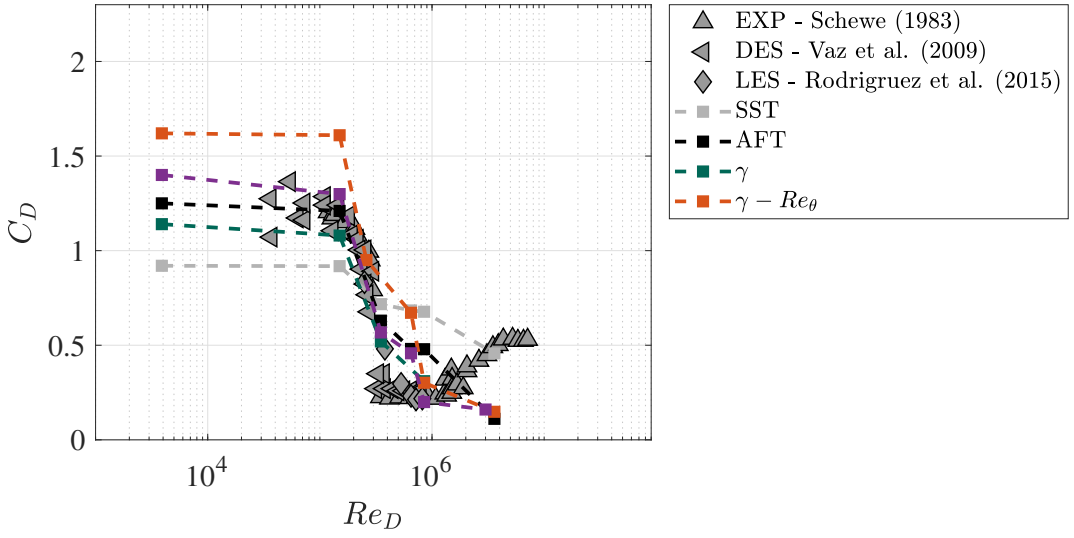

(a) $Tu = 0.4\%$

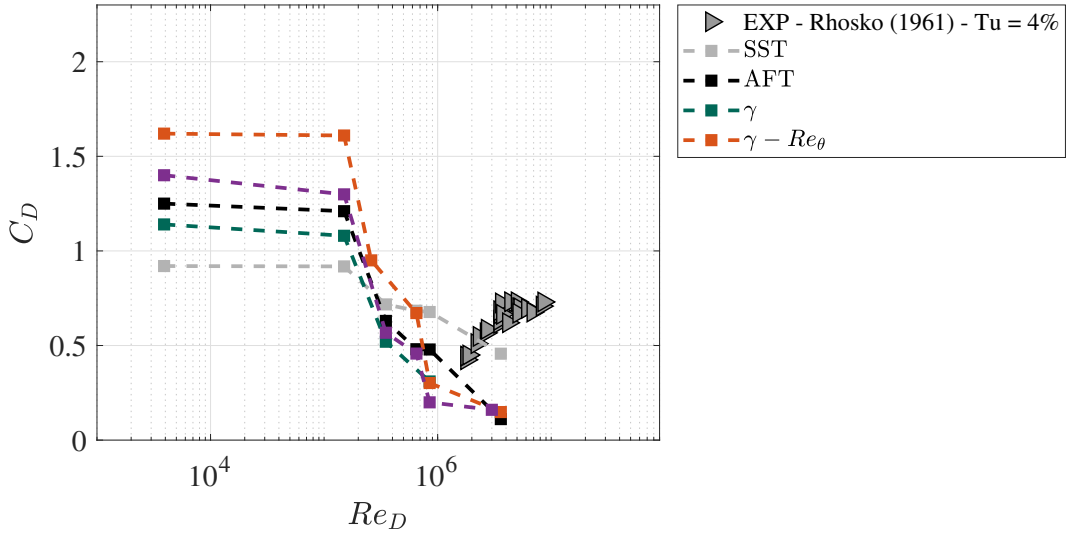

(b) $Tu = 4\%$

FIGURE 7.21: (a) C_D variation with Reynolds number using AFT, AFT-RSM and AFT-DDEs along Menter (1993), Langtry and Menter (2009), Menter et al. (2015) model predictions and literature data DES by Vaz et al. (2009), LES by Rodríguez et al. (2015) and experimental data by Schewe (1983) with $Tu = 0.4\%$, (b) C_D variation with Reynolds number using AFT, AFT-RSM and AFT-DDES along Menter (1993), Langtry and Menter (2009), Menter et al. (2015) model predictions and experimental data by Roshko (1961) with $Tu = 4\%$.

behaviour to transitional URANS methods and the agreement is good with Rodríguez et al. (2015), but over-predicting the values given by Schewe (1983) and Liu et al. (2019).

At the super-critical regime, the St predicted by transitional URANS rise from the critical regime but shows an almost constant behaviour with values approximately $St \approx 0.3 - 0.35$. The behaviour of the St is opposite to C_D. As commented above, the St

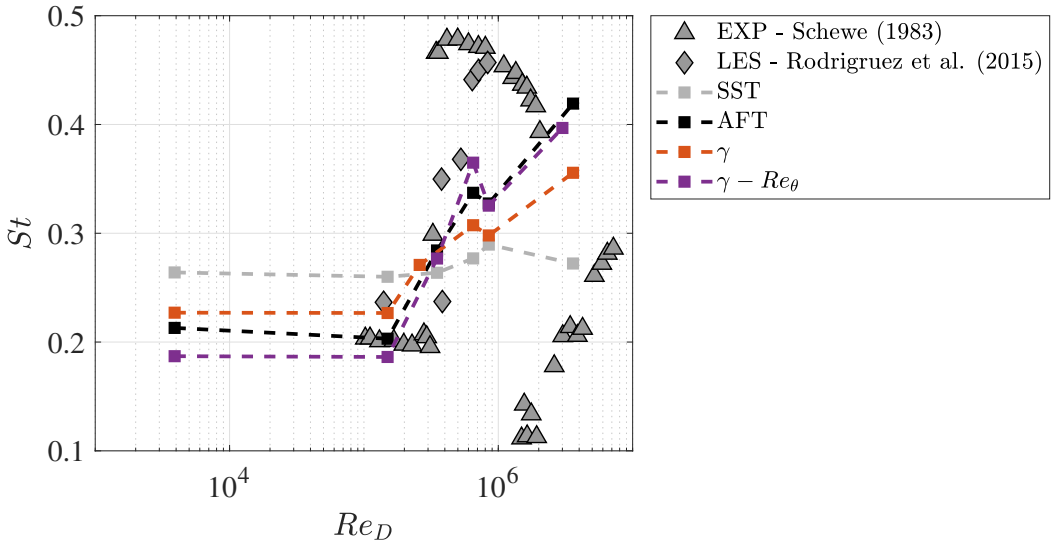

(a) $Tu = 0.4\%$

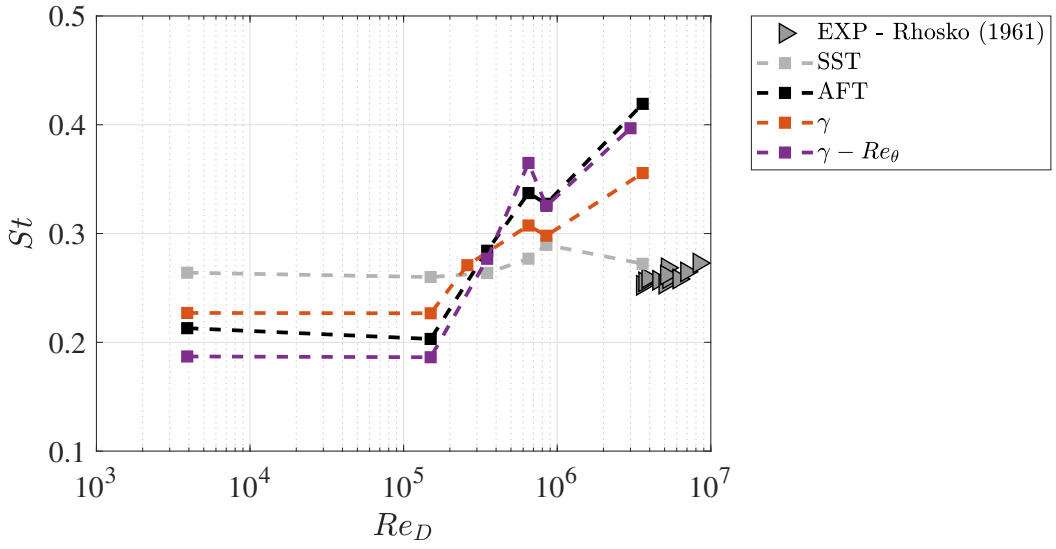

(b) $Tu = 4\%$

FIGURE 7.22: (a) St variation with Reynolds number using AFT, AFT-RSM and AFT-DDEs along Menter (1993), Langtry and Menter (2009), Menter et al. (2015) model predictions and literature data DES by Vaz et al. (2009), LES by Rodríguez et al. (2015) and experimental data by and Schewe (1983) with $Tu = 0.4\%$, (b) St variation with Reynolds number using AFT, AFT-RSM and AFT-DDES along Menter (1993), Langtry and Menter (2009), Menter et al. (2015) model predictions and experimental data by Schewe (1983) with $Tu = 4\%$.

number predicted by the fully turbulent SST model, does not show a large different behaviour from previous regimes ($St = 0.27 - 0.29$) as transitional URANS. Beyond $Re_D > 10^7$, the continuous rise of St by the transitional URANS is consistent with the continuous reduction of the C_D. The SST instead, shows a good agreement to literature data as for C_D beyond $Re_D > 10^7$.

Predictions using AFT-DDES at $Re_D = 8.5 \times 10^5$ show a better agreement than transitional URANS to literature data provided by Rodríguez et al. (2015) and Schewe (1983), as the turbulent structures within the wake are predicted. Similarly to transitional URANS, the AFT-DDES shows improvements against fully turbulent behaviour within the super-critical regime. Further predictions using AFT-DDES beyond $Re_D > 10^7$ are not performed in this thesis, but it is considered as future work.

As discussed in the C_D section, the constant behaviour of the St and the value predicted by the transitional URANS methods is consistent with the literature data given in Figure 7.22. Furthermore, this behaviour is consistent with Zdravkovich (1997) observations regarding the "stabilization effect" throughout the sub-critical regime.

With the interaction of separation and transition location as Reynolds increases to $Re_D = 3.5 \times 10^5$, the turbulent eddies roll up further away from the cylinder surface stretching the L_r/D and narrowing the wake. Thus, the shedding frequency increases as it is predicted by the transitional URANS models and the AFT-DDES too. The wake by the SST predictions remains almost unaltered and therefore the St predictions show a similar value all over the Reynolds spectrum.

As the Reynolds keeps increasing, the formation of the second bubble stabilizes the flow and the wake remains almost constant throughout the super-critical regime. This behaviour is consistent with transitional URANS predictions and the AFT-DDES given at $Re_D = 8.5 \times 10^5$. Nonetheless, the estimation is still underpredicted as the separation of the turbulent boundary layer is not close to the results reported by literature data as discussed in the super-critical section.

7.4.3 Minimum pressure ($-C_{p,min}$) and separation point $\phi_{i,sep}$

Predictions of the minimum pressure and the separation point are discussed together in this section and shown in Figure 7.23(a) and Figure 7.23(b) respectively for different Reynolds numbers for flow past a circular cylinder.

In the sub-critical regime, the behaviour of the $-C_{p,min}$ and separation point remains almost constant, or the changes are not significantly large as can be seen in both Figures. Transitional URANS tend to overpredict the minimum pressure value as well as the separation point as analysed in Sub-critical section. The change observed in the fully turbulent SST does not resemble an almost constant prediction of the minimum pressure but the turbulent separation point remains at approximately $\phi_{t,s} = 100°$, overpredicting transitional URANS values and literature results.

Predictions using AFT-DDES show a reduced $-C_{p,min}$ compared to transitional URANS, and consequently an earlier separation point as shown in Figure 7.23(b). However, the behaviour is shown to remain almost constant although there is a bit of an increase

regarding the minimum pressure from 1.2 to 1.4, but falls within the scatter data of the DES predictions given by Liu et al. (2019) within the sub-critical regime as the magenta triangle indicates.

Within the critical regime, transitional URANS show an increase of the $-C_{p,min}$, as well as the angle of the separation point as shown in Figure 7.23(a) and Figure 7.23(b). This trend persists in the super-critical regime. Predictions using AFT-DDES also predict this behaviour, which is in fact in agreement with literature data like Achenbach (1968) and Liu et al. (2019).

In the super-critical range, the behaviour remains almost constant with transitional URANS predictions. A similar behaviour is observed by the fully turbulent SST although this behaviour is already fully turbulent as changes in C_D and St are not comparable to those with the transitional approach.

Similarly to transitional approaches using URANS methods, the AFT-DDES shows a rise in the minimum pressure prediction and a delay of the turbulent separation compared to prior regimes. The rise is still underpredicted when compared to Rodríguez et al. (2015) in the super-critical regime, which is mainly due to the early separation predicted by the model.

Physically, the transitional URANS models and the AFT-DDES capture the constant behaviour throughout the sub-critical and super-critical regime, where the flow field does not change drastically with the increase of Reynolds number. The trend regarding the early laminar separation and the delayed turbulent separation sub-critical and super-critical respectively is physically sound although still underpredicted compared to literature data.

7.4.4 Base pressure $-C_{p,b}$ and recirculating length L_r/D

The base pressure and the recirculating length for the increased Reynolds number are shown in Figure 7.24(a) and Figure 7.24(b), respectively. Overall, transitional AFT and AFT-RSM show a decrease with the increase of Re_D. In fact, the L_r/D correlates to this with a decrease in the recirculating length for $Re_D > 1.5 \times 10^5$.

Predictions by AFT-DDES also show sensitivity to different regimes for flow past a circular cylinder. Throughout the sub-critical regime, for $Re_D < 1.5 \times 10^5$, both $-C_{p,b}$ and L_r/D is shown to be almost constant. With the increased complexity of the flow and the roll-up of the transition vortices downstream the wake, the wake is stretched as expected to values of $L_r/D = 1.1$ within the critical regime, although over the surface the flow still resembles sub-critical. $-C_{p,b}$ falls and L_r/D shows a drastic increase up to $L_r/D = 1.1$. With a further increase of Reynolds number, the flow enters the super-critical regime, where the AFT-DDES is capable of producing the laminar separation

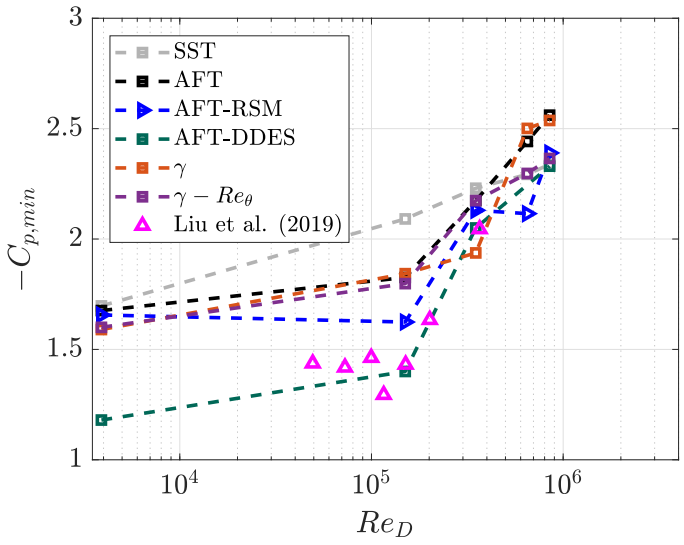

(a)

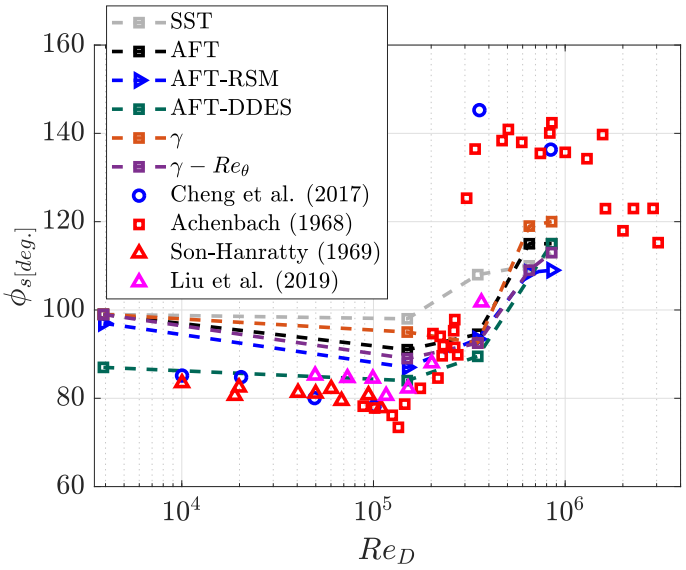

(b)

FIGURE 7.23: (a) $-C_{p,min}$ variation with Reynolds number using AFT, AFT-RSM and AFT-DDEs along Menter (1993), Langtry and Menter (2009), Menter et al. (2015) model predictions and literature LES by Rodríguez et al. (2015) and Cheng et al. (2017). (b) ϕ_s variation with Reynolds number using AFT, AFT-RSM and AFT-DDEs along Menter (1993), Langtry and Menter (2009), Menter et al. (2015) model predictions and literature LES by Rodríguez et al. (2015) and Cheng et al. (2017).

bubble as a difference of turbulent DDES hybridizations. This prediction is closer to full LES performance, where laminar boundary layers are solved. $-C_{p,b}$ reduces at supercritical, following the tendency given by Cheng et al. (2017) LES estimations. Similarly, L_r/D is also reduced but overpredicting the LES estimations of Rodríguez et al. (2015).

In this case, the relation for transitional URANS predictions is easy to see, since the reduction of $-C_{p,b}$ is translated in a shortening of the L_r/D. On the other hand, the

fully-turbulent approach does not show any significant relation as with an increase in Reynolds number, the recirculating length is constant.

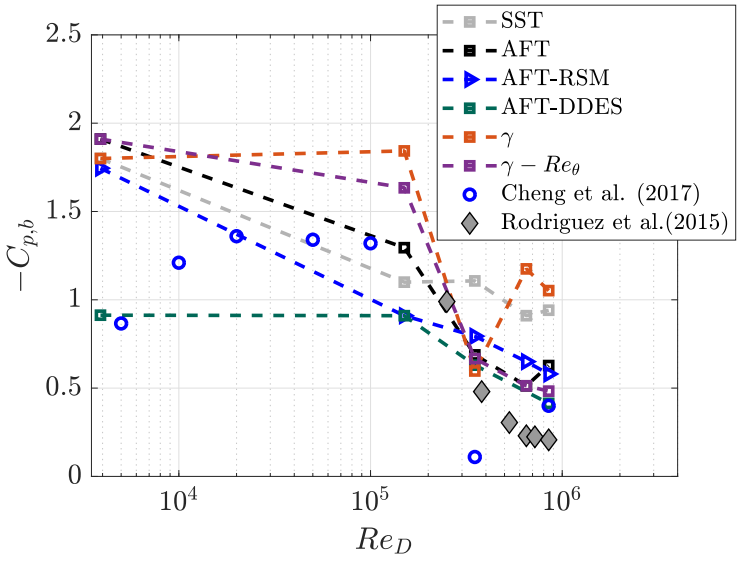

(a)

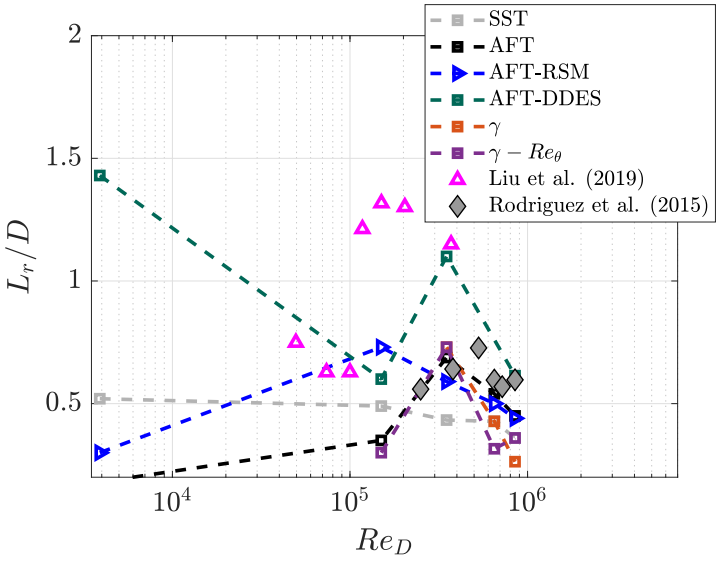

(b)

FIGURE 7.24: (a) $-C_{p,b}$ variation with Reynolds number using AFT, AFT-RSM and AFT-DDEs along Menter (1993), Langtry and Menter (2009), Menter et al. (2015) model predictions and literature LES by Rodríguez et al. (2015) and Cheng et al. (2017) and (b) L_r/D variation with Reynolds number using AFT, AFT-RSM and AFT-DDEs along Menter (1993), Langtry and Menter (2009), Menter et al. (2015) model predictions and literature LES by Rodríguez et al. (2015) and Liu et al. (2019)

7.5 Summary

In this section, the superior performance achieved by the AFT and AFT-RSM has been demonstrated compared to fully-turbulent approaches when transition occurs over the cylinder surface. The key improvements are seen in the laminar boundary layer description throughout the upstream face, with its consequent transition at critical and super-critical regime, where the laminar separation bubble is predicted too as summarized in Sections 7.1.3, 7.2.3 and 7.3.3.

The physical description of the transition behaviour provided by AFT and AFT-RSM also implies improvements in the prediction of C_D and St, with the change of trend within the critical region, followed by a closer description of the constant behaviour for both properties in the super-critical regime. The sensitivity for the critical and super-critical regimes are also resembled by the prediction of separation location and recirculation length. The fully turbulent approach is not sensitive and almost predicts a constant behaviour for all Reynolds numbers. This behaviour is also shown for the prediction of the separation location and the recirculation length.

Overall, the C_D and St increase and decrease respectively, when entering into the critical regime when utilising AFT and AFT-RSM for circular cylinder flow predictions. The separation point is delayed and the recirculation length is stretched as discussed by Zdravkovich (1997) and confirmed by later numerical studies.

The hybrid AFT-DDES has shown a much better performance at the lower sub-critical due to the capabilities of the LES mode to resolve the shear-layer transition when compared to AFT, AFT-RSM and evidently to fully-turbulent approaches. The improvement is also translated throughout the upper sub-critical, critical and super-critical regimes as already summarized in Sections 7.1.3, 7.2.3 and 7.3.3.

As prior, not only the C_f and C_p predictions have improved but also the overall estimations of the C_D and St, along with the separation location and the recirculation length, where the LES prediction demonstrates its superior performance to URANS.

The C_D values at the super-critical are in better agreement with numerical studies as well as the $St \approx 0.4$, where the increase is in better agreement to Schewe (1983) and LES simulations by Rodríguez et al. (2015). The separation point is shown to be delayed as the Reynolds number is increased, following similar results to AFT and AFT-RSM. Ultimately, as mentioned the activation of the LES mode away from the cylinder surface provides an improved performance compared to URANS transitional methods. In fact, in the critical region the stretching of the wake is evident up to $L_r/D = 1.2$ and once the flow enters super-critical, the L_r/D is reduced to approximately 0.6.

Hence, the superior performance by AFT, AFT-RSM and AFT-DDES over fully-turbulent approaches for flow past circular cylinder predictions at high-Reynolds numbers has been

demonstrated. However, it is important to remind the limitations when using URANS for the shear-layer transition at lower sub-critical and the wake prediction throughout the Reynolds number spectrum compared to the AFT-DDES approach.

Chapter 8

Analysis of the Amplification Factor Transport Correlations

As discussed in Chapter 6, it has been observed that the performance of transitional models where correlations are built via linear stability theory as the AFT model by Coder (2019), and transitional methods based on empirical data such as Langtry and Menter (2009) and Menter et al. (2015), have improved performance when predicting transition over the cylinder surface. This also results in improvements for overall parameters like C_D and St. This indicates that using empirical, or analytical results for a flat plate geometry as the AFT does, has an impact on transition prediction when testing over a complex flow-field like the one resulting in flow past a circular cylinder, where pressure gradient and curvature are significant. The purpose of developing these new correlations is to improve the transition predictions for flow past a circular cylinder. These new correlations have been produced via data fitting which produces an exponential form as it is presented in this Chapter.

Thus, the first part of this Chapter 8, is to use LES data for flow past a circular cylinder by Rodríguez et al. (2015) to demonstrate the differences regarding the boundary layer characteristics and rate of amplification factor to the original Falkner-Skan similarity profiles over a flat-plate. The laminar characteristics of the boundary layer developing over the cylinder surface are analysed for two Reynolds numbers, $Re_D = 1.5 \times 10^5$ and $Re_D = 5.3 \times 10^5$ and the behaviour of the four relations presented in Section 8.1 will be discussed and compared to current correlations of the AFT model.

With the results obtained by LES simulations, the second part of the chapter presents new four correlations specific for circular cylinder flow in Section 8.2, that are tested at different circular cylinder flow regimes to demonstrate, that further analysis can be used for the improvement of the predictions using transitional URANS models like AFT-based ones for flow past a circular cylinder.

8.1 Initial correlations

The amplification factor transport equation is dominated by the production term (first term on the right-hand side in Equation 3.2), which controls the rate of amplification of the most unstable frequency in terms of Re_θ. Drela and Giles (1987) proposed a correlation for $\mathrm{d}\bar{n}/\mathrm{d}Re_\theta$ based on laminar boundary layer similarity velocity profiles together with the correlation for the critical Reynolds number $Re_{\theta,\mathrm{cr}}$ as shown later in Equations 8.3 and 8.4 in terms of an integral shape factor H_{12}.

Since the AFT model does not compute any integral boundary-layer property, H_{12} is estimated via a local shape factor (H_L). The local shape factor H_L is proposed by Menter et al. (2015), based on the evaluation of a local boundary layer shape factor or pressure-gradient parameter, and is defined as

$$H_L = \frac{d_w^2}{\nu}\frac{\mathrm{d}V}{\mathrm{d}y}, \tag{8.1}$$

where d_w is the wall distance and $\mathrm{d}V/\mathrm{d}y$ denotes the gradient of the wall-normal velocity in the wall-normal direction. H_L is computed everywhere but its maximum value (approximately in the middle of the boundary layer) is the one used to establish the correlations by Coder and Maughmer (2014). This H_L estimation is related to the integral shape factor H_{12} from Falkner-Skan similarity profiles as defined in Equation 8.2.

$$H_{12} = 0.376960 + \sqrt{\frac{H_L + 2.453432}{0.653181}}. \tag{8.2}$$

$$\frac{\mathrm{d}\widetilde{n}}{\mathrm{d}Re_\theta} = 0.028(H_{12}-1) - 0.0345\exp\left[-\left(\frac{3.87}{H_{12}-1} - 2.52\right)^2\right] \tag{8.3}$$

$$\log_{10}(Re_{\theta,\mathrm{cr}}) = 0.7\tanh\left(\frac{14}{H_{12}-1} - 9.24\right) + \left(\frac{2.492}{(H_{12}-1)^{0.43}}\right) + 0.62 \tag{8.4}$$

The F_{growth} function encapsulates the effects of the growing boundary layer over separation bubbles by the use of two empirical correlations proposed by Drela and Giles (1987) based on solutions from the Falkner-Skan similarity profiles. F_{crit} is a function that determines if the local boundary-layer is capable of containing instabilities, switching on or off the production of $\tilde{n}$. Since the AFT model does not compute the momentum thickness at any point, k_{v} is needed to estimate the critical momentum-thickness Reynolds number Coder (2019). The function k_{v} describes the proportionality of the two Reynolds numbers Re_{v} and Re_θ from Falkner-Skan similarity profiles. The proportionality function is defined as

$$k_{\mathrm{v}} = 0.4036H_{12}^2 - 2.5394H_{12} + 4.3273 \;\text{ where }\; Re_{\mathrm{v}} = k_{\mathrm{v}} Re_\theta. \tag{8.5}$$

The vorticity Reynolds number ($Re_{\mathrm{v}} = Sd_w^2/(\nu + \nu_t)$) can be computed at every single point in the domain, so if it is larger than its critical value, the F_{crit} function equals 1. Otherwise it will remain zero and no unstable modes will be amplified within the boundary layer. The AFT model is coupled to a fully-turbulent approach, specifically the Spalart-Allmaras turbulence model, via the intermittency (γ) transport equation. Details of the model can be found in Coder (2019).

Even though correlations are estimated from the Falkner-Skan profiles, the physics of the transition produced by the model in a complex flow field like the flow past a circular cylinder is in reasonable agreement with experimental and LES data as discussed in Chapter 6. In the sub-critical regime, the model improves the predictions when compared to fully turbulent but the laminar separation onset requires a deeper analysis. However, the transition onset is not properly estimated at critical, super-critical regimes as shown in Chapter 6. Hence, the aim is to obtain correlations for $\mathrm{d}\tilde{n}/\mathrm{d}Re_\theta$ and $Re_{\theta,\mathrm{cr}}$ for a fixed shape factor by performing a stability analysis for velocity profiles from flow past a circular cylinder from sub-critical to trans-critical regimes to improve the transition prediction. Another thing to quantify is how the evolution of the proportionality between the local shape factor H_L and the integral shape factor H_{12} differs from the original one proposed based on similarity profiles. Similar to the evolution of H_{12} in terms of H_L, the proportionality between Re_{v} and Re_θ for flow past a circular cylinder is analysed and compared to the current correlations in Chapter 6.

Laminar velocity profiles to obtain the realistic behaviour for flow past circular cylinder are extracted from Rodríguez et al. (2015) LES simulations at $Re_D = 1\times10^5$ and $Re_D = 5.3\times10^5$, where the Reynolds number is based on the cylinder diameter. Several velocity profiles are extracted at different angles and post-processed accordingly to obtain the relations between $H_{12} = f(H_L)$ and $k_v = f(H_{12})$. Furthermore, the temporal stability analysis is computed for every velocity profile solving the Orr-Sommerfeld equation for small disturbances. The 4^{th} order differential equation is solved with a finite difference method for a range of wavenumbers (α) and Re numbers to initially achieve the neutral stability curves and consequently the critical Re for the flow around a circular cylinder at different flow regimes. From the temporal stability analysis, the spatial amplification factor ($\tilde{n}$) in terms of Re_θ can be estimated using Gaster's transformation proposed in Gaster (1969). The $\mathrm{d}\tilde{n}/\mathrm{d}Re_\theta$ profiles are approximated to slopes for a fixed shape factor similar to what is proposed by Drela and Giles (1987) and Gleyzes et al. (1985).

8.2 Circular cylinder vs Falkner-Skan profiles

This section analyses the differences for the four correlations integrated into the AFT model to determine whether and where the transition occurs, with post-processed LES data at $Re_D = 1.5 \times 10^5$ and $Re_D = 5.3 \times 10^5$. The variations of the H_L, H_{12} and k_v are determined by integrating the velocity profiles, while $Re_{\theta,cr}$ and $d\tilde{n}/dRe_\theta$ are estimated via linear stability analysis, similarly to Drela and Giles (1987), but for the LES velocity profiles of flow over a circular cylinder by Rodríguez et al. (2015).

The LES simulations were performed by a group of researchers led by Dr Ivette Rodriguez at the Barcelona Supercomuting Center (BSC) Rodríguez et al. (2015)-Rodriguez and Lehmkuhl (2021). Simulations at Reynolds number of 1×10^5 and 5.3×10^5 were provided, where the Reynolds number is defined in terms of the free-stream velocity and the cylinder diameter. The dimensions of the computational domain being of $x = [-16D, 16D]$; $y = [-10D, 10D]$ for the stream- and cross-stream directions, whereas the span-wise direction $z = [0,\ 0.5\pi D]$ is considered. The resultant blockage ratio between the size of the computational domain in the cross-stream direction and the cylinder diameter is 5%.

The velocity was set to uniform at the inflow $(u, v, w) = (1, 0, 0)$, symmetry conditions at the top and bottom boundaries of the domain, while at the outlet a pressure-based condition is used. On the cylinder surface, no-slip conditions are applied. As for the span-wise direction, periodic boundary conditions are prescribed.

To capture the complexities of the physical phenomenon in the zone close to the cylinder; i.e. delayed separation, transition to turbulence upon separation, reattachment, and further turbulent separation, amongst others; the boundary layer should be well-resolved. Control volumes are clustered towards the cylinder wall and prism layers are constructed so as the non-dimensional wall distance is kept below $y^+ < 2$.

8.2.1 Relation between the integral shape factor (H_{12}) and local shape factor (H_L)

To determine the critical Reynolds number (when the flow is unstable and is able to develop instabilities within the boundary layer), it is necessary to know the state of the boundary layer at any given point in the domain. For that, as described in Section 2.3, it is common to use the momentum-thickness θ and integral shape factor H_{12}, to provide information about the state of the boundary layer and the surrounding conditions.

Hence, the problem is how to estimate integral parameters of the boundary layer such as θ and H_{12}, without having to integrate through the wall-normal direction the boundary layer in a massively parallelized environment like current CFD frameworks. As a

workaround, the estimation of the integral shape factor H_{12} is based on a local estimation of the same, so-called local shape factor by Coder (2017). Then, a relation is established between both factors that allow H_{12} to be locally computed and to be used as the pivotal function of the rest of the correlations, as described in Section 8.1.

The definition of the local shape factor, given in Equation 8.1, is inherited from the proposal of Menter et al. (2015). The main goal behind this formulation was to simplify the complexity of the empirical correlations constructed in Langtry and Menter (2009) to determine the local pressure gradient. Menter et al. (2015) proposed this simplification by assuming the following for a flat plate:

$$\lambda_\theta = \frac{\rho\theta^2}{\mu}\frac{dU}{ds} = -\frac{\rho\theta^2}{\mu}\frac{dV}{dy} \tag{8.6}$$

where V and y are wall-normal velocity and coordinate respectively, that can be estimated for general geometries as

$$\frac{dV}{dy} \equiv \nabla(\overrightarrow{n} \cdot \overrightarrow{V}) \cdot \overrightarrow{n}. \tag{8.7}$$

From Equation 8.6, it can be seen that θ is replaced by the wall-distance d_w. This was assumed by Menter et al. (2015) because the activation of γ-model occurs at approximately the middle of the boundary layer, and at that location, the scaling of θ can be assumed as half of the boundary layer thickness and therefore $d_w = \delta/2 \sim \theta$. At that point is where a maximum of the local shape factor is present, therefore a monotonic correlation can be established. However, this is not true for the boundary layer developing over a circular cylinder, where the values of θ are approximately $\theta \sim \delta/3 - \delta/4$ for the boundary layer profiles developing over the cylinder surface. Therefore, assuming a similar pressure gradient condition estimated by $\mathrm{d}V/\mathrm{d}y$, the resultant H_L is overpredicted compared to the same scenario for flow over a circular cylinder. Consequently, a larger H_L predicts a larger H_{12} when employing the current correlations for the AFT model than the integral shape factor from circular cylinder profiles.

The local and integral shape factors are calculated from velocity profiles of flow over a circular cylinder, as shown in Figure 8.1(a) for $Re_D = 1 \times 10^5$ and 5.3×10^5, along with the original correlation proposed by Coder (2019). It can be seen that the results computed from cylinder LES data in the literature show a less pronounced growth of the H_{12}. This is due to the acceleration region in the upstream face of the circular cylinder, which delays the growth of the boundary layer. The agreement with the original AFT is similar to the original correlation at the very early stages of the boundary layer growth. However, as the boundary layer grows over the surface, the correlation is not followed by any of the two sets of LES data as the average behaviour is shown in Figure 8.1(b).

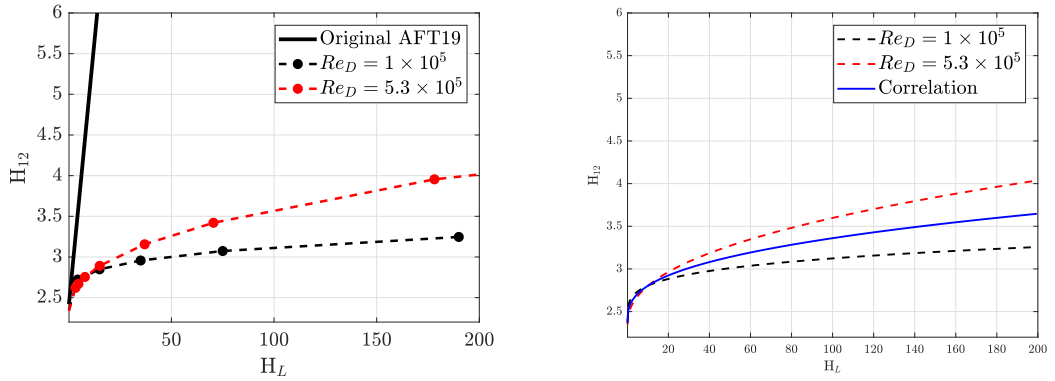

(a) (b)

FIGURE 8.1: (a) The behaviour of H_{12} in terms of H_L for LES predictions at $Re_D = 1 \times 10^5$ and 5.3×10^5 and (b) the averaged correlation from two Reynolds numbers.

Hence, the aim here is to transform the correlation line given in Figure 8.2 into an equation that can be introduced within the AFT transitional framework to predict a fixed H_{12} in terms of H_L for the development of the boundary layer for flow past a circular cylinder. Due to the scarce number of LES simulations, we opted to use an average of the results for the two Reynolds numbers, so that mainly the tendency is retained given the difference observed in the Falkner-Skan development of the H_{12} in terms of H_L. This way, the new relation between the integral shape factor and the local shape factor that substitutes Equation 8.2 reads as

$$H_{12} = 0.1663 H_L^{0.3793} + 2.406 \tag{8.8}$$

8.2.2 Relation between Re_θ and Re_V via proportionality function k_v

With the estimation of the relation between H_{12} and H_L, the information on the shape-factor is readily available at any given grid point within the computational domain. However, either the displacement thickness or momentum thickness is necessary to determine whether the flow can contain and develop instabilities. The workaround proposed by Coder and Maughmer (2014) is to find a correlation between the vorticity Reynolds number Re_V and the momentum thickness Reynolds number Re_θ. The choice of the vorticity Reynolds number is because it can be computed at any given point within the flow field and has a maximum at approximately $y \sim \delta/2$. The maximum value is taken as the Re_V value, which grows monotonically with H_{12}. On the other hand, Re_θ is defined as $Re_\theta = \theta U/\nu$ for any given velocity profile. Thus, the proportionality function k_v can be found as $k_\mathrm{v} = Re_\mathrm{v}/Re_\theta$, as given in Equation 8.5.

The original correlation from Equation 8.5 is presented in Figure 8.2(a) along with updated correlations from LES data of circular cylinder profiles. As shown in Figure 8.2(a),

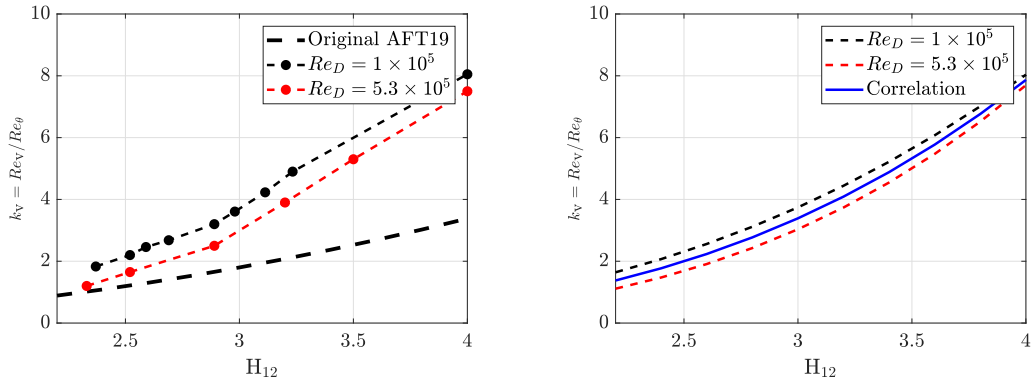

FIGURE 8.2: (a) The behaviour of k_v in terms of H_{12} for LES predictions at $Re_D = 1 \times 10^5$ and 5.3×10^5 and (b) the averaged correlation from the two Reynolds numbers.

the k_v predicted by the correlation is smaller than the computed ratio from the circular cylinder velocity profiles. The ratio differs due to the growth of the boundary layer, where the boundary layer property θ is over-predicted when compared to current boundary layer characteristics. Hence, for the velocity profiles around the circular cylinder, the momentum thickness is smaller than the one predicted by the correlations due to the definition of H_L. Therefore increasing the ratio k_v. This new tendency is estimated in the same way as Equation 8.8 and reads as

$$k_\mathrm{v} = 0.1048 H_{12}^{3.055} + 0.9875. \tag{8.9}$$

Equation 8.9 represents an average of behaviour for the proportionality function $k_\mathrm{v} = Re_v/Re_\theta$ between $Re_D = 1 \times 10^5$ and 5.3×10^5, which will replace Equation 8.5 in the original AFT that is represented in Figure 8.2(b).

8.2.3 Function for the critical Reynolds number Re_{cr}

The k_v proportionality function estimates θ in terms of the Reynolds number via Re_v at any given point, thus allowing to compare to the critical momentum-thickness expressed as a Reynolds number to determine whether instabilities can be developed. To determine the critical value of the Reynolds number in terms of θ, the Orr-Sommerfeld equation for small disturbances is solved iteratively for a given laminar velocity profile extracted from the LES simulations of flow over a circular cylinder by Rodríguez et al. (2015). Then, the neutral curve is estimated ($\alpha_i = 0$) and the furthest point with neutral amplification on the left side of the plane is taken as $Re_{\theta,cr}$.

Figure 8.3(a) shows the behaviour of the critical momentum thickness Reynolds number as a function of the integral shape factor using Equation 8.4 along with the critical value

achieved through the stability analysis for flow over a circular cylinder. For the profiles developing on the upstream face with shape factors up to approximately 2.5 to 2.6, the critical Reynolds number is predicted to be delayed when compared to the values predicted by the correlations. On the other hand, as the velocity profiles start to exhibit an inflection point, the critical Reynolds number is reduced.

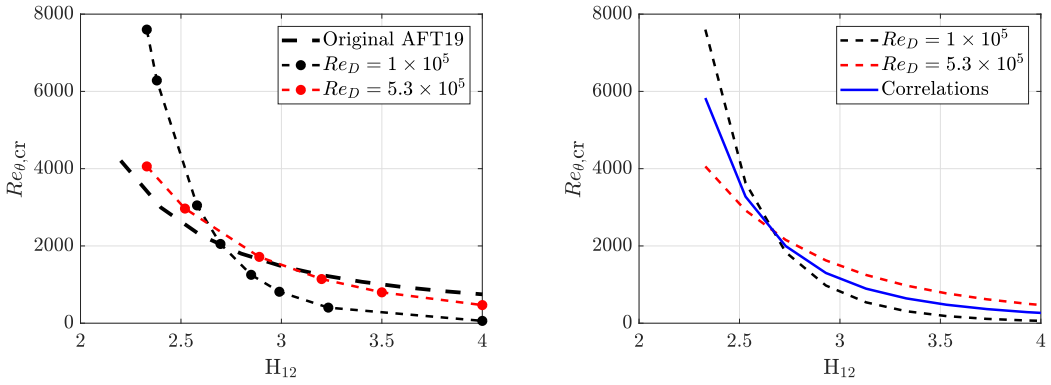

FIGURE 8.3: (a) The behaviour of $Re_{\theta,cr}$ in terms of H_{12} for LES predictions at $Re_D = 1 \times 10^5$ and 5.3×10^5 and (b) the averaged correlation from two Reynolds numbers.

Following the same rationale as the two prior new correlations, Equation 8.10 uses the average behaviour for the $Re_{\theta,\mathrm{cr}}$ that will replace Equation 8.4 in the modified AFT model and it is represented in Figure 8.3(b).

$$Re_{\theta,\mathrm{cr}} = 1.265 \times 10^6 H_{12}^{-6.361} + 2.804 \tag{8.10}$$

8.2.4 Function for the growth of amplification factor dn/dRe_θ

With the estimation of the $Re_{\theta,cr}$, the F_{crit} function discerns whether the local Re_θ is larger than $Re_{\theta,cr}$. If that is the case, the model will start to transport instabilities throughout the laminar boundary layer with the production of $\tilde{n}$ in Equation 3.2. The amplification factor is estimated along different dimensionless frequency lines within the instability region and then the locus of the maximum amplified frequencies is taken to construct the envelope curve.

Figure 8.4 shows the $\mathrm{d}\tilde{n}/\mathrm{d}Re_\theta$ for four different shape factors calculated from LES data of flow over a circular cylinder by Rodríguez et al. (2015). Over the first part of the acceleration region, the rate of amplification is reduced when compared to the original AFT correlation given in Equation 8.3. As soon as the flow gets closer to a stagnation point, with the appearance of the inflection points in the velocity profiles, the rate is shown to grow faster than predicted by the original AFT correlation. Nonetheless, it

can be seen in Figure 8.4 how the differences are not large with the increase of the amplification factor.

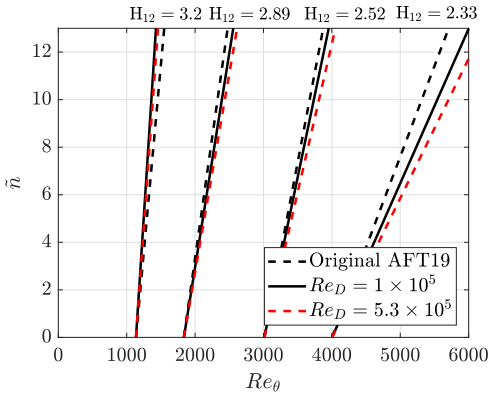

FIGURE 8.4: The behaviour of dn/dRe_θ in terms of H_{12} for LES predictions at $Re_D = 1 \times 10^5$ and 5.3×10^5.

Ultimately, the growth rate of the amplification factor using the new results from LES data by Rodríguez et al. (2015) for flow past a circular cylinder reads as

$$\mathrm{d}\tilde{n}/\mathrm{d}Re_{\theta,\mathrm{cr}} = 1.039 \times 10^{-8} H_{12}^{13.78} + 3.074 \times 10^{-3}, \tag{8.11}$$

where the rationale for using this single equation is to retain the averaged behaviour for sub-critical and super-critical regimes due to the scarce set of LES simulations obtained.

8.3 Analysis of Correlations Impact

This section aims to analyse the effect of the new correlations for flow past a circular cylinder at the sub-critical, critical and super-critical regimes. Results are compared with original estimations, which have been discussed in detail in Chapter 7. Furthermore, the limitations of the newer predictions are discussed and further work is suggested for the improvement of such estimations.

8.3.1 Sub-critical regime, $Re_D = 1 \times 10^5$

The sub-critical regime does not exhibit any transition over the cylinder surface in any of the data available in the literature. Therefore, the impact of the updated relationships is expected to be minimal. It is shown in Figure 8.5(a) how the impact on the prediction by the modified AFT model is negligible since the laminar separation point is still delayed until approximately $\phi_{sep} = 88 - 90°$. As shown as well with $Re_D = 3900$ in Chapter 7, there is always a consistent delay in the laminar separation throughout the sub-critical

regime. This is also evident with the overprediction of the $-C_{p,min}$ in Figure 8.5(b), due to the large favourable pressure gradient region.

A interesting comparison is to run a laminar case at the same Reynolds number to understand how the purely laminar flow behaves on the upstream face. Downstream from that, the transition should occur within the shear layers but up to the separation point, only the pressure gradient and the state of the boundary layer are key factors for its separation. As shown in Figure 8.5(a), the laminar solution performs as expected a separation at approximately $\phi = 82°$. This is in good agreement with Achenbach (1968) measurements at $Re_D = 10^5$. The laminar, the AFT with $N_{crit} = 9$ and $N_{crit} = 15$ show three different behaviours after the separation, which are due to the reattachment of counter-rotating vortices within the wake. These vortices are also evident in the C_p profile beyond 90° and the agreement by the use of $N_{crit} = 15$ with $-C_{p,min}$ measurements by Cantwell and Coles (1983) is better than AFT, in fact, similar to AFT-DDES shown in Chapter 7.

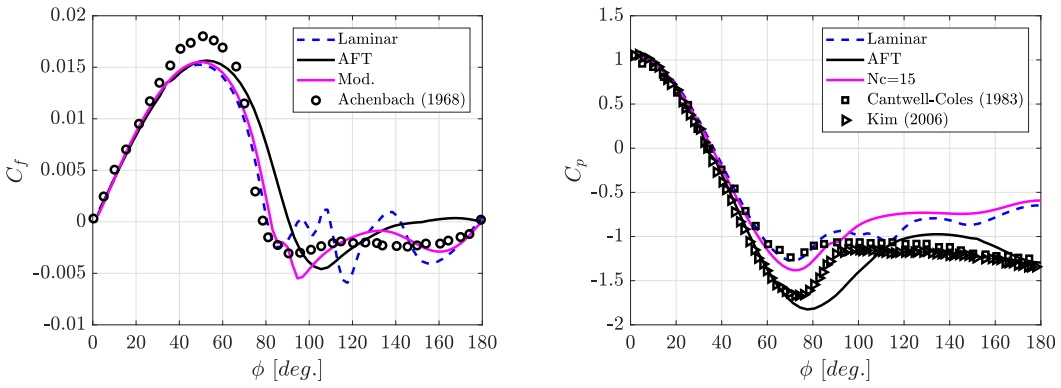

(a) (b)

FIGURE 8.5: (a) C_f predictions within the supercritical regime at $Re_D = 1.5 \times 10^5$ with the original AFT and modified version along Achenbach (1968) measurements $Re_D = 1.5 \times 10^5$ and (b) C_p with LES data by Kim (2006) and measurements by Cantwell and Coles (1983)

.

From observation of the C_f and C_p profiles predicted by the AFT, it may seem that there is an energization of the boundary layer at the vicinity of separation thus it remains attached longer than expected from measurements, and demonstrated by the laminar solution. Figure 8.6(b) shows how the growth of intermittency is rapid when the flow approaches the separation point. See in Figure 8.6(a) how intermittency reaches values of approximately 0.2-0.3 at about the separation position, and then the separation occurs right after that as averaged streamlines of mean velocity indicate. Thus, it may be possible that the boundary layer is not completely laminar at all, delaying its separation.

In Figure 8.7, the prediction with $N_{crit} = 15$ is shown. There, it can be seen how intermittency starts growing a little bit further away than observed when using $N_{crit} = 9$,

according to our boundary conditions. After the separation both show a rapid increase in the n factor. Furthermore, it can be seen how similar the averaged streamlines for the laminar solution and $N_{crit} = 15$ cases are in Figures 8.8-8.7.

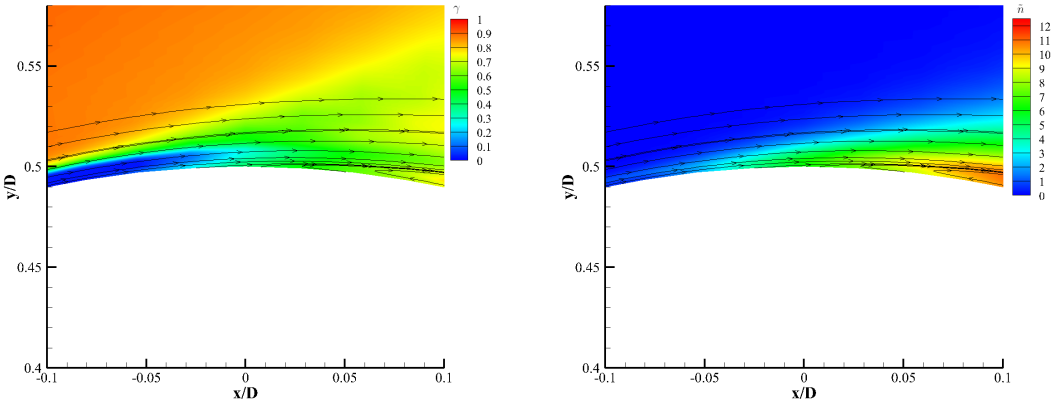

(a) (b)

FIGURE 8.6: (a) γ contour and (b) $\tilde{n}$ for AFT with $N_{crit} = 9$ with averaged streamlines.

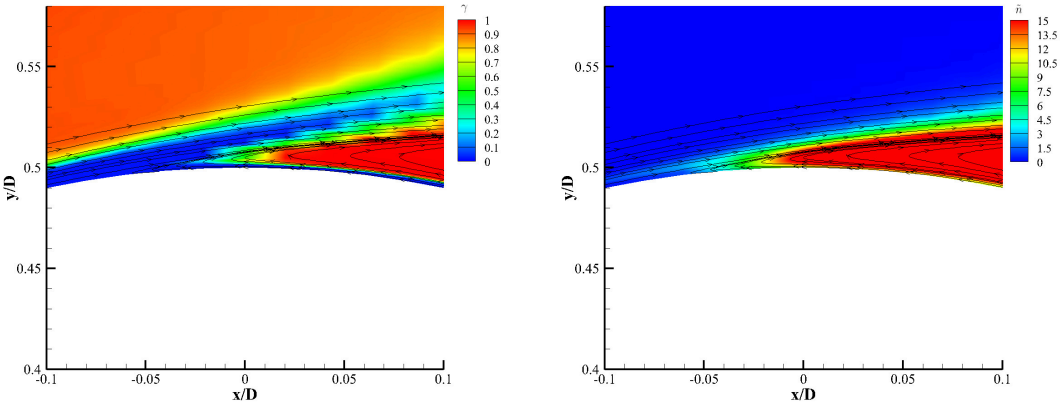

(a) (b)

FIGURE 8.7: (a) γ contour and (b) $\tilde{n}$ for AFT with $N_{crit} = 15$ with averaged streamlines.

Hence, with the delay of transition seems that the separation is predicted where it is expected theoretically. Thus, this problem requires further investigation especially since the $\tilde{n}$ grows very rapidly after the approximate position of separation and it can interfere with the final solution as demonstrated for $N_{crit} = 9$. A possibility could be to generate a ramp function for gradual growth rather than a very steep increase, since when the transition condition is delayed, the separation is not impacted.

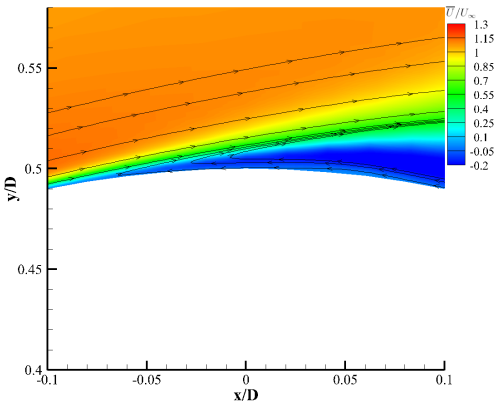

FIGURE 8.8: Velocity magnitude with averaged streamlines for laminar flow solution.

8.3.2 Critical regime, $Re_D = 3.5 \times 10^5$

The complexity of this regime is still a challenge to solve with transitional URANS models. The main problem in this regime is the intermittent appearance of one laminar separation bubble due to the interaction of the attached boundary layer and the separated shear layer. This occurrence is strongly dependent on initial conditions as discussed by Zdravkovich (1997) and presented with LES simulations by Rodríguez et al. (2015) and Cheng et al. (2017).

As shown in Figure 8.10(a), results from the original and modified AFT models still resemble a sub-critical-like behaviour on both sides of the cylinder. The separation bubble is rather small again as shown in prediction in the Chapter 7. Thus, this region can be considered a critical regime with two separation bubbles, as the C_D continues decreasing with the increased Reynolds number. The separation-transition interaction expected within this region is crucial for the description of the flow physics. In this case, when using URANS for the complete domain, the flow undergoes transition right after separation due to the rapid increase of $\tilde{n}$ after that.

Furthermore, it is necessary to further analyse a larger Reynolds number range within that regime to completely understand how integral properties vary against original Amplification Factor Transport correlations. In this case, only two Reynolds numbers were available outside of this regime.

8.3.3 Super-critical regime, $Re_D = 8.5 \times 10^5$

With the increased Reynolds number, the flow field recovers its symmetry with the appearance of two stable laminar separation bubbles on each side of the circular cylinder in the super-critical regime. In contrast to the sub-critical scenario, the flow-field enhances its momentum exchange to undergo a transition in the form of a laminar separation

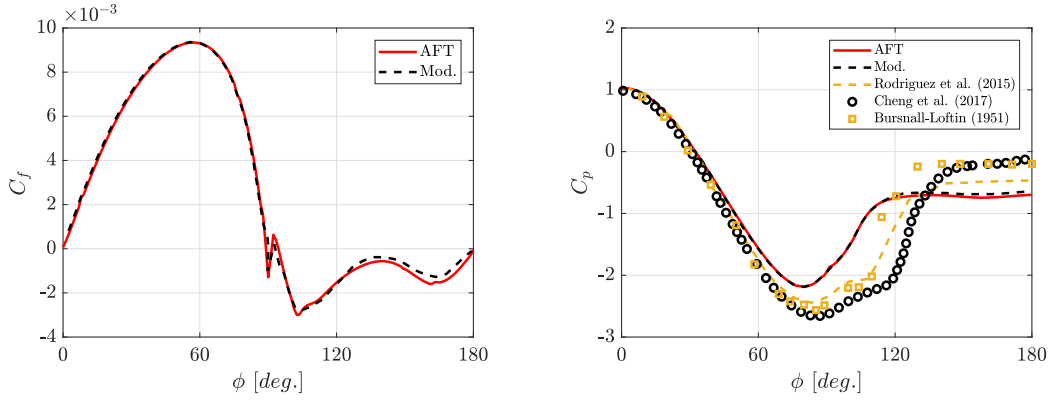

(a) (b)

FIGURE 8.9: (a) C_f predictions within the critical regime at $Re_D = 3.5 \times 10^5$ with the original AFT and modified version along Cheng et al. (2017) LES predictions at $Re_D = 3.5 \times 10^5$ and (b) C_p with LES data by Rodríguez et al. (2015), Cheng et al. (2017) and measurements by Bursnall and Loftin (1951) measurements

.

bubble and reattach back onto the cylinder surface. Then, a fully-turbulent boundary layer develops downstream until it cannot withstand the adverse pressure gradient. Separation of the turbulent boundary layer is consistently separated at $\phi_{t,sep} \sim 140°$ as discussed by Cheng et al. (2017) and Rodríguez et al. (2015).

The main problem observed in the prior analysis of the super-critical regime was the early separation onset and consequently the early turbulent reattachment and turbulent separation point. Figure 8.10(b) shows the prediction for the original AFT model along with the new modified version. It is shown how there is a small improvement in terms of separation and reattachment points when using the modified correlations. The difference is approximately consistent in 2° when compared to the original behaviour. This small displacement in the separation point is also translated to a small increment of the $-C_{p,min}$.

Thus, even the small improvement, gives some promising indications that with further experimental and high-fidelity simulations an improved prediction of transition can be achieved with the AFT method. Furthermore, as demonstrated in Chapter 6, the blending of an LES method with the transitional AFT can provide similar predictions to pure LES. Not only that, but the analysis of URANS AFT and AFT-RSM shows improvements compared to fully-turbulent SST.

8.3.4 Summary

The incorporation of the new correlations has shown promising results in the super-critical regime, while the analysis within the sub-critical regime has opened a new branch of study regarding the effect of N_{crit} over the laminar separation of the boundary layer.

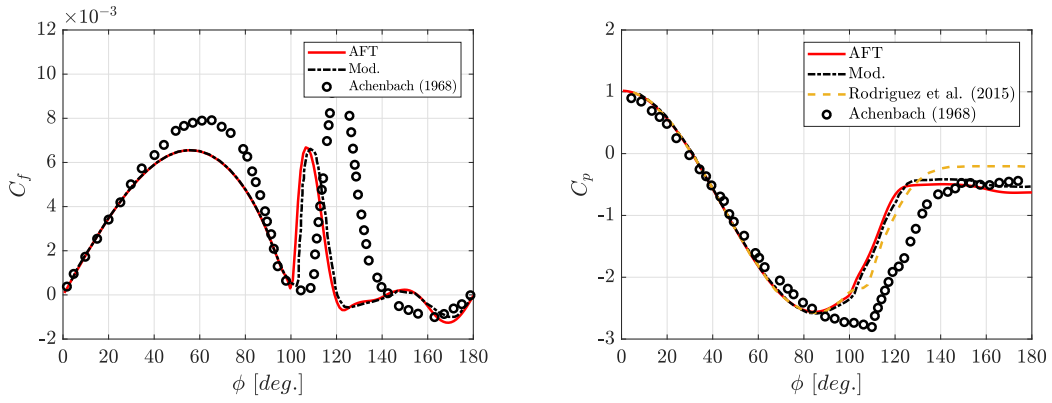

(a) (b)

FIGURE 8.10: (a) C_f predictions within the supercritical regime at $Re_D = 8.5 \times 10^5$ with the original AFT and modified version along Achenbach (1968) measurements $Re_D = 8.5 \times 10^5$ and (b) C_p with LES data by Rodríguez et al. (2015) and measurements by Achenbach (1968)

.

As shown in Section 8.3.1, there is an impact regarding the value of N_{crit} used to the location of the laminar separation position, which suggests an influence on a small portion of the boundary layer, thus delaying the separation. With the increased value of N_{crit}, the position resembles the location predicted by a fully-laminar estimation.

Evidently as expected, in the critical region there is not any improvement at all, due to the complexity of the flow field and the incapability of the URANS approaches to predict the small turbulent structures that rule the separation-transition interaction discussed in Chapter 2.

In the super-critical regime, the new correlations show a slight delay in the transition position as shown in Figure 4.10(b). With the scarce LES simulations, the prediction is improved by approximately 2° when compared to the original AFT correlations. This behaviour suggests that the correction on the integral estimation of boundary layer properties and the correction on the rate of amplification factor have an impact on the transition prediction, and it is improved compared to Falkner-Skan similarity profiles. Thus, setting a stone for further investigation and improvement of the correlations.

8.4 Conclusions

This chapter has presented the initial steps to improve the behaviour of the AFT model for flow past a circular cylinder, from the results observed and discussed in Chapter 6. Although improvements have shown only 2° in the super-critical regime, it is something that shows promising behaviour with an increase of data from LES simulations or even experimental measurements.

It has been discussed how the boundary layer parameters are important for a proper estimation of the momentum-thickness Reynolds number within the transitional framework of the AFT model. The nature of the flow field shows a completely different tendency specifically regarding the H_{12} vs H_L, which is crucial for the estimation of the θ, the critical Reynolds number and therefore the growth rate of the amplification factor. This is a path to follow to improve current correlations, and it is starting to become a new branch of research, as Yuxuan et al. (2022) produce a similar analysis for compressible predictions at super-sonic speeds.

In this case, we have only been capable of analysing two Reynolds numbers, one at sub-critical regime and another at the super-critical regime. More data is needed for a better insight into the variation of each of the aforementioned parameters of the boundary layer, and the linear stability analysis of the profiles for the estimation of the growth rate in terms of the momentum-thickness. Therefore, not only a simple averaged behaviour can be constructed but a Reynolds-sensitive relation could be explored, always trying to make it Galilean invariant if possible.

Ultimately, not only LES simulations can help gather more knowledge about the behaviour of the laminar boundary layer for flow past a circular cylinder but also measurements or experimental data. However, with the increase of Reynolds number the boundary layer becomes so thin that measurements can become rather complicated with additional uncertainties associated with such measurements.

Chapter 9

Conclusion and Future work

9.1 Contribution of the AFT

One of the major contributions of this thesis is the implementation of the original AFT model proposed by Coder (2017) into OpenFOAMv1912, followed by its validation and verification against the original implementation for finite element methods and compared to other transitional methods, such as Langtry and Menter (2009) and Menter et al. (2015). The original meaning of only positive values for the intermittency term is recovered, as the implementation is performed in a solver using the finite volume method. On the other hand, important routines such as the conditional comparison for the F_{crit} factor and the implementation of the transport equation have been presented. As shown in Chapter 3, the results for zero pressure gradient flat-plate are satisfactory and in line with other transitional estimations with different solvers.

A second contribution, in this case with its definition and implementation by the author is the AFT-RSM model. The redefinition of the production, destruction and pressure terms are discussed along with the improvements the Reynolds Stress Closure provides compared to the Boussinesq-hypothesis along curved surfaces and sudden changes of strain rate. The implementation of the model has been verified and validated in Chapter 3 and then tested for different cases in the following chapters.

Furthermore, the redefined hybrid length scale $\tilde{d}_m$ proposed by Coder (2019) has been discussed and its implementation method has also been provided. The implementation has been verified as well in Chapter 6 and Chapter 7, where the results using the hybrid approach show superior performance at lower sub-critical, upper sub-critical, critical and super-critical regime to fully turbulent approaches and URANS AFT and AFT-RSM methods.

9.2 Analysis of AFT performance

In this thesis, the focus has been put as well into the analysis of the amplification factor transport model for transitional prediction for flow past a circular cylinder from the sub-critical to the super-critical regime using the OpenFOAM CFD package.

Before investigating transitional flow using AFT-based models, the original model proposed by Coder and the extension using a Reynolds Stress Model closure has been implemented into the OpenFOAM package successfully. Throughout the verification and validation process, it has been concluded that a minimum grid resolution of $y^+ \approx 1$ and $Dx^+ \approx 25$ is sufficient to produce a correct prediction of the transition onset for both implementations. The transition prediction using AFT-RSM is consistently delayed with the use of second-order schemes. Nonetheless, the physical behaviour of the implementation is correct with the variation of the N_{crit} factor as discussed by measurements for a natural transition case.

One of the novel analyses that is presented in this thesis, before the study of the flow past a circular cylinder, is the laminar, transitional and turbulent prediction using two-dimensional AFT and AFT-RSM for backward-facing step flow reported in experiments by Armaly et al. (1983). An expansion ratio of $H/h = 1.942$ results in the appearance of three different regions using the transitional AFT and AFT-RSM using a critical factor of 9; laminar, transitional, and turbulent regime. The dimensionless primary dimensionless length increases throughout the laminar regime up to $1200 < Re_{2h} < 1300$ using transitional AFT and AFT-RSM. This trend showed good agreement to DNS simulations while proving superior performance to fully turbulent models for Reynolds number larger than $Re_{2h} \approx 700$. At this Reynolds number, the fully turbulent model starts shortening the primary recirculation length due to the short separation bubble as it has enhanced momentum compared to the fully laminar separation predicted by the AFT-based models.

Throughout the transitional regime, whose onset is located at about $1300 < Re_{2h} < 1500$ by the transitional AFT and AFT-RSM models. It is identified by the start of a decrease in the primary recirculation length and the appearance of a third separation region. This third separation bubble has not been reported by any other author using URANS transitional approach, neither using fully turbulence models. Transitional prediction using AFT and AFT-RSM show a reducing primary recirculation region, secondary and tertiary recirculation region up to $Re_{2h} \approx 4000$, with an almost constant length down to $Re_{2h} = 5500$. The AFT-RSM in this region consistently predicts a longer recirculation length for x_1 and x_2, with a slightly better agreement to the literature data. Conversely, from $Re_{2h} \approx 700$, the fully turbulent approach predicts a similar dimension for all three bubbles.

One of the limitations of the AFT method is the recovery of fully turbulent behaviour, as the onset of the fully turbulent region is not clear with the use of transitional models as the secondary bubble does not disappear in the predictions. Thus, the onset of the region can be considered where the main recirculation region and the secondary bubble show a constant behaviour with the increase of Reynolds number.

The second novel analysis is the prediction using AFT, AFT-RSM and hybrid AFT-DDES model for flow past a circular cylinder. The study comprises the sub-critical, critical, and super-critical regimes, with a previous validation analysis with a well-benchmarked case at $Re_D = 3900$, where a limitation of the AFT model is observed for the prediction of the shear-layer transition and the improved performance by the AFT-DDES with the activation of the LES mode away from the cylinder is shown.

The use of transitional AFT and AFT-RSM with two-dimensional simulations has shown improvements in the upper sub-critical regime compared to the URANS fully turbulent approach like SST presented in this dissertation. Whereas in the lower sub-critical region ($Re_D = 3900$), the dependency of the shear-layer transition within the wake showed a poor prediction with AFT and AFT-RSM. One of the main points is the difference in the state of the separation. The transitional models are capable of producing a laminar boundary layer while the SST model assumes a turbulent boundary layer until its separation. The former assumption consequently forces the separation point to be delayed to approximately 100 degrees. As opposed to the fully turbulent prediction, the laminar boundary layer undergoes an earlier separation, with an improvement presented by the AFT and AFT-RSM. The wake then is wider; consequently, the drag predictions fall closer to the measurements available in the literature, with an increase of C_D to 1.2.

The critical region has been concluded to be complex, where the appearance of a single laminar separation bubble is predicted by neither the AFT, AFT-RSM nor the hybrid AFT-DDES. In this case, the transitional models predict a wake that is stretched as opposed to fully turbulent approaches, with a consequent reduction of the C_D with the entrance in the drag crisis. The interaction between the separation and transition location has not been captured by any of the simulations, although the AFT and AFT-RSM have shown the appearance of small separation regions with the same numerical schemes and meshes, which has not been reported by any URANS transitional model to the author's best knowledge.

The super-critical region using transitional AFT and AFT-RSM showed the prediction of two laminar separation bubbles on both sides of the cylinder surface, followed by a turbulent separation. The appearance of the bubble with a simpler model than Menter's formulations has been demonstrated. Furthermore, the predictions within the wake are in better agreement with the description of the recirculation length and peak locations

regarding the variance of the streamwise and crossflow velocity fluctuations. Nonetheless, the performance achieved by all the transitional methods is superior to the use of the fully turbulent SST method.

The AFT-DDES in the super-critical regime introduces the prediction of two laminar separation bubbles in the near-wall surface alleviating the grid requirements imposed by LES simulations as the ones presented in the literature. Furthermore, the results regarding the recirculation length are improved to pure two-dimensional simulations with URANS methods, and therefore show promising results for further investigation.

Finally, the differences between the Falkner Skan correlations and the ones achieved using LES data from sub-critical and super-critical regimes are presented and discussed. In particular, the growth of the integral shape factor is based on the local shape factor and the momentum thickness parameters. With the results, four new equations have been derived and introduced into the AFT implementation in the OpenFOAM CFD package for testing. The improvement has shown to be a 2° better prediction in the location of the separation bubble and its transition using only two different Reynolds numbers.

9.3 Future Work Suggestions

Currently, only two-dimensional simulations using the AFT and AFT-RSM have been presented for backward-facing step flow as this geometry was not the primary focus of this work. Thus, the three-dimensional flow prediction using the AFT, AFT-RSM and the hybrid AFT-DDEs is suggested as the next phase of the analysis for transitional prediction in the backward-facing step type of flow, with special emphasis on the growth of the primary recirculation length compared to two-dimensional simulations and the interaction with the secondary bubble in the laminar region; the interaction between the three recirculation regions and their three-dimensional effects in the transitional regime; and the definition of the fully turbulent regime with the transitional approaches.

In addition, the use of different expansion ratios that are already well-benchmarked would be also useful to further understand the behaviour of the model, especially for the separation bubbles prediction.

A similar suggestion is also considered for future work to do for the flow past a circular cylinder with the use of the AFT, and AFT-RSM models. The main focus should be put on the separation point of the sub-critical regime since the two-dimensional simulations showed a consistently delayed position, with changes of N_{crit}. In fact, in an analogy to the term controlling the length of the transition used in Menter's models, a term could be utilised to control such impact on the separation location.

The critical regime remains a complex region to test using URANS methods or DDES approaches, thus it is complex to establish a future work suggestion in this region as in this case LES should be used for a correct physical prediction. With the further increase of the Reynolds number, the three-dimensional analysis would give an insight into the behaviour of the separation bubble that characterises the super-critical region.

Ultimately, the need of gathering more experiments and LES simulations at different high Reynolds regimes is pivotal for work on further extensions for circular cylinder flow. As Chapter 8 demonstrated, the differences with Falkner-Skan velocity profiles are significant, especially for the boundary layer characteristics like the integral shape factor and the momentum thickness estimation. The modifications to the correlations in Chapter 8 have shown improvements of approximately 2°. More published data at higher Reynolds numbers could lead to better improvements in the transition estimation with better correlations.

Bibliography

Abbott, D. E. and Kline, S. J. Experimental Investigation of Subsonic Turbulent Flow Over Single and Double Backward Facing Steps. *Journal Basic Engineering*, 84(3): 317–325, 1962.

Abu-Ghannam, B. J. and Shaw, R. Natural Transition of Boundary Layers—The Effects of Turbulence, Pressure Gradient, and Flow History. *Journal of Mechanical Engineering Science*, 22(5):213–228, 10 1980.

Achenbach, E. Distribution of local pressure and skin friction around a circular cylinder in cross-flow up to Re = 5 × 106. *Journal of Fluid Mechanics*, 34(4):625–639, 8 1968.

Achenbach, E. and Heinecke, E. On vortex shedding from smooth and rough cylinders in the range of Reynolds numbers {6×10^3 to 5×10^6}. *Journal of Fluid Mechanics*, 109(12):239–251, 1981. ISSN 14697645.

Andersson, P., Berggren, M., and Henningson, Dan S. Optimal disturbances and bypass transition in boundary layers. *Physics of Fluids*, 11(1):134–150, 1999. ISSN 10706631.

Armaly, B. F., Dursts, F., and Pereira, J. C. F. Experimental and theoretical investigation of backward-facing step flow. *Journal of Fluid Mechanics*, 127:473–496, 1983.

Bearman, P. W. On vortex shedding from a circular cylinder in the critical Reynolds number rágime. *Journal of Fluid Mechanics*, 37(3):577–585, 1969. ISSN 14697645.

Beaudan, P. and Moin, P. Numerical experiments on the flow past a circular cylinder at sub-critical Reynolds number. TF-62. Technical report, Standford University, 1994.

Biswas, G., Breuer, M., and Durst, F. Backward-facing step flows for various expansion ratios at low and moderate reynolds numbers. *Journal of Fluids Engineering, Transactions of the ASME*, 126(3):362–374, 5 2004. ISSN 00982202.

Blackwell, J. A. Preliminary Study Of Effects Of Reynolds Number And Boundary-Layer Transition Location On Shock-Induced Separation. NASA TN D-5003. Technical report, NASA, 2013.

Blair, M. F. Boundary-Layer Transition in Accelerating Flows With Intense Freestream Turbulence: Part 1-Disturbances Upstream of Transition Onset. *Journal of Fluids Engineering*, 114(3):313–321, 9 1992a. ISSN 0098-2202.

Blair, M. F. Boundary-Layer Transition in Accelerating Flows With Intense Freestream Turbulence: Part 2-The Zone of Intermittent Turbulence. *Journal of Fluids Engineering*, 114(3):322–332, 9 1992b. ISSN 0098-2202.

Boussinesq, J. *Théorie analytique de la chaleur: mise en harmonie avec la thermodynamique et avec la théorie mécanique de la lumière*. Paris, Gauthier-Villars et fils, Paris, 1 edition, 1903.

Boyle, R. J. and Simon, F. F. Mach Number Effects on Turbine Blade Transition Length Prediction. *Journal of Turbomachinery*, 121(4):694–702, 10 1999. ISSN 0889-504X.

Bradshaw, P. Turbulence: the chief outstanding difficulty of our subject. *Experiments in Fluids*, 16:203–216, 1994. ISSN 1432-1114.

Brandt, L. and De Lange, H. C. Streak interactions and breakdown in boundary layer flows. *Physics of Fluids*, 20(2), 2008. ISSN 10706631.

Breuer, M. A challenging test case for large eddy simulation: high Reynolds number circular cylinder flow. *Journal of Heat and Fluid Flow*, 21(5):648–654, 2000. ISSN 0142-727X.

Bursnall, W. J. and Loftin, L. K. Experimental Investigation of the Pressure Distribution About a Yawed Circular Cylinder in the Critical Reynolds Number Range. TN 2463. Technical report, Langley Aeronautical Laboratory, Washington, 1951.

Cantwell, B. and Coles, D. An experimental study of entrainment and transport in the turbulent near wake of a circular cylinder. *Journal of Fluid Mechanics*, 136:321–374, 1983. ISSN 14697645.

Catalano, P., Wang, M., Iaccarino, G., and Moin, P. Numerical simulation of the flow around a circular cylinder at high Reynolds numbers. *International Journal of Heat and Fluid Flow*, 24(4):463–469, 2003. ISSN 0142727X.

Cheng, W., Pullin, D. I., Samtaney, R., Zhang, W., and Gao, W. Large-eddy simulation of flow over a cylinder with ReD from 3.9 × 103 to 8.5 × 105: A skin-friction perspective. *Journal of Fluid Mechanics*, 820:121–158, 6 2017. ISSN 14697645.

Cho, N-H., Liu, X., Rodi, W., and Schönung, B. Calculation of Wake-Induced Unsteady Flow in a Turbine Cascade. *Journal of Turbomachinery*, 115(4):675–686, 10 1993. ISSN 0889-504X.

Choi, H. Y., Nguyen, V. T., and Nguyen, J. Numerical Investigation of Backward Facing Step Flow over Various Step Angles. In *Procedia Engineering 154*, volume 154, pages 420–425, 2016.

Coder, J. G. Enhancement of the Amplification Factor Transport Transition Modeling Framework. In *55th AIAA Aerospace Sciences Meeting, AIAA 2017-1709*. American Institute of Aeronautics and Astronautics Inc., 2017. ISBN 9781624104473.

Coder, J. G. Standard Test Cases for CFD-Based Laminar-Transition Model Verification and Validation. In *2018 AIAA Aerospace Sciences Meeting, AIAA 2018-0029*, number 210059. American Institute of Aeronautics and Astronautics Inc, AIAA, 2018. ISBN 9781624105241.

Coder, J. G. Further Development of the Amplification Factor Transport Transition Model for Aerodynamic Flows. In *AIAA Scitech 2019 Forum, AIAA 2019-0039*. American Institute of Aeronautics and Astronautics Inc, AIAA, 2019. ISBN 9781624105784.

Coder, J. G. and Maughmer, M. D. Computational Fluid Dynamics Compatible Transition Modeling Using an Amplification Factor Transport Equation. *AIAA Journal*, 52(11):2506–2512, 11 2014. ISSN 1533385X.

Coder, J. G. and Ortiz-Melendez, H. D. Transitional Delayed Detached-Eddy Simulation of Multielement High-Lift Airfoils. *Journal of Aircraft*, 56(4):1303–1312, 2019.

Cutrone, L., De Palma, P., Pascazio, G., and Napolitano, M. An evaluation of bypass transition models for turbomachinery flows. *International Journal of Heat and Fluid Flow*, 28(1):161–177, 2007. ISSN 0142727X.

D'Alessandro, V., Montelpare, S., and Ricci, R. Detached–eddy simulations of the flow over a cylinder at Re = 3900 using OpenFOAM. *Computers and Fluids*, 136:152–169, 9 2016. ISSN 00457930.

Denham, M. K. and Patrick, M. A. Laminar Flow over a Downstream-Facing, Step in a Two-Dimensional Flow Channel. *Transactions of the Institution of Chemical Engineers*, 52:361–367, 1974.

Denison, M. and Pulliam, T. H. Implementation and assessment of the amplification factor transport laminar-turbulent transition model. In *2018 Fluid Dynamics Conference, AIAA 2018-3382*. American Institute of Aeronautics and Astronautics Inc, AIAA, 2018. ISBN 9781624105531.

Dhawan, S. and Narasimha, R. Some properties of boundary layer flow during the transition from laminar to turbulent motion. *Journal of Fluid Mechanics*, 3(4):418–436, 1958. ISSN 14697645.

Dick, E. and Kubacki, S. Transition models for turbomachinery boundary layer flows: A review. *International Journal of Turbomachinery, Propulsion and Power*, 2(2), 4 2017. ISSN 2504186X.

Dong, S., Karniadakis, G. E., Ekmekci, A., and Rockwell, D. A combined direct numerical simulation-particle image velocimetry study of the turbulent near wake. *Journal of Fluid Mechanics*, 569:185–207, 2006. ISSN 14697645.

Dopazo, C. On conditioned averages for intermittent turbulent flows. *Journal of Fluid Mechanics*, 81(3):433–438, 1977. ISSN 14697645.

Drela, M. and Giles, M. B. Viscous-inviscid analysis of transonic and low Reynolds number airfoils. *AIAA Journal*, 25(10):1347–1355, 1987. ISSN 00011452.

Driver, D. M. and Seegmiller, H. L. Features of a reattaching turbulent shear layer in divergent channel flow. *AIAA Journal*, 23(2):163–171, 1985. ISSN 00011452.

Dryden, H. L. Turbulence and the Boundary Layer. *Journal of the Aeronautical Sciences*, 6(3):85–100, 1 1939.

Durst, F. and Tropea, C. Flows over Two-Dimensional Backward-Facing Steps. In *Dumas, R., Fulachier, L. (eds) Structure of Complex Turbulent Shear Flow. International Union of Theoretical and Applied Mechanics.*, pages 41–52, Berlin, Heidelberg, 1981. Springer.

Eisfeld, B., Rumsey, C., and Togiti, V. Verification and validation of a second-moment-closure model. *AIAA Journal*, 54(5):1524–1541, 2016. ISSN 00011452.

Emmons, H. W. The Laminar-Turbulent Transition in a Boundary Layer-Part I. *Journal of the Aeronautical Sciences*, 18(7):490–498, 7 1951.

Erturk, E. Numerical solutions of 2-D steady incompressible flow over a backward-facing step, Part I: High Reynolds number solutions. *Computers and Fluids*, 37(6):633–655, 2008. ISSN 00457930.

Fage, B. A. and Falkner, V. M. Further experiments on the flow around a circular cylinder. No. 1369. Technical report, Aeronautical Research Committee, 1931.

Falkner, V. M. and Skan, S. W. LXXXV. Solutions of the boundary-layer equations. *The London, Edinburgh, and Dublin Philosophical Magazine and Journal of Science*, 12(80):865–896, 11 1931. ISSN 1941-5982.

Farell, C. and Blessmann, J. On critical flow around smooth circular cylinders. *Journal of Fluid Mechanics*, 136:375–391, 1983. ISSN 14697645.

Fürst, J., Příhoda, J., and Straka, P. Numerical simulation of transitional flows. *Computing*, 95(1):163–182, 5 2013. ISSN 0010485X.

Gaster, M. The Structure and Behavior of Laminar Separation Bubbles. No. 3595. Technical report, Aeronautical Research Council, 1969.

Germano, M., Piomelli, U., Moin, P., and Cabot, W. H. A dynamic subgrid-scale eddy viscosity model. *Physics of Fluids A*, 3(7):1760–1765, 1991. ISSN 08998213.

Giedt, W. H. Effect of Turbulence Level of Incident Air Stream on Local Heat Transfer and Skin Friction on a Cylinder. *Journal of the Aeronautical Sciences*, 18(11):725–730, 11 1951.

Gleyzes, C., Cousteix, J., and Bonnet, J. L. Theoretical and Experimental Study of Low Reynolds Number Transitional Separation Bubbles. In *Proceeding of the conference on low Reynolds number airfoil aerodynamics*, pages 137–152, 1985.

Gostelow, J. P., Blunden, A. R., and Walker, G. J. Effects of Free-Stream Turbulence and Adverse Pressure Gradients on Boundary Layer Transition. *Journal of Turbomachinery*, 116(3):392–404, 7 1994. ISSN 0889-504X.

Greenshields, C. and Weller, H. *Notes on Computational Fluid Dynamics: General Principles*. CFD Direct Ltd, Reading, UK, 2022.

Jacobs, R. G. and Durbin, P. A. Simulations of bypass transition. *Journal of Fluid Mechanics*, 428:185–212, 2001. ISSN 00221120.

Jenkins, L. N., Neuhart, D. H., Mcginley, C. B., Choudhari, M. M., Khorrami, M. R., and Francisco, S. Measurements of Unsteady Wake Interference Between Tandem Cylinders. In *36th AIAA Fluid Dynamics Conference and Exhibit, AIAA 2006-3202*, San Francisco, California, 6 2006.

Johnson, M. W. and Ercan, A. H. A physical model for bypass transition. *International Journal of Heat and Fluid Flow*, 20(2):95–104, 1999.

Jones, W. P. and Launder, B. E. The prediction of laminarization with a two-equation model of turbulence. *International Journal of Heat and Mass Transfer*, 15(2):301–314, 2 1972. ISSN ISSN 0017-9310.

Julien, H. L., Kays, W. M., and Moffat, R. J. The turbulent boundary layer on a porous plate - An experimental study of the effects of a favorable pressure gradient. Report HMT-4. Technical report, Standford University, 4 1969.

Kendall, J. M. Experiments on boundary-layer receptivity to freestream turbulence. In *36th AIAA Aerospace Sciences Meeting and Exhibit*, pages 1–14, 1997.

Kim, S-E. Large Eddy Simulation of Turbulent Flow Past a Circular Cylinder in Subcritical Regime. In *44th AIAA Aerospace Sciences Meeting and Exhibit, AIAA 2006-1418*, Reno, Nevada, 1 2006.

Klebanoff, P. S. Effect of free-stream turbulence on a laminar boundary layer. In *Bulletin of the American Physical Society. 10, 1323*, 1971.

Klebanoff, P. S., Tidstrom, K. D., and Sargent, L. M. The three-dimensional nature of boundary-layer instability. *Journal of Fluid Mechanics*, 12(1):1–34, 1962. ISSN 14697645.

Kožulović, D. and Lapworth, B. L. An Approach for Inclusion of a Nonlocal Transition Model in a Parallel Unstructured Computational Fluid Dynamics Code. *Journal of Turbomachinery*, 131(3):031008–031015, 4 2009. ISSN 0889504X.

Kravchenko, A. G. and Moin, P. Numerical studies of flow over a circular cylinder at ReD=3900. *Physics of Fluids*, 12(2):403–417, 2000. ISSN 10706631.

Kuan, C. L. and Wang, T. Investigation of the intermittent behavior of transitional boundary layer using a conditional averaging technique. *Experimental Thermal and Fluid Science*, 3(2):157–173, 1990. ISSN 0894-1777.

Langtry, R. B. and Menter, F. R. Correlation-Based Transition Modeling for Unstructured Parallelized Computational Fluid Dynamics Codes. *AIAA Journal*, 47(12): 2894–2906, 12 2009. ISSN 00011452.

Langtry, R. B., Menter, F. R., Likki, S. R., Suzen, Y. B., Huang, P. G., and Völker, S. A correlation-based transition model using local variables - Part II: Test cases and industrial applications. *Journal of Turbomachinery*, 128(3):423–434, 2006. ISSN 0889504X.

Le, Hung, Moin, Parviz, and Kim, John. Direct numerical simulation of turbulent flow over a backward-facing step. *Journal of Fluid Mechanics*, 330:349–374, 1 1997. ISSN 00221120.

Lee, T. and Mateescu, D. Experimental and numerical investigation of 2-D backward-facing step flow. *Journal of Fluids and Structures*, 12(6):703–716, 1998.

Leib, S. J., Wundrow, D. W., and Goldstein, M. E. Effect of free-stream turbulence and other vortical disturbances on a laminar boundary layer. *Journal of Fluid Mechanics*, 380:169–203, 2 1999. ISSN 00221120.

Libby, P. A. On the prediction of intermittent turbulent flows. *Journal of Fluid Mechanics*, 68(2):273–295, 4 1975.

Liepmann, H. W. Investigations on laminar boundary-layer stability and transition on curved boundaries. Technical report, California Institute of Technology, Pasadena, 1943.

Liu, X., Thompson, D. J., and Hu, Z. Numerical investigation of aerodynamic noise generated by circular cylinders in cross-flow at Reynolds numbers in the upper subcritical and critical regimes. *International Journal of Aeroacoustics*, 18(4-5):470–495, 7 2019. ISSN 20484003.

Lourenco, L. M. and Shih, C. Characteristics of the Plane Turbulent Near Wake of a Circular Cylinder. *A Particle Image Velocimetry Study*, 1993.

Luchini, P. Reynolds-number-independent instability of the boundary layer over a flat surface: Optimal perturbations. *Journal of Fluid Mechanics*, 404:289–309, 2 2000. ISSN 00221120.

Lysenko, D.A., Ertesvåg, I. S., and Rian, K. E. Large-eddy simulation of the flow over a circular cylinder at reynolds number 3900 using the openfoam toolbox. *Flow, Turbulence and Combustion*, 89(4):491–518, 12 2012. ISSN 13866184.

Ma, X., Karamanos, G. S., and Karniadakis, G. E. Dynamics and low-dimensionality of a turbulent near wake. *Journal of Fluid Mechanics*, 410:29–65, 5 2000. ISSN 00221120.

Mack, L. M. Transition and Laminar Instability. NASA-CR-153203. Technical report, Jet Propulsion Laboratory, Pasadena, 5 1977.

Malkiel, E. and Mayle, R. E. Transition in a Separation Bubble. *Journal of Turbomachinery*, 118(4):752–759, 1996.

Mayle, R. E. The Role of Laminar-Turbulent Transition in Gas Turbine Engines. *Proceedings of the ASME 1991 International Gas Turbine and Aeroengine Congress and Exposition. Volume 5: Manufacturing Materials and Metallurgy; Ceramics; Structures and Dynamics; Controls, Diagnostics and Instrumentation*, 113(4), 1991.

Mayle, R. E. and Schulz, A. Heat Transfer Committee and Turbomachinery Committee Best Paper of 1996 Award: The Path to Predicting Bypass Transition. *Journal of Turbomachinery*, 119(3):405–411, 1997. ISSN 0889-504X.

Medina, H. and Early, J. Modelling transition due to backward-facing steps using the laminar kinetic energy concept. *European Journal of Mechanics, B/Fluids*, 44:60–68, 2014. ISSN 09977546.

Menter, F. R. Zonal Two Equation k-\omega Turbulence Models for Aerodynamic Flows. In *23rd Fluid Dynamics, Plasmadynamics and Lasers, AIAA 93-2906*, 1993.

Menter, F. R. Two-equation eddy-viscosity turbulence models for engineering applications. *AIAA Journal*, 32(8):1598–1605, 1994. ISSN 00011452.

Menter, F. R., Esch, T., and Kubacki, S. Transition Modelling Based On Local Variables. In *5th International Symposium on Turbulence Modeling and Measurements*, pages 555–564, 2002. ISBN 9780080441146.

Menter, F. R., Langtry, R. B., Likki, S. R., Suzen, Y. B., Huang, P. G., and Völker, S. A Correlation-Based Transition Model Using Local Variables—Part I: Model Formulation. *Journal of Turbomachinery*, 128(3):413–423, 2006.

Menter, F. R., Smirnov, P. E., Liu, T., and Avancha, R. A One-Equation Local Correlation-Based Transition Model. *Flow, Turbulence and Combustion*, 95(4):583–619, 12 2015. ISSN 15731987.

Michelassi, V., Martelli, F., Denós, R., Arts, T., and Sieverding, C. H. Unsteady Heat Transfer in Stator–Rotor Interaction by Two-Equation Turbulence Model. *Journal of Turbomachinery*, 121(3):436–447, 7 1999. ISSN 0889-504X.

Michelassi, V., Wissink, J. G., Fröhlich, J., and Rodi, W. Large Eddy Simulation of Flow around a Turbine Blade with Incoming Wakes. *AIAA Journal*, 41(11):2143–2156, 2003.

Mockett, C, Perrin, R, Reimann, T, Braza, M, and Thiele, F. Analysis of Detached-Eddy Simulation for the Flow Around a Circular Cylinder with Reference to PIV Data. In *IUTAM Symposium on Unsteady Separated Flows and their Control*, pages 417–427, 2009.

Morkovin, M. V. On the many faces of transition. In *Wells, C.S. (eds) Viscous Drag Reduction*, Boston, MA, 1969. Springer. ISBN 978-1-4899-5581-4.

Moss, W. D., Baker, S., and Bradbury, L. J. S. Measurements of Mean Velocity and Reynolds Stresses in Some Regions of Recirculating Flow. In *Turbulent Shear Flows I*, pages 198–207, Berlin, 1979. Springer.

Mouza, A. A., Pantzali, M.N., Paras, S. V., and Tihon, J. Experimental and numerical study of backward-facing step flow. In *5th National Chemistry Engineering Conference*, 2005.

Norberg, C. An experimental investigation of the flow around a circular cylinder: Influence of aspect ratio. *Journal of Fluid Mechanics*, 258:287–316, 1994. ISSN 14697645.

Ong, L and Wallace, J. The velocity field of the turbulent very near wake of a circular cylinder. In *Experiments in Fluids 20*, pages 441–453. Springer-Verlag, 1996.

Parnaudeau, P., Carlier, J., Heitz, D., and Lamballais, E. Experimental and numerical studies of the flow over a circular cylinder at Reynolds number 3900. *Physics of Fluids*, 20(8), 2008. ISSN 10706631.

Pereira, F. S., Vaz, G., Eça, L., and Girimaji, S. S. Simulation of the flow around a circular cylinder at Re=3900 with Partially-Averaged Navier-Stokes equations. *International Journal of Heat and Fluid Flow*, 69:234–246, 2 2018. ISSN 0142727X.

Pont-Vílchez, A., Trias, F. X., Gorobets, A., and Oliva, A. Direct numerical simulation of backward-facing step flow at Reτ = 395 and expansion ratio 2. *Journal of Fluid Mechanics*, 863:341–363, 3 2019. ISSN 14697645.

Pope, Stephen B. *Turbulent Flows*. Cambridge University Press, Cambridge, 2000. ISBN 9780511840531.

Prasad, A. and Williamson, C. H. K. The instability of the shear layer separating from a bluff body. *Journal of Fluid Mechanics*, 333:375–402, 2 1997. ISSN 00221120.

Rani, H. P., Sheu, Tony W. H., and Tsai, Eric S. F. Eddy structures in a transitional backward-facing step flow. *Journal of Fluid Mechanics*, 588:43–58, 10 2007. ISSN 14697645.

Ratha, D. and Sarkar, A. Analysis of flow over backward facing step with transition. *Frontiers of Structural and Civil Engineering*, 9(1):71–81, 4 2015. ISSN 20952449.

Roberts, S. K. and Yaras, M. I. Boundary-layer transition affected by surface roughness and free-stream turbulence. *Journal of Fluids Engineering*, 127(3):449–457, 2 2005. ISSN 00982202.

Rodriguez, I. and Lehmkuhl, O. On the characteristics of the super-critical wake behind a circular cylinder. *Fluids*, 6(11), 11 2021. ISSN 23115521.

Rodríguez, I., Lehmkuhl, O., Chiva, J., Borrell, R., and Oliva, A. On the flow past a circular cylinder from critical to super-critical Reynolds numbers: Wake topology and vortex shedding. Technical report, 2015.

Roshko, Anatol. Experiments on the flow past a circular cylinder at very high Reynolds number. *Journal of Fluid Mechanics*, 10(3):345–356, 1961. ISSN 14697645.

Schäfer, F., Breuer, M., and Durst, F. The dynamics of the transitional flow over a backward-facing step. *Journal of Fluid Mechanics*, 623:85–119, 2009. ISSN 14697645.

Schewe, Günter. On the force fluctuations acting on a circular cylinder in crossflow from subcritical up to transcritical Reynolds numbers. *Journal of Fluid Mechanics*, 133: 265–285, 1983. ISSN 14697645.

Schilichting, H. *"Zur Enstehung der Turbulenz bei der Plattenströmung". Nachrichten der Gesellschaft der Wissenschaften – enshaften zu Göttingen, Mathematisch – Physikalische zu Göttingen, Mathematisch – Physikalische Klasse.* 1931.

Schubauer, G. B. and Klebanoff, P. S. Contributions on the Mechanics of Boundary-Layer Transition. NACA-TR-1289. Technical report, 1956.

Schubauer, G. B. and Skramstad, H. K. Laminar Boundary-Layer Oscillations and Stability of Laminar Flow. *Journal of the Aeronautical Sciences*, 14(2):69–78, 2 1947.

Schultz, Michael P. and Volino, Ralph J. Effects of Concave Curvature on Boundary Layer Transition Under High Freestream Turbulence Conditions. *Journal of Fluids Engineering*, 125(1):18–27, 2003. ISSN 0098-2202.

Shih, W. C.L., Wang, C., Coles, D., and Roshko, A. Experiments on flow past rough circular cylinders at large Reynolds numbers. *Journal of Wind Engineering and Industrial Aerodynamics*, 49(1):351–368, 1993. ISSN 01676105.

Shur, Mikhail L., Spalart, Philippe R., Strelets, Mikhail K., and Travin, Andrey K. A hybrid RANS-LES approach with delayed-DES and wall-modelled LES capabilities. *International Journal of Heat and Fluid Flow*, 29(6):1638–1649, 12 2008. ISSN 0142727X.

Smagorinsky, J. General Circulation Experiments with the Primitive Equations. *Monthly Weather Review*, 91(3):99–164, 1963.

Smith, A. and Gamberoni, N. Transition, Pressure Gradient, and Stability Theory. Technical report, Douglas Aircraft Company, El Segundo, California, 1956.

Spalart, P. R. and Allmaras, S. R. A One-equation Turbulence Model for Aerodynamic Flows. In *AIAA 30th Aerospace Sciences Meeting and Exhibit, AIAA 92-0439*, pages 5–21, 1994.

Spalart, P. R., Deck, S., Shur, M. L., Squires, K. D., Strelets, M. Kh, and Travin, A. A new version of detached-eddy simulation, resistant to ambiguous grid densities. *Theoretical and Computational Fluid Dynamics*, 20(3):181–195, 7 2006. ISSN 09354964.

Spalart, P.R, Jou, W.-H., Strelets, M., and Allmaras, S.R. Comments on the feasibility of LES for wings, and on hybrid RANS/LES approach. In *Advances in DNS/LES*, pages 137–148. Greyden Press, 1997. ISBN 1570743657.

Spitzer, Robert Edward. *Measurements of Unsteady Pressures and Wake Fluctuations for Flow Over a Cylinder at Supercritical Reynolds Number. Engineer's thesis.* PhD thesis, California Institute of Technology, 1965.

Steelant, J. and Dick, E. Modelling of bypass transition with conditioned Navier-Stokes equations coupled to an intermittency transport equation. *International Journal for Numerical Methods in Fluids*, 23(3):193–220, 1996. ISSN 0271-2091.

Suzen, Y. B., Huang, P. G., Hultgren, Lennart S., and Ashpis, David E. Predictions of separated and transitional boundary layers under low-pressure turbine airfoil conditions using an intermittency transport equation. *Journal of Turbomachinery*, 125(3): 455–464, 8 2003.

Tollmien, Walter. Grenzschichttheori. In *Handbuch der Experimentalphysik IV, 1*, pages 239–287, Leipzig, 1931.

Travin, A., Shur, M., Strelets, M., and Spalart, P. Detached-Eddy Simulations Past a Circular Cylinder. *Flow, Turbulence and Combustion*, 63:293–313, 1999.

van Ingen, J. L. A Suggested Semi-empirical Method for the Calculation of the Boundary Layer Transition Region. Technical report, Delf University of Technology, Delft, 1956.

Van Ingen, J. L. The eN method for transition prediction. Historical review of work at TU Delft. In *38th Fluid Dynamics Conference and Exhibit, AIAA 2008-3830*, Seattle, 2008.

Vancoillie, G. and Dick, E. A Turbulence Model for the Numerical Simulation of Transitional Boundary Layers. In *Kozlov, V.V. (eds) Laminar-Turbulent Transition. International Union of Theoretical and Applied Mechanics*, volume 1, Berlin, Heidelberg, 1988. Springer. ISBN 978-3-642-82464-7.

Vaz, G., Mabilat, C., van der Wal MARIN, R., and Gallagher, P. Viscous Flow Computations on a Smooth Cylinders: A Detailed Numerical Study With Validation. In *ASME 2007 26th International Conference on Offshore Mechanics and Arctic Engineering*, 2009.

Volino, R. J. A New Model for Free-Stream Turbulence Effects on Boundary Layers. *Journal of Turbomachinery*, 120(3):613–620, 1998. ISSN 0889-504X.

Volino, R. J. and Simon, T. W. Boundary Layer Transition Under High Free-Stream Turbulence and Strong Acceleration Conditions: Part 2-Turbulent Transport Results. *Journal of Heat Transfer*, 119(3):420–426, 1997. ISSN 0022-1481.

Wang, L., Hu, R., Li, L., and Fu, S. Detached-eddy simulation of flow past a backward-facing step with a harmonic actuation. In *Congress of the international council of the aeronautical sciences*, 2014.

Warming, R. F. and Beam, Richard M. Upwind second-order difference schemes and applications in aerodynamic flows. *AIAA Journal*, 14(9):1241–1249, 1976. ISSN 00011452.

Weidman, P. *Wake transition and blockage effects on cylinder base pressures. Engineer's thesis,*. PhD thesis, California Institute of Technology, 1968.

West, G. S. and Apelt, C. J. The effects of tunnel blockage and aspect ratio on the mean flow past a circular cylinder with Reynolds numbers between 104 and 105. *Journal of Fluid Mechanics*, 114:361–377, 1982. ISSN 14697645.

Westin, K. J.A., Boiko, A. V., Klingmann, B. G.B., Kozlov, V. V., and Alfredsson, P. H. Experiments in a boundary layer subjected to free stream turbulence. Part 1. Boundary layer structure and receptivity. *Journal of Fluid Mechanics*, 281(4): 193–218, 12 1994. ISSN 14697645.

White, Frank M. *Viscous Fluid Flow*. McGraw-Hill, New York, third edition edition, 2006.

Wilcox, David. *Turbulence Modelling for CFD*. DCW Industries, Incorporated, 1994. ISBN 9780963605108.

Wu, X. and Durbin, Paul A. Boundary Layer Transition Induced by Periodic Wakes. *Journal of Turbomachinery*, 122(3):442–449, 11 1998. ISSN 0889-504X.

Wu, X., Jacobs, R. G., Hunt, Julian C.R., and Durbin, Paul A. Simulation of boundary layer transition induced by periodically passing wakes. *Journal of Fluid Mechanics*, 398:109–153, 11 1999. ISSN 00221120.

Wu, X., Moin, P., Wallace, James M., Skarda, J., Lozano-Durán, A., and Hickey, J. P. Transitional-turbulent spots and turbulent-turbulent spots in boundary layers. *Proceedings of the National Academy of Sciences of the United States of America*, 114 (27):E5292–E5299, 7 2017. ISSN 10916490.

Yuxuan, W., Jiakuan, X., Lei, Q., Yang, Z., and Junqiang, B. Improved Amplification Factor Transport Transition Model for Transonic Boundary Layers. In *AIAA AVIATION 2022 Forum, AIAA 2022-4030*, 2022.

Zdravkovich, M. M. *Flow around Circular Cylinders. Volume I: Fundamentals*, volume 1. Oxford Science Publications, 1997. ISBN 9780198563969.

Zheng, Z. and Lei, J. Application of the Γ-ReΘTransition Model to Simulations of the Flow Past a Circular Cylinder. *Flow, Turbulence and Combustion*, 97(2):401–426, 9 2016. ISSN 15731987.